UNIVERSITÄT
DUISBURG
ESSEN

Open-Minded

Beyond Universality

Deviations of spectral statistics and collective short time phenomena in many-body quantum chaos

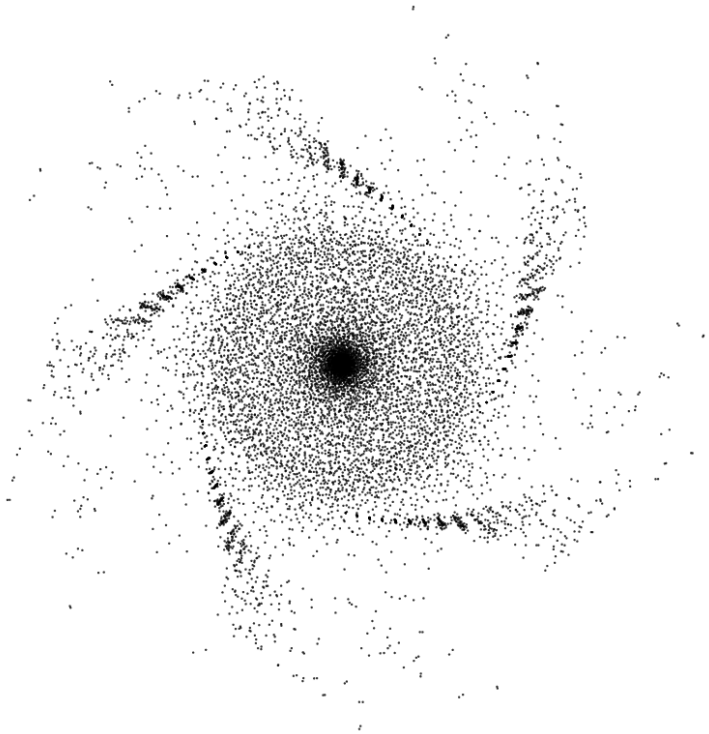

Dissertation by **Maram Akila** from Münster

November, 2017

Beim Fachbereich Physik der Universität Duisburg-Essen zum
Erwerb des Doktorgrades „Dr. rer. nat.“ vorgelegte Dissertation.

Tag der Disputation:	15. Februar 2018
Erstgutachter:	Prof. Dr. Thomas Guhr
Zweitgutachter:	Prof. Dr. Klaus Richter
Drittgutachter:	Prof. Dr. Klaus Hornberger
Komissionsvorsitz:	Prof. Dr. Heiko Wende
weiterer Prüfer:	Dr. habil. Alfred Hucht

inter·esse (*lat.*): to lie in-between

Acknowledgment

The essential ingredient to a journey is not its destination, but the road traveled. To this end, I'd like to thank all those people who kept me company throughout the years. This includes my former office mates Martin Theissen, who showed me new ways of living, Joachim Sicking and Lukas Gathmann as well as Sebastian Krause and all other current and former members of our group. I owe further thanks to Daniel Waltner and Petr Braun, who were always there when I had questions regarding our common projects. All along the way, Boris Gutkin was at my side making this as much his journey as it was mine. I feel deep gratitude for his presence and assistance. With his keen intellect and observant eye he pointed out many of the trek's vistas. Yet, while I traversed unknown lands it was due to Thomas Guhr's persistent efforts and guidance that I did not go astray and finally reached the harbor. I'd like to thank him, and the other collaborators, for their patience. Both for when I felt the need to explore the surroundings but more so for when I got lost at see. Last, not least, I also owe thanks to my mother and late grandmother for their support through all phases of this endeavour.

Spektralstatisitk abseits der standard Universalitätsklassen

Zufallsmatrixtheorie (RMT) und Semiklassik stellen zwei Methoden zum Studium chaotischer Quantenspektren dar. Erstere beschreibt für gewöhnlich die Spektralstatistik auf Skalen des mittleren Niveauabstandes, für welche man universelle Eigenschaften findet. Ausgehend vom semiklassischen Ansatz, dass eine Korrespondenz zwischen dem quantenmechanischen Spektrum und der klassischen Dynamik eines Systems besteht, wird dieser Bereich gleichermaßen durch klassische Langzeiteigenschaften beschrieben. Im ersten Teil dieser Arbeit nutzen wir diesen Zusammenhang für Studien an einem Quantengraphen mit gebrochener Zeitumkehrinvarianz. In physikalsichen Systemen ist diese Invarianz oft jedoch nicht vollständig gebrochen, was wir durch eine Rang-1 Störung im Quantensystem abbilden. Dies führt zu einem RMT Model abseits der standard Universalitätsklassen. Weiterhin zeigt sich, dass das Ergebnis sowohl von spezifischen Eigenschaften des Graphen als auch vom Rang der Störung abhängt. Der zweite Teil der Arbeit widmet sich einem diametralen Grenzfall: anstelle langer Zeiten untersuchen wir, innerhalb einer Spinkette, kurze Zeitskalen, auf denen Univeralität nicht zu erwarten ist. In diesen Systemen spielt die Teilchenzahl eine ähnliche Rolle wie die Zeit, entsprechend weist das Kurzzeitverhalten bemerkenswerte Übereinstimmungen zum Langzeitverhalten von Systemen mit wenigen Freiheitsgeraden auf. Zum Beispiel ist es möglich einen „Zeitentwicklungsoperator“ in räumlicher Richtung aufzustellen. Dieser Zugang ermöglicht es uns Spektralstatistik auf langreichweitigen Energieskalen zu studieren und, zum ersten Mal, periodische Bahnen im Quantenspektrum eines Vielteilchensystems zu identifizieren.

Spectral Statisitic Beyond the Standard Universality Classes

Random matrix theory (RMT) and semi-classical methods are both used to study the spectra of chaotic quantum systems. The former is usually applied to small distances within the spectrum residing on scales of the mean level spacing where the phenomenon of universality emerges. Through the quantum-classical correspondence provided by semi-classics this regime is, conversely, described by long time dynamical properties of the classical system. In the first half of this thesis we explore such a connection for the study of spectral properties of quantum graphs with dynamically broken time reversal invariance. In physical systems this invariance is often not fully broken and to emulate this we include a rank-1 perturbation on the quantum level resulting in a RMT model outside of the usual universality classes. As we further show, the outcome can depend on graph specific properties and the rank of the perturbation. For the second half of the thesis we consider an opposite limit: instead of long times we study short times, on which universality can not be expected, in a chain-like spin system. In these systems the number of spins takes on a similar role as time, therefore the short time behavior in long chains has remarkable similarities to long time dynamics in few-body system. For instance, the formulation of an "evolution" operator in spatial direction is possible. Exploring this spatial-time duality we address long range spectral statistic in many-body systems and, for the first time, resolve periodic orbits in a genuine many-body system from the traces of its quantum evolution.

List of Publications

Parts of this thesis are included in the following publications:

[1] M. Akila and B. Gutkin, *Spectral statistics of nearly unidirectional quantum graphs*, Journal of Physics A **48**, 34 (2015)

[2] M. Akila, D. Waltner, B. Gutkin, and T. Guhr, *Particle-time duality in the kicked Ising spin chain*, Journal of Physics A **49**, 37 (2016)

[3] M. Akila, D. Waltner, B. Gutkin, P. Braun, and T. Guhr, *Semiclassical Identification of Periodic Orbits in a Quantum Many-Body System*, Phys. Rev. Lett. **118**, 16 (2017)

[4] M. Akila, B. Gutkin, P. Braun, D. Waltner, and T. Guhr, *Semiclassical Prediction of Large Spectral Fluctuations in Interacting Kicked Spin Chains*, Annals of Physics **389**, 250 (2018)

[5] M. Akila, D. Waltner, B. Gutkin, P. Braun and T. Guhr, *Collectivity and Periodic Orbits in a Chain of Interacting, Kicked Spins*, Acta Physica Polonica A **132**, 6 (2017)

The following publication is not part of this thesis:

[6] D. Waltner, P. Braun, M. Akila, and T. Guhr, *Trace formula for interacting spins*, Journal of Physics A **50**, 8 (2017)

Author Contributions

[1] The publication concerns the nearest neighbor spacing distribution of (perturbed) unidirectional quantum graphs. The theoretical and numerical calculations were performed by me under supervision of Boris Gutkin. The text was written by me as well, and includes corrections of Boris Gutkin.

[2] In this article we generalize a newly developed duality relation, going back to B. Gutkin and V. Osipov, from coupled cat maps to physically realizable kicked spin systems. The study of quantum many-body systems has a long tradition within this group, and the research was supervised and guided by Thomas Guhr. The work has a strong focus on numerical results, which were my responsibility. The theoretical calculations were performed by me as well as Boris Gutkin, Daniel Waltner additionally contributed to the Jordan-Wigner transformation for the unitary operator. The text was partially written by Boris Gutkin and by me.

[3] This letter informs on a semi-classical extension of the spin chain in [2] and presents a study of classical periodic orbits in the (quantum) many-body system. The calculations are my own work, the text is a collaborative effort of all authors.

[4] The article reports on the details behind [3] and largely extends the previous results, including new methods. The discovery of the papers results goes back to me, but some of their theoretical explanations emerged during joint discussions between Boris Gutkin and myself. For those the text is a collaboration, and otherwise written by me.

[5] A conference proceeding that summarizes the results from [3] and [4], the text was written by Thomas Guhr.

Contents

1. Introduction

The appearance of the physical world strongly depends on the scales on which it is probed. While this statement holds for a wealth of possible examples one of the most prominent ones is found in the discrepancy between classical mechanics and quantum theory. As an example we may consider the Hydrogen atom, a single electron bound to a proton. From the point of classical physics this problem is equivalent to a planet orbiting the sun. But, due to its microscopic scale the atom belongs to the quantum realm with all its peculiarities, for instance the system energy is quantized. It is not surprising that in the 1910's the first attempts to understand this, nowadays referred to as old quantum theory [7–10], were solely grounded on classical reasoning. They are based on a heuristically introduced quantization of the integrals of motion, *i.e.* the conserved quantities, of the classical system, including the energy. Although, at the time this Bohr-Sommerfeld-quantization [10] had no formal justification, it could explain the energy spectra of (simple) integrable systems correctly. However, this scheme only works for integrable systems as they posses a sufficient number of conserved quantities. While it can explain the Hydrogen spectrum it fails already on the level of the 3-body interaction present in neutral Helium. This already hints at a delicate connection between classical and quantum mechanics.

To surmount its shortcomings the old quantum theory had to be replaced by the modern one based on the Schrödinger equation. It describes all physical systems independently of their classical dynamics. But, the classical world still lurks in the background. This resembles the relationship between the Maxwell wave equations and geometrical ray optics. In a similar way a transition towards a classical description of quantum mechanics is achieved if the exact propagator is replaced with the Van-Vleck approximation developed in 1929 [11, 12]. It describes the evolution of wave-functions in terms of classical paths. The conditions for its applicability are rather similar to the ones of geometrical optics, namely the wavelength, in quantum mechanics governed by $\hbar$, has to be significantly shorter than all (relevant) classical length scales in the system. The field of semi-classics thrives on this limiting case where the classical features of a quantum system emerge.

In the 1970's Gutzwiller used the Van-Vleck propagator as a starting point to return to the questions of old quantum theory. In this way he connected the periodic orbits of the classical system to the problem of determining the quantum spectrum. Importantly, this freed the semi-classical theory from its shackles to integrability and allowed its application to chaotic systems [13]. In these cases the sum over all classical

periodic orbits, the Gutzwiller trace formula, encodes the spectrum. Equipped with these tools the field of semi-classics could finally treat systems like the Helium atom [14] and a systematic study of quantum chaos became possible. It thus found application to spectral properties in a variety of chaotic systems, for instance the Hydrogen atom in a strong magnetic field [15, 16], all possible forms of quantum billiards [17] and systems with a more conceptual focus such as the kicked tops and rotors [18–21] or quantum graphs [22–25]. Other directions in quantum chaos use approximations to the propagation and treat *e.g.* transport problems, such as conductance, which arise in mesoscopic physics [26, 27].

While this semi-classical method forms one of the pillars of quantum chaos the other one is provided by random matrix theory (RMT) [28, 29]. In many cases of complex systems, especially if composed of many constituents, a straightforward calculation based on first principles quantum mechanics is not feasible. For instance, this was, and still is, the case for heavy nuclei. As a way to analyse statistical properties of their spectra Wigner suggested in the 1950's a comparison to the spectra of random matrix ensembles [30, 31]. This led to the fairly surprising discovery of spectral universality. If probed on scales of the mean level spacing Δ between the eigenvalues both, the measured nuclear spectrum and a random matrix, have similar spectral statistics. For the random matrix only the fundamental symmetries of the physical system, foremost the presence or absence of time reversal invariance, have to be preserved [33]. This distinguishes three different classes with differing statistics. Figure 1.1 depicts the spacing distribution $p(s)$ between the nearest neighboring levels on scales of Δ of one of these nuclear measurements. The solid lines give a comparison to RMT results. A prominent feature is the level repulsion between the eigenvalues, *i.e.* $p(s) \propto s^\beta$, indicative of a spectral rigidity. This feature is common to all three classes while the value of $\beta = 1, 2, 4$ differentiates between them. Shown is the case with intact invariance, $\beta = 1$ (GOE), and, for comparison, the outcome for completely independent levels (Poisson) where level repulsion is absent.

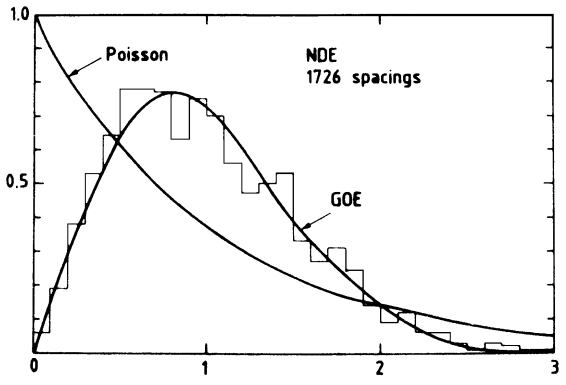

Fig. 1.1.: $p(s)$ for the nuclear data ensemble (histogram) and RMT comparison (bold lines), figure taken from [32] via [28]

It became an important question where the limits of this universality would lie. How much of the complexity of the nucleus as an interacting many-body system would be needed? Unexpectedly, it turned out that already a single particle quantum system

may exhibit universal spectral statistics provided its classical counter part has (fully) chaotic dynamics. After initial observations by [34] this famous conjecture was put forward by Bohigas-Giannoni-Schmit (BGS) in the 1980's [35], but its justification remained an open question. Since RMT is a heuristic method, it does not rely on any specifics of the underlying model for its conclusions. On the downside, it also provides no insight into the internal workings of the underlying physical model. For this, one has to resort to first principle theories. For (fully) chaotic systems the Gutzwiller trace formula could be used to justify the BGS conjecture. Along its lines Berry obtained in 1985 [36] the leading order of the spectral form factor by taking into account diagonal correlations between periodic orbits. But to understand the full RMT result non trivial correlations between the orbit actions have to be considered. This was achieved in 2001 when Sieber and Richter discovered the corresponding correlation mechanism, see [37], which they used to derive the next order correction. Soon thereafter this approach was extended in 2004 to obtain the full fledged RMT result [38].

According to these arguments universality is only recovered for long dynamical times, of the order of the Heisenberg time $T_H \propto \hbar/\Delta$ associated with the mean level spacing Δ, where the correlation between orbits arises in a statistical fashion. If shorter, classical times or, equivalently, larger energy ranges are considered, universality breaks down. Instead, resulting spectral features can be traced to the influence of few, short periodic orbits which are highly system specific in nature [36]. The other case where universality no longer applies is related to the breaking of symmetries. The presence of additional symmetries, beyond the time reversal invariance, may cause a switch from one symmetry class to another [39], where the outcome depends on the type of representation of the involved symmetry groups. If, however, one of the symmetries is only weakly broken, consider for instance adding a weak magnetic field, this usually requires a modification of the random matrix ensemble that leads to spectral statistics outside of the standard universality classes.

Despite the many-body origin of RMT the application of semi-classical trace formulas was, so far, restricted to systems with few degrees of freedom. But, in recent years many-body systems moved into the focus, driven, in parts, by the progress on the experimental side. Noteworthy are the improvements in the field of ultra-cold atoms which allow a high control over various types of lattice-like models, for a review see [40]. This allows the experimental realisation of many standard models employed on the theoretical side, for instance Bose-Hubbard models including their phase transitions [41–44] or spin chains [45–47] and many-body localization therein [48]. These systems are built by confining the cold atoms in optical lattices. It is therefore quite easy to open this concept to non-stationary effects or dissipation. This encourages the investigation of quantum thermalisation [49] or driven systems in general [50–52].

The transition to many-body systems poses several major challenges both fundamental and practical in nature. On the quantum mechanical side the (effective) dimension of the Hilbert space grows exponentially with the number of particles N

which limits the experimental resolution of single eigenenergies and poses a severe constraint to numerical calculations. Therefore, all (computational) methods involving large numbers of particles need to reduce the complexity of the problem, in most cases by approximations that are tailored to specific systems and questions. As a further complication quantum particles are, in many set-ups, indistinguishable and follow either Bose- or Fermi-statistics. Treating this aspect from a semi-classical point of view is a subject of ongoing research, see for instance [53–56].

On the classical side the complexity grows as well. Although the phase-space dimension grows only linear in N the number of periodic orbits proliferates exponentially not only with time but also with the number of particles. Due to the increased phase-space dimension many-body systems often also present a much richer dynamical structure. As a specific and important feature class we may look at collective forms of motions. In these cases particles conspire to move or behave in a correlated fashion leading to macroscopic phenomena [57, 58]. Examples of this kind range from sound waves (even present in fully chaotic Boltzmann gases [59]) over Bose-Einstein condensation (including deviations of its ground state [60, 61]) and superparamagnetism [62] to giant resonances in heavy nuclei [63–66]. All these phenomena afford a description in terms of few, macroscopic variables neglecting the myriad of underlying degrees of freedom, which leads to simplified models and dynamics. But quite often these phenomena are transient and decay over time. This ephemerality should leave a broad imprint on the spectral statistics not covered by universality and it is thus tempting to address it via semi-classical methods.

Discussing the semi-classical limit of a many-body system introduces the particle number as a second parameter in addition to the wavelength, and the interplay between both quantities can lead to novel outcomes. In [67] Gutkin and Osipov gave an example of this kind based on a chain-like system. If the chain is sufficiently long compared to the inverse wavelength new types of orbit correlations emerge besides the ones discussed by Sieber and Richter. The difference between both limits can further be illustrated on a Bose-Hubbard chain. If the number of bosons B is significantly higher than the number of sites L the on-site occupation can be approximated by a smooth function. This allows the introduction of a semi-classical limit modeling this function, as done in [54, 56]. On the other hand B/L could be a fixed ratio too low for such a semi-classical approach. Still, in the limit $L \to \infty$ Bose-Einstein condensation occurs which one might think of as a form of semi-classical limit. In most systems a concurrence between both large parameters should be present resulting in new outcomes.

2. Basic Concepts

BEFORE we present the new developments in this thesis this chapter offers a brief recapitulation of basic concepts in quantum chaos. We will restrict the review mostly to those parts relevant to understand conceptual aspects of the later discussions. Although the statements made in this section are not restricted to single particle systems the many-body case warrants further remarks relegated to the second part of the thesis, chapter 4. First, we present how chaos manifests in the classical world, section 2.1, and then show its impact on quantum mechanics, section 2.2. The latter follows along the lines of random matrix theory as it offers immediate insight into spectral statistics. For the last part, section 2.3, we formally merge both sides and give an introduction to the ideas behind semi-classics.

2.1. Classical Chaos

One of the most remarkable consequences of chaos is its high sensitivity to slight changes in the initial conditions. As many other works on quantum chaos we begin with a comparison of two billiards. To recall the basic definition of a mathematical billiard, it consists of a point-particle moving freely within the billiard domain and undergoing specular reflection at the boundary. Despite these superficially simple dynamical rules billiards are among the most favorite quantum chaos toy-models since they afford both experimental realizations and relatively easy theoretical computations. It is easy to see that for the rectangle billiard in figure 2.1 the absolute values of the momentum components, $|p_x|$ and $|p_y|$, are conserved. These two conserved quantities reveal it as an integrable system. The figure shows two different trajectories, colored blue and orange, which differ slightly in their initial conditions. To be precise, we included a small angle between both trajectories leading to a subtle variation of the conserved quantities. Over time this deviation grows linearly. Figure 2.2 depicts a very similar situation for a billiard where a circular area was removed from the interior. This turns the integrable rectangle billiard into the famous Sinai

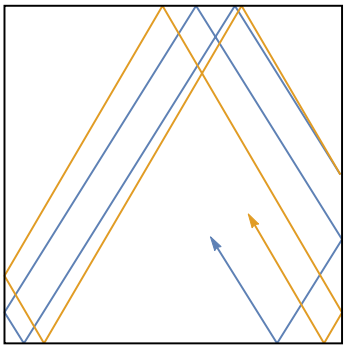

Fig. 2.1.: Rectangle Billiard

Billiard which is fully chaotic. Although free propagation only leads to a linear growth of deviations the reflection on boundary segments with negative curvature leads to an exponential growth of the initial deviations.

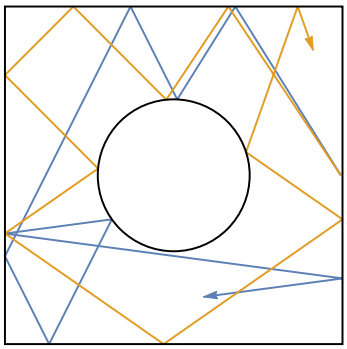

Fig. 2.2.: Sinai Billiard

This instability with respect to small deviations is crucial to understand the origin of chaos. Following the lines of [68] we may look at the deviation between a trajectory $\vec{z} = (q, p)$ in phase-space,

$$\vec{z}(t) = \phi(\vec{z}_0, t) \qquad \text{where} \quad \vec{z}_0 = \vec{z}(0)\,, \tag{2.1}$$

described by the Hamiltonian flow ϕ, and its slightly perturbed counterpart

$$\vec{z'}(t) = \phi(\vec{z}_0 + \epsilon\delta\vec{z}_0, t)\,. \tag{2.2}$$

Therein $\delta\vec{z}_0$, with $|\delta\vec{z}_0| = 1$, represents the direction of the initial deviation whose magnitude is given by a small parameter ϵ. For infinitesimal perturbation the resulting deviation at time t,

$$\delta\vec{z}(t) = \lim_{\epsilon\to 0} \frac{1}{\epsilon} \Big(\phi(\vec{z'}(0), t) - \phi(\vec{z}(0), t)\Big) = \underline{J}(t)\,\delta\vec{z}(0)\,, \tag{2.3}$$

is described by linearized dynamics around the trajectory. They are encoded in the time dependent Jacobi matrix $\underline{J}(t)$, which, owing to the Hamiltonian structure of classical mechanics, is symplectic. We restrict the further discussion on stability to a specific type of trajectories relevant for the later semi-classical analysis, namely periodic orbits (POs) γ, which return to their initial starting point after some period duration $T_\gamma^{(P)}$, *i.e.* $\vec{z}(0) = \vec{z}(T_\gamma^{(P)})$. For those, we can easily determine the stability along the whole trajectory after one period,

$$\delta\vec{z}_1 = \underline{M}_\gamma\,\delta\vec{z}_0\,, \tag{2.4}$$

which removes the explicit time dependence and introduces the monodromy matrix $\underline{M}_\gamma = \underline{J}(T_\gamma^{(P)})$ of the considered PO γ. Within the linearized regime deviations for further repetitions are found by consecutive application of $\underline{M}_\gamma$, we therefore find for the r-th repetition $\delta\vec{z}_r = \underline{M}_\gamma\,\delta\vec{z}_{r-1} = \underline{M}_\gamma^r\,\delta\vec{z}_0$. The shortest possible time required to close the orbit is denoted as prime period $T_\gamma^{(P)}$ and we measure repetitions of the PO with respect to this time. All information on the behavior of the initial deviation, and thus also on the stability of the orbit, is encoded in the eigenvalues and eigenvectors of the monodromy matrix. Naturally, $\underline{M}_\gamma$ inherits the symplectic properties of $\underline{J}$, specifically this implies that all its eigenvalues, which we denote by $\mathrm{e}^{\Lambda_\pm}$, appear in pairs of $\Lambda_+ = -\Lambda_-$.

We can distinguish four different cases of these pairings, shown in figure 2.3. If Λ are purely real numbers, the hyperbolic case, the deviations will grow (or decay)

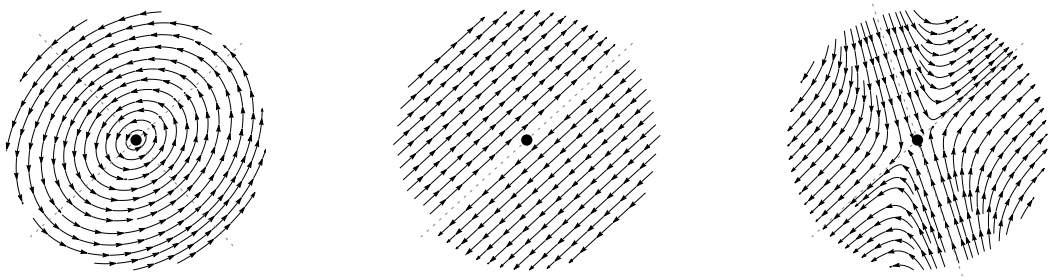

(a) elliptic **(b)** marginal **(c)** hyperbolic

Fig. 2.3.: Schematic drawing of the three possible types of linearized stability around a periodic orbit (central dot). The arrows indicate the direction in which a perturbation $\delta\vec{z}(t)$ would propagate. In the hyperbolic case almost all directions are unstable, only those two precisely located on the direction corresponding to $\Lambda_- < 0$ converge towards the PO. Due to its higher dimension the loxodromic type is not depicted.

exponentially in direction of the corresponding eigenvector. This is the mechanism behind the exponential divergence observed for the chaotic Sinai billiard, recall figure 2.2, marking unstable orbits. In this case the Λ may be seen as the Lyapunov exponents that measure the strength with which a deviation grows. As a side remark, $e^{\pm\Lambda}$ may be negative numbers in the inverse hyperbolic case. If, on the contrary, the Λ are purely imaginary the deviation is called elliptic and encircles the original trajectory. In the cases of larger dimensions, *i.e.* $\dim \underline{M}_\gamma \geq 4$, quadruples of eigenvalues $e^{\pm\Lambda}$ together with $e^{\pm\Lambda^*}$ may occur, where Λ^* denotes the complex conjugate of Λ. These loxodromic directions still lead to exponentially growing deviations.

The last case of marginal directions $\Lambda_\pm = 0$ warrants a more detailed discussion. They indicate that deviations either stay invariant or grow at most linearly with time. Such directions are created by two different mechanisms. Under a change of system parameters an orbit may change its stability, for instance from elliptic to hyperbolic, which necessarily implies a transition of Λ through zero. Through these bifurcation events periodic orbits within the system are created or annihilated. The second possibility is the presence of conserved quantities, which lead to a foliation of phase-space dynamics. For any trajectory a perturbation orthogonal to the isosurface of the conserved quantity leads to an only linear growth of initial deviations, as seen in the rectangle billiard. But, this is a too weak growth to result in non-zero Lyapunov exponents [69]. The application of the symmetry operation corresponding to the conservation law generates the other marginal directions. In terms of a concrete example, for time independent Hamiltonian systems energy is conserved and the system remains invariant under "translation" in time. The dynamics, even if otherwise chaotic, is thus constraint to the energy shell. Perturbing the PO in energy direction leads generically to almost the same trajectory and mostly results in a changed speed of propagation. Transport

in time, *i.e.* $\vec{z}(0) \to \vec{z}(\epsilon)$, leads to a "new" trajectory which follows the original one closely. As energy conservation is a rather common phenomenon monodromy matrices for Hamiltonian systems are often defined keeping only the directions orthogonal to those two.

Conclusively, the local stability around a trajectory reveals much about whether or not a system is chaotic or regular. While considered toy-models often fall into one of the two extremes, full integrability with sufficient conserved quantities or full chaos, where all trajectories posses hyperbolic dynamics, generic systems often exhibit a mixed phase-space where this property differs by region. To give more meaning to this explanation figure 2.4 shows the standard map [70] for a parameter choice with mixed dynamics. Maps generically yield kicked dynamics that does not conserve energy and therefore chaos can already develop for only a single degree of freedom. Trajectories within these systems are represented by sets of discrete points $\{(q_t, p_t)\}$ that are iteratively mapped onto the next time-step, *i.e.* $(q_{t+1}, p_{t+1}) = \Phi(q_t, p_t)$. This reduction of complexity, while preserving most aspects of chaos, turned kicked systems into preferred study objects. Especially, their phase-space is easily visualized in two dimensions. The figure follows the trajectories of several randomly selected initial points, visible are both an chaotic region which is uniformly filled by the trajectories as well as elliptic islands where the trajectories encircle stable periodic orbits. Although visually highly telling this scheme works well only for low dimensional systems where dynamics can be projected on two dimensional sections. There are, however, some works [71, 72] that extend this approach to four dimensional maps. In higher dimensional phase-space the picture is more complicated. The spectrum of $\underline{M}_\gamma$ is not necessarily exclusively elliptic or hyperbolic, instead mixtures of all types are possible and common.

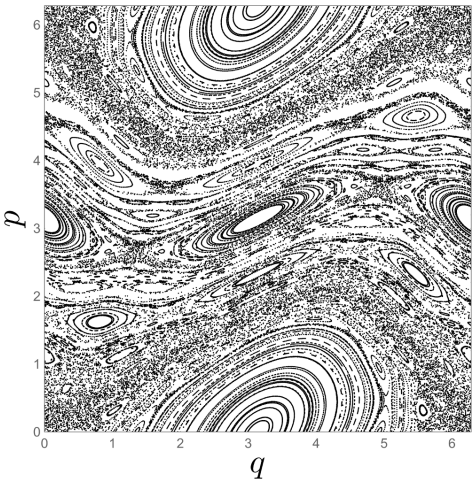

Fig. 2.4.: Standard Map

2.2. Random Matrix Theory

Spectral universality for chaotic systems enables us to explain their basic statistical properties by RMT means, for an overview see for instance [28, 29]. As the agreement between the spectrum of a physical Hamiltonian and a random matrix can only be statistical in nature, the correspondence is usually revealed by averages over ensembles

of matrices. For the ensembles many different distributions of random matrices are suitable, but due to universality there precise properties are usually not important. However, for computational convenience commonly the Gaussian ensembles, which we give below, are used. Recalling the discussion from the introduction, one finds three different classes of spectral universality. To mark them one commonly introduces the parameter β which can take on the values 1, 2 and 4. On the physical side these classes are distinguished by the basic properties of the system under time reversal which we explain in the following.

To begin with, a generic Hamiltonian is given by a self-adjoint operator $\hat{H} = \hat{H}^\dagger$. The corresponding Gaussian unitary ensemble (GUE) is given (up to normalization) by the probability distribution

$$P(\underline{H}) \propto \exp\left(-\frac{N}{\zeta} \operatorname{Tr} \underline{H}^2\right), \tag{2.5}$$

where the domain of $\underline{H}$ are the $N \times N$ complex hermitian matrices. The scaling parameter ζ governs the magnitude of the matrix elements and conclusively the width of the resulting eigenvalue distribution. This class describes physical systems without time reversal invariance (TRI) and corresponds to $\beta = 2$. The presence of TRI leads to further constraints on $\hat{H}$. At this point we have to distinguish two cases: if we denote with $\hat{T}$ the time reversal operator, then its twofold application $\hat{T}^2 = \alpha$ should be proportional to unity, the proportionality constant α may be either plus or minus one [29]. In the first case, $\hat{T}^2 = 1$ and $\beta = 1$, we obtain conventional TRI systems where we have to restrict the matrix space to real symmetric matrices $\underline{H} = \underline{H}^T$. Up to this change of domain, the distribution of the Gaussian orthogonal ensemble (GOE) $P(\underline{H})$ is formally identical to the one given in (2.5). The last class, $\hat{T}^2 = -1$ and $\beta = 4$, is identified with the Gaussian symplectic ensembles (GSE). For them the distribution (2.5) is defined over hermitian quaternionic $N \times N$ matrices. Closer to the name, the quaternions are often replaced by 2×2 matrices increasing the size of the matrix to $2N \times 2N$. From a physical point of view this class is commonly associated with (TRI) half-integer spin systems.

For the above discussion we assumed that no further symmetries are present in the system. However, in many cases the Hamiltonian commutes with a symmetry group G. This implies that $\hat{H}$ can be brought into a block-diagonal form where each block corresponds to an irreducible representation of G. In this case RMT

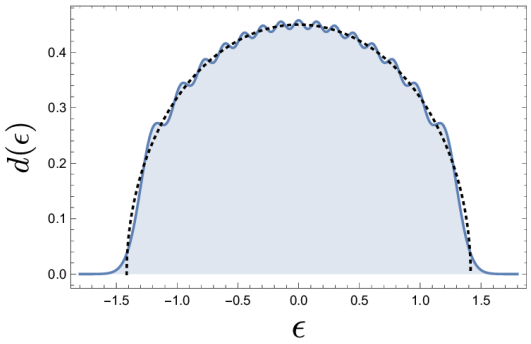

Fig. 2.5.: Semi-Circle Law

applies separately to each, now symmetry free, sub-block. This decomposition might lead to changes of the sub-blocks symmetry class [39, 73, 74], where the resulting one depends on the corresponding irreducible (co-)representation [75].

Already in the introduction we pointed out that universality holds only on the scales of mean level spacing (MLS) and the spectral statistics are therefore given with respect to it. If we look at the full density $d(\epsilon)$ of eigenvalues for a random matrix we see a semi-circle structure. Figure 2.5 shows the corresponding probability density function for GUE, both for finite matrix size (solid line) and the $N \to \infty$ result (dashed). Necessarily, the distance between eigenvalues closer to the rim is larger than for those near the center. To compensate this distortion a deconvolution of the spectrum is in order. Decomposing the density,

$$d(\epsilon) = \sum_n \delta(\epsilon - \epsilon_n) = d_{\mathrm{sm}}(\epsilon) + d_{\mathrm{osc}}(\epsilon)\,, \tag{2.6}$$

into a smooth and an oscillating part where the former corresponds to the semi-circle, we can introduce the smooth monotonic step-function

$$\mathcal{N}(\epsilon) = \int_{-\infty}^{\epsilon} \mathrm{d}\epsilon'\, d_{\mathrm{sm}}(\epsilon')\,. \tag{2.7}$$

It provides us with a definition of an adjusted spectrum $\tilde{\epsilon}_n = \mathcal{N}(\epsilon_n)$ which fulfills our requirement of an on average equidistant level spacing.

To concretize this statement we can look at the nearest neighbor spacing distribution $p(s)$, which describes the distance $s_n = \tilde{\epsilon}_{n+1} - \tilde{\epsilon}_n \geq 0$ between adjacent levels. On this deconvolved scale it is normalized such that

$$\int_0^\infty \mathrm{d}s\, p(s) = \int_0^\infty \mathrm{d}s\, s\, p(s) = 1\,, \tag{2.8}$$

where the first condition is the normalization and the second one the average distance. No exact analytical expressions for $p(s)$ exist, but in the limit of $N \to \infty$ it is approximately given by the Wigner-Dyson distributions,

$$p(s) \approx \begin{cases} \frac{\pi}{2} s\, \mathrm{e}^{-\pi/4\, s^2} & \text{GOE} \\ \frac{32}{\pi^2} s^2\, \mathrm{e}^{-4/\pi\, s^2} & \text{GUE} \\ \frac{2^{18}}{3^6 \pi^3} s^4\, \mathrm{e}^{-64/(9\pi)\, s^2} & \text{GSE} \end{cases}. \tag{2.9}$$

The parameter β governs the initial growth proportional to s^β and describes the strength of level repulsion indicative of spectral rigidity. In comparison, for a generic integrable system $p(s)$ is given by the Poisson distribution

$$p(s) = \exp(-s) \qquad \text{(Poisson)}\,, \tag{2.10}$$

which occurs for uncorrelated random numbers. All four are presented in figure 2.6. A word of caution is in order, some integrable systems are non-generic, for instance harmonic oscillator posses equidistant eigenvalues.

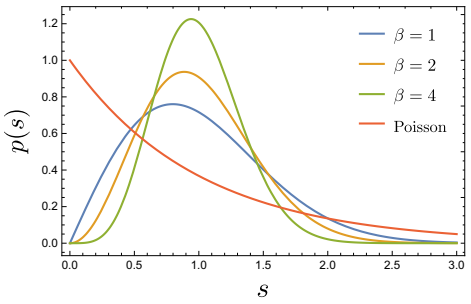

Fig. 2.6.: Spacing Distribution $p(s)$

The rigidity of the chaotic spectrum has a further consequence. It implies that the eigenvalues "feel" each others presence. In fact, their distribution can equivalently be modeled by an interacting one dimensional gas with long range interaction [33]. Therefore, not only the average distance changes in the fringes of the eigenvalue distribution but also the deconvolved results will be affected by the asymmetry of the edge. In consequence, universality holds strictly only in the bulk of the spectrum, *i.e.* a region around zero which scales weaker with N than the rim of the distribution.

RMT reveals the universal aspects of a spectrum on the small scales of MLS. But, we may introduce long-range statistical measures. The example used in this thesis is the form-factor defined as,

$$K_2(t) = \frac{1}{\dim \hat{H}} \left| \mathrm{Tr} \exp\left(-\frac{\mathrm{i}}{\hbar} \hat{H} t \right) \right|^2 , \tag{2.11}$$

the absolute square of the time evolution operator's trace. Besides this abstract definition it has a physical definition as the Fourier transformation of $R_2(s)$. The latter describes the probability to find an energy level, not necessarily the next nearest one, in a distance s from an existing level. As a minor remark, in (2.11) we exponentiate $\hat{H}$, which, strictly speaking, turns the Gaussian into circular ensembles, *e.g.* GOE to COE. Without going into detail figure 2.7 shows the behavior of K_2 for the three different universality classes. All curves tend towards a saturation value which they reach roughly at $T_H \propto \dim \hat{H}$, the Heisenberg time of the system. On a rescaled time $\tau = t/T_H > 0$ their analytic form is given by

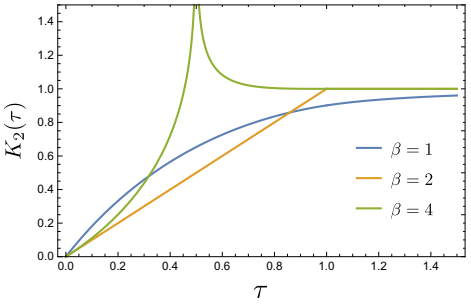

Fig. 2.7.: Form-Factor $K_2(\tau)$

$$K_2^{(\mathrm{COE})}(\tau) = \begin{cases} 2\tau - \tau \ln(1+2\tau) , & \tau \leq 1 \\ 2 - \tau \ln \frac{2\tau+1}{2\tau-1} , & \tau \geq 1 \end{cases} \tag{2.12}$$

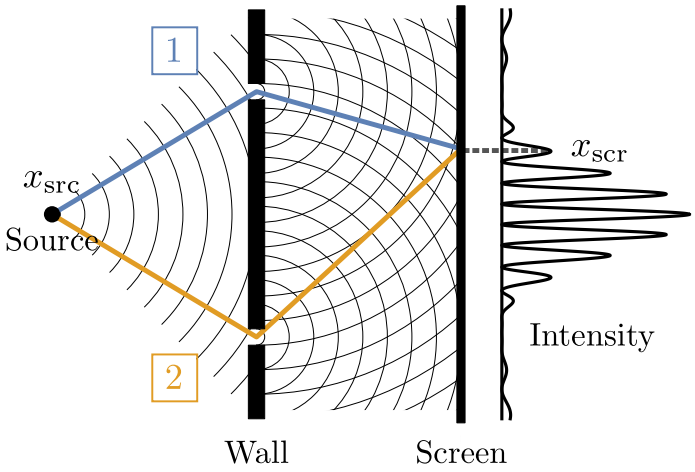

Fig. 2.8.: Drawing of the double slit experiment. A particle is emitted from the source and passes through the slits, forming the well known interference pattern on the screen. Besides the particles wave nature, two solid lines show (classical) trajectories, which can also be used to explain the experiments outcome.

for the GOE case and by the simpler expression

$$K_2^{(\mathrm{CUE})}(\tau) = \begin{cases} \tau\,, & \tau \leq 1 \\ 1\,, & \tau \geq 1 \end{cases} \tag{2.13}$$

for GUE, compare [18], specifically also for the form of $K_2^{(\mathrm{CSE})}$. The time-scales corresponding to $\tau \sim 1$ are still large enough to be governed by universality. But on short times, implying large distances within the spectrum, deviations of K_2 from the RMT predictions reveal system specific properties [39, 76].

2.3. Semi-Classics

Semi-classical theory provides a way to connect the quantum time evolution with the classical one. Its basic idea may be sketched on the example of the double slit experiment, see figure 2.8. Drawn are both the waves passing through the slits and the resulting interference pattern. The most straightforward explanation of this phenomenon, however, involves not the waves but instead the interference between a pair of classical trajectories (solid lines in figure) passing through the separate slits.

The appearance of these trajectories can be understood through the Feynman path-integral formalism, which serves as a possible basis for the semi-classical approximation. It states that the quantum propagator from the source x_{src} to some point x_{scr} on the

screen can be expressed exactly as the sum over all possible paths connecting both points in time t:

$$\langle x_{\mathrm{scr}}|\hat{U}|x_{\mathrm{src}}\rangle = \int_{x_{\mathrm{src}}}^{x_{\mathrm{scr}}} \mathrm{D}x \exp\left(\frac{\mathrm{i}}{\hbar}\mathcal{S}[x]\right), \tag{2.14}$$

herein $\hat{U} = \exp\left(-\mathrm{i}\hat{H}t/\hbar\right)$ denotes the quantum evolution operator. The right hand side is meant as a functional integral over every conceivable trajectory connecting the two points. The exponent in the integrand contains the classical action

$$\mathcal{S}[x] = \int_0^t \mathrm{d}\tau L(x(\tau), \dot{x}(\tau)) \qquad \text{with} \quad x(0) = x_{\mathrm{src}}\,, x(t) = x_{\mathrm{scr}}\,, \tag{2.15}$$

associated to the trajectory $x(\tau)$ of the corresponding classical system. As the exponent in (2.14) is a highly fluctuating quantity, its dominant contributions are given by those trajectories for which (2.15) is stationary under variation, *i.e.* where the action possesses an extremum. Such trajectories fulfill the Euler-Lagrange equations and are thus solutions to the classical problem. We can expand $\mathcal{S}[x]$ up to second order around the classical solutions and what remains are path-integrals of a Gaussian type that can be solved analytically. For the double slit the resulting trajectories are the two indicated ones,

$$\langle x_{\mathrm{scr}}|\hat{U}|x_{\mathrm{src}}\rangle \approx B_1 \mathrm{e}^{\mathrm{i}\mathcal{S}_1/\hbar} + B_2 \mathrm{e}^{\mathrm{i}\mathcal{S}_2/\hbar}\,, \tag{2.16}$$

where $\mathcal{S}_i$, for a free particle, is proportional to the length of the trajectory. The prefactors B_i are given by the second order contributions which, after some transformations [68], are related to the Jacobian (2.3). This approximation needs the classical actions to be significantly larger compared to $\hbar$ such that the classical trajectories possess a sufficient weight as extremal points of the full integral. Generically, this limit corresponds to short (de Broglie) wavelengths of the involved particles allowing them to resolve all classical features of the system. This condition is usually implied by the semi-classical limit $\hbar_{\mathrm{eff}} = \hbar/\mathcal{S} \to 0$, where $\mathcal{S}$ represents a typical action within the system. In addition, for such an approximation to work as a sum over both trajectories, they need to be sufficiently separated in phase-space. The width of this separation, and therefore the scale of the necessary distance, is measured in terms of $\hbar_{\mathrm{eff}}$. This semi-classical approximation is referred to as Van-Vleck propagator and despite its reliance on the classical trajectories it can be employed for times much larger than the Ehrenfest time scales on which the quantum system behaves classically.

The Van-Vleck formula may be used to evaluate the traces of the propagator in a semi-classical approximation, which form a central building block of the thesis' many-body part:

$$\mathrm{Tr}\,\hat{U}(t) = \int \mathrm{d}x_0 \,\langle x_0|\hat{U}(t)|x_0\rangle \sim \int \mathrm{d}x_0 \sum_{\vartheta(x_0,t)} B_\vartheta \exp\left(\frac{\mathrm{i}}{\hbar}\mathcal{S}[\vartheta]\right), \tag{2.17}$$

where the sum runs over all trajectories ϑ connecting $\vartheta(0)=x_0$ back to $\vartheta(t)=x_0$ in time t. The remaining integral can be treated in a similar saddle point fashion leaving only those trajectories that close in both coordinate and momentum,

$$\operatorname{Tr}\hat{U}(t) \sim \sum_{\gamma(t)} A_\gamma \mathrm{e}^{\mathrm{i}\mathcal{S}_\gamma/\hbar}, \tag{2.18}$$

such that $\gamma(t)$ denotes the periodic orbits (POs) of the system. Besides prime POs that only close themselves after time t the sum also contains repetitions of orbits with shorter (prime) period $T_\gamma^{(P)}$ such that $t=r_\gamma^{(T)}T_\gamma^{(P)}$ where $r_\gamma^{(T)} \in \mathbb{N}$ denotes the number of repetitions. The prefactors A_γ are given in terms of the monodromy matrices as

$$A_\gamma = \frac{T_\gamma^{(P)}\mathrm{e}^{\mathrm{i}G_\gamma}}{\sqrt{\left|\det\left(\underline{M}_\gamma - \mathbb{1}\right)\right|}}. \tag{2.19}$$

The Maslov phase $\mathrm{e}^{\mathrm{i}G_\gamma}$ in the numerator is related to turning points of the classical trajectory [18] and takes on discrete values of $G_\gamma = \pi z/2$ with $z \in \mathbb{Z}$. As this is only a phase contribution it plays no significant role for most applications of (2.18). For the magnitude of the stabilities the denominator is decisive. Assuming an unstable PO with large Lyapunov exponents, $\underline{M}_\gamma$ contains large eigenvalues resulting in a small value of $|A_\gamma|$. For repeated orbits the number or repetitions $r_\gamma^{(T)}$ enters as a power to the prime orbit's $\underline{M}_\gamma$ and thus multiplies its Lyapunov exponent. On the other hand, for POs with elliptic directions the eigenvalues of $\underline{M}_\gamma$ have an absolute value of one independent of $r_\gamma^{(T)}$, giving stable orbits a larger weight.

The presence of marginal directions, apparently, leads to a divergence as the denominator turns to zero. These cases require special treatment as they also violate the original assumptions of isolated orbits. In the integrable case this is rectified by an integration over the manifold of periodic orbits with identical actions. Their presence leads to an algebraic divergence $A_\gamma \sim \hbar_{\mathrm{eff}}^{(-D+1)/2}$ of the stability prefactor where D denotes the number of degrees of freedom. In the other case with marginal directions,bifurcations, a small number of previously isolated orbits converges to a single point in phase-space under variation of the system parameters and exchanges stabilities and/or annihilates. Their treatment is more involved and requires higher order semi-classical corrections, an expansion of the action in (2.14) up to only the second order will be insufficient. These bifurcation are classified according to the number of involved orbits and lead, in all cases, to a divergence of $A_\gamma \propto \hbar_{\mathrm{eff}}^{-\alpha}$ similar to the integrable case. For systems with only one non-trivial $\Lambda_\pm$ pair, *e.g.* systems with $D=1$ or $D=2$ and conserved energy [77, 78], their effect is well understood [77–81] and the fractional exponent α depends on the class of bifurcation. Exact bifurcations where the $\Lambda_\pm$ pair is precisely zero often require a fine tuning of the system parameters, more common are quasi-marginal directions that are only approximately zero. Their

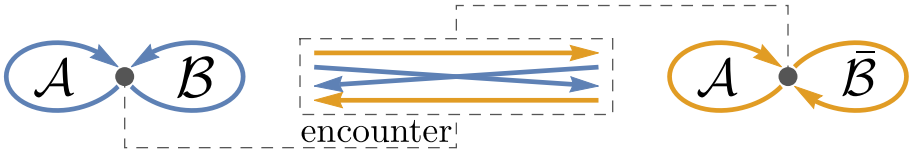

Fig. 2.9.: Conceptual drawing of a Sieber-Richter pair. Both orbits traverse the trajectory segment $\mathcal{A}$. But, the orbits directionality may be flipped during the encounter event (zoomed in middle panel) such that the right PO moves from $\mathcal{A}$ onto $\bar{\mathcal{B}}$ instead of $\mathcal{B}$.

contribution depends on the value of $\hbar_{\text{eff}}$ which measures separation in phase-space. If its value is insufficiently large nearby orbits are not resolved and their effect on A_γ will be similar to a bifurcation and can be treated by uniform approximations [77, 79]. However, in the strict limit $\hbar_{\text{eff}} \to 0$, any finite distance between the orbits will be sufficient to resolve them as fully isolated from one another.

The traces of $\hat{U}(t)$ contain all information on the spectrum and their semi-classical approximation allows us to recover, in the fully chaotic case, the Gutzwiller trace formula. It relates the spectral density of the system,

$$d_{\text{osc}}(\epsilon) \sim \frac{1}{\pi\hbar} \sum_\gamma \frac{T_\gamma^{(P)}}{\sqrt{|\det\left(\underline{M}_\gamma - \mathbb{1}\right)|}} \cos\left(\mathcal{S}/\hbar - G_\gamma\right), \tag{2.20}$$

to a sum over all periodic orbits, no longer for a fixed time but for all times up to the Heisenberg time related to the scales of MLS. For its derivation, and all the other fine-print details we conveniently ignored, we refer to the text books [18, 68].

To complete our exposition of semi-classics we outline the underlying mechanism that distinguishes the different universality classes, specifically GUE and GOE. For this, we return to the form-factor K_2, see (2.11). It contains not only a single trace of $\hat{U}$ but a product of two of them, which we might approximate via

$$|\operatorname{Tr}\hat{U}(t)|^2 \sim \left|\sum_{\gamma(t)} A_\gamma \mathrm{e}^{\mathrm{i}\mathcal{S}_\gamma/\hbar}\right|^2 = \sum_{\gamma(t)} |A_\gamma|^2 + \sum_{\gamma(t)\neq\gamma'(t)} A_\gamma A_{\gamma'}^* \mathrm{e}^{\mathrm{i}(\mathcal{S}_\gamma - \mathcal{S}_{\gamma'})/\hbar}, \tag{2.21}$$

where $*$ denotes complex conjugation. On the right hand side we divided the arising double sum into a diagonal contribution $\gamma = \gamma'$ and an off-diagonal one. If we are interested in long times $t \propto T_H$ to resolve the universal spectral scales the number of POs will be exponentially large and we may treat the terms in a statistical fashion. Assuming an implicit average over system parameters the off-diagonal sum amounts to zero if the PO actions are uncorrelated. Precisely this is the case for the leading order contributions in τ to the GUE form-factor where TRI is broken. But, with intact invariance one finds correlations between the orbits that challenges this reasoning. As

a simple example, every orbit γ has a time reversed counter part $\bar{\gamma}$ with identical action and stability. This amounts to a second "diagonal" contribution in (2.21) and explains why the initial slope for $K_2(\tau)$ in the GOE case, equation (2.12), is twice larger compared to the GUE one, equation (2.13). An additional correlation, giving the next order correction in powers of τ, was found by Sieber and Richter [37]. Long orbits perform intricate loops and generically come close to themselves. For a basic example we consider an orbit which traverses the trajectory segments $\mathcal{AEBE}$, where we denote the encounter stretches by $\mathcal{E}$, as shown in figure 2.9. At those stretches, where the orbit comes close to itself under a small angle, a small perturbation might change the trajectory such that one of the larger segments is passed in opposite direction, *e.g.* $\mathcal{AE\bar{B}E}$. As a result, every orbit with a sufficiently long encounter comparable to the Ehrenfest time has a partner orbit which follows an almost identical path but partially with different time order. Both POs of the pair have a similar action and stability, which gives rise to a non-trivial contribution to the off-diagonal sum in (2.21). Along these lines it is possible to obtain the full fledged form-factor [38, 82].

Part I.

Single Particle Chaos

3. Dynamical Breaking of TRI

THROUGHOUT the last chapter we discussed the dependence of the universal spectral statistics on the underlying symmetries. While these properties followed from RMT considerations we also presented how their emergence can be understood in a semi-classical framework through Sieber-Richter pairs. In this chapter we build upon this dynamical understanding and consider a more elaborate way to influence a system's universality class. To this end we consider a class of systems where the phase-space is ergodically separated into two components corresponding to the time reversed version of one another [83–85]. These systems are called unidirectional as each of the components singles out a certain "directionality" of motion. A straightforward example would be a classical circular billiard, particles launched in clockwise direction will keep moving clockwise and the same holds for those launched in anticlockwise direction. The only exception is given by particles hitting the boundary perpendicular, they form a marginal set of non-rotating trajectories.

While the circle is an illustrative example its integrable nature defies chaos. However, the notion of directionality is not bound to conserved quantities such as the angular momentum. Instead, it persists in many other systems, among them generalizations of circles. These constant width billiards are the type of system that motivated this part of the thesis. Similar to a circle their diameter is constant in every direction, but these diameters do not posses a common midpoint. Two examples, including their classical phase-space, are given in figure 3.1. The one to the left is an experimental realisation of a billiard with smooth boundaries from [86]. Although TRI is, in a strict sense, not broken trajectories can not reverse their direction. This implies that the Sieber-Richter pairs, discussed in section 2.3, do not exist and, in consequence, we might expect GUE instead of GOE statistics. In this case the underlying spectrum was, indeed, found to consist (primarily) of quasi-degenerate pairs that exhibit GUE behaviour. Qualitatively, the degeneracy can be understood from the fact that "left-moving" and "right-moving" modes, due to TRI, contribute (almost) equally to a given energy. Although classically these two motions are ergodically disconnected, quantum mechanically the two modes are still weakly coupled due to dynamical tunnelling through an integrable region of KAM-tori around the bouncing ball modes (marked blue in the figure). This explains why the eigenvalues are only quasi-degenerate.

For billiards with non-smooth boundaries such as the Reuleaux polygon, the second example shown in figure 3.1(b), the splittings between quasi-degenerate states behave quite differently. In this case the dynamical barrier in the middle of the phase space

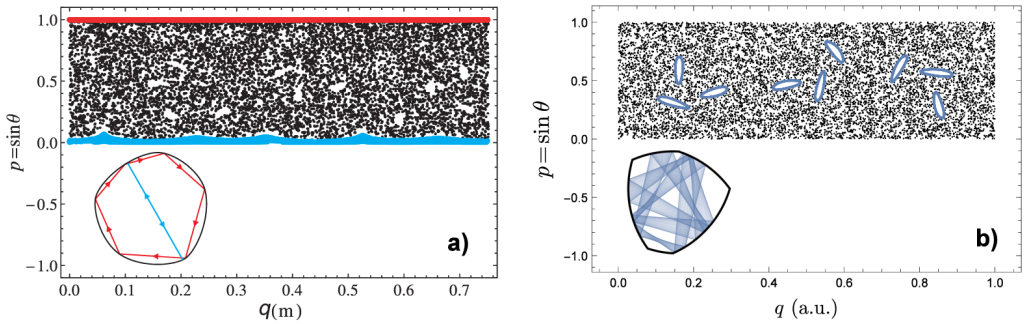

Fig. 3.1.: Shown are the classical phase spaces of two constant width billiards with in case (a) smooth boundaries (figure taken from [86]) and in (b) with corners. Due to the unidirectionality of the systems trajectories in the upper part of the phase-space can not access the lower half, yet as the systems posses TRI the not shown halves look identical. On the left hand side the smooth boundaries give rise to bouncing ball modes (cyan) with adjacent KAM tori (cyan, $p \approx 0$) which separate the phase space into two components, for further information see [86]. In contrast, the separating trajectories in the Reuleaux billiard, figure (b), are singular lines hitting the corners.

shrinks to zero and the tunnelling occurs due to diffractional orbits hitting the corners of the billiard domain. In contrast to billiards with smooth boundaries this tunnelling effect is much stronger leading to large splittings comparable to the mean level spacing, see for instance figure 3.2 showing a doublet of the Reuleaux billiard. The effect induced by the billiard corners is reminiscent of singular perturbations; on the semi-classical level both cases give rise to quite similar, singular (diffractional) classical orbits. Although it is known, compare [87, 88], that normally neither the presence of corners nor singular perturbations affects the spectral statistics, one can anticipate essentially different results for unidirectional billiards. Contributions arising from diffractional orbits break down the unidirectionality of the billiard dynamics, thus effectively changing the universality class of the system. As a result, the spectral statistics of these systems do not belong to any of the three standard classes.

Studying this effect on billiards, while possible, would yield results dependent on the specifics of the considered geometry. It is a highly non-trivial task to continuously deform the boundary such that a reasonable degree of control over the diffractional contributions can be gained. Instead, we restrict ourselves to significantly simpler toy models of (unidirectional) quantum graphs. In these systems the degeneracy between the eigenvalues is exact and full control over the rank, *i.e.* the number of back-scattering elements, and their respective strength possible. For our investigations we limit ourselves to the rank-1 case corresponding to only a single point where unidirectionality is violated.

We will first introduce the concept of quantum graphs and how they can be realized

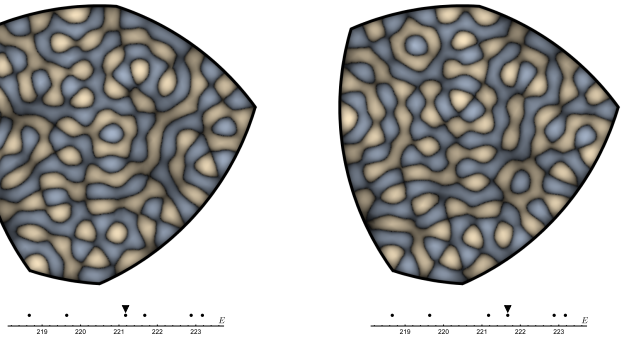

Fig. 3.2.: A doublet (eigenmodes 221 and 222) of the Reuleaux polygon whose classical phase space is shown in figure 3.1(b). Dark areas correspond to negative values of the wavefunction, light to positive. Black "lines" in-between denote the nodal lines. The energy scale below is given in units of MLS.

in a unidirectional way in the next section. Subsequently, we detail in section 3.1 how to add backscattering elements. The remaining part is devoted to an analytical calculation of the splitting distribution based on RMT methods, section 3.3, and its numerical verification on several different types of quantum graphs, section 3.4. While the exact calculations give unwieldy results they can be replaced, similar to the Wigner surmise, by a simple heuristic equation, section 3.5. At the end of this chapter we provide a short summary of the results and comment on the implications of higher rank perturbations.

3.1. Unidirectional Quantum Graphs

Quantum graphs are a widely used toy-model of chaotic quantum systems. We will first sketch below their general properties (for a more detailed account see for instance the review [23] or [22]) and then introduce the family of unidirectional quantum graphs.

A (closed) quantum graph consists of a set of B edges of finite length l_j which are connected at V vertices. The edges can be thought of as ideal 1D waveguides on which a wave function ψ propagates. In our case the propagation is free, *i.e.* $H\psi_j = -\triangle\psi_j = k^2\psi_j$, therefore $\psi_j = a_j e^{+ikx} + b_j e^{-ikx}$ holds on each edge j. The true complexity of such systems stems from the boundary conditions at the graph's vertices. At any given vertex i we are faced with a number of incoming waves, forming the vector $\vec{\psi}^{(i)}_{\text{in}}$, and an equal number of outgoing waves on the same edges forming the vector $\vec{\psi}^{(i)}_{\text{out}}$. The boundary condition at the vertex is described by a unitary matrix σ_i,

$$\vec{\psi}^{(i)}_{\text{out}} = \sigma_i \vec{\psi}^{(i)}_{\text{in}} \,, \tag{3.1}$$

matching both vectors. It is often referred to as "local scattering" matrix, and its unitarity ensures the conservation of local probability.

Using the local scattering matrices, an internal scattering matrix S for the total graph can be constructed. It maps the vector of directed, incoming wave-function amplitudes $\vec{\Psi}_{\text{in}} = (\vec{\psi}_{\text{in}}^{(1)}, \vec{\psi}_{\text{in}}^{(2)}, \ldots, \vec{\psi}_{\text{in}}^{(V)})^T$ onto the outgoing ones $\vec{\Psi}_{\text{out}} = (\vec{\psi}_{\text{out}}^{(1)}, \vec{\psi}_{\text{out}}^{(2)}, \ldots, \vec{\psi}_{\text{out}}^{(V)})^T$. For the eigenstates of the system the outgoing wave functions acquire the phases $\mathrm{e}^{+\mathrm{i}kl_j}$ during propagation along the respective edges and turn into incoming wave functions again. We can represent this by a self consistent equation

$$S \cdot \underbrace{\mathrm{diag}(\mathrm{e}^{\mathrm{i}kl_1}, \ldots, \mathrm{e}^{\mathrm{i}kl_{2B}})}_{\mathcal{L}(k)} \vec{\Psi}_{\text{out}} = \vec{\Psi}_{\text{out}} \,. \tag{3.2}$$

As we describe every edge by two directions, each length l_j appears twice in $\mathcal{L}(k)$. The eigenenergies of the graph are now those k_n^2 for which we can find a $\vec{\Psi}_{\text{out}}$ fulfilling above equation. In other words, the matrix $1 - S\mathcal{L}(k)$ needs to have a zero eigenvalue at $k = k_n$. If the lengths l_j are non commensurate, *i.e.* they are given by rationally independent numbers, one in general expects either GOE or GUE statistics (depending on the symmetry of the local scatterers) for the graphs spectrum [24].

Starting from this general set-up only small adjustments are needed to introduce the family of unidirectional quantum graphs. The classical "dynamics" on a graph Γ can be thought of as free motion of a point-like particle on edges of the graph combined with stochastic transitions at its vertices. The probability to pass from edge i to edge j is defined by the element $|S_{i,j}|^2$ of the scattering matrix. For a unidirectional graph we need to fix the vertex matrices σ_i in such a way that it would be impossible to switch the direction of motion along the edges. To this end we split an undirected graph Γ into two directed "halves" $\Gamma_\pm$ such that the n-th edges of Γ_+ and Γ_- correspond to two possible directions of motions on the n-th edge of Γ. In addition, we require that the number of outgoing and incoming edges at each vertex of $\Gamma_\pm$ would be identical. Such a splitting of Γ is possible if and only if it possesses an even number of edges per vertex (in such a case Γ admits euler cycles which can be used to assign the directions along the edges). The following structure of the vertex scattering matrices,

$$\sigma_i = \begin{pmatrix} 0 & U_i \\ U_i^T & 0 \end{pmatrix} \qquad \text{with} \quad U_i U_i^\dagger = U_i^\dagger U_i = \mathbb{1} \,, \tag{3.3}$$

ensures that the dynamics on $\Gamma_\pm$ are completely decoupled, compare figure 3.3. Here we arranged $\vec{\psi}_{\text{in}}^{(i)} = (\vec{\psi}_{\text{in}}^{(i+)}, \vec{\psi}_{\text{in}}^{(i-)})^T$ such that all entries $\vec{\psi}_{\text{in}}^{(i+)}$ of Γ_+ are listed first, which makes the underlying block structure apparent. Necessarily, all outgoing directions on Γ_+ are incoming directions of Γ_- and the other way around. Therefore, both directions are present in equal number making U_i a square matrix, which is a requirement to make U_i unitary. Due to the off-diagonal structure of the σ's the transition from graph Γ_+ to Γ_- (and vice versa) is impossible. In other words, a particle launched in one direction cannot switch to the opposite one. Further on, choosing the same U_i for both blocks,

Fig. 3.3.: *Right hand side:* Illustration of a graph vertex with four attached leads which feature two separate directions, dark/blue and light/orange. Locally the scattering matrix does not couple those directions, *e.g.* waves entering through an incoming orange edge only leave via an outgoing orange edge, as indicated in Equation (3.3). This ensures unidirectionality on a local scale.
Left hand side: Directed graph Γ_+ corresponding to a unidirectional De Bruijn quantum graph. Its symmetric counterpart Γ_- is obtained by reversing the direction of each edge. We highlighted two possible positions (light red/middle and light green/left) at which a backscattering vertex $\tilde{\sigma}$, Equation (3.5), could be placed. Note though that for a rank one perturbation only one scatter can be introduced. We comment on the differences of both positions in Section 3.4.

implying $\sigma_i = \sigma_i^T$, ensures that the system possesses TRI. The block structure in (3.3) already indicates that the corresponding quantum graph features an exactly double degenerate spectrum. This becomes apparent when we cast S into a block-diagonal form as well. To this end we reorder the directed edges of Γ in such a way that entries of Γ_+ appear first, *i.e.* $\vec{\Psi}_{\text{out}} = (\psi_+^{(1)}, \ldots, \psi_+^{(B)}, \psi_-^{(1)}, \ldots, \psi_-^{(B)})^T$. Within such order S takes the form:

$$S = \begin{pmatrix} \mathcal{S} & 0 \\ 0 & \mathcal{S}^T \end{pmatrix} . \tag{3.4}$$

Both directions Γ_+ and Γ_- form a chiral basis and are dynamically disconnected. Furthermore, as they are related via a transpose of $\mathcal{S}$ we have $l_j = l_{j+B}$ for the entries of the (also reordered) diagonal matrix $\mathcal{L}(k)$.

3.2. Breaking Unidirectionality

We will now consider graphs where unidirectionality is broken at just one of the graph's vertices. To this end we augment one of the edges of a unidirectional graph Γ_0 with a backscattering vertex. A general 2×2 TRI backscattering matrix serving this purpose can be written as

$$\tilde{\sigma} = \mathrm{e}^{\mathrm{i}\alpha+\mathrm{i}\gamma} \begin{pmatrix} r & t \\ t & -r^* \end{pmatrix} \qquad \text{with} \quad r = \mathrm{i}\mathrm{e}^{\mathrm{i}\beta} \sin\alpha\,, \quad t = \cos\alpha\,, \tag{3.5}$$

where $*$ denotes complex conjugation. The parameter α controls the strength of back-scattering: In the case of $\alpha = 0$ the vertex becomes transparent with the back-reflection $r = 0$ and all incoming waves pass through (acquiring a phase $\mathrm{e}^{\mathrm{i}\gamma}$). In the opposite case, for $\alpha = \pi/2$, the transmission t becomes zero and the degeneracies are lifted with the splittings reaching their maximum values. The parameter β allows back-scattered waves on $\Gamma_\pm$ to acquire different phases. But, the spectrum is unaffected by the choice of this parameter as can be inferred from semi-classical arguments. A trajectory starting on Γ_+ (respectively Γ_-) on this nearly unidirectional graph needs to back-scatter twice at $\tilde{\sigma}$ to return to Γ_+ (Γ_-). This leads to a cancellation of the phase associated with β for all closed orbits. The "global" phase γ leads to a shift of the spectrum which does not change the spectral statistics, *e.g.* the spacing distribution.

Given such an additional scatterer the matrix S for the total graph can be written in the form

$$S = S_0(\gamma) + (\mathrm{e}^{2\mathrm{i}\,\alpha} - 1) S_0(\gamma)\, |\psi\rangle\, \langle\psi| = S_0(\gamma) \cdot \exp\left(2\mathrm{i}\,\alpha\, |\psi\rangle\, \langle\psi|\right) \tag{3.6}$$

$$\text{with} \qquad |\psi\rangle = \frac{\mathrm{e}^{\mathrm{i}\beta/2}}{\sqrt{2}}\, |\mathrm{in}_+\rangle + \frac{\mathrm{e}^{-\mathrm{i}\beta/2}}{\sqrt{2}}\, |\mathrm{in}_-\rangle \ , \tag{3.7}$$

Herein S_0 is the unperturbed scattering matrix of a unidirectional quantum graph, containing $\tilde{\sigma}$ in its transparent form, *i.e.* for $\alpha = 0$, and $|\psi\rangle\, \langle\psi|$ is a rank 1 perturbation. According to our definition S_0 depends on γ, only for $\gamma = 0$ the introduction of $\tilde{\sigma}$ does not change the spectrum of the original graph Γ_0. The non-zero components of $|\mathrm{in}_\pm\rangle$ in equation (3.7) correspond to the incoming directed edges on $\Gamma_\pm$ leading to the scatterer. The action of $S_0(\gamma)$ on these vectors should be understood in the form $S_0(\gamma)\, |\mathrm{in}_\pm\rangle = \mathrm{e}^{\mathrm{i}\gamma}\, |\mathrm{out}_\pm\rangle$, *i.e.* as mapping incoming wave functions onto outgoing ones. Instead of adding an additional vertex to the graph we could also change the local scattering matrix of a 4 edge vertex of Γ_0 such that it corresponds to the standard Neumann boundary conditions ($\sum_{i=1}^{4} \partial\psi_i = 0$). In this case the decomposition (3.6) of S into "unidirectional" and "singular" parts holds as well. In fact, all the presented results are applicable to quantum graphs possessing this particular form of scattering matrix. Due to the singular type of perturbation we call these graphs *nearly unidirectional*.

Secular Equation — We can develop some systematic insight into the graph's spectral properties by looking at the eigenvalues of the unitary quantum evolution operator:

$$S\mathcal{L}(k)\, |\lambda_m\rangle = \mathrm{e}^{\mathrm{i}\lambda_m}\, |\lambda_m\rangle \, . \tag{3.8}$$

Using equation (3.6) it is straightforward to obtain a secular equation which relates the eigenvalues $\mathrm{e}^{\mathrm{i}\lambda_m}$ of the perturbed system ($\alpha \neq 0$) to the doubly degenerate eigenvalues $\mathrm{e}^{\mathrm{i}\epsilon_m}$ of the unperturbed one ($\alpha = 0$). Expanding the eigenvectors $|\lambda_m\rangle$ in terms of the old $\alpha = 0$ basis $|\epsilon_m\rangle$ yields

$$\frac{-\mathrm{i}\mathrm{e}^{-\mathrm{i}\alpha}}{2\sin\alpha} = \sum_{m=1}^{B} \frac{\mathrm{e}^{\mathrm{i}\epsilon_m} |A_m|^2}{\mathrm{e}^{\mathrm{i}\lambda} - \mathrm{e}^{\mathrm{i}\epsilon_m}} \, , \tag{3.9}$$

where the left hand side depends only on α. Solutions to this equation in λ provide the spectrum of eigenphases $\{\lambda_m\}$ of the perturbed system. Importantly, this equation only determines one half of the $2B$ eigenvalues of the matrix $S\mathcal{L}(k)$. The other half are pinned to their initial values ϵ_m for $\alpha = 0$. Indeed, since the original spectrum of the unidirectional graph is doubly degenerate one half of all eigenvalues is not affected by a rank 1 perturbation. (A simple way to see this is to notice that the spectra of the original and the perturbed graphs satisfy the interlacing property, see below.) The coefficients $|A_m|^2 = |\langle\epsilon_m|\mathrm{in}_+\rangle|^2 + |\langle\epsilon_m|\mathrm{in}_-\rangle|^2$ are the absolute values of the $|\epsilon_m\rangle$ eigenvectors' component corresponding to the edge(s) where $\tilde{\sigma}$ is located.[1] In the physically interesting cases where one of the eigenvalues λ is 0, *i.e.* equation (3.2) holds, the corresponding A_m are the amplitudes of the stationary wave solution on the graph.

At first the complex secular equation appears overdetermined to give B real solutions for λ. This, however, is not true since the real part of this equation is trivially fulfilled due to the completeness condition $\sum_{m=1}^{B} |A_m|^2 = 1$ while the imaginary part yields

$$\cot\alpha = \sum_{m=1}^{B} |A_m|^2 \cot\left(\frac{\lambda - \epsilon_m}{2}\right). \tag{3.10}$$

A prominent feature of equation (3.10) is the interlacing property satisfied by its solutions, which is an immediate consequence of the fact that S is a rank 1 perturbation of S_0. Specifically, for a positive α we find that the following inequality holds, $\epsilon_i \leq \lambda_i \leq \epsilon_{i+1}$. Similarly, in the case of $\alpha < 0$ we have $\epsilon_{i-1} \leq \lambda_i \leq \epsilon_i$. This becomes apparent by noticing that the right hand side of equation (3.10), as a function of λ, possesses poles at each ϵ_m. Therefore, the solutions λ_m lie in between those poles, see figure 3.4. In the limiting case of $\alpha \to 0$ they will coincide with the poles as the system's spectrum is double degenerate.

Large B limit — Equation (3.10) can be simplified further in the case of graphs with a large number of edges. The eigenphases ϵ_m reside on the 2π interval parametrising the unit circle. Their distance therefore scales like $O(1/B)$ with the number of edges. Considering that $\cot x = 1/x + O(x)$, only the $N \sim \sqrt{B}$ closest ϵ_m will have an impact on the precise location of a solution λ_i between two ϵ-eigenphases. To demonstrate this we split the sum in (3.10) into three parts, the central sum with $N \sim \sqrt{B}$ elements and two surrounding contributions with $1/2(B - N)$ entries. It is straightforward to see that due to the periodicity of the cotangent the contributions of the outer sums on average cancel each other. Furthermore, it can be shown that the fluctuations of those sums scale with $O(1/B)$ and therefore are negligible in the limit of large graphs. After the expansion of the cotangent, we obtain for the remaining sum, up to corrections of

[1] For $\alpha = 0$, $|A_m|^2$ is identical on both edges (*i.e.* $|\langle\epsilon_m|\mathrm{in}_\pm\rangle|^2 = |\langle\epsilon_m|\mathrm{out}_\pm\rangle|^2$) and independent of the direction of $|\epsilon_m\rangle$ (*i.e.* whether $|\epsilon_m\rangle$ resides on Γ_+ or Γ_-). Yet, the incoming and outgoing amplitudes are related via $\exp(\mathrm{i}kl^{(\mathrm{in})})A_m^{(\mathrm{in})} = \exp(\mathrm{i}\epsilon_m)A_m^{(\mathrm{out})}$. This explains the appearance of the phase factor in the numerator of equation (3.9).

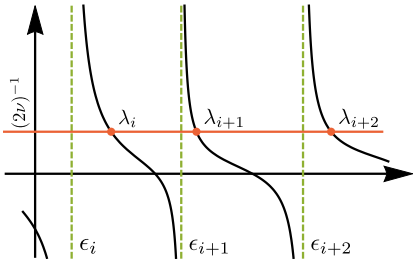

Fig. 3.4.: Schematic representation of the right-hand side of equations (3.10, 3.11) as a function of λ. One finds a solution to the secular equation whenever this sum is equal to $(2\nu)^{-1}$, $\nu = \tan\alpha$ as indicated by the horizontal, grey line. This graphical procedure nicely illustrates the interlacing property as all the λ_i can be found in between adjacent ϵ_i, ϵ_{i+1} who define the poles of the sum.

$O(1/B)$:

$$\frac{1}{2\nu} = \sum_{m=1}^{N} \frac{|A_m|^2}{\lambda - \epsilon_m} \qquad \text{with} \quad \nu = \tan\alpha\,. \tag{3.11}$$

The solutions of this equation obey the same interlacing property as before in equation (3.10).

Remarkably, equation (3.11) is identical to a secular equation considered in [89]. This work is concerned with the study of relations between old ϵ_m and new λ_m-eigenvalues in a perturbed Hamiltonian system, $H = H_0 + \nu N\,|\psi\rangle\,\langle\psi|$, where H_0 is drawn from a GUE ensemble of $N \times N$ random matrices. Leaving aside differences in the physical interpretation this allows us to build upon the results of [89] in the next section, where we consider the spectral statistics of $\{\lambda_m\}$. As we demonstrate later, the spectral statistics of the graph's physical spectrum $\{k_n\}$ determined by equation (3.2) can, in the large B limit, be obtained from these results by a simple rescaling.

3.3. Analytic Calculations — RMT approach.

Throughout this section we derive the nearest neighbour distance distribution $p_\nu(s)$ for nearly unidirectional quantum graphs using a RMT like approach. In addition to the exact results presented here we provide a compact, heuristic surmise in section 3.5.

Recall that the perturbed spectrum consists of two parts, the pinned ϵ-eigenvalues, and in between the λ eigenvalues, $\epsilon_i \le \lambda_i \le \epsilon_{i+1}$, moving under perturbation (see section 3.2). Because of this it is natural to split $p_\nu(s)$ into two parts,

$$p_\nu(s) = \frac{1}{2}\Big(p_\nu^{\mathrm{ex}}(s) + p_\nu^{\mathrm{in}}(s)\Big)\,, \tag{3.12}$$

where $p_\nu^{\mathrm{in}}(s)$ is the internal splitting distribution for the distances between ϵ_i and the next λ_i to the right while $p_\nu^{\mathrm{ex}}(s)$ covers the expanse from λ_i to the next ϵ_{i+1}. The

derivation of both splitting distributions follows along the same lines but we focus mainly on $p_\nu^{\rm in}(s)$ presenting results for $p_\nu^{\rm ex}(s)$ at the end of this section. In addition, only the case $\nu > 0$ has to be treated. As can be inferred from the secular equation, the result for $\nu < 0$ is obtainable by exchanging the roles of $p_\nu^{\rm in}(s)$ and $p_\nu^{\rm ex}(s)$, *i.e.*

$$p_\nu^{\rm ex}(s) = p_{-\nu}^{\rm in}(s) \quad \text{and} \quad p_\nu^{\rm in}(s) = p_{-\nu}^{\rm ex}(s)\,. \tag{3.13}$$

Let us emphasize that the results we present below for $\nu > 0$ would not yield meaningful splitting distribution if negative ν are entered, instead one should use the above relations.

Relating the splitting distributions $p(s)$ to the gap probability is a well established procedure in RMT since the later quantity is often easier to calculate, *cf.* [18]. In our case we have two different sub-spectra and the gap probability $E = E(\epsilon_{\rm min}, \epsilon_{\rm max}; \lambda_{\rm min}, \lambda_{\rm max})$ is defined as probability that no eigenvalue of the respective kind, *i.e.* ϵ_i and λ_j, can be found in the intervals $[\epsilon_{\rm min}, \epsilon_{\rm max}]$ and $[\lambda_{\rm min}, \lambda_{\rm max}]$, where, in principle, the two intervals should be thought of as being independent.

To establish the connection between E and $p_\nu(s)$ let us first consider the probability to find an ϵ-eigenvalue in an interval $[\epsilon_{\rm min} - \delta_\epsilon, \epsilon_{\rm min}]$, in the limit of $\delta_\epsilon \to 0$. This is the probability not to have an ϵ gap at this position and thus can be expressed as $1 - E(\epsilon_{\rm min} - \delta_\epsilon, \epsilon_{\rm min}; 0, 0)$. Divided by the length δ_ϵ of the interval the result is the mean level density $\bar\rho^{(\epsilon)}$ for the ϵ spectrum

$$\bar\rho^{(\epsilon)}(\epsilon_{\rm min}) = \frac{\partial}{\partial \epsilon_{\rm min}} E(\epsilon_{\rm min}, \epsilon_{\rm max}; 0, 0)\Big|_{\epsilon_{\rm min}=\epsilon_{\rm max}}\,. \tag{3.14}$$

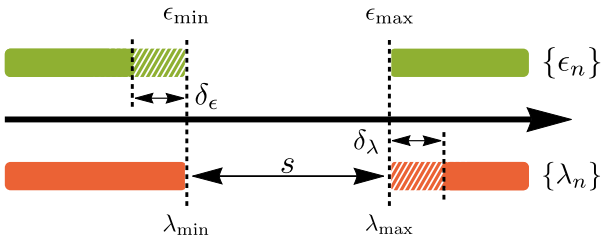

Fig. 3.5.: Drawing of a gap in the $\{\epsilon_n\}$,$\{\lambda_n\}$ spectrum with size s. To take derivatives of the gap probability E we expand it linearly around small perturbations of the respective gap boundary, which one can think of as small δ extensions of the original gap, see shaded intervals in the figure.

We now extend our consideration to the gap intervals $[\epsilon_{\rm min}, \epsilon_{\rm max}]$, $[\lambda_{\rm min}, \lambda_{\rm max}]$ where $\epsilon_{\rm min} = \lambda_{\rm min}$, $\epsilon_{\rm max} = \lambda_{\rm max}$ while the endpoints are separated by some finite distance $s = \bar\rho^{(\epsilon)}(\epsilon_{\rm min})|\lambda_{\rm min} - \epsilon_{\rm max}|$ measured on the scales of MLS $\bar\rho^{-1}$, see figure 3.5. Let $p^{(\epsilon\lambda)}$ be the probability (density) to find an ϵ-eigenvalue in the interval $[\epsilon_{\rm min} - \delta_\epsilon, \epsilon_{\rm min}]$ simultaneously with another λ-eigenvalue in the interval $[\lambda_{\rm max}, \lambda_{\rm max} + \delta_\lambda]$ such that no other eigenvalues are present in-between. Following the same line of reasoning as before,

it is given by a double derivative of E with respect to both edges $\epsilon_{\min}$ and $\lambda_{\max}$. On the other hand, $p^{(\epsilon\lambda)}$ is also equal to the probability density $\bar{\rho}^{(\epsilon)}$ to find an ϵ-eigenvalue in the interval $[\epsilon_{\min} - \delta_\epsilon, \epsilon_{\min}]$ times the probability density to find the next λ-eigenvalue in the distance s. The later one is exactly the sought $p_\nu^{\text{in}}(s)$. Therefore we may express it as

$$p_\nu^{\text{in}}(s) = \frac{1}{\bar{\rho}^{(\epsilon)}(\epsilon_{\min})} \frac{\partial^2}{\partial\epsilon_{\min}\partial\lambda_{\max}} E(\epsilon_{\min}, \epsilon_{\max}; \lambda_{\min}, \lambda_{\max})\Big|_{\substack{\epsilon_{\min}=\lambda_{\min}=-s/2\,\bar{\rho}^{(\epsilon)}(0) \\ \epsilon_{\max}=\lambda_{\max}=+s/2\,\bar{\rho}^{(\epsilon)}(0)}}, \tag{3.15}$$

where, for the sake of convenience, we have chosen the gap symmetrically around zero.

A similar result holds for $p_\nu^{\text{ex}}(s)$. In principle only the boundary derivatives have to be exchanged,

$$p_\nu^{\text{ex}}(s) = \frac{1}{\bar{\rho}^{(\lambda)}(\lambda_{\min})} \frac{\partial^2}{\partial\lambda_{\min}\partial\epsilon_{\max}} E(\epsilon_{\min}, \epsilon_{\max}; \lambda_{\min}, \lambda_{\max})\Big|_{\substack{\epsilon_{\min}=\lambda_{\min}=-s/2\,\bar{\rho}^{(\lambda)}(0) \\ \epsilon_{\max}=\lambda_{\max}=+s/2\,\bar{\rho}^{(\lambda)}(0)}}, \tag{3.16}$$

where $\bar{\rho}^{(\lambda)}$ denotes the mean level density of the λ-spectrum. In our case $\bar{\rho}^{(\lambda)} = \bar{\rho}^{(\epsilon)}$ holds.

3.3.1. Gap Probability E

We now present the derivation of the gap probability E for nearly unidirectional quantum graphs employing a RMT model. Our calculations rest upon the secular equation (3.11), where the N distinct ϵ-eigenvalues are distributed in accordance with the Circular Unitary Ensemble (CUE) describing the distribution of eigenvalues in TRI unidirectional quantum graphs. Further on, we assume, in accordance with [89, 90], a Gaussian distribution for the overlaps $|A_m|$:

$$p(|A_m|^2) = N \exp\left(-N|A_m|^2\right), \tag{3.17}$$

which can be expected for large graphs. The validity of this assumption is discussed towards the end of section 3.4.

This RMT model was employed previously in [89] to calculate the two-point correlation function between the $\{\epsilon_i\}$ and $\{\lambda_i\}$ spectra, to which end the following joint probability distribution $P(\{\epsilon_i\}, \{\lambda_j\})$ for the total spectrum was derived:

$$P(\{\epsilon_i\}, \{\lambda_j\}) \propto \left(\prod_{\substack{i,j=1 \\ i>j}}^{N} 4 \sin\frac{\epsilon_i - \epsilon_j}{2} \sin\frac{\lambda_i - \lambda_j}{2} \right) \exp\left(-\frac{N}{2\nu} \sum_{i=1}^{N} (\lambda_i - \epsilon_i) \right). \tag{3.18}$$

The ϵ and λ eigenvalues run from $[-\pi, +\pi]$ under the constraint of the interlacing property. Please observe that $\{\epsilon_i\}$ is taken without degeneracy and $\{\lambda_i\}$ only consists

of the shifted eigenvalues, similar to the usage in the secular equations. We will now utilize (3.18) in order to calculate the gap probability function:

$$E(\epsilon_{\min},\epsilon_{\max};\lambda_{\min},\lambda_{\max}) \propto \int_{-\pi}^{+\pi} \mathrm{d}\epsilon_1 \int_{\epsilon_1}^{\pi} \mathrm{d}\lambda_1 \int_{\lambda_1}^{\pi} \mathrm{d}\epsilon_2 \ldots \int_{\epsilon_N}^{+\pi} \mathrm{d}\lambda_N \, P(\{\epsilon_i\},\{\lambda_j\}) \\ \times \prod_{k=1}^{N} \Big(\big(1-\theta(\epsilon_k-\epsilon_{\min})\theta(\epsilon_{\max}-\epsilon_k)\big)\big(1-\theta(\lambda_k-\lambda_{\min})\theta(\lambda_{\max}-\lambda_k)\big)\Big) . \tag{3.19}$$

A special feature of the gap probability is that it relates to all eigenvalues of the spectrum in a uniform manner, visible in its product structure, which allows to take all integrals by standard methods, *cf.* [18]. In the following we briefly sketch this procedure.

Expanding the sine functions into exponentials,

$$\prod_{\substack{i,j=1\\ i>j}}^{N} \sin\left(\frac{\epsilon_i-\epsilon_j}{2}\right) \propto \prod_{\substack{i,j=1\\ i>j}}^{N} \mathrm{e}^{-\mathrm{i}/2(\epsilon_i+\epsilon_j)} \left(\mathrm{e}^{\mathrm{i}\epsilon_i}-\mathrm{e}^{\mathrm{i}\epsilon_j}\right) = \Delta\{\mathrm{e}^{\mathrm{i}\epsilon_i}\} \prod_{j=1}^{N} \mathrm{e}^{-\frac{\mathrm{i}}{2}(N-1)\epsilon_j} , \tag{3.20}$$

one finds Vandermonde determinants Δ of ϵ variables with a similar result for the λ part. Upon reordering the domains of integration,

$$\int_{-\pi}^{+\pi} \mathrm{d}\epsilon_1 \int_{\epsilon_1}^{\pi} \mathrm{d}\lambda_1 \int_{\lambda_1}^{\pi} \mathrm{d}\epsilon_2 \ldots \int_{\epsilon_N}^{+\pi} \mathrm{d}\lambda_N \to \int_{-\pi}^{+\pi} \mathrm{d}\epsilon_1 \int_{\epsilon_1}^{+\pi} \mathrm{d}\epsilon_2 \ldots \int_{\epsilon_{N-1}}^{+\pi} \mathrm{d}\epsilon_N \int_{\epsilon_1}^{\epsilon_2} \mathrm{d}\lambda_1 \ldots \int_{\epsilon_{N-1}}^{\epsilon_N} \mathrm{d}\lambda_{N-1} \int_{\epsilon_N}^{+\pi} \mathrm{d}\lambda_N , \tag{3.21}$$

the integrals over the λ variables can be drawn into the corresponding determinant form:

$$D\{\epsilon_i\} = \begin{vmatrix} \int_{\epsilon_1}^{\epsilon_2} \mathrm{d}\lambda_1 f_1(\lambda_1) & \int_{\epsilon_1}^{\epsilon_2} \mathrm{d}\lambda_1 f_2(\lambda_1) & \ldots & \int_{\epsilon_1}^{\epsilon_2} \mathrm{d}\lambda_1 f_N(\lambda_1) \\ \vdots & \vdots & \ddots & \vdots \\ \int_{\epsilon_{N-1}}^{\epsilon_N} \mathrm{d}\lambda_{N-1} f_1(\lambda_{N-1}) & \int_{\epsilon_{N-1}}^{\epsilon_N} \mathrm{d}\lambda_{N-1} f_2(\lambda_{N-1}) & \ldots & \int_{\epsilon_{N-1}}^{\epsilon_N} \mathrm{d}\lambda_{N-1} f_N(\lambda_{N-1}) \\ \int_{\epsilon_N}^{\pi} \mathrm{d}\lambda_N f_1(\lambda_N) & \int_{\epsilon_N}^{\pi} \mathrm{d}\lambda_N f_2(\lambda_N) & \ldots & \int_{\epsilon_N}^{\pi} \mathrm{d}\lambda_N f_N(\lambda_N) \end{vmatrix} , \tag{3.22}$$

where $f_j(\lambda_i)$ is a shorthand for $\exp\left(\mathrm{i}(j-1)\lambda_i + \mathrm{i}(N-1)\lambda_i/2 - N\lambda_i/(2\nu)\right)$. The remaining integral over the ϵ variables

$$E(\epsilon_{\min},\epsilon_{\max};\lambda_{\min},\lambda_{\max}) \propto \int_{-\pi}^{+\pi} \mathrm{d}\epsilon_1 \int_{\epsilon_1}^{+\pi} \mathrm{d}\epsilon_2 \ldots \int_{\epsilon_{N-1}}^{+\pi} \mathrm{d}\epsilon_N D\{\epsilon_i\}\Delta\{\mathrm{e}^{\mathrm{i}\epsilon_i}\} \prod_{j=1}^{N} \mathrm{e}^{\frac{\mathrm{i}N\epsilon_j}{2}\left(1-\frac{1}{N}-\frac{\mathrm{i}}{\nu}\right)} , \tag{3.23}$$

can then be treated as follows. Adding the last line of the determinant $D\{\epsilon_i\}$ to the second last and then continuing recursively sets the upper boundary to π in all integrals

and shows the antisymmetry of $D\{\epsilon_i\}$ under exchange of $\epsilon_i \leftrightarrow \epsilon_j$. Therefore, the integrand in equation (3.23) is a symmetric function, implying that the boundaries of integration can be extended to the full domain $[-\pi, +\pi]$ (up to a factor).

Finally, we exploit the fact that Vandermonde determinants can be expanded into alternating sums

$$\Delta\{\mathrm{e}^{\mathrm{i}\epsilon_i}\} = \sum_{\{\sigma\}} (-1)^{|\sigma|} \mathrm{e}^{\mathrm{i}\sigma(1)\epsilon_1} \mathrm{e}^{\mathrm{i}\sigma(2)\epsilon_2} \dots \mathrm{e}^{\mathrm{i}\sigma(N)\epsilon_N} \,, \tag{3.24}$$

wherein $\{\sigma\}$ represents the set of all permutations of the numbers $(0,\ 1,\ \dots\ N-1)$, $|\sigma|$ denotes the permutation's parity and $\sigma(i)$ yields the number associated to i under permutation σ. The symmetry of the integrand in (3.23) allows us to absorb the single factors into the second determinant, leading to

$$E(\epsilon_{\min}, \epsilon_{\max}; \lambda_{\min}, \lambda_{\max}) = \frac{\det F(\epsilon_{\min}, \epsilon_{\max}; \lambda_{\min}, \lambda_{\max})}{\det F(0,0;0,0)} \,, \tag{3.25}$$

where $F(\epsilon_{\min}, \epsilon_{\max}; \lambda_{\min}, \lambda_{\max})$ is a $N \times N$ matrix with elements

$$\begin{aligned} F_{kl} = &\int_{-\pi}^{+\pi} \mathrm{d}\epsilon \int_{\epsilon}^{+\pi} \mathrm{d}\lambda \, \mathrm{e}^{-\frac{N}{2\nu}(\lambda-\epsilon)} \mathrm{e}^{\mathrm{i}(k-1)\epsilon - \mathrm{i}\frac{N-1}{2}\epsilon} \mathrm{e}^{\mathrm{i}(l-1)\lambda - \mathrm{i}\frac{N-1}{2}\lambda} \\ &\times \Big(\big(1-\theta(\epsilon-\epsilon_{\min})\theta(\epsilon_{\max}-\epsilon)\big)\big(1-\theta(\lambda-\lambda_{\min})\theta(\lambda_{\max}-\lambda)\big) \Big) \,. \end{aligned} \tag{3.26}$$

The denominator of E ensures that the probability to find gaps of zero width in both spectra is unity. It is related to the omitted normalisation of P in Equation (3.18). The integral in (3.26) consists of four parts, depending on the combinations of Heaviside θ-functions, which can be calculated explicitly. For the sake of compactness of exposition the resulting expressions are not presented here. They can be found in appendix A.1.

3.3.2. Splitting Distribution

Using equations (3.15, 3.25) and taking into account that $\bar{\rho}^{(\lambda)} = \bar{\rho}^{(\epsilon)} = N/(2\pi)$ we can write the nearest neighbour distribution as

$$p_\nu^{\mathrm{in}}(s) = \left(\frac{2\pi}{N}\right) \frac{\partial_{\delta_\epsilon}\partial_{\delta_\lambda} \det F^{(\mathrm{num})}(s\pi/N, \delta_\epsilon, \delta_\lambda)}{\partial_{\delta_\epsilon} \det F^{(\mathrm{den})}(s\pi/N, \delta_\epsilon)}\Big|_{\delta_\epsilon=\delta_\lambda=0} \,, \tag{3.27}$$

where the matrices in the numerator and denominator are given by

$$F^{(\mathrm{num})}(z, \delta_\epsilon, \delta_\lambda) := F(-z-\delta_\epsilon, z; -z, z+\delta_\lambda) \,, \tag{3.28}$$

$$F^{(\mathrm{den})}(z, \delta_\epsilon) := F(-z-\delta_\epsilon, -z; 0, 0). \tag{3.29}$$

For an illustration of the gap position please refer to figure 3.5. Expression (3.27) can be straightforwardly evaluated expanding $F^{(\mathrm{num})}$ and $F^{(\mathrm{den})}$ up to linear order in $\delta_\epsilon \cdot \delta_\lambda$ (resp. δ_ϵ) and then taking the large N-limit. (The resulting expressions are given by equations (A.6) and (A.7) in the appendix.) At this point it is convenient to introduce a pair of auxiliary N-dimensional vectors $|u\rangle, |u^*\rangle$:

$$\langle j\,|u\rangle = \mathrm{e}^{+\mathrm{i}j\frac{\pi}{N}s}\,, \quad \langle j\,|u^*\rangle = \mathrm{e}^{-\mathrm{i}j\frac{\pi}{N}s}\,, \tag{3.30}$$

and $N \times N$ matrices:

$$\Lambda_{kl} = \left(\mathrm{i}k + \frac{N}{2\nu} - \mathrm{i}\frac{N+1}{2}\right)\delta_{kl}\,, \qquad R_{kl} = \delta_{kl} - \left(\frac{\sin{(k-l)\pi/Ns}}{(k-l)\pi}\right)_{kl}\,. \tag{3.31}$$

Here, $\mathbb{1} - R$ is the well known sine-kernel matrix. This notation enables us to write the leading order expansion of both matrices (3.28, 3.29) in a compact form:

$$F^{(\mathrm{den})} = -2\pi\Lambda + \delta_\epsilon\Lambda\,|u\rangle\,\langle u| + O(1/N)\,, \tag{3.32}$$

$$F^{(\mathrm{num})} = -2\pi\Lambda R + |u\rangle\,\langle u| - g\big(\delta_\epsilon\Lambda\,|u^*\rangle - |u^*\rangle\big)\,\big(\,\langle u|\,\Lambda\delta_\lambda - \langle u|\,\big) + O(1/N)\,, \tag{3.33}$$

where $g = \exp\big(\mathrm{i}(N+1)\frac{\pi}{N}s - \frac{\pi}{\nu}s\big)$. The corrections stand for neglected terms of order $O(1/N)$ in the elements of F. Employing the relationship

$$\det(A + |x\rangle\,\langle y|) = \det(A)\,\big(1 + \langle y|\,A^{-1}\,|x\rangle\big) \tag{3.34}$$

the determinant of $F^{(\mathrm{den})}$ can easily be calculated:

$$\det(F^{(\mathrm{den})}) = (-2\pi)^N \det(\Lambda)(1 - N\delta_\epsilon/2\pi)\,. \tag{3.35}$$

Taking also into account

$$\big(A + |u\rangle\,\langle v|\,\big)^{-1} = A^{-1} - \frac{A^{-1}\,|u\rangle\,\langle v|\,A^{-1}}{1 + \langle v|\,A^{-1}\,|u\rangle}\,, \tag{3.36}$$

we can perform a similar expansion for the determinant of $F^{(\mathrm{num})}$, leading finally to

$$\begin{aligned} p_\nu^{\mathrm{in}}(s) = 2\frac{g\pi}{N^2}\det R \times \Big(\,&\langle u|\,R^{-1}\Lambda\,|u^*\rangle - \frac{1}{2\pi}\,\langle u|\,\Lambda^{-1}R^{-1}\,|u\rangle\,\langle u|\,R^{-1}\Lambda\,|u^*\rangle \\ &+ \frac{1}{2\pi}\,\langle u|\,R^{-1}\,|u\rangle\,\langle u|\,\Lambda^{-1}R^{-1}\Lambda\,|u^*\rangle\Big) + O(1/N)\,. \end{aligned} \tag{3.37}$$

Although this quantity explicitly depends on N, it has a well defined limit for $N \to \infty$. The leading denominator is compensated by the corresponding scaling of the scalar products. Furthermore, due to the presence of the exponent g the above expression turns out to be purely real.

Along the same lines we are able to obtain the result for $p_\nu^{\mathrm{ex}}(s)$ using equation (3.16). Expanding the double derivative up to the leading order in $\delta_\epsilon, \delta_\lambda$ yields:

$$p_\nu^{\mathrm{ex}}(s) = \frac{\det R}{N^2}\Big(\langle u^*|R^{-1}|u^*\rangle \langle u|\Lambda^{-1}R^{-1}\Lambda|u\rangle - \langle u|\Lambda^{-1}R^{-1}|u^*\rangle \langle u^*|R^{-1}\Lambda|u\rangle \Big) + O(1/N)\,. \tag{3.38}$$

It is interesting to compare this result with the GUE nearest neighbour distribution $p^{\mathrm{GUE}}(s)$ which should emerge from (3.38) in the limit of $\nu \to 0$. To this end note that $p^{\mathrm{GUE}}(s)$ is related to the R matrix, [18], as:

$$p^{\mathrm{GUE}}(s) = \partial_s^2 \det R = \det R \times \left(\partial_s^2 \operatorname{Tr}\log R + (\partial_s \operatorname{Tr}\log R)^2\right)\,. \tag{3.39}$$

Further on, the derivative of R can be expressed as a rank 2 projector on $|u\rangle$ and $|u^*\rangle$. In particular

$$\partial_s \operatorname{Tr}\log R = \operatorname{Tr}\frac{\partial_s R}{R} = -\frac{1}{2N}\left(\langle u|\, R^{-1}\,|u\rangle + \langle u^*|\, R^{-1}\,|u^*\rangle\right)\,. \tag{3.40}$$

The second derivative can be treated in the same fashion and, after some cancellation, we obtain

$$p^{\mathrm{GUE}}(s) = \frac{\det R}{N^2}\Big(\langle u^*|R^{-1}|u^*\rangle \langle u|R^{-1}|u\rangle - \langle u|R^{-1}|u^*\rangle \langle u^*|R^{-1}|u\rangle \Big)\,, \tag{3.41}$$

which bears an apparent structural similarity to (3.38).

3.4. Comparison with Quantum Graph Spectra

Both expressions (3.37,3.38) depend on the inverse of the sine-kernel matrix R^{-1} which is not known explicitly. Nevertheless, they serve as a very useful tool to numerically calculate the nearest neighbour distribution. As we neglected terms of the order $O(1/N)$, the dimension N of the matrix R should be large enough to reach the limiting distribution with a sufficient precision. For practical purposes we found $N=100$ to be sufficient for all ranges of the parameter strength ν.

The resulting nearest neighbour distributions obtained evaluating equations (3.37, 3.38) are presented in figure 3.6. In all cases we found a perfect agreement with the distribution (not shown here) of eigenvalues drawn from the Random Matrix Ensembles of section 3.3. Without perturbation, *i.e.* for $\nu=0$, $p_\nu^{\mathrm{ex}}(s)$ is given by the GUE nearest neighbour distribution while $p_\nu^{\mathrm{in}}(s)$ is just a δ-spike at 0 due to the exact degeneracy of the system. Under a small perturbation this spike erodes, but both parts of the splitting distribution, $p_\nu^{\mathrm{in}}(s)$ and $p_\nu^{\mathrm{ex}}(s)$, are still distinguishable. With increasing perturbation strength both distributions become more similar. From the secular equation (3.11) one can infer that, in the limit $\nu \to \infty$, they are actually identical.

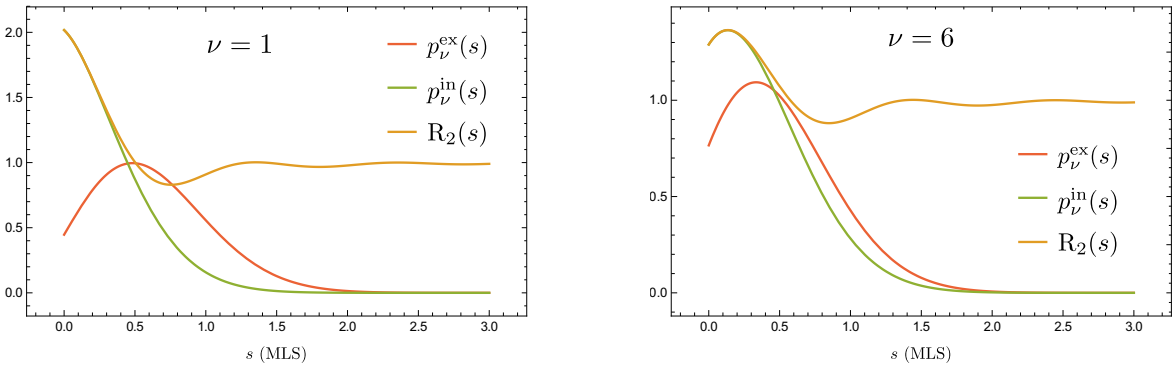

Fig. 3.6.: Analytic results for $p_\nu^{\mathrm{in}}(s)$, $p_\nu^{\mathrm{ex}}(s)$ and the $R_2(s)$ two point correlator derived by [89] shown together for $\nu = 2$ and $\nu = 6$. As expected $p_\nu^{\mathrm{in}}(s)$ and $R_2(s)$ are almost identical for small s. But for larger values $p_\nu^{\mathrm{in}}(s)$ decays to 0 as the nearest neighbour can not be arbitrarily far, while $R_2(s)$ saturates towards 1 as farther away values are no longer correlated. With increasing perturbation strength, see right panel, $p_\nu^{\mathrm{in}}(s)$ and $p_\nu^{\mathrm{ex}}(s)$ tend towards the same limiting distribution.

It is quite remarkable that the perturbation does not lead to a strict level repulsion as for any ν one finds $p_\nu^{\mathrm{in}}(0) > 0$. Furthermore, under onset of the perturbation there is no longer a strict repulsion between λ_i and the ϵ_{i+1} eigenvalue to the right either, *i.e.* $p_\nu^{\mathrm{ex}}(0) > 0$ if $\nu > 0$. For comparison we present here the two point correlation function $R_2(s)$ between the ϵ and the λ part of the spectrum which was derived in [89, 91] (for related quantities also refer to [92]). For small distances s this function naturally agrees with $p_\nu^{\mathrm{in}}(s)$ as is visible in figure 3.6.

Nearly unidirectional quantum graphs — In what follows we compare the above results with the nearest neighbour distributions of actual quantum graph spectra $\{k_n\}$. For this we use several families of nearly unidirectional quantum graphs constructed according to the guidelines in section 3.1. To find numerical solutions to the equation

$$\det\left(1 - S\mathcal{L}(k_n)\right) = 0 \tag{3.42}$$

we used the (by definition) positive singular eigenvalues of $1-S\mathcal{L}(k)$ and searched for the points where the lowest one becomes 0, see *e.g.* [93] for details of this method. Noticing that, for not too small graphs, the lowest lying eigenvalues depend approximately linearly on k it is straightforward to follow the downwards slope within a few iterations. We found this approach to work rather fast and accurately, such that 9 significant post-decimal digits can easily be achieved.

In addition to the actual $\{k_n\}$ spectrum of the graph we also computed the splitting distribution between the eigenphases of the unitary quantum map $S\mathcal{L}(k)$. In the large B limit both spectra are known to possess the same statistics after rescaling the MLS to 1, [23, 94]. Indeed, the average "velocity" of the eigenphases over k depends on the (fixed)

average edge length $\bar{l}_i$ while fluctuations decrease with increasing bond number. As a result, both spectral statistics coincide in the large B limit. But, since we obtain $2B$ eigenvalues for any arbitrary k, this approach is numerically significantly less expensive.

If not stated otherwise we set the back-scattering matrix $\tilde{\sigma}$, equation (3.5), to

$$\begin{aligned} \alpha = -\arctan\nu\,, \quad \beta = 0\,, \quad \gamma = 0 \\ \rightarrow \qquad r = \frac{\nu}{\mathrm{i}-\nu}\,, \quad t = \frac{\mathrm{i}}{\mathrm{i}-\nu}\,. \end{aligned} \tag{3.43}$$

This choice is reminiscent of placing an actual strength ν δ-potential on an edge ($H = \Delta + \nu\delta(x)$), where transmission and reflection rates of the free wave propagation are given by r and t. We omit here the k dependence of such type of perturbation. The graph lengths were chosen randomly from the interval $[0, 1]$ and rescaled such that the mean length is 1.

Fully connected graph — This graph is composed of V vertices, which are interconnected by $B = V(V-1)/2$ bonds. At his point we do not allow self-loops, *i.e.* a vertex cannot be connected to itself. The U_i scattering matrices for each vertex, see equation (3.3), are drawn randomly. Figures 3.7 and 3.8 demonstrate that both, $p_\nu^{\mathrm{in}}(s)$ and $p_\nu^{\mathrm{ex}}(s)$, agree quite nicely with the analytic predictions. The latter figure is obtained from the phases of the scattering matrix showing additionally the strong statistical correspondence to the quantum graph's spectrum.

Binary De Bruijn Graphs — The 2^p vertices of these graphs can be labelled by binary sequences of length p. Each vertex $a_1a_2\ldots a_p$, $a_i = \{0, 1\}$ is connected with several (generically 4) others labelled by the sequences $ba_1a_2\ldots a_{p-1}$, $b = \{0, 1\}$, or $a_2a_3\ldots a_pc$, $c = \{0, 1\}$, which are obtained by adding one symbol to the left and removing one on the right or vice versa, see [95]. A sketch of such a graph for $p=3$ can be found in figure 3.3. As opposed to the fully connected graphs, De Bruijn graphs feature several short cycles – the alternating pattern $1010\ldots0 \rightarrow 0101\ldots1 \rightarrow 1010\ldots0$ is of length 2, while the vertices $11\ldots1$ and $00\ldots0$ have attached self-loops. The scattering matrices at each vertex are identical and chosen in such a way that the original graph is unidirectional.

The results for the nearest neighbour distributions turn out to be quite sensitive to the choice of the back-scatterer position. If $\tilde{\sigma}$ is placed on a generic edge we once again find a good agreement with the RMT predictions, see figure 3.9a,b. As can be seen on figure 3.10, the same stays true if we change the scattering matrix at some generic vertex of the original unidirectional quantum graph Γ_0 to correspond to Neumann boundary conditions (thus breaking unidirectionality). On the other hand, if we place the back-scatterer on one of the self-loops (see figure 3.3) this has a drastic effect on the resulting splitting distribution, see figure 3.9c,d.

To explain these findings let us recall that in the analytic RMT model we made an assumption, equation (3.17), on the uniform (random wave) distribution of the

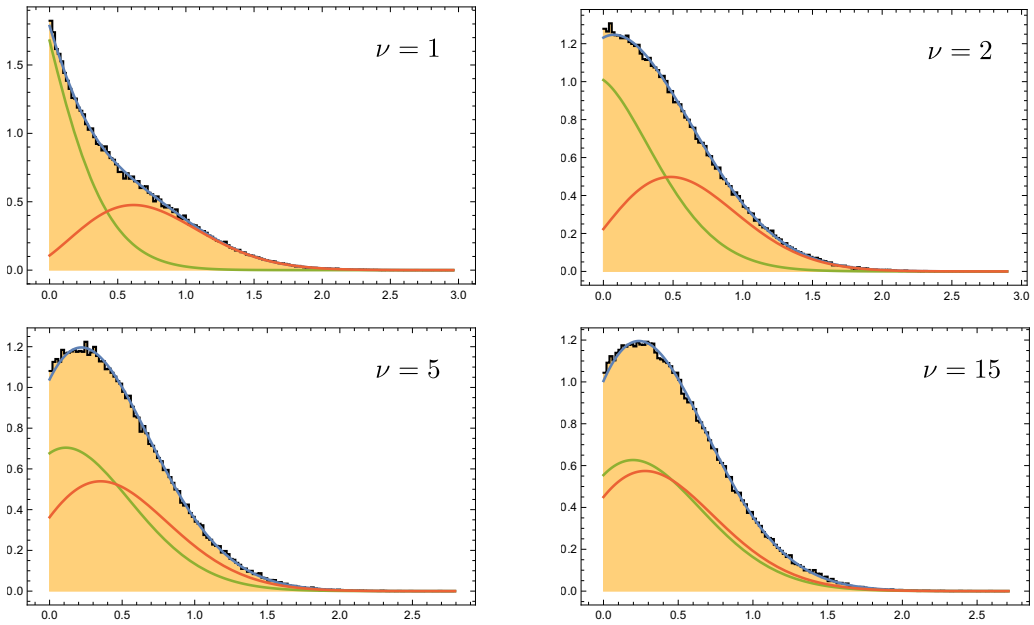

Fig. 3.7.: Histograms of the nearest neighbour distances for the 130,000 lowest k-eigenvalues obtained from a fully connected graph with 17 vertices plus back-scatterer, see text. The blue line shows the analytic result derived in section 3.3 for comparison. The green and, respectively, red lines indicate the contributions of the single $p_\nu^{\text{in}}(s)$ and, respectively, $p_\nu^{\text{ex}}(s)$ to the analytical result, where always $p_\nu^{\text{in}}(0) \geq p_\nu^{\text{ex}}(0)$ holds. The lower panels demonstrate the onset of saturation for strong perturbations in which the distribution of both sub-splittings will become identical. MLS is adjusted to $\langle \epsilon_{i+1} - \epsilon_i \rangle = 1$. (Weaker perturbation strengths can be found in figure 3.8)

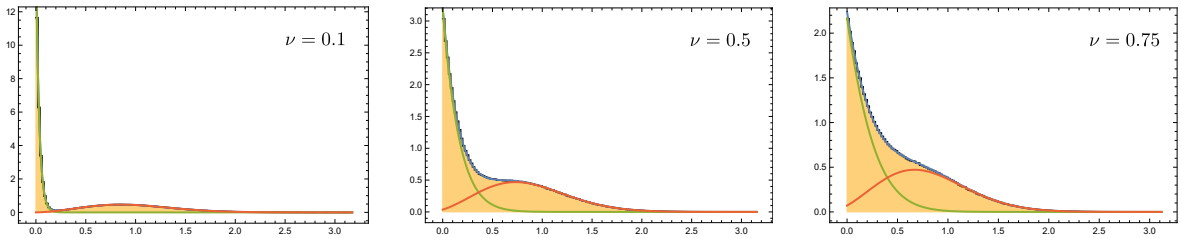

Fig. 3.8.: Histograms for $p_\nu(s)$ obtained from 2.7×10^6 eigenphases of the graph's quantum map. Further details as in figure 3.7.

wave-function's probability density $|A_m|^2$ at the scatterer position. On the other hand, wave functions on certain types of graphs are known to exhibit enhanced localisation (scars) on some edges [25, 96]. To shed further light onto the sensitivity of $p_\nu(s)$ to such enhancements we analysed the distribution of $|A_m|^2$ at different edges of the graph. Figure 3.11 shows the results for two different edges of a De Bruijn graph illustrating the significant differences between the actual result and our original assumption, equation (3.17).

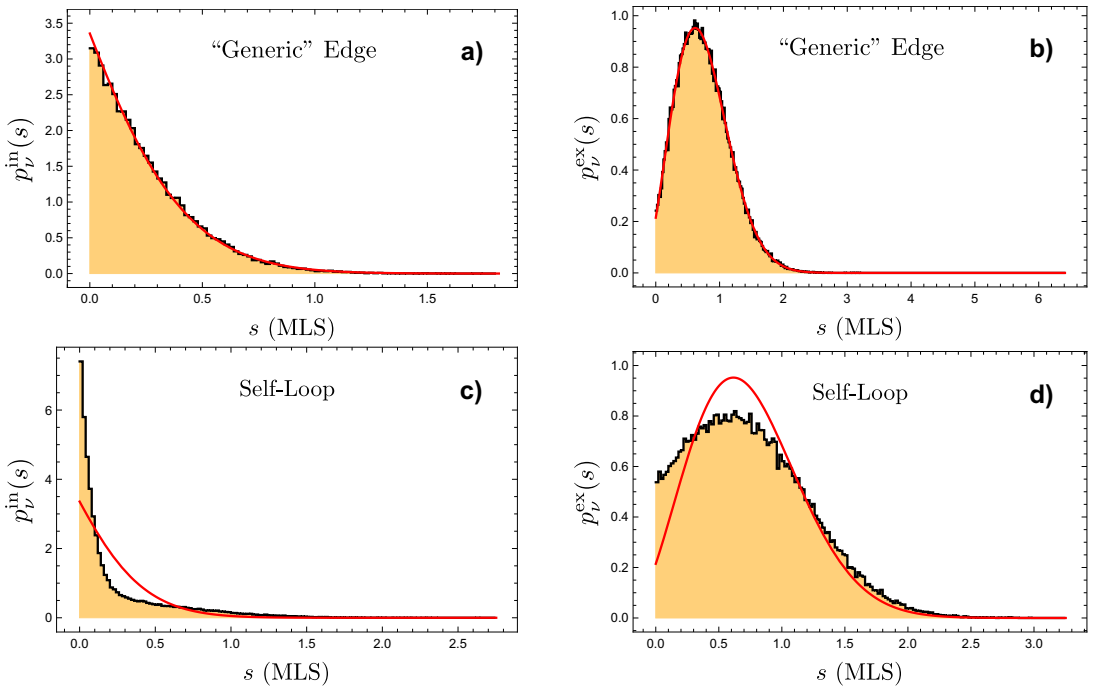

Fig. 3.9.: Histogram for the splitting distributions in binary De Bruijn graphs. In the lower row the back-scattering element is located on a self-loop of the graph while in the upper it is far away from short cycles. It is plainly visible that the "self-loop" distributions deviate largely from the anticipated analytic results (black lines) while for the "generic" case the agreement is comparable to the results obtained from the fully connected graph, figures 3.7 and 3.8. Further on, it appears that the effect is strongest for small splittings s and therefore mainly affects the internal splitting $p_\nu^{\mathrm{in}}(s)$.

Other systems — Besides the case of fixed local scattering matrices σ_i we also investigated the case of a random choice for the De Bruijn graphs, as well as completely randomly constructed unidirectional graphs with low connectivity. Above deviation was present in all short cycles (containing up to 4 edges) of the tested graphs, decaying with increasing cycle length. Notwithstanding, the choice of the local scattering matrices σ_i along the cycles also has an important impact on the strength of the effect.

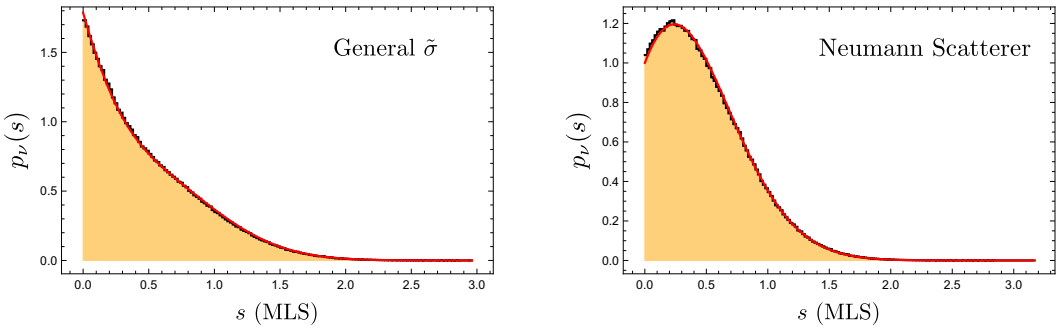

Fig. 3.10.: Depicted are nearest neighbour distance distributions for a De Bruijn graph with 64 vertices. On the left-hand side we placed, on a "generic" edge (see figure 3.11), a general scatterer with $\alpha = \pi/4$, $\beta = \pi/3$ and $\gamma = 4/5\,\pi$, which corresponds to $\nu = 1$ as indicated by the analytic black line. On the right-hand side no scatterer is placed at all, as a substitute we replace σ_i of one vertex with Neumann boundary conditions. The plotted analytical result represents $\nu \to \infty$. Minor deviations can be attributed to the mismatch in $p(|A_m|^2)$ for De Bruijn graphs, see right-hand side of figure 3.11

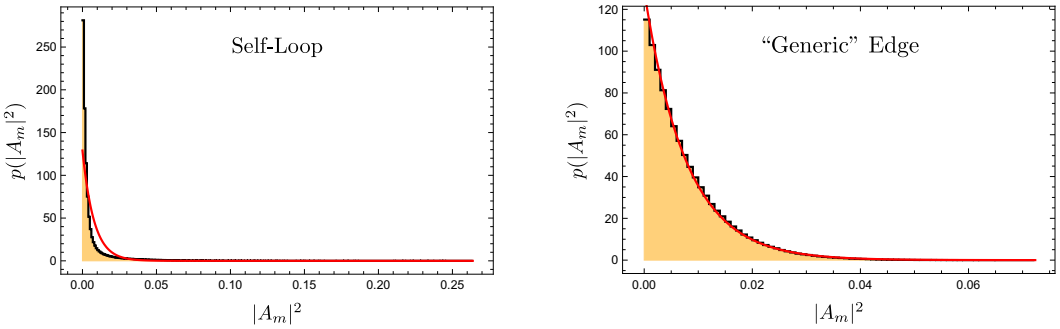

Fig. 3.11.: Histograms showing the distribution of wave functions (absolute square) on two edges of a De Bruijn graph. Either on a self-loop or far away from any short cycles (right panel). In the generic case one finds the expected uniform distribution as in equation (3.17). But for the self-loop the wave function either avoids the edge, *i.e.* increased probability for very small A_m or it has an enhanced localisation. A logarithmic scaling would reveal an (exponentially decaying) strong tail for large A_m where the distribution is orders of magnitudes larger than our assumption suggested. For instance $|A_m|^2 > 0.2$ denotes that at least one fifth of the wave-function is localised on this edge, implying a much smaller weight on the other 127 edges.

3.5. Heuristic Surmise

The formulas (3.37,3.38) for the nearest neighbour distribution, although exact, require to calculate the inverses of large matrices. It would therefore be of interest to have a simple, analytical expression approximating $p_\nu^{\rm in}(s)$ and $p_\nu^{\rm ex}(s)$. In the following we obtain such an expression based on the Wigner Surmise, recall also section 2.2, providing the nearest neighbour distribution for GUE:

$$p^{\rm W}(s) = 32\,\frac{s^2}{\pi^2}\exp\left(-\frac{4s^2}{\pi}\right). \tag{3.44}$$

First observe that independently of the perturbation strength ν, the ϵ and the shifted λ part of the spectrum are both GUE distributed if considered separately, [88]. Yet, these distributions are not independent, since we have the interlacing property – a new eigenvalue λ_i is at least as far from λ_{i-1} as from ϵ_i. To take into account correlations between the $\{\epsilon_i\}$ and $\{\lambda_i\}$ spectra let us make a crude assumption that ϵ_i and λ_{i-1} are separated by a fixed distance $c_{\rm in}$. Since the distances between λ_{i-1} and λ_i are distributed according to the Wigner Surmise, the resulting distribution between ϵ_i and λ_i,

$$p^{\rm s}(s,c_{\rm in}) = p^{\rm W}(s+c_{\rm in})/\mathcal{N}(c_{\rm in}) \qquad \text{with} \quad \mathcal{N}(c_{\rm in}) = \frac{4}{\pi}c_{\rm in}\,e^{-\frac{4c_{\rm in}^2}{\pi}} + \operatorname{erfc}\left(\frac{2c_{\rm in}}{\sqrt{\pi}}\right), \tag{3.45}$$

is the sought approximation for $p_\nu^{\rm in}(s)$ (for $s\geq 0$). Here $\mathcal{N}(c_{\rm in})$ is fixed by the normalisation condition and the optimal value of $c_{\rm in}(\nu)$ has yet to be determined. Similarly, we can look at the splitting distribution $p_\nu^{\rm ex}(s)$ between λ_i and ϵ_{i+1}, which we can express based on the same $p^{\rm s}(s)$ but with another cutting value $c_{\rm ex}(\nu)$.

To identify the correct threshold c's, we demand $p^{\rm s}(0,c_{\rm in}) = p_\nu^{\rm in}(0)$, as well as $p^{\rm s}(0,c_{\rm ex}) = p_\nu^{\rm ex}(0)$. Using the exact solutions for $s=0$ from the analytical calculations in Section 3.3 we obtain:

$$p_\nu^{\rm in}(0) = 1 + \frac{1}{\nu} - \frac{1}{2\pi\nu}\operatorname{Tr}\Lambda^{-1}, \tag{3.46}$$

$$p_\nu^{\rm ex}(0) = 1 - \frac{1}{2\pi\nu}\operatorname{Tr}\Lambda^{-1}, \tag{3.47}$$

see equations (3.37, 3.38) and, for the definition of Λ, (3.30). Although further analytic treatment of $\operatorname{Tr}\Lambda^{-1}$ is possible, it is more convenient to use the $R_2(s)$ function calculated in [89] which is depicted in Figure 3.6. Recalling that $R_2(0) = p_\nu^{\rm in}(0)$ holds we obtain

$$\lim_{N\to\infty}\operatorname{Tr}\Lambda^{-1} = 2\arctan\pi\nu\,. \tag{3.48}$$

This provides us with the necessary relation to determine $c_{\rm in}$, $c_{\rm ex}$ from ν analytically. For instance, in the limit $\nu\to\infty$ where $p_\nu^{\rm in}(0)\to 1$, $\mathcal{N}(c_{\rm in}) = p^{\rm W}(c_{\rm in})$ (likewise for $c_{\rm ex}$) gives $c_{\rm in} = c_{\rm ex} \approx 0.641$.

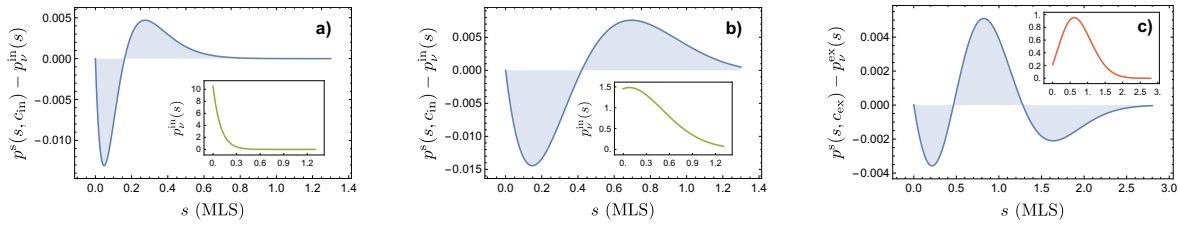

Fig. 3.12.: Shown are the absolute deviations between the heuristic surmise p^{s} and a corresponding analytical curve, which itself is plotted in the inset. In the cases a) and b) $p_\nu^{\mathrm{in}}(s)$ is depicted for $\nu=0.3$ and $\nu=4$. The last panel displays $p_\nu^{\mathrm{ex}}(s)$ for $\nu=1$. While the error stays relatively constant for $p_\nu^{\mathrm{in}}(s)$, in this case it decreases as $\nu\to 0$, whereat $p_\nu^{\mathrm{ex}}(s)$ approaches the GUE nearest neighbour distribution. Due to the discrepancy between the exact nearest neighbour distribution and $p^{\mathrm{W}}(s)$ the error will not vanish completely though. MLS is adjusted such that $\bar{\rho}^{(\epsilon)}=1$.

Surprisingly this simple surmise shows a very good agreement with the exact result for all ranges of perturbation strength. The comparison with the analytics is shown in figure 3.12.

3.6. Conclusion and Outlook

The main part of this chapter is devoted to the analytical calculation of the nearest neighbour spacing distribution $p_\nu(s)$ for the spectra of nearly unidirectional quantum graphs. Furthermore, based on the Wigner distribution for GUE we were able to obtain a simple surmise giving a good approximation for $p_\nu(s)$ valid for an arbitrary perturbation strength ν. These results show an excellent agreement with the data obtained from numerical calculations for generic (*e.g.* fully connected) graphs. However, for some classes of graphs essential deviations were found if the perturbation is placed on edges belonging to short loops. It was demonstrated that such deviations can be attributed to a strong scarring effect at these edges.

To investigate this scarring effect further it would be instructive to switch to a dynamical, semi-classical approach based on periodic orbit theory. This would allow the derivation of non-universal corrections to the RMT result based on the specific properties of the graph's edges. The semi-classical approach is also needed to address the original motivation of the splitting distribution in the spectrum of unidirectional billiard systems such as the Reuleaux polygons we showed in the beginning. As in the case of graphs, it might be expected that spectral deviations from standard statistics of GUE arise here due to the presence of diffractive orbits. While in graphs such orbits are caused by backscattering at specially designed vertices, in the unidirectional billiards the same role could be played by singular classical orbits hitting the billiard's corners.

So far, our results were restricted to rank one perturbations. However, for billiards

an effective rank of "perturbation" should (at least) depend on the number of corners. As the rank of the perturbation increases it is expected that the originally double degenerate GUE distribution must transform to the non-degenerate GOE. As a small outlook on this transition we numerically determined the nearest neighbour distribution for a graph with two/four backscattering vertices (effectively a rank two/four perturbation), presented in figure 3.13. Besides loosing the interlacing property and the split up into two sub-spectra, we find that the nearest neighbour distribution vanishes as $s \to 0$. This immediately implies level repulsion among energy levels of the system, which is absent for rank one perturbations.

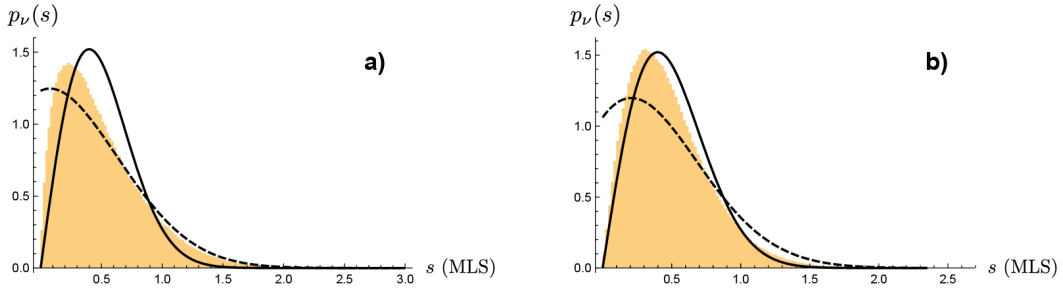

Fig. 3.13.: The images show the nearest neighbour distribution for a De Bruijn graph with 64 regular vertices and 2 (a) or 4 (b) scatterers placed on different, non-anomalous edges. Even for one additional scatterer (a) we see a strong deviation from our rank 1 result (dashed line) and instead find similarity to a GOE distribution (continuous line) which increases with larger numbers of scatterers. In both cases we find strict level repulsion as $p_\nu(0) = 0$.

Part II.

Many–Body Chaos

4. Prelude on Many-Body Systems

ALTHOUGH parts of quantum chaos, specifically its RMT side, originated from many-body systems, its other half, semi-classics was mostly restricted to systems of only a few constituents [18, 68]. At first glance this might be surprising as the theory is formally independent of the particle number N. An important ingredient to the trace-formula (2.20) is, however, the underlying chaoticity of the system dynamics. One might naively presume that a growing number of system constituents also implies a stronger tendency to chaos. In the introduction we briefly touched the difference between Hydrogen and Helium, where the 3-body interaction broke up integrability in the latter. Along this line of reasoning the solar system with its (currently) eight planets should be even more chaotic and should suffer from the resulting unpredictabilities, see section 2.1. But its current dynamic state is marked by surprising regularity, indicating that the involved Lyapunov times are at least very long [97]. On the other hand, one can easily imagine that within the solar system's phase-space, even for the same energy, initial conditions exist that truly show dynamic instability. Therefore, a clear distinction has to be made between the complexity of a system and its chaoticity — only the former naturally increases with N. Strict integrability and full chaos, as used in the Gutzwiller trace-formula, are rare occurrences. And while for single particle systems it is quite often possible to realize either extremal case, it is much harder to maintain those for their many-bodied counterparts. Instead, their dynamics will be of a mixed type, marked by forms of motion in-between the regular and chaotic ones. Already in the introduction collective forms of dynamics were given as examples of such a regular motion within a "chaotic" system. In chapter 7 we will encounter periodic orbits whose structure also follows such a "collective" pattern.

The tremendous success of quantum chaos for single particle systems rests upon the discovery and subsequent explanation of universality. This progress was guided both by the heuristic predictions of RMT and their semi-classical justification. For our further discussion we ought recapitulate the prerequisites of both theories. In the case of RMT universality emerges if the dimension of the considered (random) matrix tends to infinity, see section 2.2. On the semi-classical side we observe that for single particle quantum systems the effective dimension of the Hilbert space is controlled by $\hbar_{\text{eff}}^{-1}$ and sending it to infinity, *i.e.* $\hbar_{\text{eff}} \to 0$, corresponds to the usual semi-classical limit. But, in many-body systems N offers a further possibility to increase the Hilbert space dimension. The total system space will be a direct product of the single particle Hilbert spaces and thus grows exponentially with an increasing number of constituents.

While this imposes a severe technical limitation on many-body calculations in general, which we address in the next chapter, it also implies that random matrix theory might be applicable outside of the conventional semi-classical limit. Extensive studies have been made on specific classes of random matrices, the embedded ensembles, which emulate the interaction of many constituents while still $\hbar_{\text{eff}}$ tends to zero for each of the individual particles, see for instance [98–100]. They form a natural extension to the original considerations regarding the atomic nucleus. But, RMT also holds for far more accessible systems such as the spin-$1/2$ chain, considered in section 6, where $\hbar_{\text{eff}}$ is effectively two. In both scenarios most core results of conventional RMT, for instance the spacing distribution, are reproduced.

The presence of two large parameters, namely $\hbar_{\text{eff}}^{-1}$ and N, leads to a more involved limit process. To illustrate the arising complication we may look at the mean level spacing $\Delta \sim \hbar^{D-1}$. As generically the degrees of freedom $D \propto N$ increase with N this spacing tends to zero for $N \to \infty$ making these scales hard to resolve. Already for fixed $D > 2$ the semi-classical method warrants some discussion on its validity, for which we refer to [101, 102]. However, it is certainly a reasonable assumption that the semi-classical theory as an expansion in periodic orbits is applicable in a strict limiting sense where $\hbar_{\text{eff}}$ may be arbitrarily small while N remains fixed. Notwithstanding, this might not always be the most physical choice. Instead, it could well happen that for a given system the realized $\hbar_{\text{eff}}^{-1}$ is of the same order or even smaller than N. We thus have to ask ourselves how strongly $\hbar_{\text{eff}}$ has to tend to zero in relation to the particle number for the usual semi-classical considerations to retain validity, and, even more interestingly, what happens if they don't. Spin chains might proof a paradigm model for this type of questions as $\hbar_{\text{eff}}$ is easily tuned by changing the spin quantum number j. We approach them in chapter 7 for varying values of j.

Statements about spectral statistics usually concern scales related to the mean level spacing where universality is found in terms of statistical correlations between long periodic orbits whose duration is comparable to the Heisenberg time T_H, see section 2.3. For chaotic systems their number proliferates exponentially with time which makes such a statistical approach feasible in the first place. If one considers instead short, classical times the system behavior is dominated by only few (short) periodic orbits, implying that universality cannot be expected [36]. But, in the case of many-body systems this statement should be taken with a grain of salt. Already for short times the number of orbits can proliferate exponentially with N [67]. From a semi-classical perspective this indicates a complexity for short time behavior in many-body systems on par with long times in single particle dynamics. In the special case of chain like systems precisely this regime of short times and many particles can be explored using a duality approach first developed in [67]. Its precise working will be detailed in the next chapter.

5. Duality for Kicked Chains

Interaction among the particles of a many-body system automatically imposes a corresponding "structure" for the overall system dynamics. Throughout the second part of this thesis we study kicked spin chains with nearest neighbor interaction. The strict locality of this interaction brings to mind wave-like equations and there finite speed of propagation. Compared to, *e.g.* the counter part of a fully interacting system, any form of information or excitation has to traverse along the chain to reach another particle. Importantly, this type of structure admits a dual perspective to its dynamics which helps us overcome the problem of the enormous Hilbert space dimension typical for many-body systems. It is based on an exchange of time and particle directions. As this duality method resides at the core of all subsequent chapters we present it here in an abstract form to lay the necessary framework. Concretisations for the respective forms of the spin chains are provided later in sections 6.1.2 and 7.3.

5.1. Classical Duality

A convenient way to introduce the notion of time and particle duality is in terms of a classical field $\varphi(x,t)$ defined over a cyclic coordinate $0 \leq x < N$ including periodic boundaries, *i.e.* $\varphi(N,t) = \varphi(0,t)$. The dynamics of this field is given by the partial differential equation (PDE)

$$m\partial_t^2\varphi(x,t) + \omega^2\partial_x^2\varphi(x,t) = V(\varphi(x,t))\,. \tag{5.1}$$

It is straightforward to see that up to an exchange of the parameters m and ω^2 the equation is symmetric in $x \leftrightarrow t$. If we restrict ourselves to solutions which are additionally periodic in time with period T, *i.e.* where $\varphi(x,0) = \varphi(x,T)$ holds, the situation is fully symmetric. This implies that such periodic solutions are not only solutions to the original dynamic in time, but also solutions to a dual dynamic in coordinate space. Such a dynamical interpretation is only possible as long as (5.1) is local in space as well as in time. In particular, the dual dynamics can only be of a Hamiltonian form as long as the spatial derivative is of second order and thus plays a similar role as momentum in time.

Instead of differential equations we study, to simplify the problem, discretized dynamics both in time and space. To this end we consider N-particle systems composed

of two types of dynamics,

$$H(t) = H_I + H_K \sum_{T=-\infty}^{\infty} \delta(t-T)\,, \tag{5.2}$$

which are given by the kick part H_K and the interaction part H_I. The regular pattern of kicks provides the discretization of time and we measure, for convenience, the time in-between kicks in unit steps. The interaction part couples only nearest neighbors such that

$$H_I = \sum_{n=1}^{N} H_I^{(n)}(q_n, p_n; q_{n+1}, p_{n+1}) \tag{5.3}$$

involves only the coordinates q and momenta p of particles next to one another. The boundary conditions remain periodic, *i.e.* $q_{N+1} = q_1$ and $p_{N+1} = p_1$. The kick part is assumed to act strictly locally, meaning on each of the particles separately,

$$H_K = \sum_{n=1}^{N} H_K^{(n)}(q_n, p_n)\,. \tag{5.4}$$

Throughout the thesis we will restrict ourselves to translation invariant systems for whom $H_I^{(n)}$ and $H_K^{(n)}$ do not explicitly depend on n. This is not a strict requirement for the method to work but it simplifies the further discussion.

Within these models time and particle direction still stand on equal footing. To illustrate this we look at the symplectic map Φ: $(\vec{q}_t, \vec{p}_t) \to (\vec{q}_{t+1}, \vec{p}_{t+1})$, $\vec{q}_t = (q_{1,t}, \dots q_{n,t})$, $\vec{p}_t = (p_{1,t}, \dots p_{n,t})$, which maps the state of the system from one integer time step t to the next one. The corresponding Newtonian equations, which yield a new position $q_{n,t+1}$ for the n-th particle, read

$$q_{n,t+1} = \phi(q_{n,t}, q_{n,t-1}; q_{n-1,t}, q_{n+1,t})\,. \tag{5.5}$$

Similar to the PDE they offer a dual dynamical interpretation as they can be used to connect "future" coordinates $q_{n+1,t}$ in space through its spatial predecessors:

$$q_{n+1,t} = \tilde{\phi}(q_{n,t}, q_{n-1,t}; q_{n,t-1}, q_{n,t+1})\,. \tag{5.6}$$

Under the condition that such an inversion is unique this defines the second map $\tilde{\Phi}$: $(\vec{q}_n, \vec{p}_n) \to (\vec{q}_{n+1}, \vec{p}_{n+1})$, $\vec{q}_n = (q_{n,1}, \dots q_{n,T})$, $\vec{p}_n = (p_{n,1}, \dots p_{n,T})$ which we call dual. As for the differential equation, it corresponds to the propagation in "space", *i.e.* in particle index, rather than in time.

For a simple and explicit example we may turn to a chain of coupled harmonic oscillators. In this case the Hamiltonians are given by

$$H_I^{(n)}(q_n, q_{n+1}) = \frac{\omega^2}{2}(q_n - q_{n+1})^2 + v(q_n) \quad \text{and} \quad H_K^{(n)}(p_n) = \frac{p_n^2}{2m}\,, \tag{5.7}$$

which include a quadratic potential between neighboring spins as interaction and the free evolution as "kick". Within both terms we have the freedom to add arbitrary potentials v, as long as they do not couple the particles. For instance we could choose $v(q_n) \propto \cos q_n$ to obtain a model reminiscent of N interacting kicked rotors. Inserting (5.7) into (5.2) the dynamics, written in coordinate form, is described by the map

$$m\left(q_{n,t+1} - 2q_{n,t} + q_{n,t-1}\right) + \omega^2\left(q_{n+1,t} - 2q_{n,t} + q_{n-1,t}\right) = v'(q_{n,t})\,, \tag{5.8}$$

where $q_{n,t}$ stands for the coordinate of the n-th particle at time t. Apparently, these equations are a discretized version of the PDE (5.1) and also stay invariant under an exchange of the particle and time indices $n \leftrightarrow t$ if one simultaneously exchanges the model parameters $m \leftrightarrow \omega^2$. In this case we can therefore always define a dual map, which coincidentally also corresponds to a chain of coupled harmonic oscillators.

5.2. Quantum Duality

Such a duality between two classical types of motion implies a one-to-one correspondence between the periodic orbits of both systems. As we saw in section 2.3 the periodic orbits form the backbone of the associated quantum system. Accordingly, we should find a semi-classical correspondence between the traces of time T, $\operatorname{Tr}\hat{U}^T$, for one of the systems with those of time N for the other, $\operatorname{Tr}\tilde{W}^N$. This line of reasoning motivated the original work in [67] on a model system which has exactly these dual properties. While the duality on the classical side depends on the existence of $\tilde{\Phi}$ the picture on the quantum side is more robust. As we show below, a dual operator can be defined independent of whether or not a classical dual dynamic exists or whether the system reaches a semi-classical limit. In the former case the dual operator $\tilde{W}$ will turn out to be non-unitary and a dynamical interpretation is more challenging.

Formally, the quantum system to (5.2) is found replacing $H_i \to \hat{H}_i$. Due to the presence of regularly spaced kicks it is most meaningful to discuss the system evolution in terms of Floquet operators,

$$\hat{U} = \hat{U}_I\hat{U}_K \quad \text{with} \quad \hat{U}_i = \exp\left(-\frac{\mathrm{i}}{\hbar}\hat{H}_i\right), \tag{5.9}$$

where $\hat{U}_I$, $\hat{U}_K$ correspond to the interaction and kick part of the dynamics, respectively. As a side remark, replacing $\hat{H}_K$ with $\hat{H}_I$ as kick and vice versa leads to the same evolution $\hat{U}$ up to an exchange of the K and I order. For our discussion of the duality we consider a product Hilbert space of finite dimension $(2j+1)^N$. Keeping in mind the further application to spin chains we denote the basis by

$$|\vec{\sigma}\rangle = |\sigma_1\rangle \otimes |\sigma_2\rangle \otimes \cdots \otimes |\sigma_N\rangle\,, \tag{5.10}$$

where $|\sigma_n\rangle \in \{|-j\rangle, |-j+1\rangle, \dots |j\rangle\}$ are the discrete single particle states and $2j$ is a positive integer. As in the classical case the interaction part $\hat{U}_I$ couples only nearest-neighbors and is translation invariant with respect to the particle number. In addition, we assume that it is diagonal in the basis (5.10). Its matrix elements are thus given by

$$\langle\vec{\sigma}|\hat{U}_I|\vec{\sigma}'\rangle = \exp\left(\sum_{n=1}^{N} f_I(\sigma_n, \sigma_{n+1})\right)\delta_{\vec{\sigma},\vec{\sigma}'}\,, \tag{5.11}$$

where we introduced the function f_I which represents the interaction between neighboring particles as specified in $\hat{H}_I$. To maintain the unitarity of $\hat{U}_I$, f_I should be purely imaginary but is otherwise unconstrained. The kicking part $\hat{U}_K$ acts on each particle individually, compare (5.4), and is therefore a direct product

$$\hat{U}_K = \bigotimes_{n=1}^{N} \hat{u}_K \qquad \text{with} \quad \langle\sigma|\hat{u}_K|\sigma'\rangle = \mathrm{e}^{f_K(\sigma,\sigma')}\,. \tag{5.12}$$

Again, f_K may be arbitrary as long as $\hat{u}_K$ is a unitary matrix. It is, however, crucial that both f_I and f_K are defined on the same support, $\{\sigma_i\} \times \{\sigma_i\} \to \mathbb{C}$. At this point we can introduce the dual matrix $\tilde{W} = \tilde{W}_I\tilde{W}_K$ via

$$\langle\vec{\sigma}|\tilde{W}_I|\vec{\sigma}'\rangle = \exp\left(\sum_{t=1}^{T} f_K(\sigma_t, \sigma_{t+1})\right)\delta_{\vec{\sigma},\vec{\sigma}'}\,, \tag{5.13}$$

$$\tilde{W}_K = \bigotimes_{t=1}^{T} \hat{w}_K \quad \text{with} \quad \langle\sigma|\hat{w}_K|\sigma'\rangle = \mathrm{e}^{f_I(\sigma,\sigma')}\,, \tag{5.14}$$

where we exchanged the position of f_I and f_K and consider a chain of T spins. In contrast to the work of [67], this new operator is generically non-unitary; this also holds for $\tilde{W}_I$ and $\tilde{W}_K$ separately.

Between both operators $\hat{U}$ and $\tilde{W}$ we find a remarkable duality

$$\operatorname{Tr}\hat{U}^T = \operatorname{Tr}\tilde{W}^N\,, \tag{5.15}$$

which relates the traces of $\hat{U}$ of the N-particle system at time T to those of the dual operator $\tilde{W}$ for a T-particle system and "times" N. While the dimension of $\hat{U}$ is given by $(2j+1)^N \times (2j+1)^N$, which grows exponentially with N, the dimension of $\tilde{W}$, $(2j+1)^T \times (2j+1)^T$, remains fixed for arbitrary N. Specifically, as long as the considered times T are short its dimension will be small, which gives us access to the regime of many particles. To recover (5.15) we rewrite the trace on the left hand side as 2D partition function by inserting identities for the different times t,

$$\operatorname{Tr}\hat{U}^T = \sum_{\{\vec{\sigma}(t)\}} \langle\vec{\sigma}(1)|\hat{U}|\vec{\sigma}(T)\rangle\, \langle\vec{\sigma}(T)|\hat{U}|\vec{\sigma}(T-1)\rangle\, \langle\vec{\sigma}(T-1)|\dots|\vec{\sigma}(1)\rangle\,, \tag{5.16}$$

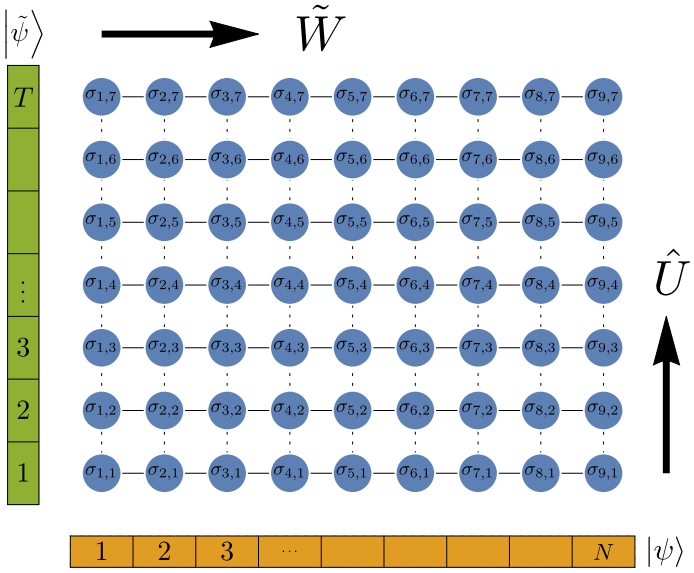

Fig. 5.1.: A trace of the evolution operator $\hat{U}$, which evolves the usual N-particle states $|\psi\rangle$ in time, in the power T can be represented as a classical partition function of a periodic two dimensional $N \times T$ model. Instead of a sum over all quantum states the summation then contains all possible configurations of the local sites. In the same fashion this sum can be contracted again onto a new operator $\tilde{W}$ which effectively "propagates" states for T particles along the chain.

and expressing this further as a sum over all possible combinations of $\sigma_{n,t} \in \{-j, \ldots, j\}$ per time-step and spin index,

$$\operatorname{Tr} \hat{U}^T = \sum_{\sigma_{n,t} \in \{-j,\ldots,j\}} \exp\left(\sum_{n=1}^{N} \sum_{t=1}^{T} f_I(\sigma_{n,t}, \sigma_{n+1,t}) + f_K(\sigma_{n,t}, \sigma_{n,t+1}) \right). \tag{5.17}$$

Since the result is symmetric under the exchange $n \leftrightarrow t$, $N \leftrightarrow T$, $f_I \leftrightarrow f_K$, an analogous procedure leads to the same expression for $\operatorname{Tr} \tilde{W}^N$. One might see (5.17) as the classical partition function of the model and the operators $\hat{U}$ and $\tilde{W}$ as transport operators along the "temporary" and "spatial" directions which express this partition in two different ways, as shown in figure 5.1. Although a dynamical interpretation of the dual operator remains challenging, we provide some semi-classical insight on its behavior in section 7.6.2. But most of the upcoming discussion will focus on properties of its (non-unitary) spectrum.

6. Quantum Kicked Ising Chain

Spin chains, with their binary on-site state-space, are among the "most quantum" quantum systems. Despite their seeming simplicity they proof a fruitful field for research, see for instance [48, 103–105] for theoretical works or [45, 106–108] for experimental realizations. For our studies based on the trace duality (5.15) we require nearest neighbor interaction, recall chapter 5. That such a short ranged interaction has consequences for the quantum dynamics can be seen in their successful description by approximate methods such as matrix product states [109–112]. Near *e.g.* the ground state entanglement is only present between nearby sites leading to an effectively reduced Hilbert space dimension. Similar to other approximate methods, such as mean field approaches [113], they are not suitable for highly excited states in the bulk of the spectrum. The dual approach, on the other hand, provides us via the traces with information on the spectrum as a whole.

As a concrete model we look at the kicked Ising chain (KIC) for spin-$1/2$ particles first introduced in [114]. Its spectrum was found to follow RMT statistics in certain parameter regions. As this system does not afford a meaningful classical interpretation this property can not be explained on semi-classical grounds. Instead, one is restricted to quantum observations: for instance the spin-spin correlations decay exponentially [115], which can be seen as a typical sign of chaotic dynamics. While this might give a further motivation to why RMT occurs, it can not explain why universality is violated on short times. The usual explanation of short periodic orbits does not apply in this case [116]. Using instead the dual approach to consistently capture deviations on these time-scales is the central point of this chapter.

The outline is as follows: in the next section we present the KIC model and give an explicit form to the dual operator. Due to its non-unitary nature a study of its spectrum for different parameter regimes completes the exposition. The two remaining sections are devoted to the actual applications of $\tilde{W}$. First, in section 6.2, to the coarse grained structure of the spectral density and subsequently, in section 6.3, to the spectral form factor. At the end of the chapter we offer a brief summary and outlook on topics which strictly relate to the system at hand. A small remark regarding the notation: in consistence with [2] we mark, throughout this chapter, both operators $\hat{U}$ and $\tilde{W}$ by their respective "particle" numbers N or T to emphasize the dimensional difference.

6.1. On the Model

Throughout this section we introduce the kicked Ising chain (KIC) model. We follow along the path set out in chapter 5 and present the concrete operators in the next subsection. Due to the simple form of a spin-1/2 chain we can give a very explicit form of the resulting dual operator, presented in section 6.1.2, which will be of the same form as the original chain. But, as already pointed out before, this operator will (generically) be non-unitary and we analyze its spectrum in 6.1.3.

6.1.1. Definitions

The KIC model [76, 114–117] is defined as a ring of N spins with homogeneous nearest neighbor coupling and an additional magnetic field kicking the system. The Hamiltonian is therefore a sum of two contributions as presented in (5.2). The interaction part,

$$\hat{H}_I = J \sum_{n=1}^{N} \hat{\sigma}_n^z \hat{\sigma}_{n+1}^z \,, \tag{6.1}$$

is given by the standard Ising-Hamiltonian for spins $\hat{\vec{\sigma}}_n = (\hat{\sigma}_n^x, \hat{\sigma}_n^y, \hat{\sigma}_n^z)$ where the components $\hat{\sigma}_n^j$ are the Pauli matrices for spin n. The parameter J governs the coupling strength. The second part contains a homogeneous magnetic field $\vec{b} = (b^x, b^y, b^z)$ providing the action

$$\hat{H}_K = \sum_{n=1}^{N} \vec{b} \cdot \hat{\vec{\sigma}}_n \tag{6.2}$$

of the kicks. As long as we demand translation invariance along the chain, we may, without loss of generality, restrict the magnetic field to the (x, z) plane, such that

$$\vec{b} = b(\sin\varphi, 0, \cos\varphi) \,. \tag{6.3}$$

The Floquet operator, compare (5.9), for one period of the time evolution is thus given by the product

$$\hat{U}_N = \hat{U}_I(J)\hat{U}_K(b, \varphi) \,, \tag{6.4}$$

where $\hat{U}_I(J)$ and $\hat{U}_K$ correspond to free evolution and kicks, respectively.

Depending on the strength of the coupling J and the magnetic field $\vec{b}$ the KIC shows different regimes ranging from integrable dynamics to full chaos. Recalling the initial discussion we will base the presence of chaos on whether or not the spacing distribution of the spectrum agrees with the RMT predictions. Due to symmetries it is sufficient to consider the parameters (J, b, φ) in the interval of 0 to $\pi/2$ only. Further on, the model is exactly integrable if either b^x or b^z vanishes, *i.e.* $\varphi = 0, \pi/2$. In the latter case, to which we refer to as non-trivially integrable, it can be mapped to a system of non-interacting fermions using the Jordan-Wigner transformation [118] also given in appendix B.1.

6.1.2. Duality Relation

The entire information on the spectrum of the time evolution operator $U(T) = U^T$, where U is the corresponding Floquet operator, is stored in the traces of its powers,

$$Z(N,T) = \operatorname{Tr} \hat{U}_N^T \,. \tag{6.5}$$

In accordance with (5.17) they can be equivalently represented as a partition function of a classical 2-dimensional Ising model defined on a $T \times N$ cyclic lattice. As basis (5.10) we use the σ^z eigenstates $|\pm 1\rangle$ for each of the spins. Since $|\vec{\sigma}_t\rangle$ are eigenstates of $\hat{U}_I$ we only need to study the matrix elements of $\hat{U}_K$ in more detail to obtain an explicit expression for Z and the dual operator.

The kick operator factorizes into kick operations $\hat{u}_K^{(n)}$ for the single spins n for which we can use the relation

$$\hat{u}_K^{(n)} = \mathrm{e}^{-\mathrm{i}\,\vec{b}\cdot\vec{\hat{\sigma}}_i} = \cos b - \mathrm{i}\,(\sin\varphi\,\hat{\sigma}_i^x + \cos\varphi\,\hat{\sigma}_i^z)\sin b \,. \tag{6.6}$$

This implies the following form for the different matrix elements,

$$\begin{aligned}
\left\langle +1|\hat{u}_K^{(n)}|+1\right\rangle &= \cos b - \mathrm{i}\cos\varphi\sin b = \mathrm{e}^{-\mathrm{i}K}\mathrm{e}^{\eta}\mathrm{e}^{-ih}\,,\\
\left\langle -1|\hat{u}_K^{(n)}|-1\right\rangle &= \cos b + \mathrm{i}\cos\varphi\sin b = \mathrm{e}^{-\mathrm{i}K}\mathrm{e}^{\eta}\mathrm{e}^{ih}\,,\\
\left\langle +1|\hat{u}_K^{(n)}|-1\right\rangle &= \left\langle -1|\hat{u}_K^{(n)}|+1\right\rangle = -\mathrm{i}\sin\varphi\sin b = \mathrm{e}^{\mathrm{i}K}\mathrm{e}^{\eta}\,,
\end{aligned} \tag{6.7}$$

of the operator $\hat{U}_K$ in the $|\pm 1\rangle$ basis. The complex quantities K and η as well as h are given in terms of b and φ as

$$\mathrm{e}^{-4iK} = 1 - \frac{1}{x^2}\,, \quad e^{4\eta} = x^2(x^2-1)\,, \quad e^{-2ih} = \frac{\cos b - i\sin b\cos\varphi}{\cos b + i\sin b\cos\varphi} \tag{6.8}$$

with $x = \sin b\,\sin\varphi$. The ansatz on the right side of (6.7) allows one to rewrite the matrix elements of $\hat{U}_K$ in the form

$$\langle\vec{\sigma}_t|\hat{U}_K|\vec{\sigma}_{t+1}\rangle = \exp\left[-\mathrm{i}\sum_{n=1}^{N}\left(\frac{h}{2}(\sigma_{n,t}+\sigma_{n,t+1}) + K\sigma_{n,t}\sigma_{n,t+1} + \mathrm{i}\eta\right)\right] . \tag{6.9}$$

Including $\hat{U}_I$ we may therefore cast the partition function into the form

$$Z(N,T) = \sum_{\{\sigma_{n,t}=\pm 1\}} \exp\left(-\mathrm{i}\sum_{n=1}^{N}\sum_{t=1}^{T}\left(J\sigma_{n,t}\sigma_{n+1,t} + K\sigma_{n,t}\sigma_{n,t+1} + h\sigma_{n,t} + i\eta\right)\right) . \tag{6.10}$$

Apart from the constant factor $\mathrm{e}^{NT\eta}$ the equation above is identical to the partition function of a 2-dimensional classical Ising model with complex coupling constants J, K

and h. Within this classical model, h plays the role of a magnetic field and the model is exactly solvable if h vanishes. This indicates that also the KIC model should be exactly solvable for parameters with $h = 0$. They correspond, *cf.* (6.8), to $\varphi = \pi/2$, which brings the KIC into the non-trivially integrable regime solvable by a Jordan Wigner transformation, see B.1.

Equation (6.5) shows that the $2^N \times 2^N$ matrix $\hat{U}_N$ can be viewed as the transfer operator of the corresponding Ising model. The explicit representation (6.10) nicely illustrates the symmetry under exchange of time and particle indices $n \leftrightarrow t$, $N \leftrightarrow T$, if J and K are also exchanged, which is identical to the symmetry of (5.17). In the special case of the non-trivially integrable regime, where $h=0$ another transformation by Wannier and Kramers [119, 120] relates a partition function with large parameters J, K to an equivalent one with small parameters, usually interpreted as an equivalence between high and low temperatures or ordered and disordered phase, respectively. Using the former exchange symmetry, valid for arbitrary h, it is natural to consider the dual transfer operator $\tilde{W}_T$ with a dimension of $2^T \times 2^T$. This operator can again be split into Ising and kick parts,

$$\tilde{W}_T = g^T \hat{U}_I(K) \hat{U}_K(\tilde{b}, \tilde{\varphi}) \,, \tag{6.11}$$

where the dual parameters are determined by

$$\mathrm{e}^{-4\mathrm{i}J} = 1 - \frac{1}{\tilde{x}^2}, \quad \tilde{x} = \sin\tilde{b} \sin\tilde{\varphi}, \quad g^4 = \frac{x^2(x^2-1)}{\tilde{x}^2(\tilde{x}^2-1)}. \tag{6.12}$$

These equations are obtained by an ansatz of the same form as in (6.7), now for $\tilde{W}_T$ with the replacements $b \to \tilde{b}$, $\varphi \to \tilde{\varphi}$ and the exchange $J \leftrightarrow K$. However, these new parameters are not real anymore causing $\tilde{W}_T$ to be (generically) non-unitary. In $\hat{U}_K(\tilde{b}, \tilde{\varphi})$ they give rise to a parameter $\tilde{\eta}$ different from η. We take this into account by introducing

$$g = \mathrm{e}^{\eta - \tilde{\eta}} \,, \tag{6.13}$$

which yields the third of the equations in (6.12). The parameter h in the dual picture remains unchanged as compared to the original $\hat{U}_N$. With (6.7) we find the following relation

$$\tan b \cos\varphi = \tan\tilde{b} \cos\tilde{\varphi} \tag{6.14}$$

between b, φ and $\tilde{b}$, $\tilde{\varphi}$. As a result of this change of viewpoint we obtain the already stated, exact identity between traces of the unitary evolution for N-particles and the non-unitary "evolution" operator for T-particles

$$\mathrm{Tr}\, \hat{U}_N^T = \mathrm{Tr}\, \tilde{W}_T^N \,. \tag{6.15}$$

The matrix $\hat{U}_N$ has dimension $2^N \times 2^N$. Even for this small base this imposes a severe limitations concerning the study of large particle numbers $N > 20$. In contrast, the dimension of $\tilde{W}_T$ is independent of N, but given by $2^T \times 2^T$.

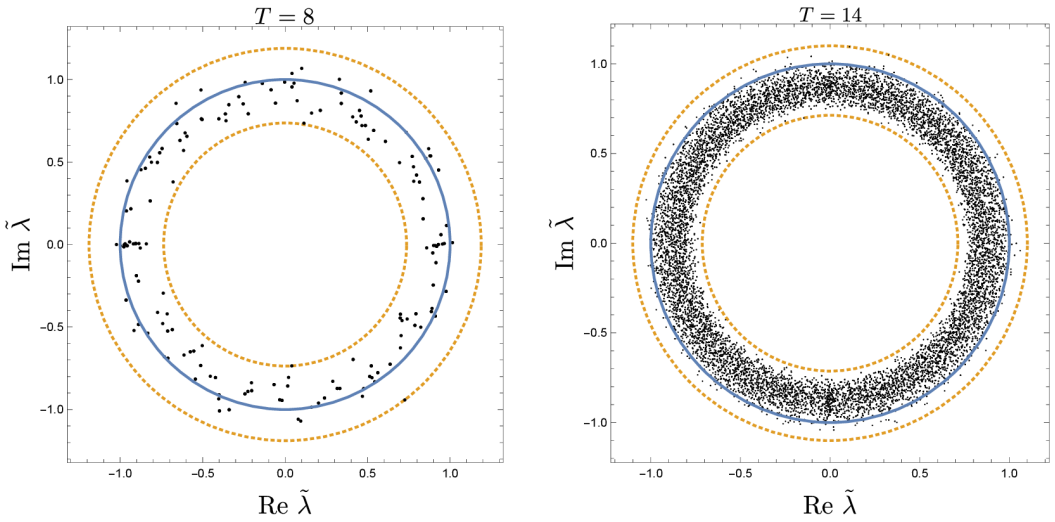

Fig. 6.1.: Complex spectrum $\{\tilde{\lambda}_i\}$ of the dual operator for $T = 8$ (left) and $T = 14$ (right). The parameters are identical in both cases and within the chaotic region: $J = 0.7$, $b = 0.9\sqrt{2}$, $\varphi = \pi/4$. The blue (full) line is the unit circle, the red (dashed) lines indicate the edges of the spectrum.

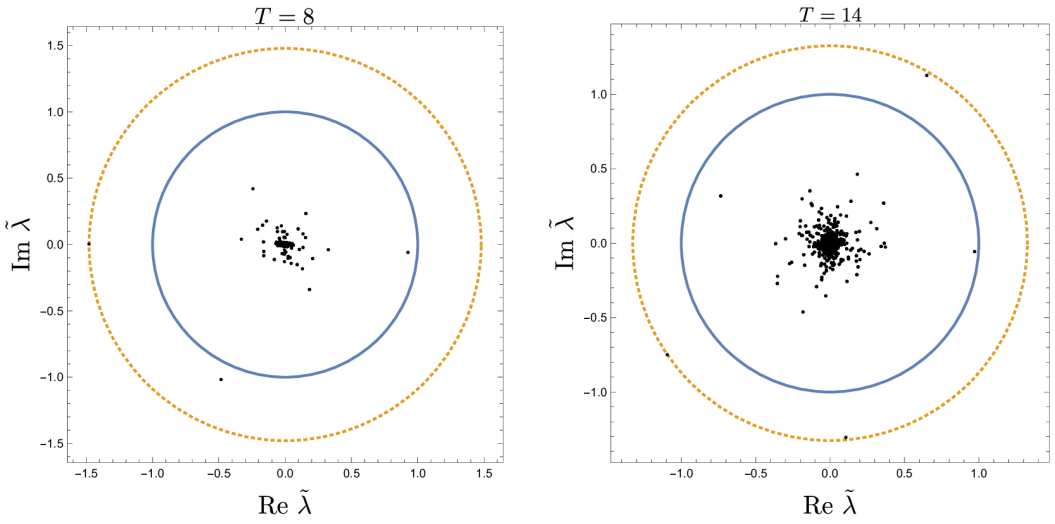

Fig. 6.2.: Spectrum of the dual operator for $T = 8$ (left) and $T = 14$ (right). The parameters are identical in both cases and close to the trivially integrable region: $J = 0.7$, $b = 0.9\sqrt{2}$, $\varphi = \pi/15$.

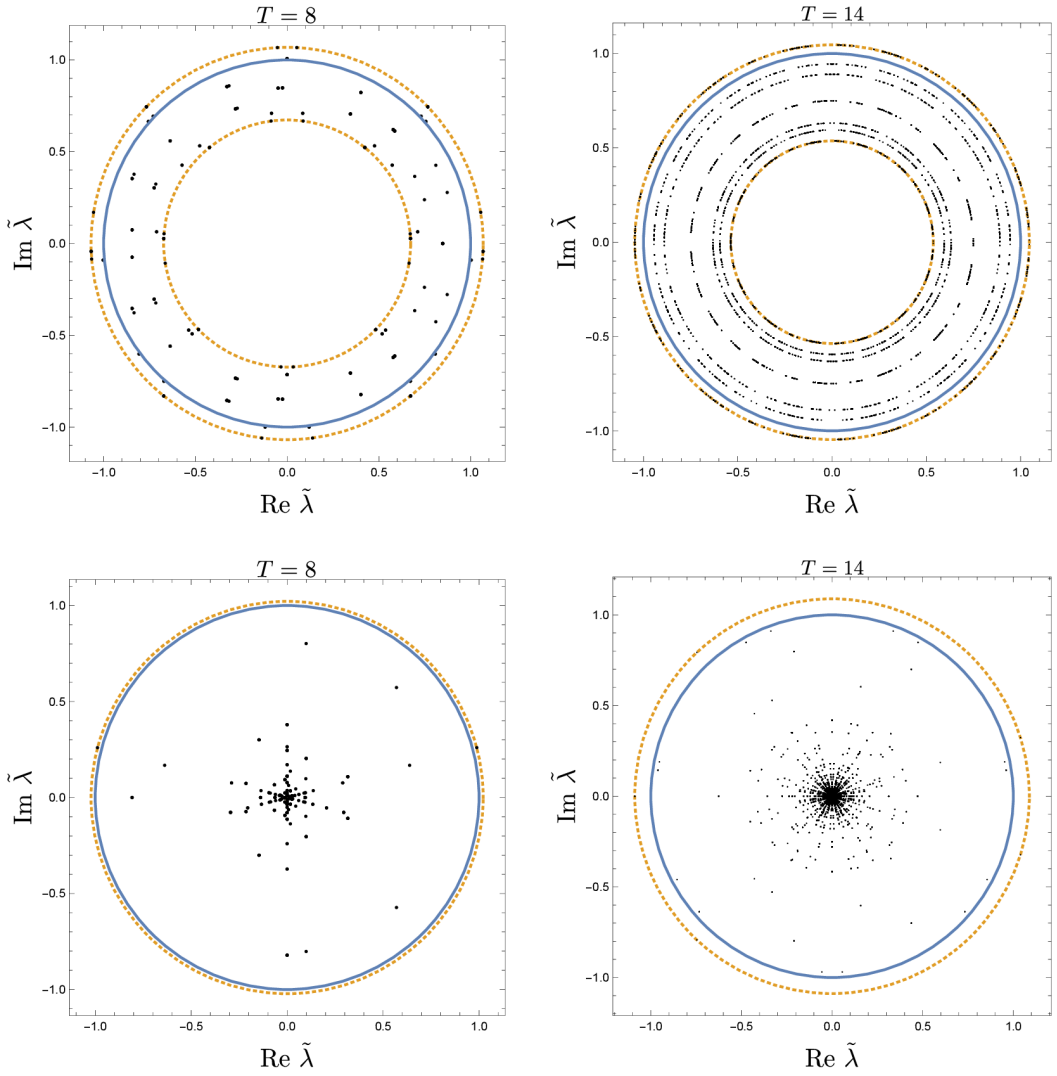

Fig. 6.3.: At the non-trivially integrable point ($\varphi = \pi/2$) the behavior of the dual spectrum strongly depends on the choice of parameters. The upper row shows $J = 0.7$ and $b = 0.9$ (corresponding to $n = 3$ (left) and $n = 6$ (right)), while in the lower one b is changed to $b = 0.9\sqrt{2}$ ($n = 1$ resp. 2).

6.1.3. Spectrum of the Dual Operator

By the duality relation (6.15) the entire information on the spectrum of $\hat{U}_N$ can, in principle, be extracted from the spectra of the dual operators $\tilde{W}_T$ for $T = 1, 2, \ldots$. Thus, it is of great interest to understand how the spectrum of $\tilde{W}_T$ depends on the system parameters and time T.

We start by providing numerically calculated eigenvalue distributions of $\tilde{W}_T$ that are typical for the different parameter regimes of J and $\vec{b}$. Afterwards, we explain in detail how the spectrum of the dual operator is obtained from (6.11)-(6.14) for the non-trivially integrable case where the problem is analytically solvable.

The properties of the dual eigenvalue spectrum $\{\tilde{\lambda}_i\}$ crucially depend on the regime considered. In the chaotic case, see figure 6.1, the bulk of the eigenvalues is placed within the unit disc, such that its boundary serves as the edge of the spectrum. Increasing T this boundary becomes sharper while the gap between the largest eigenvalues and the bulk of the spectrum shrinks to zero. Generically, $\tilde{W}_T$ is non unitary. However, along the line $J = \pi/4$, $\varphi = \arcsin(\sqrt{2}\sin b)^{-1}$ and $b \in [\pi/4, \pi/2]$ we find $J = K$, $b = \tilde{b}$, $\varphi = \tilde{\varphi}$ which implies that both $\hat{U}_N$ and $\tilde{W}_T$ are unitary and differ only by their dimension. This special case is reminiscent of [67], where the dual operator is strictly unitary. Although this line is in the chaotic regime it features two special points for $b = \pi/3$ and $b = \arcsin\sqrt{7/8}$ on which the spectrum is highly degenerate with constant level spacing or Poisson distributed level spacing, respectively.

Close to the trivially integrable regime, as seen in figure 6.2, most of the eigenvalues are localized in the vicinity of zero with a large gap separating the bulk from the largest eigenvalues. In the limit of $b^x \to 0$ the entire spectrum except for two eigenvalues collapses to zero. In the non-trivially integrable regime $b^z \to 0$ the spectrum of $\tilde{W}_T$ has a regular structure, see figure 6.3, with large degeneracies in the absolute values of the eigenvalues. In this case we can distinguish two qualitatively different regimes, the upper row in figure 6.3 is reminiscent of the chaotic region with its minimal inner radius. In the lower one, the inner gap is closed and this reminds visually of the trivially integrable regime. Understanding the distribution of the eigenvalues in more detail is possible, as they are analytically accessible by a map onto an equivalent system of free fermions.

For the sake of simplicity, we only consider spin-chains with an even number N of total spins. But it is straightforward to generalize this to odd N, see B.1 for details. We are interested in the number of eigenvalues with the largest absolute value and their respective degeneracies as they play a central role in the sequel.

If the operator $\hat{U}_N$ belongs to the non-trivially integrable regime this holds as well for the dual operator as can be inferred from (6.14) because $\cos\varphi = 0$ implies $\cos\tilde{\varphi} = 0$. In this case both of the other parameters, K and $\tilde{b}$, turn out to be imaginary up to a constant real part,

$$K = -\frac{\pi}{4} + \frac{\mathrm{i}}{4}\ln\cot^2 b^x\,, \tag{6.16}$$
$$\tilde{b} = \operatorname{arccot}\exp\left(-\mathrm{i}\frac{\pi}{2} - 2\mathrm{i}J\right) = -\frac{\pi}{4} + \frac{\mathrm{i}}{4}\ln\cot^2 J\,.$$

In B.1 we derive an analytic form of the eigenvalues of $\hat{U}_N$ and $\tilde{W}_T$ in this regime. In both operators the eigenvalues are given by structurally similar combinatorial products. In particular, for even T each eigenvalue of $\tilde{W}_T$ can be labeled by a sequence of symbols $\boldsymbol{\varepsilon} = \varepsilon_1 \ldots \varepsilon_T$, $\varepsilon_j \in \{1, \ldots, 4\}$ such that

$$\tilde{\lambda}_{\boldsymbol{\varepsilon}} = \prod_{j=1}^{T/2} \Lambda_{\varepsilon_j}(k_j), \qquad k_j = \pi(2j+1)/T. \tag{6.17}$$

Here, each factor $\Lambda_{\varepsilon_j}(k_j)$ is drawn out of a set of four elements,

$$\Lambda(k) = \{\mu_-(k),\, 1,\, 1,\, \mu_+(k)\}\,, \tag{6.18}$$

where $\mu_+(k)\mu_-(k) = 1$, $\mu_\pm(k) = \alpha(k) \pm \sqrt{\beta(k)}$, with real valued functions α, β provided in B.1. The index ε_j denotes which of the elements contributes to (6.17).

Whereas for $\hat{U}_N$ the absolute values of $\mu_\pm(k)$ are always one, making its spectrum unitary, we find that for $\tilde{W}_T$ this is not necessarily the case. Instead, it depends on the sign of $\beta(k)$. Specifically, $|\mu_\pm(k)| = 1$ only if $\beta(k)$ is negative, in which case $\mu_\pm(k)$ is complex, in the other case $\mu_\pm(k)$ is real. It is therefore apparent that different $\boldsymbol{\varepsilon}$ combinations which have identical values ε_j for all real $\mu_\pm(k)$ lead to eigenvalues with identical absolute value. However, they must not necessarily be degenerate as they can differ in phase due to the complex $\mu_\pm(k)$. Under the variation of the system parameters it might happen that one of the $\beta(k)$'s changes its sign. At these parameters a pair of circles merges which also leads to a change in the degeneracies of the absolute values of $\tilde{\lambda}_{\boldsymbol{\varepsilon}}$.

We are particularly interested in the outer circle of the spectrum, *i.e.* the eigenvalues of $\tilde{W}_T$ with the largest magnitude, as they provide the dominant contribution to traces of the evolution operator (see (6.15)) in the large N limit. The degeneracy of the eigenvalues is characterized by a non-negative integer parameter $n \leq T/2$ counting the number of sets $\Lambda(k)$ with a negative $\beta(k)$. Figure 6.4 shows its value in dependence of J and b. For the eigenvalues with the largest modulus all $\mu_\pm(k)$ for which $\beta(k) > 0$ have to contribute in (6.17) leaving only n sets from which the entries can be chosen freely. As the entry 1 appears twice in the set (6.18) both choices do not affect the value of $\tilde{\lambda}_{\boldsymbol{\varepsilon}}$ and thus lead to a degeneracy.

In general, the spectrum at each circle can be split into ℓ multiplets, where the i-th multiplet $i = 1, \ldots \ell$ is composed of m_i distinct eigenvalues having the same degeneracy d_i. By simple combinatorial arguments we show in B.1 that for the outer spectral circle

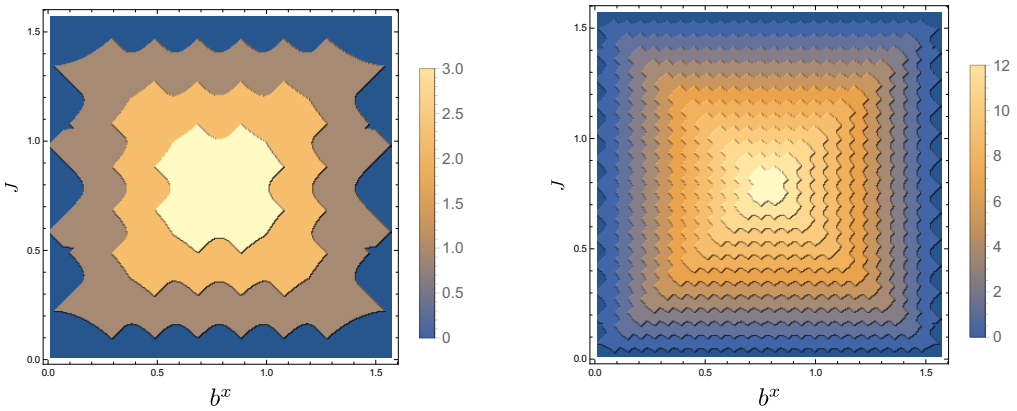

Fig. 6.4.: Value of n (defined for $b^z = 0$) for different parameters of J and b^x with either $T = 8$ (left) or 26 spins (right). The number of layers grows with T but retains the pyramidal form. One can notice a slight deviation from the mirror symmetry in the indention pattern for $n = 0$, 1, depending on whether one is close to the J or the b^x axes. Along the diagonal $J = b^x$ it can occur that both parities $\mathcal{P}$ contribute to the largest eigenvalues, which is not resolved in the figure.

these numbers are given by

$$d_i = 2^{2i}, \qquad m_i = 2^{n-2i}\binom{n}{2i}, \quad \ell = \lfloor n/2 \rfloor = \text{floor}\,(n/2)\,. \tag{6.19}$$

Using (6.19) we can express the total number of eigenvalues as

$$\sum_{i=0}^{\lfloor n/2 \rfloor} d_i m_i = 2^{2n-1} \tag{6.20}$$

and the number of distinct eigenvalues by

$$\sum_{i=0}^{\lfloor n/2 \rfloor} m_i = (1 + 3^n)/2\,. \tag{6.21}$$

As figure 6.4 suggests we find abrupt transitions of these numbers in the parameter space which occur whenever the outer circle is replaced by one of the inner circles taking on its role.

6.2. Density of States

As a first quantity we look at the density of states. We present an approximation based on the largest dual eigenvalues and find sharp transitions between the asymptotic densities

for $N \gg 1$ when varying the system parameters, see section 6.2.1. Subsequently, we look at the limit of small parameters, section 6.2.2, which comes close to the continuous limit. in this case the largest eigenvalue has an analytic approximation.

6.2.1. Spectral Density for the KIC

The spectrum of the quantum evolution operator $\hat{U}_N$ comprises 2^N unitary eigenvalues $\mathrm{e}^{\mathrm{i}\vartheta_n}$ with quasi-energies ϑ_n. The corresponding spectral density can be written as a Fourier series of traces of the evolution operator,

$$\rho(\vartheta) = \frac{1}{2^N} \sum_{n=1}^{2^N} \delta(\vartheta - \vartheta_n) = \frac{1}{2\pi} + \frac{1}{2^N \pi} \operatorname{Re} \sum_{T=1}^{\infty} \mathrm{e}^{-\mathrm{i}T\vartheta} \operatorname{Tr} \hat{U}_N^T \,. \tag{6.22}$$

We are interested in the non-constant term on the right hand side of (6.22) representing the oscillating part $\rho_{\mathrm{osc}}(\vartheta)$ of the density. For large N the traces can be approximated by powers of the eigenvalues with the largest magnitude of the dual operator,

$$\operatorname{Tr} \hat{U}_N^T = \operatorname{Tr} \tilde{W}_T^N \underset{N\gg 1}{\approx} \sum_{m=1}^{m_{\mathrm{cut}}} \tilde{\lambda}_{\mathrm{max},m}^N(T) \,, \tag{6.23}$$

where $\tilde{\lambda}_{\mathrm{max},m}$ are the eigenvalues of $\tilde{W}_T$ ordered such that they decrease in magnitude. The cut-off parameter m_{cut} depends on N and has to be chosen such that the error resulting from the neglected eigenvalues is small. Ordering the $|\tilde{\lambda}_{\mathrm{max}}(T)|$ for all time steps according to their absolute value,

$$|\tilde{\lambda}_{\mathrm{max}}(T_1)| \geq |\tilde{\lambda}_{\mathrm{max}}(T_2)| \geq |\tilde{\lambda}_{\mathrm{max}}(T_3)| \geq \dots \,, \tag{6.24}$$

introduces a hierarchy of the corresponding points in time, $T_1, T_2 \dots$. However, these points need not necessarily be different, for instance due to degeneracies. Clearly, in the large N limit $\tilde{\lambda}_{\mathrm{max}}^N(T_1)$ dominates the rest of the eigenvalues and T_1 determines the asymptotic period of the $\rho_{\mathrm{osc}}(\vartheta)$ oscillations. Since the value of T_1 depends on the parameters of the KIC, the asymptotic form of $\rho_{\mathrm{osc}}(\vartheta)$ undergoes abrupt transitions under the change of $\vec{b}$ and J. To illustrate this we color code the largest components for some parameter regime in figure 6.5. Previously, similar transitions in the oscillatory behavior of $\rho(\vartheta)$ were observed in the two-dimensional KIC [121].

For a finite N several values $\tilde{\lambda}_{\mathrm{max}}(T_k)$, $k \leq k_{\mathrm{cut}}$ can be used to approximate $\rho_{\mathrm{osc}}(\vartheta)$. Restricting the sum in (6.22) to these few terms yields

$$\rho_{\mathrm{osc}}(\vartheta) \approx \frac{1}{\pi 2^N} \operatorname{Re} \sum_{k=1}^{k_{\mathrm{cut}}} \mathrm{e}^{-\mathrm{i}T_k\vartheta} \, \tilde{\lambda}_{\mathrm{max}}^N(T_k) \,, \tag{6.25}$$

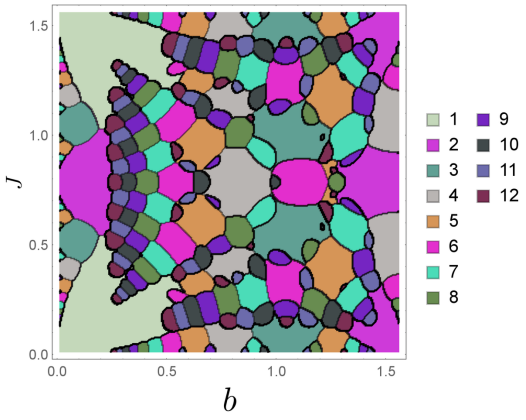

Fig. 6.5.: Depicted is the time T_1 for which the set of dual operators $\tilde{W}_T$ for fixed parameters but $1 \leq T \leq 12$ contains the eigenvalue with the largest magnitude compared to the other times. The third system parameter $\varphi = \pi/8$ is chosen such that the picture covers a large region with non-integrable system behavior.

which is usually a good approximation to $\rho_{\text{osc}}(\vartheta)$ already for a relatively small cut-off parameter k_{cut}. Particularly, in the near integrable regime, a good approximation is obtained by just a few leading modes, see figure 6.6. This is reflected in a very pronounced oscillating structure of $\rho_{\text{osc}}(\vartheta)$. In the chaotic regime there are no large gaps in the spectrum of the eigenvalues $\tilde{\lambda}_{\text{max}}(T)$. This leads to a much more uniform density of eigenvalues, with a larger cut off parameter k_{cut} necessary to resolve the fine structure of $\rho_{\text{osc}}(\vartheta)$, compare figure 6.7.

6.2.2. Small Parameters Limit

As an intermediate step between the discrete case and continuous dynamics we look at the limit of small parameters J and $\vec{b}$. For $J = 0, \vec{b} = 0$ the (rescaled) dual operator $\tilde{W}/2$ is a rank one projection operator. This suggests that for small parameters its eigenvalues can be evaluated by perturbation theory. To this end we introduce a small parameter η which rescales the parameters of our KIC model, *i.e.* $J = \eta J_0, \vec{b} = \eta \vec{b}_0$. To second order in η the largest eigenvalue of $\tilde{W}$ is given by $\tilde{\lambda}_1(\eta) = 2 + \eta\tilde{\lambda}_1'(0) + \tilde{\lambda}_1''(0)\eta^2/2$, while the rest of the eigenvalues $\tilde{\lambda}_i$ $(i > 1)$ are of order $O(\eta)$. Exploiting that these $\tilde{\lambda}_i(0) = 0$ for $i > 1$ the respective derivatives can be expressed through the traces,

$$\partial_\eta \operatorname{Tr} \tilde{W}_T^2 \Big|_{\eta=0} = 2\tilde{\lambda}_1(\eta)\tilde{\lambda}_1'(\eta) \Big|_{\eta=0}, \tag{6.26}$$

$$\partial_\eta^2 \operatorname{Tr} \tilde{W}_T^3 \Big|_{\eta=0} = \left(3\tilde{\lambda}_1''(\eta)\tilde{\lambda}_1^2(\eta) + 6\tilde{\lambda}_1'^2(\eta)\tilde{\lambda}_1(\eta)\right) \Big|_{\eta=0}. \tag{6.27}$$

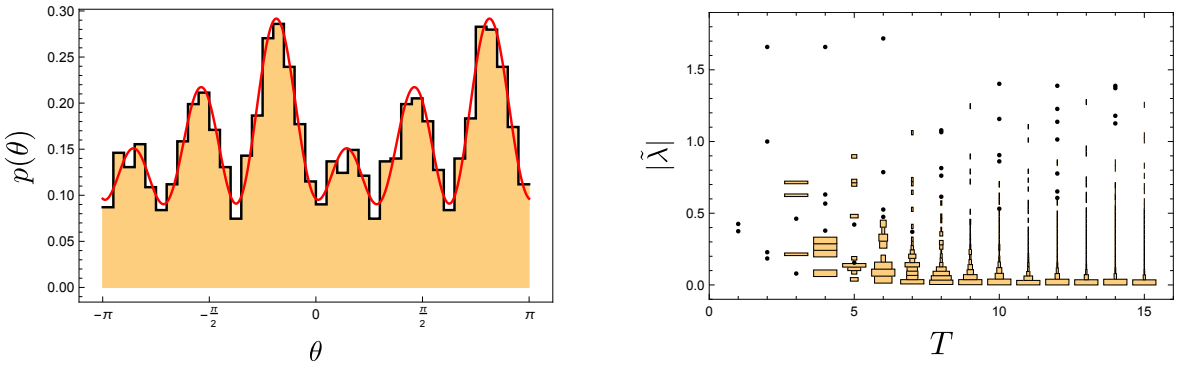

Fig. 6.6.: Histogram of the spectral density (left) for $J = 1$, $b_x = 1.4$, $b_z = 0.4$ and $N = 14$, the red line shows an approximation to the density using the 3 largest Fourier components as given by the dual spectrum. The right hand side shows histograms of the dual spectrum (absolute value) over T for the same parameter. Bar thickness corresponds to local eigenvalue density, single points to isolated eigenvalues. Clearly visible are the 3 outliers which contribute to $\rho_{\text{osc}}(\vartheta)$.

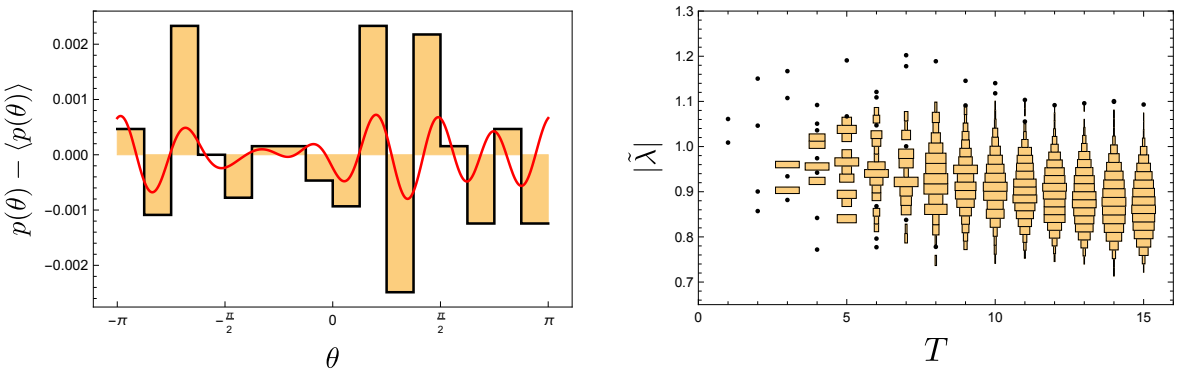

Fig. 6.7.: Histogram of the spectral density (left) for $J = 0.7$, $b = 0.9\sqrt{2}$, $\varphi = \pi/4$ and $N = 14$, the red line shows an approximation to the density using the 4 largest Fourier components as given by the dual spectrum. Due to the small size of the fluctuations only the relative change compared to the flat background is shown. The right hand side shows histograms of the dual spectrum (absolute value) in the same fashion as before in figure 6.6. But, in this chaotic case no clear outliers exist, making the approximation visibly less accurate.

At this point we can inverse the duality relation, leading to

$$\partial_\eta^k \operatorname{Tr} \tilde{W}_T^p \Big|_{\eta=0} = \partial_\eta^k \operatorname{Tr} \left(e^{-\mathrm{i}\eta \hat{H}_I^{(p)}} e^{-\mathrm{i}\eta \hat{H}_K^{(p)}} \right)^T \Big|_{\eta=0}, \tag{6.28}$$

where $\hat{H}_I^{(p)}, \hat{H}_K^{(p)}$ are now p-spin Hamiltonians for the base parameters J_0 and $\vec{b}_0$. Taking the derivatives and substituting $\eta = 0$ this yields

$$\tilde{\lambda}_1'(0) = 0 \quad \text{and} \qquad 12\tilde{\lambda}_1''(0) = -T^2 \operatorname{Tr}(\hat{H}^{(3)})^2, \tag{6.29}$$

where $\hat{H}^{(3)} = \hat{H}_I^{(3)} + \hat{H}_K^{(3)}$ is the sum of the kicked and Ising Hamiltonians for a 3 particle spin chain. For the largest eigenvalue we therefore obtain by (6.27)

$$\tilde{\lambda}_1(\eta) = 2\left(1 - \frac{T^2\eta^2}{48} \operatorname{Tr}(\hat{H}^{(3)})^2\right) + O(\eta^3) = 2\exp\left(-\frac{T^2\eta^2}{48} \operatorname{Tr}(\hat{H}^{(3)})^2\right) + O(\eta^3)\,. \tag{6.30}$$

The trace in the exponent can easily be evaluated for an arbitrary number of spins p, see [122], leading to

$$\frac{2^{-p}}{p} \operatorname{Tr}(\hat{H}^{(p)})^2 = J_0^2 + b_0^2\,. \tag{6.31}$$

Substituting (6.30) into (6.22) we can approximate the density of eigenstates by the sum

$$\rho(\theta) \approx \frac{1}{\pi} \sum_{T=-\infty}^{+\infty} \exp\left(-\mathrm{i}T\theta - \frac{1}{4}T^2\sigma^2\right), \tag{6.32}$$

where $\sigma^2 = 2N(J^2 + b^2)$. Due to the Poisson summation formula we finally obtain

$$\rho(\theta) \approx \frac{1}{\sigma\sqrt{\pi}} \sum_{n=-\infty}^{+\infty} \exp\left(-\frac{(\theta + 2\pi n)^2}{\sigma^2}\right), \tag{6.33}$$

which is a periodized sum of Gaussians with widths given by σ. Figure 6.8 shows that this Gaussian approximation nicely agrees with the observed density. In structure this Gaussian is similar to the results obtained in [122–124] for the time-continuous Ising chain, given an appropriate re-scaling. In those cases the dual approach is applicable as well [2].

6.3. Spectral Form Factor

In section 6.3.1 we recapitulate the predictions for the form factor $K_2(T)$ based on Random Matrix Theory (RMT), as introduced in section 2.2, valid for large times T in the chaotic regime. In 6.3.2 we use the duality relation to obtain analytic expressions for the short time form factor at arbitrary particle numbers. For longer times we give approximations, considering separately the integrable and the chaotic case, in sections 6.3.3 and 6.3.4.

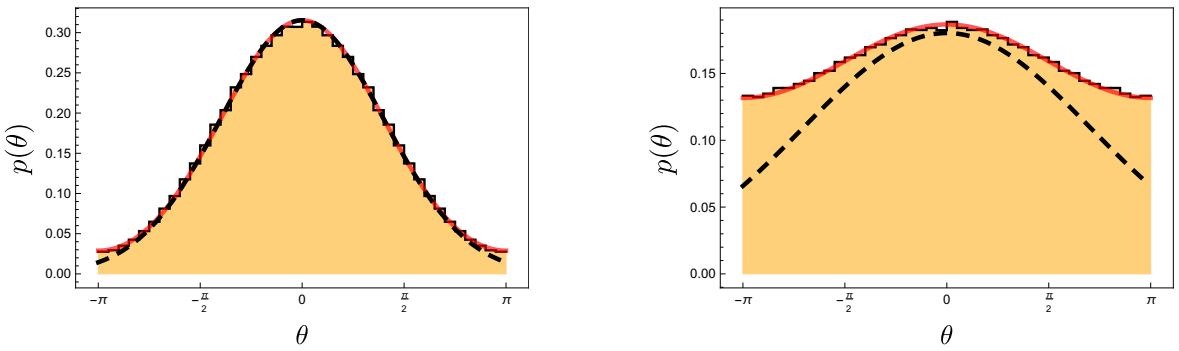

Fig. 6.8.: Histogram of the quasi energies for $J = b = 0.2$ (left) and $J = b = 0.35$ (right), both for $\varphi = \pi/2$ and $N = 20$. The red (continuous) curve is given by the Gaussian approximation (6.33). The dotted black curve shows, for comparison, the contributions from $n=0$ to (6.33), only.

6.3.1. Form Factor via RMT

The spectral form factor is defined as the Fourier transform of the two-point spectral correlation function, see *e.g.* [18, 76]. Using the duality relation it can be represented in the form

$$K_2(T) = \frac{1}{2^N} |\operatorname{Tr} \hat{U}_N^T|^2 = \frac{1}{2^N} |\operatorname{Tr} \tilde{W}_T^N|^2 \,. \tag{6.34}$$

By its very definition $K_2(T)$ carries information about the correlations between eigenphases ϑ_n on the scales of $1/T$. If the system is in the chaotic regime, for large times T comparable with the Heisenberg time of the system $T_H = 2^N$, one expects that $K_2(T)$ has the universal form provided by the relevant RMT ensemble. For the KIC the total spectrum can be split into $(N-2)/2$ (resp. $(N-1)/2$) doubly degenerate and 4 (resp. 2) non-degenerate subspectra if N is even (odd). Each sector has orthogonal symmetry, and as $\hat{U}$ is unitary, this implies spectral statistics comparable to the circular orthogonal matrix ensembles (COE). Indeed, in the KIC such universal spectral correlations can be observed in the chaotic parameter regime, see [76] for details. Furthermore, in the large-T limit all subspectra can be considered as independent. Therefore the expected total form factor in the chaotic regime is

$$K_2(T) = 2K_2^{(\mathrm{COE})}(NT/2^N) \,, \tag{6.35}$$

with the universal COE form factor as given in (2.12). We assumed that N is large, such that the four (respectively two) special sectors can be ignored.

6.3.2. Short Times

In [76] Pineda and Prosen studied the spectral form factor numerically also at short times for up to 20 particles. They found a behavior not consistent with RMT.

In this context we can apply the duality relation (6.15) to analytically compute the spectral form factor for arbitrary numbers of particles in the short time regime. For $T \leq 3$, the spectrum of the dual operator $\tilde{W}_T$ can be calculated analytically and a closed expression for $K_2(T)$ can be provided. In particular, for the one time step form factor we have

$$K_2(1) = \frac{1}{2^N} |\tilde{\lambda}_+^N + \tilde{\lambda}_-^N|^2 \,, \tag{6.36}$$

where $\tilde{\lambda}_\pm$ are the two eigenvalues of

$$\tilde{W}_1 = g \begin{pmatrix} \mathrm{e}^{-\mathrm{i}K}(\cos\tilde{b} + \mathrm{i}\cos\tilde{\varphi}\sin\tilde{b}) & -\mathrm{i}\mathrm{e}^{-\mathrm{i}K}\sin\tilde{b}\sin\tilde{\varphi} \\ -\mathrm{i}\mathrm{e}^{-\mathrm{i}K}\sin\tilde{b}\sin\tilde{\varphi} & \mathrm{e}^{-\mathrm{i}K}(\cos\tilde{b} - \mathrm{i}\cos\tilde{\varphi}\sin\tilde{b}) \end{pmatrix} , \tag{6.37}$$

given by

$$\tilde{\lambda}_\pm = \cos b\, \mathrm{e}^{-\mathrm{i}J} \pm \sqrt{\mathrm{e}^{2\mathrm{i}J} - \sin^2 b \, \left(\mathrm{e}^{2\mathrm{i}J}\sin^2\varphi + \mathrm{e}^{-2\mathrm{i}J}\cos^2\varphi\right)} \,. \tag{6.38}$$

For small N, the function $K_2(1)$ strongly fluctuates in dependence of N, see figure 6.9. However, in the limiting case of $N \gg 1$ only the eigenvalue with the larger absolute magnitude, denoted by $\tilde{\lambda}_{\max}$, will contribute to the form factor. Asymptotically, we therefore find

$$\frac{1}{N}\log K_2(1) \sim \log\left(|\tilde{\lambda}_{\max}|^2/2\right) . \tag{6.39}$$

To compare this result to the RMT universal form factor, where, for $N \to \infty$, $\log K_2(1) \sim -N\log 2$ is expected, we distinguish 3 asymptotically different behaviors: 1) $|\tilde{\lambda}_{\max}| < 1$ where the form factor decays faster than the corresponding COE, 2) $1 < |\tilde{\lambda}_{\max}| < \sqrt{2}$ where the decay is slower and 3) $|\tilde{\lambda}_{\max}| > \sqrt{2}$, where $K_2(1)$ grows with N. Figure 6.10 shows the boundary lines for both integrable regimes $\varphi{=}0$ and $\varphi{=}\pi/2$ as well as the transition from one to the other.

Similarly, for the two step form factor we find

$$K_2(2) = \frac{1}{2^N}|\operatorname{Tr}\hat{U}_N^2|^2 = \frac{1}{2^N}|\operatorname{Tr}\tilde{W}_2^N|^2 = \frac{1}{2^N}|\tilde{\lambda}_0^N + \tilde{\lambda}_1^N + \tilde{\lambda}_2^N + \tilde{\lambda}_3^N|^2 \,, \tag{6.40}$$

where $\tilde{\lambda}_k$ are the four eigenvalues of $\tilde{W}_2$, given by

$$\tilde{W}_2 = g^2\mathrm{e}^{2\eta} \begin{pmatrix} \mathrm{e}^{2\mathrm{i}(h-J-K)} & \mathrm{e}^{\mathrm{i}h-2\mathrm{i}K} & \mathrm{e}^{\mathrm{i}h-2\mathrm{i}K} & \mathrm{e}^{2\mathrm{i}J-2\mathrm{i}K} \\ \mathrm{e}^{\mathrm{i}h+2\mathrm{i}K} & \mathrm{e}^{2(-\mathrm{i}J+\mathrm{i}K)} & \mathrm{e}^{2\mathrm{i}(J+K)} & \mathrm{e}^{-\mathrm{i}h+2\mathrm{i}K} \\ \mathrm{e}^{\mathrm{i}h+2\mathrm{i}K} & \mathrm{e}^{2\mathrm{i}(J+K)} & \mathrm{e}^{2(-\mathrm{i}J+\mathrm{i}K)} & \mathrm{e}^{-\mathrm{i}h+2\mathrm{i}K} \\ \mathrm{e}^{2\mathrm{i}J-2\mathrm{i}K} & \mathrm{e}^{-\mathrm{i}(h+2K)} & \mathrm{e}^{-\mathrm{i}(h+2K)} & \mathrm{e}^{-2\mathrm{i}(h+J+K)} \end{pmatrix} . \tag{6.41}$$

Using the translational symmetry of the system it is easy to see that the fully anti-symmetric state $|{+1}, {-1}\rangle - |{-1}, {+1}\rangle$ is also an eigenstate of $\tilde{W}_2$ with the eigenvalue

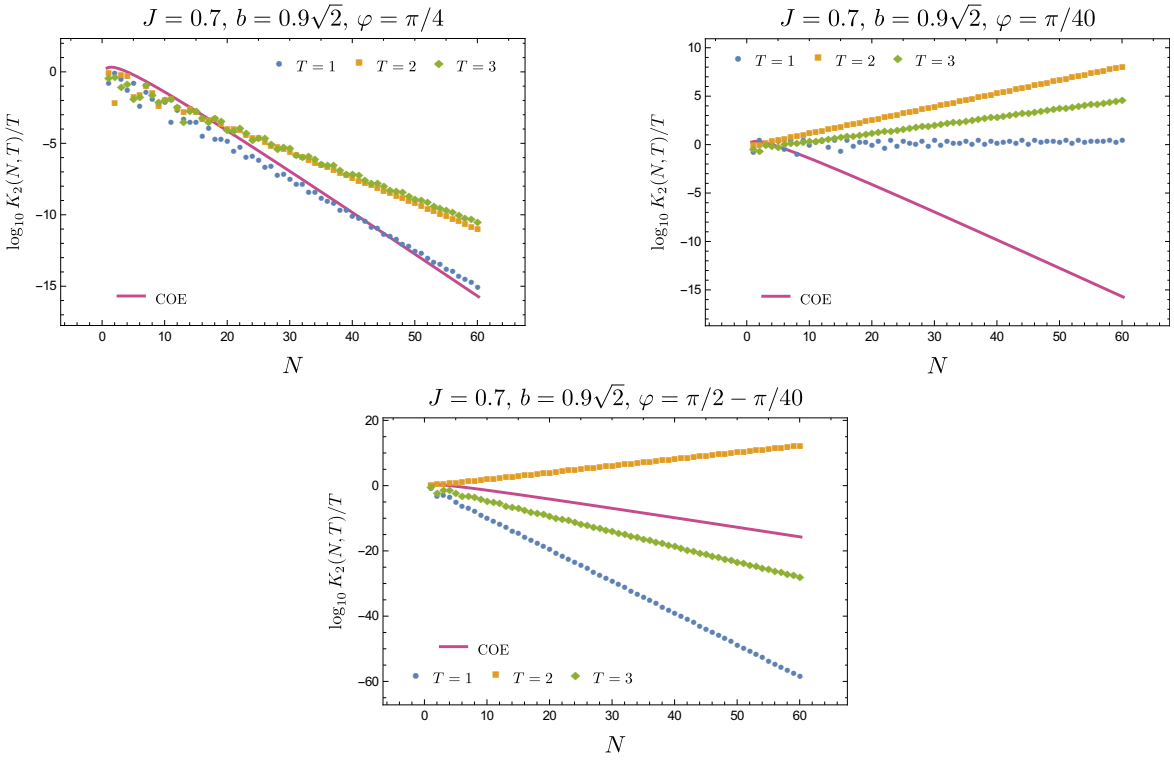

Fig. 6.9.: Logarithm of the form factor $K_2(N,T)$ as a function of N for the total spectrum and short times T. As comparison we plot the COE result $\log_{10}(N2^{2-N})$ (continuous line). The upper left panel shows the chaotic regime, where the form factor follows RMT predictions more closely, for details see text. The other two panels consider parameters close to the integrable points and depict strong deviations.

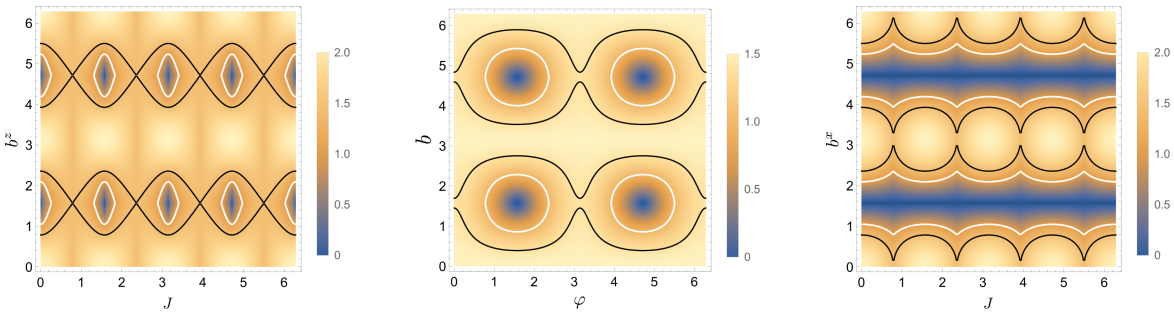

Fig. 6.10.: Absolute value of $\tilde{\lambda}_{\max}$ at $T=1$ for different parameters of J and b in the trivially integrable case ($\varphi=0$) (left) and the non-trivially integrable case ($\varphi=\pi/2$) (right). The contour lines indicate the special cases of $|\tilde{\lambda}_{\max}|=1$ (white) or $\sqrt{2}$ (black) respectively. The middle panel shows the transition from one integrable domain to another and back when varying φ. The coupling is fixed to $J=0.7$.

$\tilde{\lambda}_0 = g^2 e^{2iK} = -2\mathrm{i}\sin^2\varphi\,\sin^2 b \sin 2J$. The rest of the dual spectrum can be found as eigenvalues of the remaining 3×3 matrix,

$$\tilde{W}_2^{(\mathrm{sym})} = g^2 \mathrm{e}^{2\eta} \begin{pmatrix} \mathrm{e}^{-2\mathrm{i}(J+K-h)} & \mathrm{e}^{+2\mathrm{i}(J-K+h)} & \sqrt{2}\mathrm{e}^{-2\mathrm{i}(K-h)} \\ \mathrm{e}^{+2\mathrm{i}(J-K-h)} & \mathrm{e}^{-2\mathrm{i}(J+K+h)} & \sqrt{2}\mathrm{e}^{-2\mathrm{i}(K+h)} \\ \sqrt{2}\mathrm{e}^{+2\mathrm{i}K} & \sqrt{2}\mathrm{e}^{+2\mathrm{i}K} & 2\mathrm{e}^{2\mathrm{i}K}\cos 2J \end{pmatrix} . \tag{6.42}$$

In the case of $K_2(3)$ the dual matrix can be decomposed into one 4×4 block and two 2×2 blocks. Figure 6.9 shows the resulting form factors for all three time steps together with the RMT prediction (6.35). As stated in the beginning of this section, [76] pointed out that the (short-time) form factor in the chaotic case stays systematically and significantly below the expected RMT results. As seen in the figure this behavior changes with increasing N, as only $|\tilde{\lambda}_{\max}|$ determines the asymptotic result.

6.3.3. Long Times — Integrable Regimes

In the integrable regimes the behavior of the spectral form factor is expected to differ from the RMT result, even for long times. For the trivially integrable case $b^x = 0$ the form factor can be easily calculated for an arbitrary time. Because of

$$K_2(T) = \frac{1}{2^N}\left|\mathrm{Tr}\, e^{-\mathrm{i}T\hat{H}_I} e^{-\mathrm{i}T\hat{H}_K}\right|^2 , \tag{6.43}$$

it is given by the same expression (6.38) as the one-step form factor for $\varphi = 0$,

$$K_2(T) = \frac{1}{2^N}|\tilde{\lambda}_+^N + \tilde{\lambda}_-^N|^2 , \tag{6.44}$$

$$\tilde{\lambda}_\pm(T) = \mathrm{e}^{-\mathrm{i}JT}\left(\cos(bT) \pm \sqrt{\mathrm{e}^{\mathrm{i}4JT} - \sin^2(bT)}\right) , \tag{6.45}$$

with rescaled parameters $b \to bT$, $J \to JT$.

Although in the non-trivially integrable regime $K_2(T)$ can be obtained explicitly, the resulting expression is quite cumbersome and its asymptotic analysis at $N \to \infty$ is difficult. It is instructive to use for this purpose the duality approach. In the dual picture the form factor for large particle numbers is strongly dominated by the eigenvalues with the largest absolute magnitude $\tilde{\lambda}_{\max}$. Restricting thus the sum to the outer circle of $\tilde{W}_T$, yields

$$K_2(T) = \frac{1}{2^N}\left\langle \left| \sum_{i=0}^{2^T} |\tilde{\lambda}_i|^N \mathrm{e}^{\mathrm{i}N\tilde{\vartheta}_i} \right|^2 \right\rangle \approx \frac{|\tilde{\lambda}_{\max}|^{2N}}{2^N} \left\langle \left| \sum_{\substack{\text{outer} \\ \text{circle}}} \mathrm{e}^{\mathrm{i}N\tilde{\vartheta}_i} \right|^2 \right\rangle , \tag{6.46}$$

To smoothen the large fluctuations of the form-factor we take an average $\langle\cdots\rangle$ over the parameters J, b^x of the spin chain, such that both n and $\tilde{\lambda}_{\max}$, compare section 6.1.3,

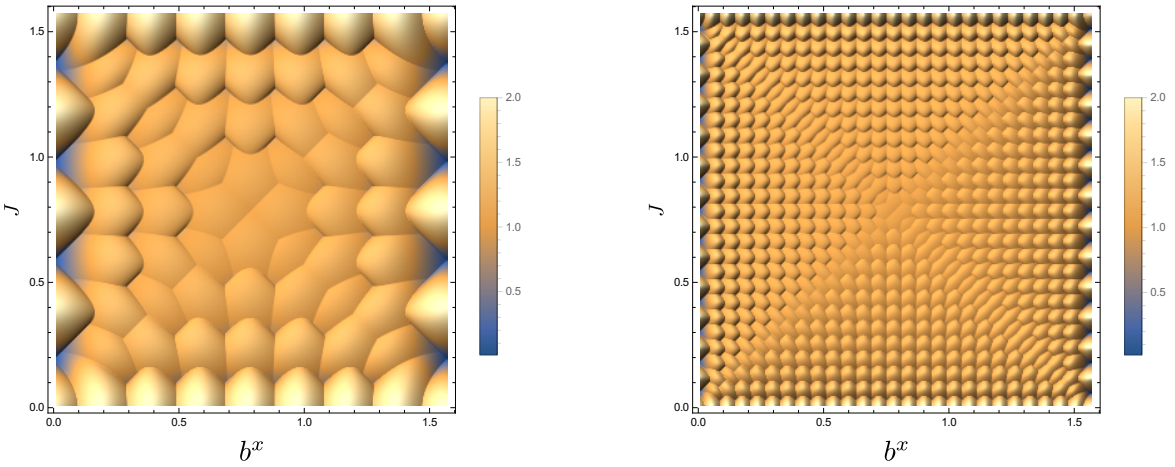

Fig. 6.11.: Absolute value of the largest dual eigenvalue $|\tilde{\lambda}_{\max}|$ over the (J, b^x) plane in the non-trivially integrable regime for $T=8$ (left) and $T=26$ spins (right).

are kept fixed. The dependence of n on the parameters and on T is shown in figure 6.4, while the dependence of $\tilde{\lambda}_{\max}$ is given in figure 6.11.

As follows from (6.46) the behavior of $K_2(T)$ as a function of T is controlled in this large N regime by $\tilde{\lambda}_{\max}(T)$ and $n(T)$. Assuming that N is larger than the number of distinctive eigenvalues at the outer circle we can apply the diagonal approximation to the right-hand side of (6.46). The resulting sum depends only on the degeneracies d_i and multiplicities m_i of the eigenvalues $\tilde{\lambda}_{\max}\mathrm{e}^{\mathrm{i}\tilde{\vartheta}_i}$ and can be evaluated explicitly, resulting in

$$\left\langle \left| \sum_{i=1}^{2^{2n-1}} \mathrm{e}^{\mathrm{i}N\tilde{\vartheta}_i} \right|^2 \right\rangle \approx \sum_{i=0}^{\lfloor n/2 \rfloor} m_i\, d_i^2 = 2^{n-1}\Big(3^n + (-1)^n\Big)\,, \tag{6.47}$$

where the respective summands are given in (6.19). Up to jumps of the order of unity n can be approximated by a "smooth" linear function of T,

$$n(T) = \nu T + \mathcal{O}(1), \quad \nu(J, b^x) = \frac{2}{\pi}\min\{J, b^x, \frac{\pi}{2} - J, \frac{\pi}{2} - b^x\}\,, \tag{6.48}$$

valid for the default parameter range $J, b^x \in [0, \pi/2]$. To verify the validity of this diagonal approximation we perform a numerical average of (6.47) in dependence of N, the result is shown in figure 6.12. To complete the analysis we still need to evaluate $\tilde{\lambda}_{\max}(T)$. Due to the structure of the $\tilde{\lambda}$, compare (6.17), it can be written as

$$\log|\tilde{\lambda}_{\max}| = \sum_{k=1}^{\lfloor T/2 \rfloor} \Theta(\beta(k)) \log\Big(|\alpha(k)| + \sqrt{\beta(k)}\Big) + T\log g\,, \tag{6.49}$$

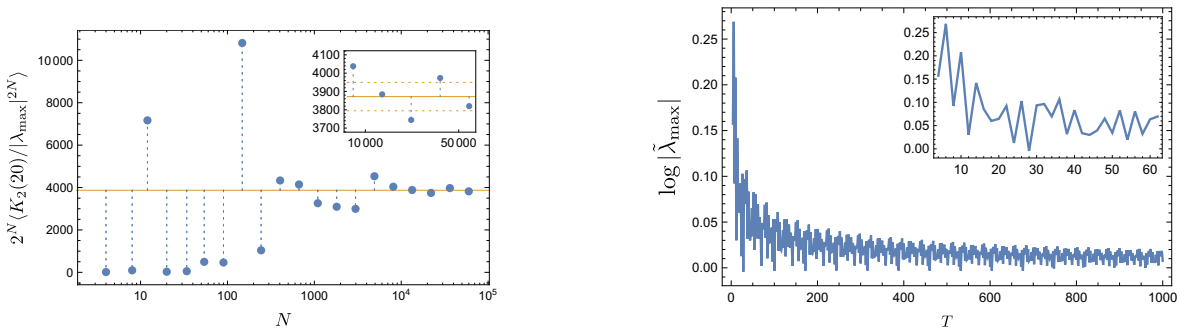

Fig. 6.12.: *To the left:* convergences of the approximation (6.47). The blue dots correspond to the average form factor for $T=20$ and $n=5$. The average is taken over 136 000 points along a closed $|\tilde{\lambda}_{\max}|$ contour. The straight line shows the expected result of (6.47) for the given n. The inset shows the remaining deviations for large N, dashed lines indicate 2% deviation. *To the right:* $|\tilde{\lambda}_{\max}|$ in dependence of T for $J=0.48$, $b^x=1.2$, $N=10^4$. The inset magnifies the initial fluctuations for short times.

where Θ is a Heaviside-Step-Function and the parameters are given by

$$\begin{aligned}\alpha(k) &= -\frac{1}{g^2}\left(\cos 2b^x \cos 2J - \cos 2\vartheta(k)\right) , \\ \beta(k) &= \alpha(k)^2 - 1 ,\end{aligned} \tag{6.50}$$

with

$$g^2 = \sin 2b^x \sin 2J \qquad \text{and} \qquad \vartheta(k) = \frac{2\pi}{T}\left(2k+1\right) . \tag{6.51}$$

From the numerically obtained graph, presented in figure 6.12, it can be deduced that $\log|\tilde{\lambda}_{\max}(T)|$ saturates to a fixed value C_0 dressed by time dependent fluctuations $\xi(T)$. Incorporating this into (6.47) we obtain for the form factor

$$K_2(T) \sim \exp\Big(\left(C_0 + \xi(T)\right) N + T\nu \log 6\Big) . \tag{6.52}$$

This expression suggests that for short times the form factor grows exponentially with T. However, such an exponential growth would be difficult to detect as it is masked by the large fluctuating term $\xi(T)N$.

We recall in passing the phase transition of the classical Ising model for vanishing external field, *cf.* [125]. Due to the relation between the classical partition function and the traces of the quantum evolution operator one might expect to find some signature of this transition also in the 1D chain. Indeed, for $J=b^x$ one finds that the degeneracy of $|\tilde{\lambda}_{\max}|$ increases as two outer circles merge, which is reminiscent of a quantum phase transition.

6.3.4. Long Times — Chaotic Regime

It was observed in [76] that for the KIC with parameters $J, \vec{b}$ in the chaotic regime the spectral statistics of $\hat{U}_N$ obey the universal RMT predictions. For the spectral form factor this implies a linear growth with time,

$$\mathcal{K}(T,N) = 2^N K_2(T) = 4NT\left(1 + O\left(\frac{NT}{2^N}\right)\right) . \tag{6.53}$$

Strictly speaking, (6.53) should be expected when T is of the same order as the Heisenberg time $2^N/N$ for an individual sector. However, for a Hamiltonian systems with underlying chaotic classical dynamics the linear growth of $\mathcal{K}(T,N)$ persists up to much shorter classical time scales. From the semi-classical point of view this can be attributed to diagonal correlations between periodic orbits in the double sum representing $K_2(T)$, see [36], while non diagonal correlations can arise only for time scales larger than the Ehrenfest time [126–128]. Interestingly, similar considerations give rise to the linear growth for the KIC as well. To illustrate this we cast (6.10) into a "semi-classical" form,

$$Z(N,T) = \sum_{\boldsymbol{\sigma}} A_{\boldsymbol{\sigma}} \exp\left(-\mathrm{i}S(\boldsymbol{\sigma})\right) , \tag{6.54}$$

where

$$A_{\boldsymbol{\sigma}} = \exp\left[-\mathrm{i}\sum_{n=1}^{N}\sum_{t=1}^{T}\left(K\sigma_{n,t}\sigma_{n,t+1} + \mathrm{i}\eta\right)\right] , \tag{6.55}$$

$$S(\boldsymbol{\sigma}) = \sum_{n=1}^{N}\sum_{t=1}^{T} J\sigma_{n,t}\sigma_{n+1,t} + h\sigma_{n,t} . \tag{6.56}$$

Equation (6.54) is reminiscent of the Gutzwiller trace formula with $S(\boldsymbol{\sigma})$, $A_{\boldsymbol{\sigma}}$ as the actions and stabilities of 2^{NT} "periodic orbits" which are labeled by all possible spin configurations $\boldsymbol{\sigma} = \{\sigma_{n,t} = \pm 1\}$. Applying the well known diagonal approximation, see [36], yields

$$\mathcal{K}(T,N)/4NT = \sum_{\boldsymbol{\sigma}} \left|A_{\boldsymbol{\sigma}}\right|^2 . \tag{6.57}$$

Substituting therein the amplitudes $A_{\boldsymbol{\sigma}}$ we obtain

$$\begin{aligned} \mathcal{K}(T,N)/4NT &= \left(\sum_{\boldsymbol{\sigma}} \exp\left(-2K_0\sum_{t=1}^{T}\sigma_t\sigma_{t+1} - 2\eta_0 T\right)\right)^N \\ &= \left(1 + (-\tanh 2K_0)^T\right)^N , \end{aligned} \tag{6.58}$$

where we introduced $\eta = \mathrm{i}\pi/4 - \eta_0$ and $K = \pi/4 - \mathrm{i}K_0$, *cf.* (6.8). The sum over all configurations $\boldsymbol{\sigma}$ now covers only individual particles for fixed n, the summation over different particles is replaced by the N-th power. In the limit of large N and T the right hand side tends to unity leading to the expected RMT result.

Alternatively, such a linear growth can be seen as a symmetry factor from the dual perspective. Indeed, we have

$$\mathcal{K}(T,N) = \mathrm{Tr}(\tilde{W}_T)^N \sim T \tag{6.59}$$

since $\tilde{W}_T$ has T different subspectra due to translational invariance, which for large N can be thought of as uncorrelated.

6.4. Recapitulation

As we continue to use the duality approach throughout the remainder of this thesis, a proper conclusion is relegated to chapter 8. However, some of the presented aspects are specific to this chapter, while others reappear in different form. It therefore appears appropriate to give a guide to the latter and discuss the former.

Due to its non-unitary nature the dual operator features a much richer spectral structure compared to its unitary counter part. Interestingly, this structure correlates with the dynamical state of the system. In the chaotic case the eigenvalues are distributed over a ring, implying an inner gap of the spectrum, while in the integrable regimes they are highly ordered. Close to the trivially integrable one ($b^x = 0$) all besides two eigenvalues tend to zero. In the non-trivially integrable regime ($b^z = 0$) they are situated on multiple concentric circles and highly degenerate. In this case the spectrum may have an inner gap, *i.e.* a finite radius for the smallest circle, or posses eigenvalues at zero. This brings it structurally close to either the chaotic or the trivially integrable regime, which might affect the transition behavior when integrability is weakly broken. Similarly, the structure of the dual operator will play a pronounced role in the next chapter.

In the limit of small parameters almost all eigenvalues of $\tilde{W}_T$ tend to zero, implying that its effective dimension is significantly smaller than its size would suggest. This might open a road to transfer the duality method also to non-kicked systems. In the present form we require the kicks as they introduce a natural discretization of time. But, time continuous dynamics can be emulated if at the same time the interval between the kicks and their respective strengths tends to zero. To reach finite dynamical times with such an approach the number T of kicks has to become infinite. In a naive formulation this also increases the dimension $2^T \times 2^T$ of the dual operator to infinity. Yet, in the ensuing small parameter limit the effective dimension might be controllable.

In general the non-unitarity leads to the presence of (usually few) largest eigenvalues $\tilde{\lambda}_{\mathrm{max}}$ within the spectrum of $\tilde{W}_T$. Even if the other eigenvalues are non-zero, sufficiently

large powers N of the dual operator often ensure that its traces are well approximated by only those $\tilde{\lambda}_{\max}$. This revealed some insight into the fluctuations of the smoothed spectral density, which were markedly large near the integrable parameter regimes. Furthermore, the largest eigenvalues allow an asymptotic description of the (short time) form-factor $K_2 \sim (\tilde{\lambda}_{\max}/2)^N$ which only rarely coincides with the RMT predictions. Regarding this last point, the spectrum of $\hat{U}_N$ decomposes into N sectors and RMT holds, if at all, for each of them separately. For this reason usually the form-factor is decomposed as well, but as figure 6.13 demonstrates for chaotic parameters, in this case the differences between the global form factor and these sectors is not necessarily much larger than the difference among the sectors themselves.

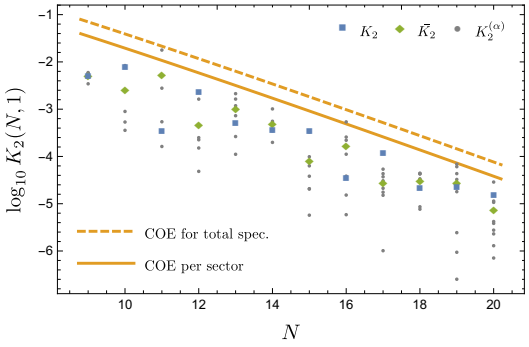

Fig. 6.13.: Logarithm of the form factor $K_2(N,1)$ for $T=1$ as a function of N, compare figure 6.9, for the chaotic parameters $J=0.7$ and $b^x=b^z=0.9$. In addition to the total form factor (blue squares) we also show all form factors for the independent sub-spectra (gray dots) and their average value (green diamonds).

7. Semi-Classical Kicked Spin Chain

INCREASING the spin quantum number $j = \hbar_{\text{eff}}$ converts the spin chain into a model that admits a semi-classical treatment in terms of classical vectors rotating on Bloch spheres. But, the accompanying increase of the dual operator's dimension limits us to very short times of one or two periods. As we will see in this chapter, the single particle case of our chain corresponds to the well known kicked top model [20, 21, 129] that features a rich dynamical structure, from fully integrable to almost fully chaotic. The latter point reveals that this system will often be of a mixed type. It is usually hard to control the regular periodic orbits (POs) as their repetitions tend to bifurcations, an almost identical statement applies for the POs if instead of time the system dimension is increased. Due to these circumstances we often encounter bifurcations in the classical system that lead to an algebraic divergence of the stability prefactor $A_\gamma \sim \hbar_{\text{eff}}^{-\alpha}$ on the semi-classical side, recall the discussion in section 2.3. Following the trace formula (2.18) we may expect that this scaling carries over to the quantum mechanical trace, especially so if the number of involved orbits on the classical side is not too large. In the previous chapter large traces were connected to enhanced spectral fluctuations, compare figure 6.6, and this mechanism should be kept in mind for the further discussion of marginally stable POs.

The presence of N as a large parameter adds a peculiar twist to the study of bifurcations. For integrable systems it is quite natural that $\alpha(N) \sim N/2$ grows with N as the number of conserved quantities is proportional to it. In comparison, fully chaotic systems posses no scaling at all and the effect of single bifurcations can not provide any N dependence, this case thus leads to significantly weaker spectral fluctuations. Still, the number of eigenvalues e^{Λ} of the monodromy matrix increases linearly with N. While it is unlikely that a relevant part of them is precisely zero as for the integrable case the many-body nature of our problem offers a dynamical freedom much larger than for few-body systems. Unexpectedly, the chain of coupled kicked tops features four dimensional PO manifolds which are marked by highly correlated, collective dynamics. Spins in a fixed distance $N_\gamma^{(P)}$ perform identical motions giving the POs a very regular spatial structure. Given the manifolds low dimensionality only four Λ are precisely zero but the remaining $2N - 4$ eigenvalues are to varying degree quasi-marginal ensuring the manifolds continued importance for larger N. This already indicates a delicate connection between $\hbar_{\text{eff}}$ and N. In a strict semi-classical limit where the number of particles is held fixed while $\hbar_{\text{eff}}$ is send to zero we recover spectral fluctuations whose scaling exponent α is independent of N. But, if N is increased simultaneously with $\hbar_{\text{eff}}^{-1}$

the growing amount of quasi-marginal directions leads to a non-trivial scaling.

We start this chapter by an introduction of the (quantum) kicked top and its classical dynamics, which we both generalize to an interacting chain forming the general j reformulation of the Ising spin chain used in the last chapter. An overview on the system's POs is given, subsequently, in section 7.2, a strong focus here will lie on the description of the orbit manifolds. As previously, we offer a concretized version of the duality relation in section 7.3. Building on the classical dynamics we can also present a dual form of stability matrix, section 7.4, that admits a new perspective on the bifurcation mechanism within the system. For the accessible times of $T=1,2$, section 7.5 presents a semi-classical analysis in which we identify periodic orbits in an action spectrum obtained from the genuine quantum many-body system. Attention is given to the effect of the manifold, which dominates the spectrum, and bifurcations in general. To fully appreciate the properties of the former we have to resort to the dual operator and its "semi-classical" interpretation in section 7.6. A more holistic perspective on the manifolds emerges under a slight extension of the spin chain in section 7.7. Finally, section 7.8 offers a short summary.

7.1. Model

Throughout this section we introduce the kicked spin chain model [114–117] for general spin quantum numbers j as well as its classical counterpart. The kicked structure of the dynamics remains identical to (5.2), but on the quantum side we introduce a minor modification compared to (5.9). As will become apparent later on $j+1/2$ takes on the role of the inverse Planck constant $\hbar^{-1}$. We can thus use the slightly less conventional form,

$$\hat{U} = \hat{U}_I \hat{U}_K \qquad \text{with} \qquad \hat{U}_{I,K} = \mathrm{e}^{-\mathrm{i}(j+1/2)\hat{H}_{I,K}} \,, \tag{7.1}$$

for the (Floquet) evolution operator.

7.1.1. Kicked Top

To begin with, we recall the kicked top [18, 130] as the $N=1$ special case of the model. The corresponding Hamiltonians, compare section 5.1, are

$$\hat{H}_K^{(\mathrm{KT})} = \frac{2\,\vec{b}\cdot\hat{\vec{S}}}{j+1/2} \,, \tag{7.2}$$

$$\hat{H}_I^{(\mathrm{KT})} = \frac{4J^{(\mathrm{KT})}}{(j+1/2)^2}\,(\hat{S}^z)^2 \tag{7.3}$$

with the spin operator $\hat{\vec{S}} = (\hat{S}^x,\ \hat{S}^y,\ \hat{S}^z)^{\mathrm{T}}$ for spin quantum number j, *i.e.* $(\hat{\vec{S}})^2 = j(j+1)$. Here $\hat{H}_I^{(\mathrm{KT})}$ contains a non-trivial quadratic term which can be thought of as a shear

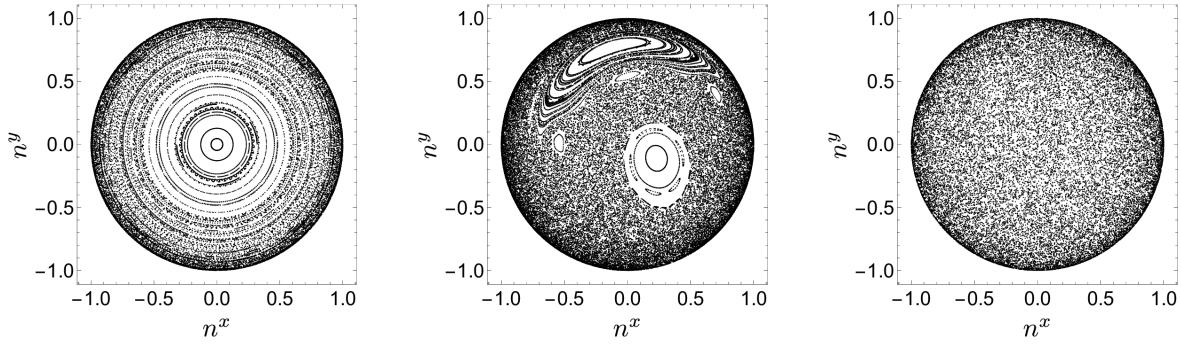

Fig. 7.1.: Upper hemisphere ($n^z > 0$) of the classical phase-space for the kicked top, see equation (7.6), after 200 iterations for several hundred randomly chosen initial points. Parameters are chosen as $J^{(\mathrm{KT})}=0.7$, $b=0.9\sqrt{2} \approx 1.27$. The angle varies with $\varphi = 0,\ 0.2,\ \pi/4$ (from left to right).

or torsion. This term singles out the z-direction and, again, the magnetic field $\vec{b}$ in $\hat{H}_K^{(\mathrm{KT})}$ can be restricted, without loss of generality, to the xz-plane, $\vec{b} = (b^x,\, 0,\, b^z)^T = b\,(\sin\varphi,\, 0,\, \cos\varphi)^T$. To avoid a dependence of the coupling parameter strengths on j in the classical limit we rescale both Hamiltonians by their respective powers in $\hat{S}$. Minimal uncertainty is given in terms of j for spin coherent states, which therefore replaces $\hbar^{-1}$ as a measure of Planck cell size.

The corresponding classical model can be found after replacing $\hat{\vec{S}}$ by a spin vector $\sqrt{j(j+1)}\vec{n}$, $|\vec{n}| = 1$, precessing on the Bloch sphere. Its relation to the canonical coordinates (q, p) is given by [18, 131]

$$\vec{n} = \left(\sqrt{1-p^2}\cos q,\, \sqrt{1-p^2}\sin q, p\right)^T \tag{7.4}$$

with the corresponding Hamiltonian

$$H(q,p) = 4J^{(\mathrm{KT})}p^2 + 2\left(b^z p + b^x\sqrt{1-p^2}\cos q\right)\sum_{T=-\infty}^{\infty}\delta(t-T) \tag{7.5}$$

having only a single degree of freedom.

The classical action of the kick onto $\vec{n}$ is a rotation around the $\vec{b}$-axis by the angle $2b$, denoted by $\underline{R}_{\vec{b}}(2b)$. The second part of the evolution also acts as a rotation around the z-axis, however, its angle depends on the value of n^z creating the torsion. Combining both rotations one finds the new position of $\vec{n}$ after a single time step as

$$\vec{n}(T+1) = \underline{R}_z\left(8J^{(\mathrm{KT})}n^z\right)\underline{R}_{\vec{b}}(2b)\,\vec{n}(T)\,. \tag{7.6}$$

Figure 7.1 provides Poincare sections of this dynamics for different values of φ. In the case of $\varphi = 0$, shown on the left panel, the system is integrable and the phase-space

is filled by invariant tori corresponding to fixed actions. A slight change of the angle breaks those tori, leading to mixed system dynamics, while for $\varphi = \pi/4$ the system is almost fully chaotic.

In many cases it turns out to be useful to decompose the kick action into three rotations around the coordinate axes,

$$\underline{R}_{\vec{b}}(2b) = \underline{R}_z(\alpha)\underline{R}_x(\beta)\underline{R}_z(\gamma) = \underline{R}_z(\alpha - \pi/2)\underline{R}_y(\beta)\underline{R}_z(\gamma + \pi/2)\,. \tag{7.7}$$

Here α, β, γ are the corresponding Euler angles and for our choice of $\vec{b}$, namely $b^y = 0$, they are given by

$$\alpha = \gamma, \quad b^z \tan(\pi/2 - \alpha) = b \cot b, \quad \cos\beta = \left(\frac{b^z}{b}\right)^2 + \left(\frac{b^x}{b}\right)^2 \cos 2b\,. \tag{7.8}$$

Due to $\underline{R}_z(x)\underline{R}_z(y) = \underline{R}_z(x+y)$ this allows us, classically, to express the whole dynamics in terms of alternating x, z or y, z rotations, respectively.

7.1.2. Kicked Spin Chain

For the N-body extension of the kicked top into a one dimensional chain we revisit the homogeneous bilinear coupling between neighboring spins, see also (6.1),

$$\hat{H}_I = \sum_{n=1}^{N} \left(\frac{4J\, \hat{S}^z_{n+1} \hat{S}^z_n}{(j+1/2)^2} + \frac{4V\, (\hat{S}^z_n)^2}{(j+1/2)^2} \right)\,, \tag{7.9}$$

with the inter-spin Ising coupling J and an additional local torsion governed by V. We restrict ourselves mostly to the special case $V = 0$ and assume this condition if not stated otherwise. Discussion of the $V \neq 0$ extension is relegated to section 7.7. The kicked part is kept local and the same as in (7.2) or (6.2),

$$\hat{H}_K = \sum_{n=1}^{N} \frac{2\,\vec{b} \cdot \hat{\vec{S}}_n}{j+1/2}\,. \tag{7.10}$$

For the duality approach to work the boundary conditions are chosen periodic, *i.e.* $\hat{S}^z_{N+1} = \hat{S}^z_1$, making the system translation invariant. In consequence, in the special case of $N = 1$ the kicked spin chain corresponds to the kicked top above with $J^{(\mathrm{KT})} = J + V$. The system remains integrable for $b^x = 0$ and arbitrary N. In the special case of $j = 1/2$ the spin operators are expressible through the Pauli matrices, $\hat{S}^i = \sigma^i/2$, and this model turns into the previously considered Ising chain where the on-site torsion V only acts as a trivial constant. The non-trivially integrable regime we discussed for this case ceases to exist for higher spin quantum numbers.

The modifications on the classical side compared to (7.6) and (7.5) are straightforward. The Hamiltonian (7.5) is adjusted to

$$H(\vec{q},\vec{p}) = \sum_{n=1}^{N} \left[4Jp_{n+1}p_n + 4Vp_n^2 + \; 2\left(b^z p_n + b^x\sqrt{1-p_n^2}\cos q_n\right) \sum_{T=-\infty}^{\infty} \delta(t-T) \right] , \tag{7.11}$$

which includes additional interaction between neighboring momenta. The Hamiltonian equations of motions give rise to the rotation of N classical spin vectors $\vec{n}_m$,

$$\vec{n}_m(T{+}1) = \underline{R}_z\big(4J\chi_m\big)\, \underline{R}_{\vec{b}}(2b)\, \vec{n}_m(T)\,, \tag{7.12}$$

where $\chi_m = n^z_{m-1} + n^z_{m+1} + 2\mu\, n^z_m$ with $\mu{=}V/J$. In this case the rotation angle $4J\chi_m$ encodes the bilinear interaction between the neighboring spins.

7.2. Periodic Orbits

For the semi-classical analysis knowledge of the PO actions and their stabilities is essential. Recalling section 2.3, in the limit of large j the trace of the propagator can be expressed by a Gutzwiller-type of sum over POs γ of period T:

$$\mathrm{Tr}\ \hat{U}^T \sim \sum_{\gamma(T)} A_\gamma \mathrm{e}^{\mathrm{i}(j+1/2)\mathcal{S}_\gamma}\,, \tag{7.13}$$

therein we replaced $\hbar^{-1}$ by its effective value $j+1/2$. This relation was explicitly derived for spin systems in [6]. Here $\mathcal{S}_\gamma$ is the classical action as given in B.2 and the stability prefactor A_γ is determined by the stability of the orbit. If the orbit is sufficiently isolated in phase-space, it is given by the monodromy matrix as seen in (2.19).

After establishing basic properties of the POs due to the system's chain like structure we look, in more detail, at the case of integrable dynamics in section 7.2.2. The general case, with $V=0$, is covered by section 7.2.3, where the primary focus is on manifolds of non-isolated POs which play a crucial role in the subsequent semi-classical analysis.

7.2.1. General Properties

A periodic orbit γ of duration T_γ for N_γ spins is a set $\{\vec{n}_m\}_{m=1}^N$ of Bloch vectors satisfying

$$\vec{n}_m(T_\gamma) = \vec{n}_m(0), \qquad \text{where} \tag{7.14}$$
$$\vec{n}_m(0) = \vec{n}_m\,, \quad \vec{n}_m(T_\gamma) = \Big(\underline{R}_m(J,V,\vec{b})\Big)^{T_\gamma}\, \vec{n}_m(0)$$

with the classical propagation matrix $\underline{R}_m(J,V,\vec{b}) = \underline{R}_z\big(4J\chi_m\big)\,\underline{R}_{\vec{b}}(2b)$, compare section 7.1.2. As γ is a valid orbit for T_γ time steps it will, by further repetition, also be a valid orbit for kT_γ time steps ($k \in \mathbb{N}$). This is a direct consequence of the system's translation invariance in time. The minimal number of time steps required to close the orbit (for the first time) is the primitive time period $T_\gamma^{(P)}$. Such an orbit leads to $T_\gamma^{(P)}$ fixed point solutions to (7.14) corresponding to different initial starting points along the orbit.

By construction we have a translation symmetry not only in time but also along the chain. Accordingly, a PO of the N spin system induces, by repetition, an orbit for a kN particle system with the same parameters. For instance, every PO of the kicked top is also a PO of the kicked spin chain for $J^{(\mathrm{KT})} = J + V$. We introduce the primary spatial period $N_\gamma^{(P)}$ as the minimal number of spins required to accommodate the orbit γ. Due to the translation symmetry the cyclic permutation of the motion of individual spins along the chain does not change the overall dynamics and any given orbit is thus part of a family of $N_\gamma^{(P)}$ identical orbits with identical action and stabilities.

Periodic orbits can be expressed in terms of repetitions of the prime orbits which encompass the minimal number of particles and time steps necessary to accommodate it. These types of repetitions imply a linear scaling of the action $\mathcal{S}_\gamma$ of an orbit,

$$\mathcal{S}_\gamma = r_\gamma^{(T)} r_\gamma^{(N)}\, \mathcal{S}_\gamma^{(P)}\,, \tag{7.15}$$

where $\mathcal{S}_\gamma^{(P)}$ is the action of the prime orbit and

$$r_\gamma^{(T)} = \frac{T}{T_\gamma^{(P)}}\,, \qquad r_\gamma^{(N)} = \frac{N}{N_\gamma^{(P)}} \tag{7.16}$$

are the repetitions in time and space, respectively. The actions $\mathcal{S}_\gamma$ can be calculated as the sum of local spherical areas swept by the $\vec{n}_i$'s on the Bloch's spheres. The specific calculations are relegated to appendix B.2.

Numerics shows that for a generic choice of parameters most of the orbits comprise both hyperbolic and elliptic directions. In other words, for a typical γ the set of eigenvalues $\{\exp\Lambda_i\}$ of the corresponding monodromy matrix $\underline{M}_\gamma$ includes ones for which $|\mathrm{e}_i^\Lambda| \neq 1$, as well as ones with $|\mathrm{e}_i^\Lambda| = 1$. The relation (2.19) for the stability prefactor breaks down when one of the directions becomes marginal, *i.e.* one of the eigenvalues turns into 1 and changes from hyperbolic to elliptic, or vice versa, under infinitesimal change of the system parameters. If an orbit is marginal this also holds for its repetitions in time and space. We comment further on non-isolated orbits in section 7.5.

7.2.2. Integrable Case

For $b^x = 0$ all rotations are around the z-axis and therefore commute with the Hamiltonian making the system integrable. As a result the dynamics of the kicked system for arbitrary

times is equivalent to one at fixed time, *e.g.* $T=1$ with rescaled system parameters $J \to JT$ and $b^z \to b^z T$. Moreover, the continuous flow induced by the Hamiltonian $\hat{H}_I + \hat{H}_K$ for time T is identical to the evolution of the kicked system for T time steps with the same parameters.

For the classical trajectories p_n is a conserved quantity for each n separately and POs form N dimensional manifolds. To close a trajectory in phase-space after T iterations it is sufficient that the total change in angles Δq_n is a multiple of 2π,

$$\Delta q_n = 4T\Big(J(p_{n-1}+p_{n+1}) + 2Vp_n\Big) + 2b^z T = 2\pi m_n \,. \tag{7.17}$$

The $m_n \in \mathbb{Z}$ is a local winding number for spin n. Since the momenta are bounded by $|p_n| \leq 1$, the term $p_{n-1}+p_{n+1}$ resides within the interval $[-2,+2]$. Therefore, this equation has no solution if, for instance, $b^z > 4(J+V)$ and $4(J+V) + b^z < \pi/T$. In such cases the system does not posses any classical PO of period T or shorter. If all parameters (times T) are sufficiently small, the first accessible winding number is necessarily zero. With increasing time T the number of possible m_n grows linearly. As a result, the number of possible (distinct) POs grows algebraically. With respect to N the number of POs is determined by all admissible combinations of the winding numbers. If there is more than one allowed m_n, the growth is thus exponential in N. This exponential growth also holds for non-integrable parameter choices.

7.2.3. General Case

A perturbation of the integrable model by a non-zero b^x breaks up the N-dimensional periodic tori into isolated POs and some low dimensional manifolds of non-isolated POs. We first comment on the general properties of the isolated ones and later detail on the manifolds which, as it turns out, play a significant role in the semi-classical treatment of the corresponding quantum model.

Isolated Periodic Orbits — The observed exponential proliferation of POs for increasing N within the integrable model carries over to the general case. For large N the stabilities of orbits are of a mixed type, *i.e.* both hyperbolic and elliptic directions are present in the same orbit. The behavior of the prefactors $|A_\gamma|$, however, substantially depends on the time T. For a generic set of parameters and $T=1$ a typical orbit is well isolated, such that $\det(1-\underline{M}_\gamma)$ exponentially increases with N. On the other hand, for $T=2$ we found many γ's for which a large number of eigenvalues of $\underline{M}_\gamma$ are close to 1. In other words, an essential number of POs is almost marginal implying quite small determinants $\det(1-\underline{M}_\gamma)$. In such cases the approximation (2.19) is no longer applicable. We return to this property when we discuss orbit stabilities from a dual perspective in section 7.4.

Periodic Orbit Manifolds — Besides the isolated orbits the case $T=2$ also features low dimensional manifolds of POs, *i.e.* regions in phase-space where every point

constitutes a periodic orbit. As we explain below for $V=0$, this phenomenon occurs when the length of the spin chain is equal to $N=4k$, $k \in \mathbb{N}$. This peculiar condition can be traced back to a special feature of the four-spin system whose POs, by repetition, also induce POs of larger systems with $N=4k$. According to (7.14) for $V=0$ and $N=4$ the time evolution of the first and the third spin vectors $\vec{n}_1, \vec{n}_3$ are provided by one and the same rotation matrix $\underline{R}_z\big(4J\chi_1\big)\underline{R}_{\vec{b}}(2b)$. This immediately implies that the scalar product $(\vec{n}_1 \cdot \vec{n}_3)$ is a conserved quantity. Similarly, $(\vec{n}_2 \cdot \vec{n}_4)$ is preserved, as well. In other words, the $N=4$ spin chain possess two integrals of motion. Particularly, in the case of $b^x=0$ the system is over integrable having 6 integrals of motion rather than 4: In addition to the four momenta $p_i, i=1,\ldots,4$, the differences between coordinates q_1-q_3, q_2-q_4 are conserved under time evolution.

In the general case ($V=0$) we provide an explicit construction of the PO manifolds. Since the dynamics of spin i depends exclusively on the time evolution of the variable $\chi_i = n^z_{i-1} + n^z_{i+1}$, any trajectory satisfying the condition

$$\underline{R}_z\big(4J\chi_i^{(1)}\big)\,\underline{R}_{\vec{b}}(2b)\underline{R}_z\big(4J\chi_i^{(2)}\big)\,\underline{R}_{\vec{b}}(2b) = \mathbb{1}, \qquad i=1,\ldots,N\,, \tag{7.18}$$

where $\chi_i^{(1)}$, $\chi_i^{(2)}$ are the values at the time-steps $t=1,2$, respectively, is automatically periodic. The most simple way to satisfy this condition is to assume that $4J\chi_i^{(1)} \mod 2\pi = 4J\chi_i^{(2)} \mod 2\pi = 4J\chi$ is constant for all spins. This implies that $(\underline{R}_z\big(4J\chi_i^{(t)}\big)\,\underline{R}_{\vec{b}}(2b))^2 = \mathbb{1}$ such that $\underline{R}_z\big(4J\chi_i^{(t)}\big)\underline{R}_{\vec{b}}(2b) = \underline{R}_{\vec{\zeta}}(\pi)$ is a rotation about π around some axis $\vec{\zeta}$. This forces the value of $\chi_i^{(t)}$ to satisfy the following equation:

$$b^z \,\tan\left(2J\chi_i^{(t)}\right) = b\,\cot b, \qquad i=1\ldots,N, \qquad t=1,2\,, \tag{7.19}$$

which solutions take on the form $\chi_i^{(t)} = \chi + \pi m_i^{(t)}/2J$ with $m_i^{(t)} \in \mathbb{Z}$ and $-2 \le \chi_i^{(t)} \le 2$. Fixing the values of $\chi_i^{(t)}$ by equation (7.19) imposes restrictions onto the positions of each spin at each time-step $t=1,2$,

$$\chi_i^{(1)} = n^z_{i-1} + n^z_{i+1}\,, \tag{7.20}$$

$$\begin{aligned}\chi_i^{(2)} = {} & \sin^2 b \sin 2\varphi \left(n^x_{i-1} + n^x_{i+1}\right) + \sin\varphi \sin 2b \left(n^y_{i-1} + n^y_{i+1}\right) \\ & + \left(\cos 2b \sin^2\varphi + \cos^2\varphi\right)\left(n^z_{i-1} + n^z_{i+1}\right)\,,\end{aligned} \tag{7.21}$$

where the constants $\chi_i^{(t)}$ satisfy (7.19) for all i and t. The second equation results from the fact that the second time step $\chi_i^{(2)}$ is obtained from the original spin vectors via a rotation, implying that $\chi_i^{(2)} = \vec{e}_z \cdot \underline{R}_{\vec{b}}(2b)\,(\vec{n}_{i-1} + \vec{n}_{i+1})$ (the z-component is not changed by $\underline{R}_z(4J\chi_i^{(t)})$ and it thus does not need to be considered). For any sequence of $2N$ solutions of (7.19) obeying the conditions $-2 \le \chi_i^{(t)} \le +2$, the equations (7.20), (7.21) fix a 4-dimensional manifold of initial conditions for POs. An example of such a PO is

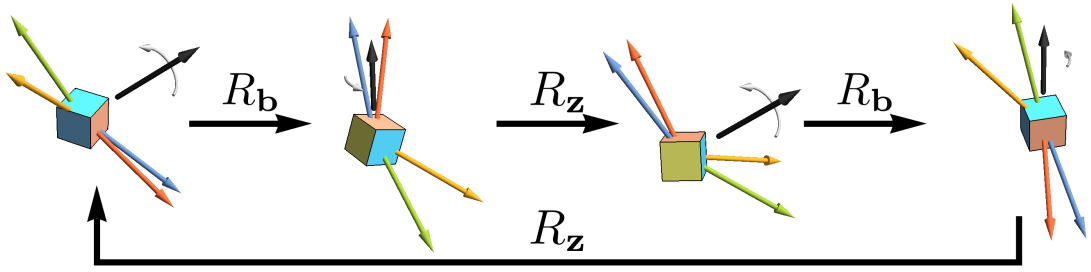

Fig. 7.2.: Trajectory of a PO on the manifold, depicted after each rotation step for $J=0.7$ and $b^x=b^z=0.9$. Spins are ordered along the chain according to their colors: blue, yellow, green and red. Visible is a solid-body rotation leaving all angles between the spins constant. The co-rotating cube serves as reference.

given in figure 7.2 which shows that the relative motion between the spins is frozen due to the identical $\underline{R}_z\big(4J\chi_i^{(t)}\big)$. As explained in appendix B.3, all POs belonging to one of these manifolds have one and the same action provided by the interaction part of the evolution,

$$\mathcal{S} = 4J\sum_{i=1}^{N}\sum_{t=1}^{2} p_i^{(t)}p_{i+1}^{(t)}\,. \tag{7.22}$$

In the special case of PO manifolds with spatial prime period $N_\gamma^{(P)}=4$ this simplifies to the elegant formula

$$\mathcal{S}^{(\mathrm{P})} = J\sum_{i=1}^{4}\sum_{t=1}^{2} \chi_i^{(t)}\chi_{i+1}^{(t)}\,, \tag{7.23}$$

where $\mathcal{S}^{(\mathrm{P})}$ denotes the prime action of the orbits.

We can distinguish three different regimes, where (7.19) has none, one or several solutions in the interval $-2 \le \chi_i^{(t)} \le +2$, each having unique consequences for the system behavior. The first case occurs, when J or b are sufficiently small, bringing the model close to the integrable/non-interacting regime. Most of the discussion is devoted to the single manifold regime, where (7.19) admits one unique solution such that $\chi_i^{(t)}=\chi$ for all i,t. In this case the action of the manifold orbits is given by

$$\mathcal{S} = N\mathcal{S}_{\mathrm{man}} \qquad \text{with} \quad \mathcal{S}_{\mathrm{man}} = 2J\chi^2 \quad \text{and} \quad N = 4k\,. \tag{7.24}$$

Furthermore, equation (7.21) reduces, using $\chi_i^{(2)}=\chi_i^{(1)}=\big(n_{i-1}^z+n_{i+1}^z\big)$, to the simpler form

$$\chi = \big(n_{i-1}^x+n_{i+1}^x\big)\cot\varphi + \big(n_{i-1}^y+n_{i+1}^y\big)\,\frac{\cot b}{\sin\varphi}\,. \tag{7.25}$$

For the case of several possible solutions $\chi_i^{(t)} = \chi+\pi m_i^{(t)}/2J$, $m_i^{(t)}\in\mathbb{Z}$ to equation (7.19) the number of different manifolds of POs starts to grow exponentially with N. This

should be compared with the role of the spin winding numbers in the integrable case. There, the number of orbits with respect to N was determined by the exponentially growing amount of different possible combinations of winding numbers. In a similar way we can exchange the possible values of $m_i^{(t)}$ along the spin chain leading to the exponential growth of different PO manifolds.

At this point, we only introduced the class of four dimensional manifolds. We can, however, impose more intricate, less symmetric restrictions which still admit two dimensional manifolds. They will play no further role in the remainder and we relegated details on their construction to appendix B.4.

7.2.4. Weak Coupling Regime.

In the special case of the non-interacting regime $J=0$, all POs are given by compositions of solutions for the single spin case. As a result, a non-interacting spin chain becomes (almost) fully chaotic if the corresponding $N=1$ kicked top possesses chaotic dynamics, as happens for certain choices of the parameters $\vec{b}$ and V. In such a case each PO of the non-interacting spin chain is isolated and fully hyperbolic. This situation still persists after introducing a weak coupling J between the spins, at least, if T is sufficiently short. In this regime POs are fully hyperbolic and can be related to their non-interacting counterparts making their identification an easy achievable goal. Accordingly, a leading order semi-classical approximation (7.13) works significantly better for weakly interacting spin chains in comparison to the general case, where the dynamics is plagued by bifurcations.

7.3. Duality Relation

The concept of the quantum duality was used explicitly in the last chapter, section 6.1.2, and previously introduced on an abstract level in section 5.2. We use the definitions of the latter and give at this point only the auxiliary functions f_I and f_K. They are given by the exponents of the respective evolution operators, compare equations (5.11) and (5.12), as

$$f_I(\sigma_n, \sigma_{n+1}) = \frac{-4\mathrm{i}}{j+1/2}\left(J\sigma_n\sigma_{n+1} + V\sigma_n^2\right) . \tag{7.26}$$

for the interaction part, and more formally by

$$f_K(\sigma, \sigma') = \mathrm{Ln}\ \langle\sigma|\exp\left(-2\mathrm{i}\,\vec{b}\cdot\hat{\vec{S}}\right)|\sigma'\rangle. \tag{7.27}$$

for the kick part. This implies a rather simple structure for the dual kick,

$$\tilde{W}_K = \bigotimes_{t=1}^{T} w_K\,, \quad \langle\sigma'|w_K|\sigma\rangle = \exp\left(\frac{-4\mathrm{i}\,(J\sigma\sigma' + V\sigma^2)}{j+1/2}\right), \tag{7.28}$$

which has an interesting resemblance to a (fractional) Fourier transform which we utilize later. The new interaction part retains a diagonal structure,

$$\langle\vec{\sigma}|\tilde{W}_I|\vec{\sigma}'\rangle = \delta_{\vec{\sigma},\vec{\sigma}'}\prod_{t=1}^{T}\langle\sigma_t|\exp\big(-2\mathrm{i}\,\vec{b}\cdot\hat{\vec{S}}\big)|\sigma_{t+1}\rangle\,, \tag{7.29}$$

which may be simplified in terms of Wigner's small d-matrix:

$$d^j_{\sigma\,\sigma'}(\beta) = \langle\sigma|\mathrm{e}^{-\mathrm{i}\beta\hat{S}^y}|\sigma'\rangle\,. \tag{7.30}$$

This matrix describes the transition elements of a unitary rotation induced by a constant magnetic field. Using the Euler decomposition (7.7) we find,

$$\langle\vec{\sigma}|\tilde{W}_I|\vec{\sigma}'\rangle = \delta_{\vec{\sigma},\vec{\sigma}'}\exp\Big(-\mathrm{i}(\alpha+\gamma)\sum_{t=1}^{T}\sigma_t\Big)\prod_{t=1}^{T}d^j_{\sigma_t\sigma_{t+1}}(\beta)\,, \tag{7.31}$$

that the dual interaction is given as product over such terms. Herein α,β,γ (with $\alpha{=}\gamma$) are the Euler angles given in (7.8) and the index t runs over all T spins constituting the dual operators. It inherits the periodic boundary conditions, *i.e.* $\sigma_{T+1}{=}\sigma_1$.

Finally, let us comment on a certain peculiarity of the integrable case ($b^x = 0$). Due to the identity $\hat{U}(J,\vec{b},V)^T = \hat{U}(TJ,T\vec{b},TV)$ the evolution for T time steps can be equivalently thought of as one for a single time step with rescaled parameters. Therefore, the dual operator takes on the form of a $(2j+1)\times(2j+1)$ matrix (rather than $(2j+1)^T\times(2j+1)^T$) for a single spin system:

$$\tilde{W}_{nm} = \exp\left(-\mathrm{i}\frac{4TJ}{j+1/2}nm - \mathrm{i}\frac{4TV}{j+1/2}m^2 - 2\mathrm{i}Tb^z n\right)\,, \tag{7.32}$$

where the indices n,m run from $-j$ to $+j$.

7.4. Classical Duality

The original formulation of the duality, see section 5.1, was motivated by the relation between the classical map Φ and its dual counter part $\tilde{\Phi}$. For the case of the considered spin chain such a dual map can be defined if b and J are sufficiently small as (5.6) possesses a unique solution only in this case. But, we can bypass this constraint if instead of a full dual dynamics we restrict ourselves to the linearized dynamics. In this way we may determine the stability of a given PO from a dual point of view, which offers new insights for the orbits behavior under repetition in N. As it turns out, the dual stability is given by a symplectic matrix $\underline{\tilde{M}}_\gamma$ times a real constant $\mathcal{D}$. In the first part of this section we present the underlying formalism and in the subsequent section 7.4.2 we employ it to construct specific examples of bifurcations in particle direction.

7.4.1. Linearized Map

In a kicked chain-like system with nearest neighbor interaction the linearized dynamics takes on a generic form,

$$\alpha^+_{n,t}\, p_{n,t+1} + \alpha^-_{n,t}\, p_{n,t-1} + \beta^+_{n,t}\, p_{n+1,t} + \beta^-_{n,t}\, p_{n-1,t} = \gamma_{n,t} p_{n,t}\,, \tag{7.33}$$

where we replaced the dependence on q by an additional time-step in p revealing the "Laplacian like" structure of these systems in both time and (particle) space, compare for instance our initial example (5.8). The prefactors α, β, γ may depend on the choice of the orbit γ. Based on this linearization we can introduce a single time-step monodromy matrix $\underline{M}_t$ that maps deviations $\vec{z}_t$ in time t to $t+1$ where

$$\vec{z}_t = (p_{1,t-1}, p_{1,t}, p_{2,t-1} \dots p_{N,t}) \tag{7.34}$$

contains both the momenta at t and $t-1$, the latter as replacement for q. We thus find for $\vec{z}_{t+1} = \underline{M}_t \vec{z}_t$ the tri-diagonal matrix

$$\underline{M}_t = \begin{pmatrix} \underline{A}_{1,t} & \underline{B}^+_{1,t} & 0 & \dots & 0 & \underline{B}^-_{1,t} \\ \underline{B}^-_{2,t} & \underline{A}_{2,t} & \underline{B}^+_{2,t} & \dots & 0 & 0 \\ 0 & \underline{B}^-_{3,t} & \underline{A}_{3,t} & \dots & 0 & 0 \\ \vdots & \vdots & \vdots & \ddots & \vdots & \vdots \\ 0 & 0 & 0 & \dots & \underline{A}_{N-1,t} & \underline{B}^+_{N-1,t} \\ \underline{B}^+_{N,t} & 0 & 0 & \dots & \underline{B}^-_{N-1,t} & \underline{A}_{N,t} \end{pmatrix}, \tag{7.35}$$

which contains the 2×2 sub-matrices

$$\underline{A}_{n,t} = \begin{pmatrix} 0 & 1 \\ -\frac{\alpha^-_{n,t}}{\alpha^+_{n,t}} & \frac{\gamma_{n,t}}{\alpha^+_{n,t}} \end{pmatrix} \qquad \text{and} \qquad \underline{B}^\pm_{n,t} = \begin{pmatrix} 0 & 0 \\ 0 & -\frac{\beta^\pm_{n,t}}{\alpha^+_{n,t}} \end{pmatrix}. \tag{7.36}$$

The full monodromy matrix $\underline{M}_\gamma$ of the orbit is obtained from the single steps as

$$\underline{M}_\gamma = \prod_{t=1}^{T} \underline{M}_t\,. \tag{7.37}$$

In an equivalent fashion we may introduce single particle dual monodromy matrices $\underline{\tilde{M}}_n$ that relate deviations of particle n to $n+1$. They are given by a matrix of the same type as in (7.35). However, the dimension changes to $2T\times 2T$ and t instead of n is the running index. Further on, α and β are exchanged in $\underline{A}$ and $\underline{B}^\pm$ such that we find

$$\underline{\tilde{A}}_{n,t} = \begin{pmatrix} 0 & 1 \\ -\frac{\beta^-_{n,t}}{\beta^+_{n,t}} & \frac{\gamma_{n,t}}{\beta^+_{n,t}} \end{pmatrix} \qquad \text{and} \qquad \underline{\tilde{B}}^\pm_{n,t} = \begin{pmatrix} 0 & 0 \\ 0 & -\frac{\alpha^\pm_{n,t}}{\beta^+_{n,t}} \end{pmatrix}. \tag{7.38}$$

for the dual counter parts.

What remains to show is that both matrices, $\underline{M}_\gamma$ and $\underline{\tilde{M}}_\gamma$, are equally suited to determine the orbit's stability. To this end we provide the following relation

$$\mathcal{C}\det(\mathbb{1}-\underline{M}_\gamma)=\det\underline{F}=\widetilde{\mathcal{C}}\det(\mathbb{1}-\underline{\tilde{M}}_\gamma)\,, \tag{7.39}$$

with some complex numbers $C,\widetilde{C}$ for whose proof we introduce the auxiliary $NT\times NT$ matrix $\underline{F}$. It is the matrix representation of (7.33),

$$\underline{F}\cdot\{p_{n,t}\}=0\,. \tag{7.40}$$

acting on the vector $\{p_{n,t}\}$ containing all NT elements in some order. In the case of an isolated orbit it has only the trivial solution $\{p_{n,t}\}=0$. Relation (7.39) becomes more apparent if we look at the characteristic polynomial

$$P_F(\lambda)=\det(\underline{F}-\lambda\mathbb{1})\,,\qquad(\underline{F}-\lambda\mathbb{1})\cdot\{p_{n,t}\}=0\,. \tag{7.41}$$

In the same way (7.33) can be contracted to the monodromy matrices the eigenvalue equation above can be contracted to a λ dependent matrix $\underline{M}_\gamma(\lambda)=\prod_{t=1}^{T}\underline{M}_t(\lambda)$ where $\underline{M}_t(\lambda)$ is obtained from (7.35) by a replacement of $\gamma_{n,t}\to\gamma_{n,t}+\lambda$ in all $\underline{A}_{n,t}$. The $\underline{M}_t(\lambda)$ still transport deviations in time, specifically, eigenvectors of $\underline{F}$ will be mapped onto themselves (given the specific choice of λ) after T steps. Therefore

$$P_M(\lambda)=\det\left(\underline{M}_\gamma(\lambda)-\mathbb{1}\right) \tag{7.42}$$

has the same roots as $P_F(\lambda)$. In the same way $P_{\tilde{M}}(\lambda)$ can be defined and also has the same roots. Conclusively, up to proportionality constants the polynomials P_F,P_M and $P_{\widetilde{M}}$ are equivalent. These constants compensate the leading order terms λ^{NT} of P_M and $P_{\widetilde{M}}$, respectively. They are given by

$$\mathcal{C}=\prod_{t=1}^{T}\prod_{n=1}^{N}\alpha^+_{n,t}\,,\quad\text{and}\quad\widetilde{\mathcal{C}}=\prod_{t=1}^{T}\prod_{n=1}^{N}\beta^+_{n,t}\,. \tag{7.43}$$

By definition the leading order of $P_F(\lambda)$ is unity. Setting $\lambda=0$ concludes the proof of (7.39).

Within our concrete spin-chain model the linearization parameters are given by

$$\alpha^+_{n,t}=1/c_{n,t},\alpha^-_{n,t}=1/c_{n,t-1},\quad\gamma_{n,t}=\frac{a_{n,t-1}}{c_{n,t-1}}+\frac{d_{n,t}}{c_{n,t}}+8K,\quad\beta^+_{n,t}=\beta^-_{n,t}=-4J\,, \tag{7.44}$$

where the further parameters

$$S(n,t)=\begin{pmatrix}a_{n,t}&b_{n,t}\\c_{n,t}&d_{n,t}\end{pmatrix} \tag{7.45}$$

result from the local differential map of (q, p) under the action of a single kick. They are given in appendix B.7. As a remark, while both $\underline{M}_\gamma$ and $\underline{\tilde{M}}_\gamma$ are symplectic matrices, proof of the later is given in B.6, the ratio

$$\mathcal{D} = \frac{\widetilde{\mathcal{C}}}{\mathcal{C}} = \prod_{t=1}^{T} \prod_{n=1}^{N} (-4Jc_{n,t}) \tag{7.46}$$

reflects a form of absorption within the dual "dynamics".

In general the eigenvalues $\exp \Lambda_i, i = 1, \ldots, 2N$ of $\underline{M}_\gamma$ are not directly related to the eigenvalues $\exp \widetilde{\Lambda}_i, i = 1, \ldots, 2T$ of $\underline{\tilde{M}}_\gamma$. For instance, while most of the periodic orbits for $T=1$ have a mixed spectrum of eigenvalues Λ_i belonging to both elliptic and hyperbolic directions, their dual counterparts $\widetilde{\Lambda}_1, \widetilde{\Lambda}_2$ are mostly of the hyperbolic type such that $\widetilde{\Lambda}_i \in \mathbb{R}$. Nevertheless, as can be deduced immediately from (7.39), marginal eigenvalues play a special role. The vanishing of $\det(\mathbb{1} - \underline{M}_\gamma)$ implies that, in most cases, also $\det(\mathbb{1} - \underline{\tilde{M}}_\gamma)$ vanishes due to a dual marginal eigenvalue. However, in special cases also the absorption constant $\mathcal{D}$ may go to zero. This is exactly the case if at least one of the $c_{n,t}=0$, which requires that the corresponding spin is located on the $q=\pi/2-\alpha$ meridian.

For orbits of higher repetitions $r_\gamma^{(N)} > 1$, equivalently to the conventional case of $r_\gamma^{(T)} > 1$, $\underline{\tilde{M}}_\gamma$ can be taken in the corresponding power and thus the stability will depend on the multiples of $\widetilde{\Lambda}_i$. Orbits fully hyperbolic in the dual picture therefore decrease exponentially in stability A_γ with N. This might happen even in the case when $\underline{M}_\gamma$ has a number of elliptic directions, as the case $T=1$ nicely demonstrates.

7.4.2. Bifurcations

Above duality relation suggests that temporal dynamical phenomena associated with the symplectic map Φ might have spatial analogs, which can be studied with the help of the dual map $\tilde{\Phi}$ (or its linearization). Below we illustrate this point on the example of bifurcations of periodic orbits.

To illustrate the concept of a bifurcation we first give a well known example of a temporal pitchfork bifurcation for a T-periodc orbit γ, as displayed in figure 7.3 (left). To deepen our previous statements of section 2.3, under the change of the system parameters one of the eigenvalues of the monodromy matrix $\underline{M}_\gamma$ acquires the value 1. At this point γ changes its stability and another periodic orbit with the same stability as the original γ but a doubled prime period $2T$ splits of. In the higher dimensional cases such a bifurcation (generically) only changes the stability along one direction leaving the other ones unaffected. Due to the additional time reversal symmetry in our system, a slightly different scenario – a so called isochronous pitchfork bifurcation might occur, as well. Instead of a single periodic orbit with period $2T$ one obtains a

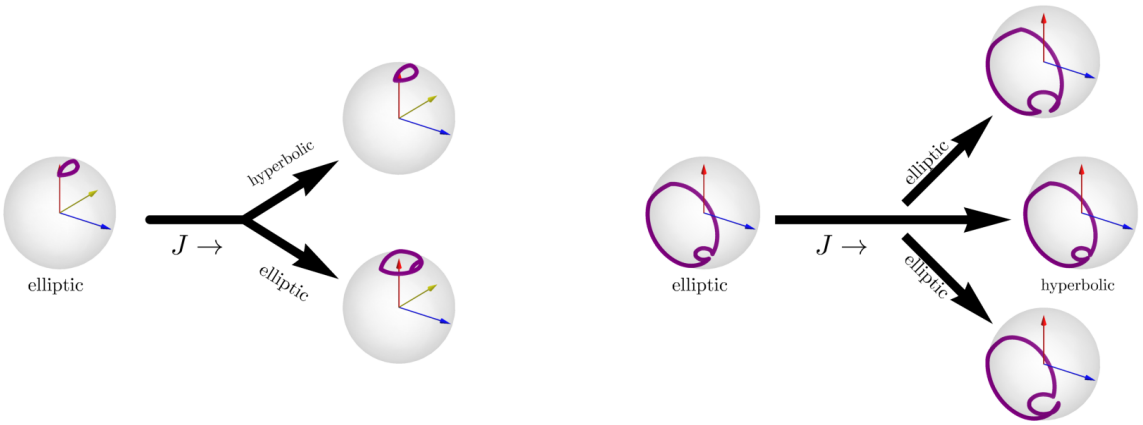

Fig. 7.3.: *Left hand side:* Structure of a pitchfork bifurcation of a $N=1$ orbit with $T_\gamma^{(P)}=1$. After the bifurcation a new orbit with doubled period is created (lower orbit). Parameters are given by $b^x=b^z=0.3$ and $J\approx 0.330+0.01-0.04$ left (-) and right (+) of the bifurcation point.
Right hand side: Structure of the (isochronous) pitchfork bifurcation for the $N=1$ orbit highlighted in figure 7.8. The shown orbits are given for $J=J_B\pm 0.02$ left (-) and right (+) of a bifurcation point chosen as $J_B=0.7$, $b^x\approx 0.94$ and $b^z\approx 0.90$.

pair of (time reversal) symmetry related orbits with prime period T, as displayed in figure 7.3 (right), compare [78]. The effect of this bifurcation on the semi-classical level is discussed in section 7.5.3. We should point out that this specific bifurcation, due to $T_\gamma^{(P)}=2$, has a more involved structure for $N>1$ as the two new orbits can be used interchangeably giving a binary alphabet for a family of 2^N identical orbits.

The most general case of a temporal bifurcation occurs when an elliptic eigenvalue of $\underline{M}_\gamma$ possesses a rational phase $\Lambda_i=2\pi ip/q$ for some integers q and p. This implies that the eigenvalue will be unity for the q-fold temporal repetition of the orbit. Passing this bifurcation threshold generically creates a new PO with an q-fold prime period qT. In the same spirit spatial bifurcations occur if one of the eigenvalues of the dual monodromy matrix $\underline{\tilde{M}}_\gamma$ carries such a rational phase. Under such a spatial bifurcation the original orbit γ, with the spatial prime period $N_\gamma^{(P)}$, changes its stability and q other periodic orbits with prime periods $qN_\gamma^{(P)}$ appear. They are related among one another by a translation of $N_\gamma^{(P)}$ spins in particle space. These new orbits can only exist in the larger system and from the perspective of the smaller system this type of bifurcation would go otherwise unnoticed. Concrete examples with $q=2,3$, respectively, are given in figure 7.4. In the latter case, $q=3$, the single particle orbit is fully hyperbolic for all system parameters in vicinity of the bifurcation point, but its repetition $r_\gamma^{(N)}=3$ possesses either additional elliptic or hyperbolic directions. These are interchanged with two pairs of either elliptic or hyperbolic directions of the longer orbit at the bifurcation point. As a remark, the $q=3$ case poses an exception as no new orbits are

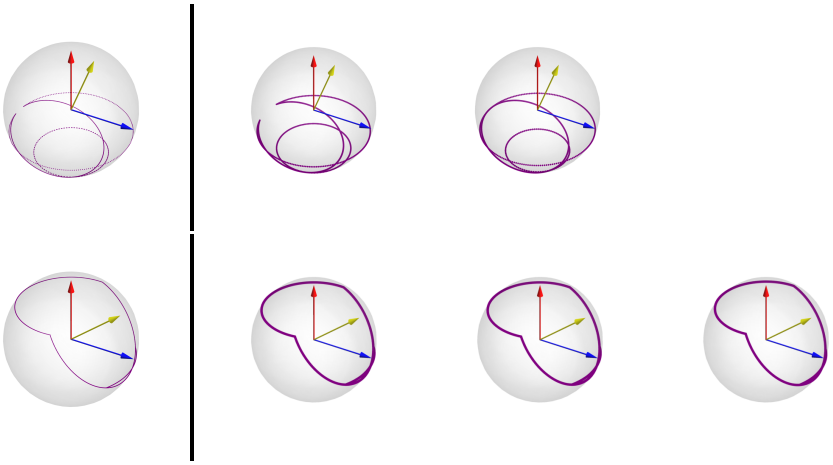

Fig. 7.4.: *Upper row:* Periodic orbit of the single particle system, $N_\gamma^{(P)} = 1$, $T_\gamma^{(P)} = 2$, to the left which undergoes a pitchfork bifurcation in particle space at $J \approx 2.235$, $b^x \approx 0.652$ and $b^z \approx 1.7332$. At this point the orbit on the right hand side and its twin, related by translation symmetry, are created.
Lower row: Periodic orbit of the single particle system, also for $N_\gamma^{(P)} = 1$, $T_\gamma^{(P)} = 2$, and an orbit of similar shape for $N_\gamma^{(P)} = 3$ which coincide for $J = 0.7$, $b^z = 0.9$ and $b^z = 1.005224$. This leads to the emergence of marginal stability as predicted by the eigenvalues of $\underline{\tilde{M}}_\gamma$. Orbits are shown for $b^z = 0.88$.

created, instead only stabilities are exchanged. This in exact correspondence to the predictions for bifurcations in the time domain. For the second example, $q = 2$, we find a (non-isochronous) pitchfork bifurcation. In this case a set of two new orbits emerges.

7.5. Action Spectrum

For quantum Hamiltonian systems the underlying classical POs can be revealed taking an appropriate Fourier transform of the spectral density with respect to an energy like parameter [68, 132–134]. For quantum maps, however, energy is not defined. Still, it is possible to extract classical POs out of traces of the quantum evolution taking a Fourier transform over the inverse of the effective Planck's constant, see *e.g.* [18, 38, 135]. The linear scaling with the spin quantum number j in the exponent of (7.13) makes it a good quantity for such a Fourier transformation. Employing this procedure we obtain

$$\begin{aligned} \rho(\mathcal{S}) &= \frac{1}{j_{\text{cut}}} \sum_{j=1}^{j_{\text{cut}}} \mathrm{e}^{-\mathrm{i}(j+1/2)\mathcal{S}} \operatorname{Tr} \hat{U}^T \\ &\sim \frac{1}{j_{\text{cut}}} \sum_{\gamma(T)} A_\gamma \, \delta_{j_{\text{cut}}}(\mathcal{S} - \mathcal{S}_\gamma) \,, \end{aligned} \tag{7.47}$$

where $\delta_{j_{\text{cut}}}$ stands for a periodized approximation of the δ-distribution with width $\sim \pi/j_{\text{cut}}$ and height j_{cut}. The cut-off j_{cut} is introduced in order to keep the dimension of $\hat{U}$, or more precisely $\tilde{W}$, numerically accessible. As $j_{\text{cut}} \to \infty$ the function $\rho(\mathcal{S})$ resolves the classical orbit actions $\mathcal{S}_\gamma$ for orbits of period T, up to a modulus of 2π. It is worth noting that for technical reasons the sum in (7.47) is restricted to integer values of j. The inclusion of half-integer j allows, in principle, the resolution of $\mathcal{S}_\gamma$ up to a modulus of 4π.

In this section we numerically study the action spectrum $\rho(\mathcal{S})$ for one and two time steps. To this end we first evaluate the spectrum of the dual operator $\tilde{W}$ for $T = 1, 2$ and then calculate $\operatorname{Tr} \hat{U}^T$ using the duality relation (5.15). As a result, we are able to obtain $\rho(\mathcal{S})$ for an arbitrarily large spin chain and some finite j_{cut}.

7.5.1. The Effect of Bifurcations

Recall that for isolated POs the prefactors A_γ are given by (2.19). Accordingly, if $\det(\underline{M}_\gamma - \mathbb{1}) \neq 0$ for all POs of period T the function $\rho(\mathcal{S})$ does not scale with j_{cut}. On the other hand, when a PO changes its stability type, one of the corresponding eigenvalues turns into $\Lambda_i = 0$. This immediately implies a divergence of (2.19). In this case the linearized dynamics in terms of $\underline{M}_\gamma$ is insufficient to describe the weight of an orbit to the sum in (7.13). Instead, higher orders have to be taken into account in the form of uniform approximations [77, 79]. The adjusted A_γ has the scaling j^α, where the exponent $\alpha > 0$ depends on the type of bifurcation, compare section 2.3. To demonstrate how bifurcations affect the action spectrum $\rho(\mathcal{S})$ we show, as an example, the result for the (isochronous) pitchfork bifurcation discussed in the previous section on the left hand side of figure 7.5. The algebraic scaling $\alpha = 1/4$ is clearly observed. In addition, we provide a slightly detuned system which shows at first algebraic growth and for larger j_{cut} tends towards saturation.

So far, studies of the bifurcation effects on the quantum spectrum have been mostly restricted to systems with a single degree of freedom [77–80]. While an exact bifurcation is a singular event nearly bifurcating orbits with $\Lambda_i \approx 1$ are generic in many-body systems with mixed dynamics. In general, for N-body systems the number of elliptic directions increases with the number of degrees of freedom N. Assuming that phases of the corresponding (elliptic) eigenvalues of $\underline{M}_\gamma$ are distributed uniformly, the probability to come close to one should grow with N. While one might argue that in the limit $j \to \infty$ equation (2.19) must be recovered for such nearly bifurcating orbits, this is only true for the pure semi-classical limit with fixed N. In practice this is never the case as j is necessarily finite. In other words, for a limit where both N and j tend to infinity the prefactors A_γ (resp. $\rho(\mathcal{S})$) might still possess a non trivial scaling $j^{\alpha(N)}$ due to the presence of quasi-marginal directions.

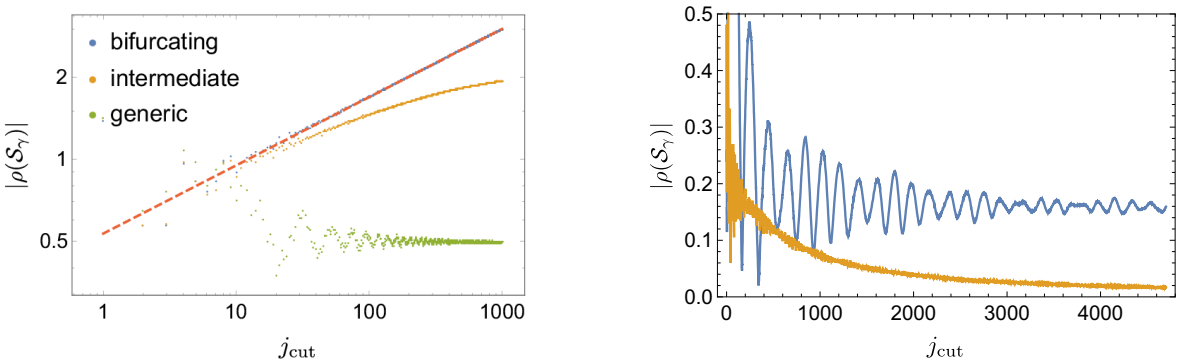

Fig. 7.5.: *Left hand side:* Scaling of the action spectrum peak height $|\rho(\mathcal{S}_\gamma)|$ for $N=1, T=2$ over the cut-off parameter j_{cut}. Shown are three cases, which feature an orbit undergoing an (isochronous) pitchfork bifurcating ($J=0.7$, $b^x \approx 0.94$ and $b^z \approx 0.90$, compare also figure 7.3), the same orbit with slightly detuned couplings ($J=0.68$) and a generic (*i.e.* isolated) orbit for the detuned parameters.
Right hand side: Dependence of the height of $|\rho(\mathcal{S}_\gamma)|$ on the cut-off parameter j_{cut} for two selected orbits of the action spectrum for $N=7$ particles given in figure 7.6. The selected orbit shown in blue is the largest one in figure 7.6 at $\mathcal{S}_\gamma \approx 5.77$, which also shows the strongest deviations from the semi-classical prediction. The other one (orange) is a small ghost orbit at $\mathcal{S}_\gamma \approx 2.75$ for the same parameters. While the first one saturates, for large j_{cut}, to a limiting value, the ghost decays exponentially.

7.5.2. Single Time Step

In the case of $T=1$ the spectrum of $\tilde{W}$ can be easily calculated for a relatively large cut-off parameter $j_{\text{cut}} \sim 10^4$, while the number of POs grows weaker with N in comparison to longer times. This allows a good resolution of the action spectrum for moderate spin chain lengths and isolated POs. Figure 7.6 shows the (absolute) action spectrum $|\rho(S)|$, see (7.47), for identical parameters but different numbers of spins. The upper row depicts numerical calculations based on the spectrum of the dual quantum operators and colored bars therein mark the positions of classical POs. For comparison the lower row contains a semi-classical approximation for which we use the right hand side of (7.13) instead of the actual traces in (7.47). In contrast to the upper row this one relies solely on classical information – actions $\mathcal{S}_\gamma$ of the POs and their stabilities A_γ provided by equation (2.19).

$\boldsymbol{N=1}$ — The left panels shows the single particle case of the Kicked Top, which features only two periodic orbits for such short times. The broader peak to the right is a ghost orbit (emerging for larger J) which is naturally not reproduced in the lower panel. Otherwise the agreement is excellent.

$\boldsymbol{N=7}$ — The middle panel shows $|\rho(\mathcal{S})|$ for $N=7$ spins, containing significantly more orbits with very good agreement between the classical positions of their actions

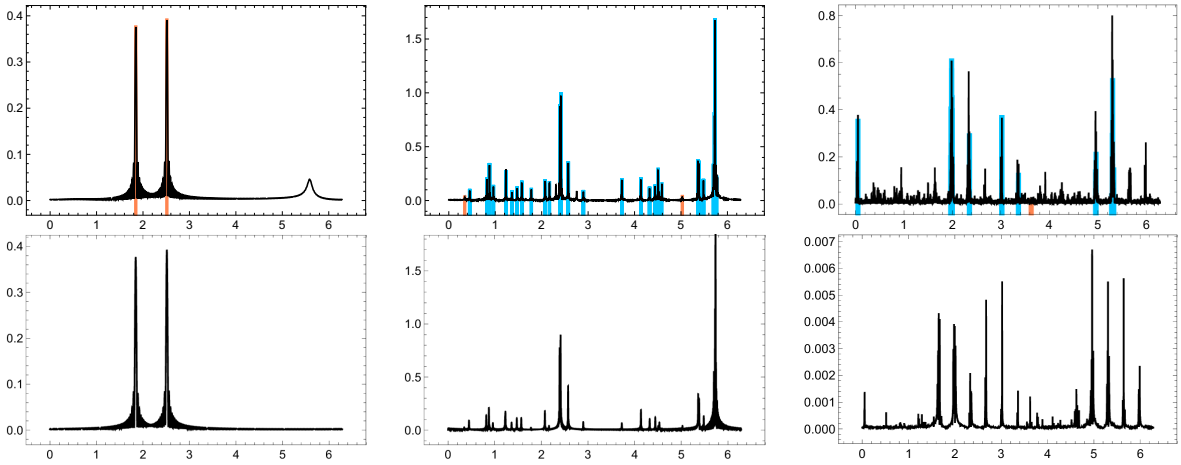

Fig. 7.6.: Absolute value $|\rho(\mathcal{S})|$ of the approximate action spectrum, equation (7.47), over $\mathcal{S}$ for different particle numbers, $N=1,7,19$ (from left to right), and a single time step. The upper row corresponds to the actual quantum data while in the lower row traces are replaced by a semi-classical approximation. System parameters are the same for all panels, $J=0.7$ and $b^x=b^z=0.9$, but the cut-off parameter is chosen differently to resolve larger particle numbers, $j_{\text{cut}}=200, 801, 4700$ (left to right). Colored bars in the upper row correspond to the position of classical orbits, the color specifies the spatial period: $N_\gamma^{(P)}=1$ (orange), $N_\gamma^{(P)}=N$ (blue).

and the corresponding peaks of $|\rho(S)|$. As N is prime, these orbits necessarily possess either $N_\gamma^{(P)}=1$ or $N_\gamma^{(P)}=7$ marked by different colors in figure 7.6. Naturally, POs with $N_\gamma^{(P)}=1$ are just repetitions of POs encountered in the $N=1$ case.

Comparison to the semi-classical approximation shows good agreement for approximately half of the POs, but the others exhibit some deviations in height due to the proliferating bifurcations. This is most apparent for the highest peak at $\mathcal{S}_\gamma \approx 5.77$ (whose height is deliberately cut in the lower panel). The particular PO contains 6 elliptic and 8 hyperbolic directions, with one of the stability eigenvalues being $\Lambda_i \approx 0.86$ bringing it sufficiently close to a bifurcation. To check it in more details we take a look at the peak heights as a function of j_{cut}, see the right hand side of figure 7.5. Indeed, the function shows strong oscillations due to the existence of accompanying orbits with close actions and saturation is achieved only for considerably high values of j_{cut}.

$\boldsymbol{N=19}$ — For the right hand panels in figure 7.6 the number of spins is increased further to $N=19$. In this case we are no longer able to resolve individual orbits despite an increased j_{cut}. The semi-classical approximation, based on ~ 2000 found orbits, resembles the actual function $|\rho(S)|$ only for some of the largest peaks. Given the huge amount of underlying POs the clear structure of the action spectrum with only a few dominant peaks is quite remarkable. The positions of these peaks, indeed, correspond to the POs with the largest prefactors A_γ. In figure 7.6 we mark only orbits γ which

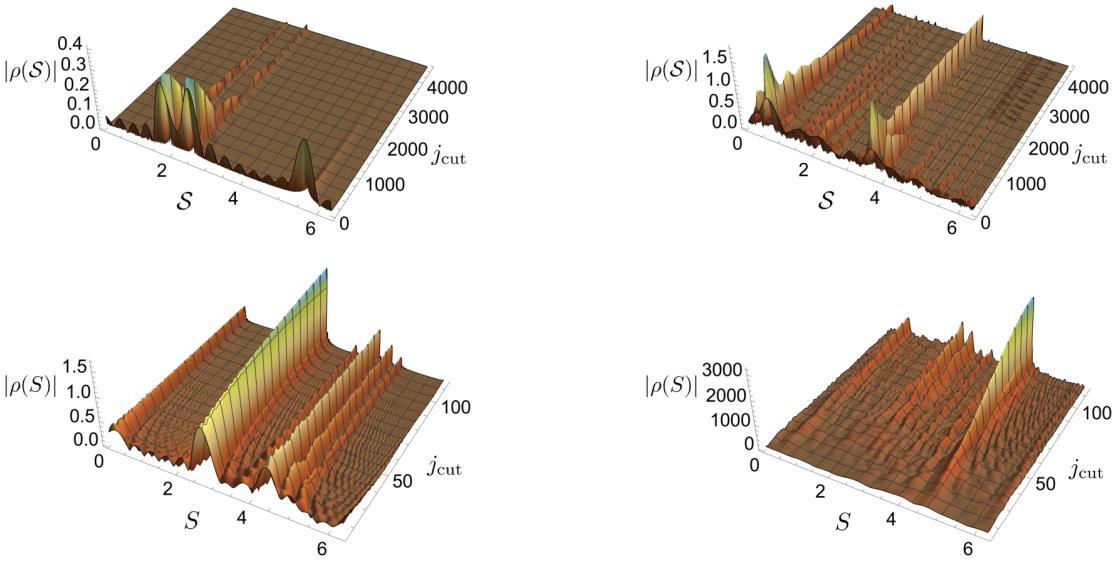

Fig. 7.7.: Approximate action spectrum plotted as function of the action $\mathcal{S}$ and the cut-off parameter j_{cut}. Upper row corresponds to $T=1$, lower to $T=2$, while the left column features $N=1$ and the right $N=10$. Model parameters are given by $J=0.7$ and $b^x=b^z=0.9$. As j_{cut} is necessarily integer, the graphic shows an interpolation.

surpass a fixed threshold, $|\det(\underline{M}_\gamma - \mathbb{1})|^{-1/2} > 10^{-3}$. As one can see, their positions coincide with the largest spikes of $|\rho(S)|$.

7.5.3. Two Time Steps

For two time steps ($T=2$) the number of POs is substantially larger in comparison to the $T=1$ case with the same parameters. Furthermore, many of them are close to bifurcations, making a semi-classical reconstruction of the spectrum even harder. In addition, significantly smaller achievable values of j_{cut} limit our resolution. We illustrate this with a direct comparison of the $T=1$ and $T=2$ cases in figure 7.7 where we depict the action spectrum using j_{cut} as additional variable. For the $T=1$ cases in the upper row we reach sufficiently high values of j_{cut} to observe both the initial interference of nearby orbits and saturation of $|\rho(S_\gamma)|$ for larger j_{cut}. As stated previously the $N=1$ case (left) also contains a separated ghost orbit whose decay becomes apparent in this visualization. For the $T=2$ case it is no longer feasible to resolve such scales and we, instead, only observe the initial growth associated with close to bifurcation orbits.

In contrast to the previous subsection we therefore omit the semi-classical reconstruction but provide, in figure 7.8, the numerically calculated action spectra for different particle numbers and identical system parameters. Remarkably, for chain

lengths divisible by 4 the action spectrum $\rho(\mathcal{S})$ turns out to be strongly dominated by the PO manifolds. This means that for $N = 4k, k \in \mathbb{N}$ one observes only few strong peaks exactly at the positions of the PO manifolds actions (7.24) while all other POs are essentially suppressed. Furthermore, for these length sequences $\rho(\mathcal{S})$ exhibits a particularly large magnitude.

As one can check, the height of the peaks at $\mathcal{S}_{\text{man}}$ follows a scaling law,

$$|\rho(\mathcal{S}_{\text{man}})| \sim (j_{\text{cut}})^{\alpha(N)} \qquad \alpha(N) \sim \alpha_0 N\,, \tag{7.48}$$

with a constant α_0 only weakly dependent on the system parameters (for further details on its value see section 7.6.1). This scaling is shown in figure 7.9 in comparison to the integrable case, where $\alpha(N) = N/2$. Clearly visible is a strong enhancement whenever the particle number is $N=4k$, *i.e.* when the PO manifolds appear. However, a linear growth of scaling with N is a general trend, independent of whether the particle number is a multiple of four or not. Compare *e.g.* the general magnitude for the $N=7$ case in figure 7.8 to the case of $N=9$, in both cases the PO manifold is absent. In contrast, $T=1$ shows no scaling of α with N. A slight, visible decay for this case in figure 7.9 can be attributed to strong interference between neighboring orbits, which influences the actual results.

While the scaling (7.48) in the integrable system is easily understood in terms of the classical N dimensional invariant tori, recall the growth of $A_\gamma \sim j^{N/2}$, the increase of α with N in the case of the four-dimensional PO manifolds seems to be, at first, a perplexing phenomenon, given that the number of their marginal directions does not grow with N. In the strict semi-classical limit $j \to \infty$ with fixed N the existence of four marginal directions would imply only the constant scaling $\alpha(N)=1$. The anomalously large scaling in the double limit case can be attributed to the increase of quasi-marginal directions for which the corresponding eigenvalues of the stability matrix $\underline{M}_\gamma$ are close to one. A hand-waving, qualitative explanation of (7.48) can be attempted in terms of counting such quasi-marginal directions. As numerics shows, their numbers do indeed grow with N, but correct accounting of such directions is already a challenge for single particle systems, see [79, 80]. Taking into account contributions of all nearly bifurcating orbits for a large N seems to be an extremely difficult task and we avoid this path in what follows. Rather, we will provide an explanation for (7.48) through the study of spectral properties of the dual operator $\tilde{W}$.

7.6. Spectrum of the Dual Operator

The question of the anomalously large spectral fluctuations associated with the PO manifolds, specifically its scaling with N as observed in the last section, can be addressed in terms of the of the dual operator spectrum. For large N the traces of $\tilde{W}^N$ are

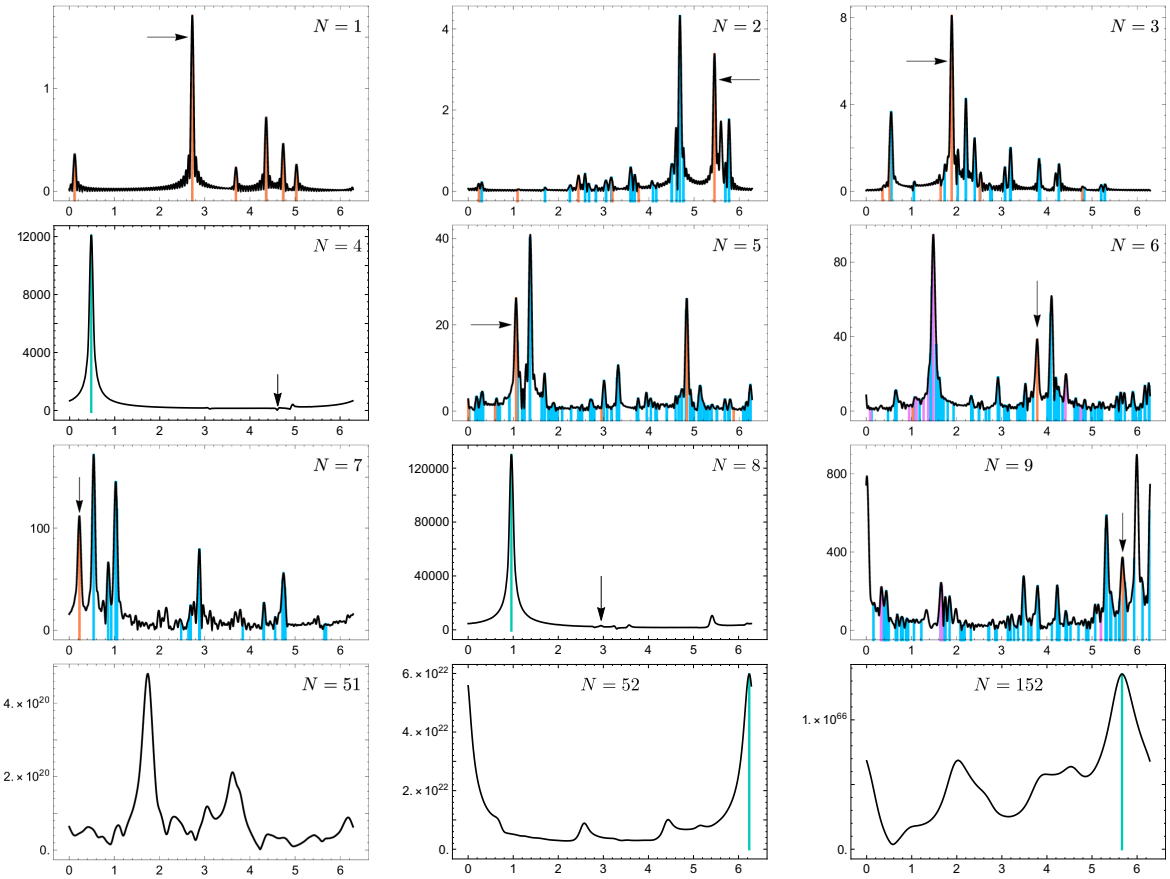

Fig. 7.8.: Absolute value $|\rho(\mathcal{S})|$ of the approximate action spectrum, equation (7.47), over $\mathcal{S}$ for $T=2$ time steps using $j_{\text{cut}}=114$. The system parameters are $J=0.7$ and $b^x=b^z=0.9$, only the number N of spins is varied. Coloured lines indicate classical orbit positions. The color corresponds to the primitive period: $N_\gamma^{(P)}=1$ (orange), $N_\gamma^{(P)}=N$ (blue) and purple otherwise. Green lines correspond to $N\mathcal{S}_{\text{man}} \mod 2\pi$, see equation (7.24), indicative of the PO manifolds position. In the cases of $N=4$ and $N\geq 6$ only selected POs are shown, see text. The arrows indicate the position of an $N_\gamma^{(P)}=1$ orbit close to an isochronous pitchfork bifurcation, compare figure 7.5. Its impact can be observed up to $N\approx 19$

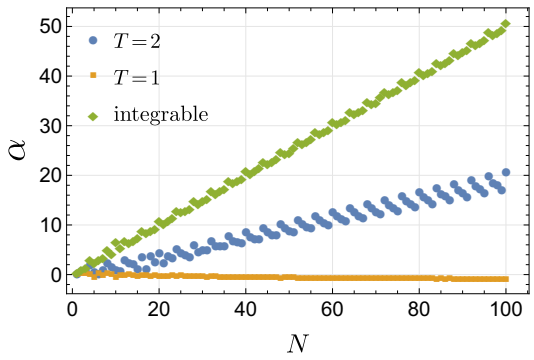

Fig. 7.9.: Estimated scaling exponent α of the largest peak in the action spectrum for various particle numbers and fixed system parameter $J=0.7$ and $b^x=b^z=0.9$ for $T=1,2$. For numerical fitting the heights in the range $j_{\text{cut}}=95$ to 114 (for $T=2$) and $j_{\text{cut}}=200$ to 400 (for $T=1$ and integrable) are taken into account. For $T=1$ a close inspection shows that the value of α is not yet fully saturated but instead slightly negative. For comparison we show the integrable case where we set $b^x=0$.

dominated by their largest eigenvalues,

$$\operatorname{Tr}\hat{U}^T = \operatorname{Tr}\tilde{W}^N = \sum_l \tilde{\lambda}_l^N (1 + O(e^{-\delta N})), \qquad \delta > 0\,, \tag{7.49}$$

where the sum can be restricted to several eigenvalues $\tilde{\lambda}_l$ with the maximal absolute value. The validity of this approximation greatly depends on the magnitude of N. In figure 7.10 we depict both the actual action spectrum (blue curve) and an approximate result (orange), for which we leave in the sum (7.49) only the largest eigenvalue. The agreement between the two curves greatly improves with the number of spins N. Besides N also j plays a role as it governs the dimension of $\tilde{W}$ and therefore the gap δ between the largest eigenvalues and the remaining spectrum.

7.6.1. Numerical Findings

As has been explained above, it is of crucial importance to understand how the largest eigenvalues of $\tilde{W}$ depend on j in the semi-classical limit $j \to \infty$. Below we provide the results of a numerical study of the dual operator spectrum and give their explanations based on a semi-classical theory in the next section.

For only a single time step $T = 1$ the spectrum $\{\tilde{\lambda}_i | i = 1, \ldots, 2j+1\}$ of $\tilde{W}$ is uniformly distributed in the angular direction, see figure 7.11 for a generic example. As the operator is non unitary, the eigenvalues are not restricted to the unit circle and, in fact, many of them reside close to the origin indicating the non-unitary nature of the dual evolution. This outcome is quite similar to what we observed previously for $j=1/2$ in section 6.1.3. For two time steps, $T = 2$, the dual spectrum $\{\tilde{\lambda}_i | i = 1, \ldots, (2j+1)^2\}$

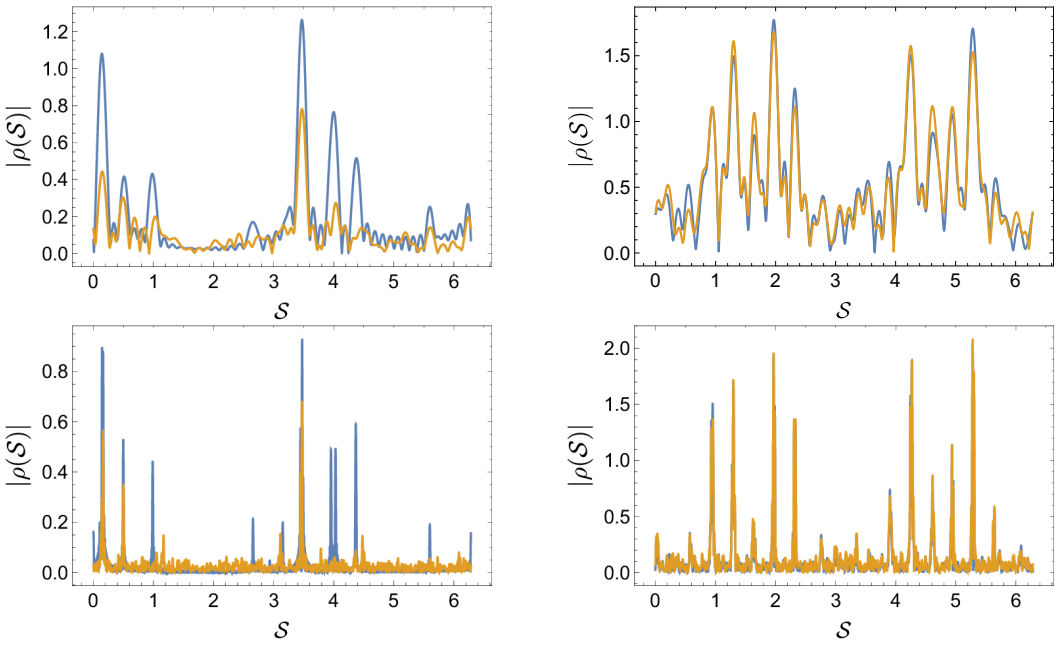

Fig. 7.10.: Comparison between the single time step action spectrum $|\rho(S)|$ (blue curves) and an approximated variant using only the largest eigenvalue in (7.49) instead of the full traces. The four panels correspond to $N=5$ (left) and $N=20$ (right), respectively. The upper row uses a low cut-off, $j_{\text{cut}}=50$, the lower one features $j_{\text{cut}}=500$. Model parameters are given by $J=0.7$ and $b^x=b^z=0.9$.

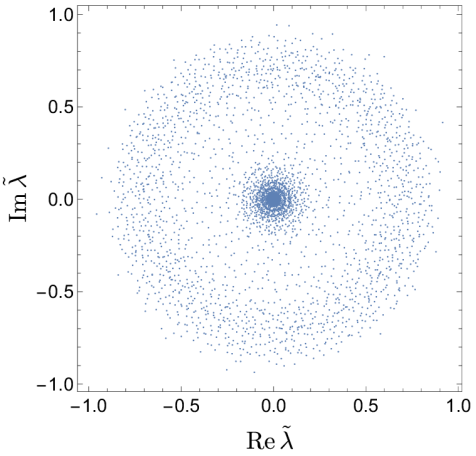

Fig. 7.11.: Eigenvalue spectrum $\tilde{\lambda}$ of $\tilde{W}$ for $T=1$ in the complex plane. System parameters are chosen as $J=0.7$ and $b^x=b^z=0.9$ with $j_{\text{cut}}=4700$.

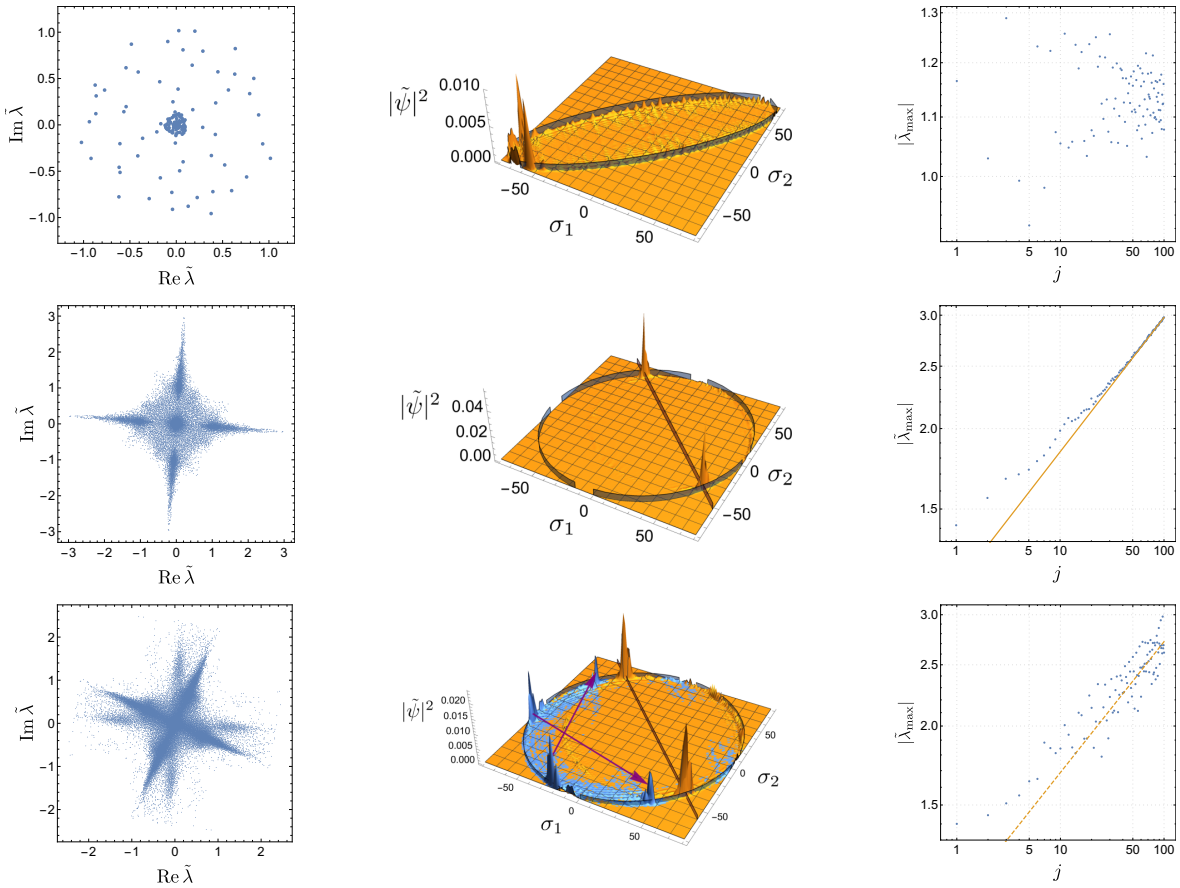

Fig. 7.12.: Shown are: the spectrum of the dual operator for $T = 2$ and $j = 100$ in the complex plane (left column), the scaling of its largest eigenvalue in dependence of j with a numerical fit of α_0 where applicable (right column) and the eigenvector corresponding to the largest eigenvalue ($j = 80$, middle column). The blue rim corresponds to the classically allowed region's boundary, see (7.56). The parameters are chosen as $J = 0.2$ and $b^x = b^z = 0.3$ (first row) where no manifold is present. In the second row $J = 0.6$ with $b^x = b^z = 0.9$ represents the single manifold regime leading to $\alpha_0 \approx 0.21$. The purple bar (middle panel) is the solution to $\sigma_1 + \sigma_2 = g$ where g is given by (7.59) for $m = 0$. In the last row $J = 0.8$, $b^x = b^z = 0.9$ yields several manifolds. The scaling lies in between $0.17 \leq \alpha_0 \leq 0.23$, the dashed line corresponds to $\alpha_0 \approx 0.21$. The middle figure, in this case, shows two different eigenvectors, blue and orange, that correspond to the largest eigenvectors of two different crosses shown on the left. The purple arrows represent the semi-classical predictions for the localization centers of the first eigenvector (blue). They correspond to $m_1 = 0$, $m_2 = -1$ and vice versa, see appendix B.5 for details. The intersection of the bar with the ellipse boundary indicates localization centers of the second eigenvector (orange, $m_1 = m_2 = 0$).

has a similar rotationally invariant distribution in the regime where no PO manifolds exist, see figure 7.12. In sharp contrast, a pronounced structure emerges whenever PO manifolds are present. To illustrate this, figure 7.12 shows the dual spectrum in the regime where either only one or several PO manifolds exist. The spectral distribution contains remarkable cross-like shapes indicating an approximate four-fold rotational symmetry, which becomes more and more pronounced for the largest eigenvalues as $j \to \infty$. This symmetry singles out sequences $N = 4k$, where, according to (7.49), the sum of the largest eigenvalues adds up coherently. On the contrary, for $N \neq 4k$ the sum of the largest eigenvalues vanishes to the leading order in j, thus significantly reducing the magnitude of the spectral fluctuations. To make a quantitative prediction it is, therefore, natural to look at the largest $\tilde{\lambda}_i$ as functions of j. Focusing on the regime where only one PO manifold exists, we find that the phases of the four largest dual eigenvalues are given by

$$\arg \tilde{\lambda}_{\max,l} = (j+1/2)\mathcal{S}_{\text{man}} + \frac{\pi l}{2} + O(1/j) \qquad l \in \{1,2,3,4\}\,. \tag{7.50}$$

As predicted, in the cases $N=4k$ the $\pi l/2$ parts in the phase cancel under summation of the eigenvalues. Remarkably, to the leading order in j, the phases are determined by the prime action $\mathcal{S}_{\text{man}}$ of the PO manifold, (7.24). Such a connection is reminiscent of the Bohr-Sommerfeld quantisation rule for the spectrum of integrable Hamiltonian systems. Furthermore, the absolute values of the largest eigenvalues scale algebraically with j,

$$|\tilde{\lambda}_{\max}| \propto j^{\alpha_0}\big(1 + O(1/j)\big)\,. \tag{7.51}$$

This explains the linear dependence of $\alpha(N)$ on N, *i.e.* $\alpha(N) \sim \alpha_0 N$ in (7.48). The same scaling carries over to the traces $\operatorname{Tr}\tilde{W}^N$ even for $N \neq 4k$, where a similar linear growth of α with N is observed, but with a constant negative offset, see figure 7.9.

In the regime of a single PO manifold, the contribution of the four largest eigenvalues is sufficient to get the total phase of the trace for large powers in N, improving with increased j, see figure 7.13. Therefore, for $T = 2$ the whole essential information about the spectral fluctuations in the system is stored in two parameters: $\mathcal{S}_{\text{man}}$ and α_0. Additional PO manifolds contribute other quadruples of eigenvalues $\tilde{\lambda}^{(\ell)}_{\max,l}$ with a similar scaling of the absolute value $|\tilde{\lambda}^{(\ell)}_{\max,l}| = C_\ell j^{\alpha_0^{(\ell)}}$, but (possibly) different phases $(j+1/2)N\mathcal{S}^{(\ell)}_{\text{man}} + l\pi/2$, $l = 1,\ldots,4$, where $\mathcal{S}^{(\ell)}_{\text{man}}$ is the action of the respective PO manifold. As a result, the total contribution in the traces of the evolution operator for $N = 4k$ is given by:

$$\operatorname{Tr}\hat{U}^2 = 4\sum_\ell C_\ell\, j^{N\alpha_0^{(\ell)}} e^{i(j+1/2)N\mathcal{S}^{(\ell)}_{\text{man}}}\,(1 + O(1/j))\,, \tag{7.52}$$

where the sum is over the distinct PO manifolds.

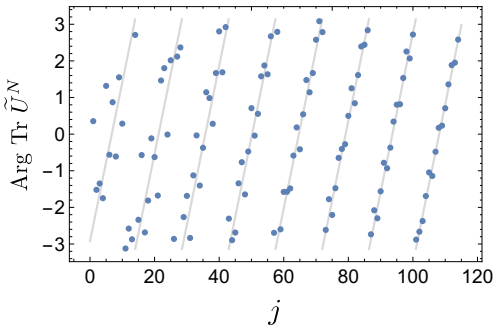

Fig. 7.13.: Phase of the trace of the dual operator as a function of the spin quantum numbers j for $T=2$ and $N=56$. The model parameters are $J=0.7$, $b^x=b^z=0.9$. The (rescaled) contribution of the manifold's action, $(j+1/2)\mathcal{S}_{\text{man}} \mod 2\pi$ is shown as the gray line. As can be observed, the agreement is more accurate for larger j.

A straightforward inspection of the eigenvectors corresponding to the maximal eigenvalues of $\tilde{W}$ reveals their remarkable localization properties, see figure 7.12. These eigenvectors comprise two parts,

$$\tilde{\psi} = \tilde{\psi}_q + \tilde{\psi}_p \,, \tag{7.53}$$

of which $\tilde{\psi}_q$ is sharply localized in the $|\sigma_1\rangle \otimes |\sigma_2\rangle$ basis while $\tilde{\psi}_p$ is localized in the momentum basis $|\bar{\sigma}_1\rangle \otimes |\bar{\sigma}_2\rangle$,

$$|\bar{\sigma}\rangle = \frac{1}{\sqrt{2j+1}} \sum_{\sigma=1}^{2j+1} e^{i2\pi\sigma\bar{\sigma}/(2j+1)} |\sigma\rangle \,, \tag{7.54}$$

obtained by Fourier transformation.

7.6.2. Semi-Classical Theory for Two Time-Steps

To understand the form of $\tilde{\lambda}_{\text{max},l}$ and the localization properties of the correponding eigenvectors, let us first recall the product structure of the dual operator $\tilde{W}_I \tilde{W}_K$. For $V=0$ the form (7.28) of the kick part $\tilde{W}_K$ is reminiscent of the kernel of the Fourier transformation, such that the correspondence becomes exact if $J=\pi/4$. The action of this part on a coherent state, localized in both momenta and coordinates, can be interpreted as an exchange of position and momenta values. The interaction part $\tilde{W}_I$, equation (7.31), is instead given by a product of transition elements of rotations:

$$\langle\sigma_1\sigma_2|\tilde{W}_I|\sigma_1\sigma_2\rangle = \langle\sigma_1|\mathrm{e}^{-2\mathrm{i}\,\vec{b}\cdot\hat{\vec{S}}}\,|\sigma_2\rangle\langle\sigma_2|\mathrm{e}^{-2\mathrm{i}\,\vec{b}\cdot\hat{\vec{S}}}\,|\sigma_1\rangle = \mathrm{e}^{-\mathrm{i}(\sigma_1+\sigma_2)(\alpha+\gamma-\pi)}(d^j_{\sigma_1\sigma_2}(\beta))^2 \,. \tag{7.55}$$

Conveniently, the uniform semi-classical limit of $d^j_{\sigma\,\sigma'}$ is well known [129]. When $j\to\infty$, the function $d^j_{\sigma\,\sigma'}$ is supported within the elliptic region,

$$\sigma'^2 + \sigma^2 - 2\sigma'\sigma\cos\beta \le (j+1/2)^2\sin^2\beta \,, \tag{7.56}$$

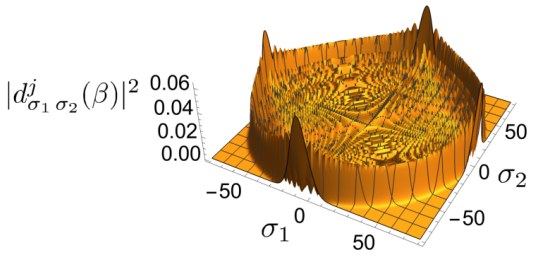

Fig. 7.14.: Absolute square of the Wigner small d-matrix $d^j_{\sigma_1\,\sigma_2}(\beta)$ for an angle $\beta \approx 1.48$ ($b^x = b^z = 0.9$) and $j{=}80$ as a function of σ_1, σ_2. The function is semi-classically supported in the elliptic region (7.56) and decays exponentially outside.

where it scales as $d^j_{\sigma\,\sigma'} \sim j^{-1/2}$ at a finite distance from the boundary and exponentially decays outside of the region (7.56), see figure 7.14. In the semi-classical limit any eigenvector of the dual matrix $\tilde{W}$ must, therefore, reside in the classically allowed region given by (7.56). The largest values of $d^j_{\sigma\,\sigma'}$ are attained along the ellipse boundary. Here, one generically finds $d^j_{\sigma\,\sigma'} \sim j^{-1/3}$ while in the vicinity of the four tangent points of the boundary, where in addition either σ or σ' take on values of $\pm j$, the scaling is $d^j_{\sigma\,\sigma'} \sim j^{-1/4}$. As we show below, such enhanced scaling at the boundary of (7.56) is responsible for large spectral fluctuations in the model at $T = 2$.

To analyze the spectrum of $\tilde{W}$ it turns out to be rather instructive to treat its second power, which can be represented as the product

$$\tilde{W}^2 = \tilde{W}_I\,\tilde{W}_0 \tag{7.57}$$

of the diagonal matrix $\tilde{W}_I$ and an "almost permutation" $\tilde{W}_0 = \tilde{W}_K\tilde{W}_I\tilde{W}_K$. More specifically, we show in appendix B.5 that, for the regime where only a single PO manifold exists, the second factor can be split into the product of two matrices, $\tilde{W}_0 = (2j+1)\tilde{P}\tilde{G}$, where $\tilde{P}$ is the following truncated permutation,

$$\langle\sigma_1\sigma_2|\tilde{P}|\sigma_1'\sigma_2'\rangle = \delta_{\sigma_1+\sigma_1',g_1}\,\delta_{\sigma_2+\sigma_2',g_2}\,, \tag{7.58}$$

and $\tilde{G}$ is a band diagonal matrix whose elements are of order 1 near the diagonal and scale as j^{-1} away from it. Here, the constants g_1, g_2 are given by

$$g_i = \lfloor\mathcal{G}_i\rfloor\,, \quad \mathcal{G}_i = (2j+1)\Big(\pi(1+2m_i) - 2\gamma\Big)/8J\,, \qquad i \in \{1,2\}, \tag{7.59}$$

with m_i's being integers such that $-2j \le g_i \le 2j$ holds. In the regime of only a single PO manifold the last condition determines m_i uniquely, *i.e.* $m_i = m$, $g_i = g$, $\mathcal{G}_i = \mathcal{G}$ for $i = 1, 2$. For the sake of simplicity of exposition we focus below on this particular case and later briefly comment on the extension of the results to the regimes where multiple PO manifolds exist.

To simplify the problem further we substitute $\tilde{G}$ with the unity matrix and consider the spectrum of $(2j+1)\tilde{W}_I\tilde{P}$ instead. Recalling the diagonal structure of $\tilde{W}_I$ it is straightforward to see that the eigenvectors of $(2j+1)\tilde{W}_I\tilde{P}$ take on a simple form:

$$\psi_{(\sigma_1,\sigma_2)} = C_1|\sigma_1,\sigma_2\rangle \pm C_2|g-\sigma_1,g-\sigma_2\rangle, \tag{7.60}$$

with the corresponding eigenvalues $\Omega_{(\sigma_1,\sigma_2)}$ given by

$$\frac{\Omega_{(\sigma_1,\sigma_2)}}{2j+1} = \pm\left(\langle\sigma_1,\sigma_2|\tilde{W}_I|\sigma_1,\sigma_2\rangle\langle g-\sigma_1,g-\sigma_2|\tilde{W}_I|g-\sigma_1,g-\sigma_2\rangle\right)^{1/2}. \tag{7.61}$$

This in turn can be written down in terms of Wigner's d-functions as

$$\Omega_{(\sigma_1,\sigma_2)} = \pm e^{-\mathrm{i}(2\gamma-\pi)g}(2j+1)d^j_{\sigma_2,\sigma_1}(\beta)\, d^j_{g-\sigma_2,g-\sigma_1}(\beta), \tag{7.62}$$

where we have explicitly separated the complex phase from the amplitude. Having at hand the approximate spectrum (7.60, 7.62) of the operator $\tilde{W}^2$ we can straightforwardly write down the corresponding eigenvalues and eigenvectors for $\tilde{W}$,

$$\psi \approx \psi_{(\sigma_1,\sigma_2)} \pm \Omega^{-1/2}_{(\sigma_1,\sigma_2)}\tilde{W}\psi_{(\sigma_1,\sigma_2)}, \qquad \tilde{\lambda} \approx \pm\Omega^{1/2}_{(\sigma_1,\sigma_2)}\,. \tag{7.63}$$

The first term $\psi_{(\sigma_1,\sigma_2)}$ is sharply localized in the (σ_1,σ_2) space. In contrast, the second term $\tilde{W}\psi_{(\sigma_1,\sigma_2)}$ is localized in momentum space $(\bar{\sigma}_1,\bar{\sigma}_2)$ due to the presence of the $\tilde{W}_K$ factor in $\tilde{W}$. This is in agreement with the previous numerical observation (7.53). It is important to emphasize that the actual eigenstates of $\tilde{W}^2$ have a finite support, while the eigenstates of the approximation $\tilde{W}_I\tilde{P}$ are point-like localized.

In order to find the largest eigenvalues of $\tilde{W}_I\tilde{P}$ (respectively $\tilde{W}$) we need to look for (σ_1,σ_2) such that $|\Omega_{(\sigma_1,\sigma_2)}|$ reaches its maximum value. By equation (7.62) this happens whenever both (σ_1,σ_2) and $(g-\sigma_1,g-\sigma_2)$ belong to the boundary of the ellipse (7.56). In other words, the localization points of the corresponding eigenvectors are located at the intersection points between the line $\sigma_1+\sigma_2=g$ and the ellipse boundary. Figure 7.12 shows such an eigenvector $\tilde{\psi}$ of $\tilde{W}$ corresponding to its largest eigenvalue as well as the respective line together with the ellipse boundary. As can be observed, the localization points of $\tilde{\psi}$ are, indeed, in a good agreement with the above prediction. By equations (7.62, 7.63) the phases of the four largest eigenvalues of $\tilde{W}$ are approximately given by

$$(2\gamma-\pi)\mathcal{G}/2 + \frac{l\pi}{2} = \left(2J\chi^2(j+1/2) + \frac{l\pi}{2}\right) \mod 2\pi, \quad l=1,2,3,4\,, \tag{7.64}$$

where on the left hand side we used (7.59) and the identity $2J\chi = (\pi/2-\gamma) \mod \pi$, see (7.8) in conjunction with (7.19). Taking into account expression (7.24) for the actions of the PO manifolds this immediately yields the previous empirically found

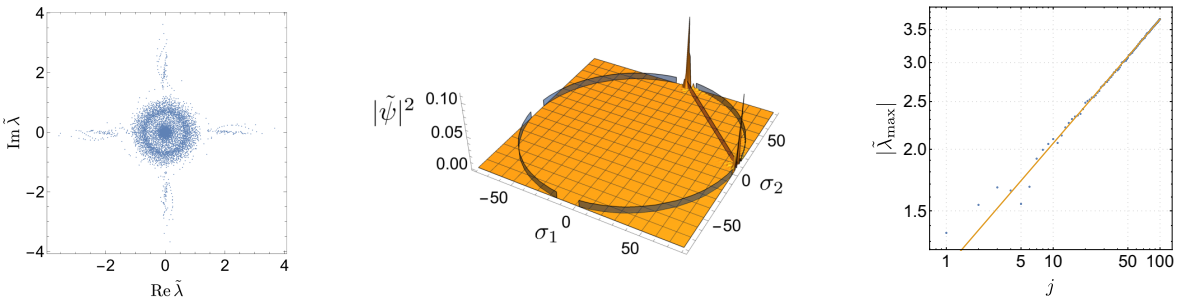

Fig. 7.15.: From left to right: spectrum of the dual operator ($j=100$), corresponding largest eigenvector ($j=80$, compare with figure 7.12) and scaling of the largest eigenvalue in dependence of j (numerical slope $\alpha_0=0.252\pm0.004$). Parameters are chosen as $T=2$, $J=0.45$, $b^x=0.789802$ and $b^z=0.483691$ such that the eigenvector localizes at the tangent points.

equation (7.50). The same approach can be used to evaluate the absolute value of $\tilde{\lambda}$. By equations (7.62, 7.63) we have $|\Omega_{(\sigma_1,\sigma_2)}|^{1/2} \sim j^{\alpha_0}$, with $\alpha_0 = 1/4$ if σ_1, σ_2 belongs to the tangent points of the ellipse and $\alpha_0 = 1/6$, otherwise. In figure 7.15 we check this prediction for specially tuned parameters such that the localization points are at the tangent points of the ellipse boundary. In this case the maximum possible scaling $\alpha_0 = 1/4$ is clearly observed, see the right hand side of figure 7.15. On the other hand, for generic parameters the scaling exponent is typically above the naive prediction 1/6. This is probably a consequence of the fact that some (small) portion of the eigenstate $\tilde{\psi}$ is always localized at the tangent points of the ellipse. A detailed investigation of this question would require taking into account the precise structure of $\tilde{G}$.

So far, we considered the case of the single manifold regime. In the parameter regime for multiple PO manifolds several combinations of different integers (m_1, m_2) exist, see appendix B.5, such that the corresponding g_1, g_2 satisfy the conditions $-2j \leq g_i \leq 2j$, $i = 1, 2$. As a result, the matrix $\hat{P}$ is provided by a sum of permutations – each one corresponds to some particular solution (m_1, m_2). To find the spectrum of eigenvalues of $\tilde{W}$ one follows the same procedure as in the single manifold case. Accordingly, for the largest eigenvalues of $\tilde{W}$ both points (σ_1, σ_2) and $(g_1 - \sigma_1, g_2 - \sigma_2)$ should belong to the boundary of the ellipse (7.56). This condition defines a pair of points on the ellipse boundary for each solution (m_1, m_2). All these points serve as centers of localization for the corresponding eigenvectors $\tilde{\psi}$, see figure 7.12.

7.7. Kicked Spin Chain Model for $V \neq 0$

So far, we considered a particular case of the kicked spin chain model as we set $V=0$ in the interaction part of the Hamiltonian (7.9). In this section we allow an arbitrary

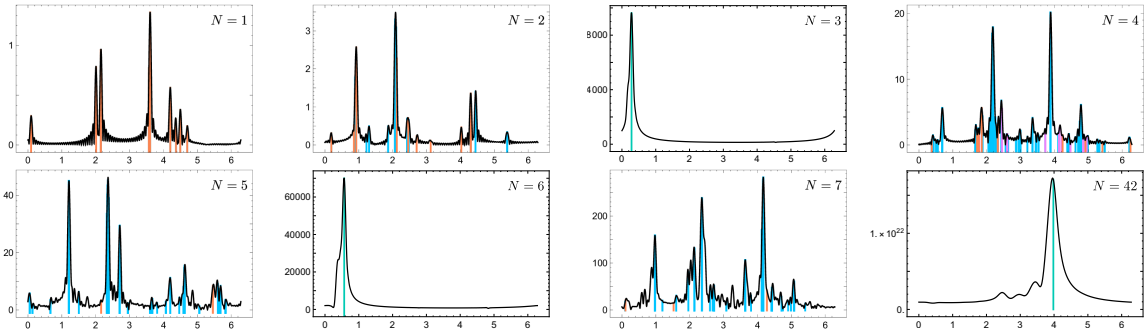

Fig. 7.16.: Absolute value $|\rho(\mathcal{S})|$ of the action spectrum for non-zero V over $\mathcal{S}$ for $T=2$ using $j_{\text{cut}}=100$. The particle number is indicated in the upper right corners. For $N=5,7$ only orbits with $A_\gamma > 0.25$ and $A_\gamma > 0.5$, respectively, are shown. The system parameters are $J=\sqrt{\pi}/3$, $V=J/2$ and $b^x=b^z=0.9$. For the color coding see figure 7.8.

strength V of the quadratic term. The kick part of the dual operator is now reminiscent of the kernel of the fractional Fourier transformation [136, 137]. As we show below, the core result of the previous sections – the emergence of the anomalously large spectral fluctuations for chain lengths $4k$, $k \in \mathbb{N}$ – reappears here again with a peculiar twist. For spin chains with lengths of $N = N_0 k$, $k \in \mathbb{N}$, the anomalously large fluctuations, dominated by PO manifolds, emerge when the ratio between interaction and torsion strength $\mu = V/J$ attains the following set of values:

$$\mu = -\cos\frac{2\pi n}{N_0} \qquad n \in \{1, 2, \ldots, N_0 - 1\}\,. \tag{7.65}$$

In other words, the model possesses large spectral fluctuations for spin chains of lengths $N = N_0 k$ with an arbitrary N_0 when the parameter μ is tuned according to (7.65). From this perspective the previous $V=0$ case is merely a special one corresponding to $N_0=4$. To illustrate this we show the action spectrum for $T = 2$ at a ratio of $\mu=1/2$ in figure 7.16. There, we find strong peaks for every $N=3k$. and the spectrum of the corresponding dual operator $\tilde{W}$ shows a three-fold symmetry, see figure 7.17. As one can observe, the absolute value of the largest eigenvalue scales algebraically with j, which explains the large spectral fluctuations in that case. Furthermore, the corresponding eigenvector looks structurally similar to what occurred in the $V=0$ case. As a second example, for $N_0=5$ and $\mu=(\sqrt{5}+1)/4$ one has large spectral fluctuations for all chains with $N=5k$, see figure 7.18. The dual operator in this case, figure 7.19, has a 5-fold symmetry.

To explain condition (7.65) we turn back to the classical dynamics of the model. Looking at POs of the system for $V \neq 0$ we again find

$$(\underline{R}_I(4J\chi_n)\underline{R}_{\vec{b}})^2 = \mathbb{1}, \qquad n = 1, \ldots N_0 \tag{7.66}$$

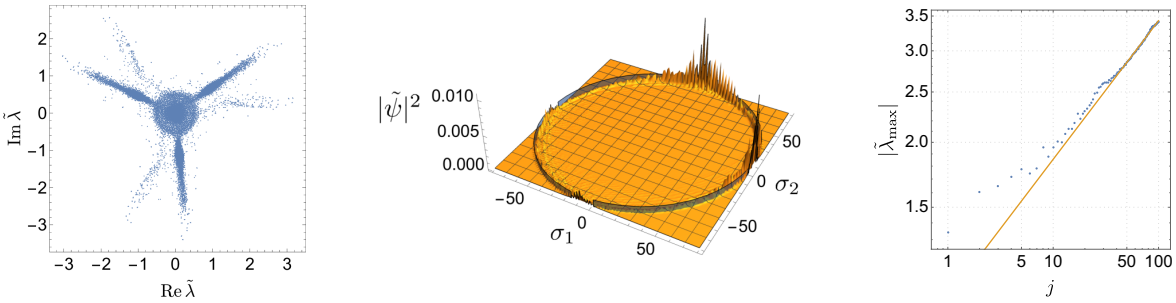

Fig. 7.17.: Spectrum of the $T=2$ dual operator containing a non-linear part for $j=100$ (left panel), corresponding largest eigenvector ($j=80$) (middle) and scaling of the largest eigenvalue in dependence of j (numerical slope $\alpha_0 \approx 0.167$). Parameters are chosen as $b^x=b^z=0.9$ and $J=\sqrt{\pi}/3$, $V=\sqrt{\pi}/6$ such that $\mu=1/2$ and $N_0=3$.

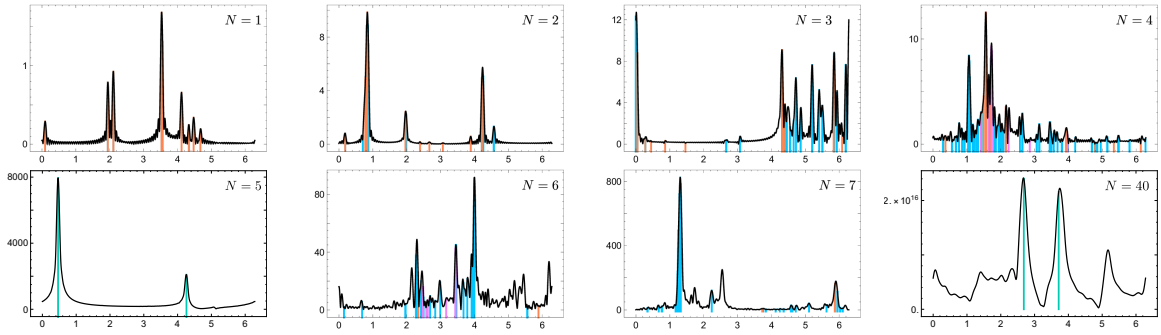

Fig. 7.18.: Absolute value $|\rho(\mathcal{S})|$ of the action spectrum over $\mathcal{S}$ for $T=2$ using $j_{\text{cut}}=100$. The particle number is indicated in the upper right corners and for $N=6,7$ only orbits with $A_\gamma > 0.5$ are shown. The other system parameters are $J=1/2$, $V=(\sqrt{5}+1)/8$ and $b^x=b^z=0.9$. For the color coding see figure 7.8.

as conditions for the existence of PO manifolds, where we introduced $\chi_n = p_{n-1} + 2\mu p_n + p_{n+1}$, compare also with (7.18). The above conditions fix uniquely (up to an addition of factors $(4J)^{-1}2\pi k_n$, $k_n \in \mathbb{Z}$) the variables χ_n, but not necessarily the p_n. The PO manifolds emerge whenever the N_0 conditions (7.66) do not resolve the set $p_1, \dots p_{N_0}$ uniquely. For instance, in the case of 3 spins and $\mu = 1/2$ one finds that all χ_n are identical to $p_1 + p_2 + p_3$. This linear dependence explains the emergence of the classical PO manifolds. We can extend this line of reasoning to arbitrary N and μ based on the cyclic $N_0 \times N_0$ dimensional band matrix

$$\underline{\mathcal{Z}} = \begin{pmatrix} 2\mu & 1 & 0 \cdots & 0 & 1 \\ 1 & 2\mu & 1 & 0 & \cdots \\ 0 & 1 & 2\mu & \cdots & 0 \\ \vdots & \ddots & \ddots & & \vdots \\ 1 & 0 & \cdots & 1 & 2\mu \end{pmatrix} \tag{7.67}$$

connecting the χ_n and p_n variables via $\vec{\chi} = \underline{\mathcal{Z}}\vec{p}$. PO manifolds appear whenever $\underline{\mathcal{Z}}$ is not of full rank. This happens if one of the eigenvalues of $\underline{\mathcal{Z}}$,

$$z_n = 2\mu + 2\cos\frac{2\pi n}{N_0} \qquad n \in \{1, 2, \dots, N_0\}\,. \tag{7.68}$$

satisfies the condition $z_n = 0$ for some n. As one can easily see, this immediately implies (7.65). All eigenvalues in (7.68) are doubly degenerate, except z_{N_0} and $z_{N_0/2}$ (for even N_0). Accordingly, for all $\mu \neq \pm 1$ from the set (7.65) $\underline{\mathcal{Z}}$ is of rank $N_0 - 2$ and we have the freedom to choose two (continuous) parameters $\eta_1^{(t)}, \eta_2^{(t)}$ at each time step $t = 1, 2$ such that $p_n^{(t)}(\eta_1^{(t)}, \eta_2^{(t)})$, while the $\chi_n^{(t)}$ are independent of $\eta_1^{(t)}, \eta_2^{(t)}$. This yields 4-dimensional PO manifolds parametrized by $\eta_1^{(1)}, \eta_2^{(1)}, \eta_1^{(2)}, \eta_2^{(2)}$. In the case $\mu = 1$ the corresponding eigenvalue $z_{N_0/2}$ is non-degenerate and the dimension of the PO manifold is 2 rather than 4 while the spectrum of the dual operator is found to be distributed isotropically. Finally, for $\mu = -1$ the parameters χ_n satisfy $\sum \chi_n = 0$ by definition. Given that all χ_n that satisfy (7.66) are equal up to an addition of $2\pi k_n/(4J)$ ($k_n \in \mathbb{Z}$) we immediately find $4J\chi_n = 0 \mod 2\pi$ for each n. Simply substituting this value back into (7.66) shows that for $\mu = -1$ this equation might hold only if $\underline{R}_{\vec{b}}$ is a rotation by π itself. Therefore, for a generic value of the magnetic field and $\mu = -1$ PO manifolds do not exist.

Remarkably, as N_0 runs through all integer numbers, the set of μ values defined by (7.65) becomes dense in the interval $[-1, 1]$. Informally speaking this implies that in the parameter space we are always "arbitrary close" to PO manifolds for $\mu \in [-1, 1]$. This in turn suggests that relatively large spectral fluctuations should be observed for any set of parameters with $|\mu| < 1$. Indeed, for such parameters we observe a non-trivial scaling j^α of the largest dual eigenvalues, with values of α similar to the $V = 0$ case. On the other hand, for $|\mu| > 1$ this scaling turns out to be close to zero, see figure 7.20.

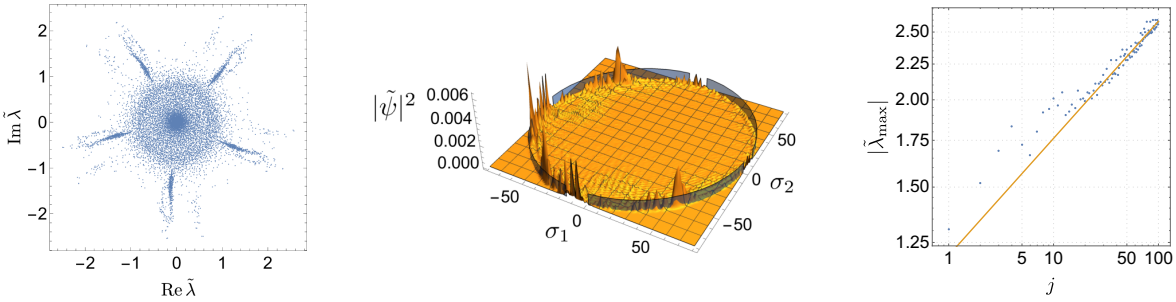

Fig. 7.19.: Spectrum of the $T=2$ dual operator containing a non-linear part for $j=100$ (left panel), corresponding largest eigenvector ($j=80$) (middle) and scaling of the largest eigenvalue in dependence of j (numerical slope $\alpha_0 \approx 0.167$). Parameters are chosen as $b^x = b^z = 0.9$ and $J=1/2$, $V=(\sqrt{5}+1)/8$ such that $\mu=-\cos(4\pi/5)$, see equation (7.65).

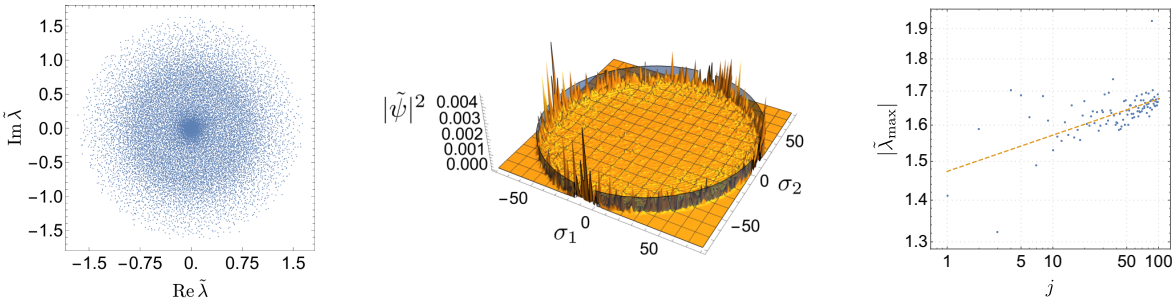

Fig. 7.20.: Spectrum of the dual operator for large $\mu=12$ (left panel, $j=100$). Besides $V=12J$ all other parameters are identical to figure 7.17. The slope indicated in the rightmost panel is $\alpha_0 \approx 0.03$. The middle panel shows the eigenvector corresponding to the largest eigenvalue at $j=80$.

7.8. Summary

In this chapter we use that the spin quantum number j plays the role of the inverse Planck's constant and thus reach semi-classical scales for $j \gg 1$. In contrast to the previous chapter, where j was strictly $1/2$, this limits us to very short times $T = 1$ and $T = 2$ to keep $\tilde{W}$ small enough to afford numerical calculations. The most significant result of our study is the observation of non-isolated 4-dimensional manifolds of POs. These feature a short spatial period and can be interpreted as signatures of collective dynamics. In particular, this happens if $T = 2$ and the ratio μ between the inter-spin coupling strength and the on-side torsion is tuned to satisfy the relation (7.65). Furthermore, provided that the spin chain length N is large and divisible by the spatial prime period of the PO manifolds, the trace formula is completely dominated by them while all isolated POs are suppressed. As our analysis shows, the PO manifolds contribute to the trace formula in terms of large prefactors $|A_\gamma| \sim j^{\alpha(N)}$ which exponentially grow with N, *i.e.* $\alpha(N) \sim \alpha_0 N$. This explains the dominance of those structures over isolated POs, where $\alpha_0 = 0$. The exponent α_0 weakly depends on the system parameters and ranges between 0 and $1/4$. Following the last chapter, such large (short time) traces impact the strength of (long range) spectral fluctuations and for parameters where manifolds are present those fluctuations are strongly enhanced. In comparison, a similar growth of $\alpha_0 = 1/2$ is observed in fully integrable systems and, informally speaking, this puts our model somewhere in-between fully integrable and fully chaotic systems (where $\alpha_0 = 0$), at least with respect to the fluctuations.

As we are limited to very short times $T = 1, 2$ it remains unanswered how the large fluctuations depend on T. For instance, further repetitions of the PO manifolds in time could give rise to similar contributions, or new structures all together could appear. In this context, one would like to understand whether the existence of PO manifolds is a necessary/sufficient condition for large traces and how general this phenomenon is. To this end, further kicked models, and eventually Hamiltonian systems with continuous time evolution, could be studied.

8. Conclusion and Outlook

WITHIN the first part of the thesis we explored the spectral statistics of unidirectional quantum graphs on the scales of mean level spacing. On those one usually finds spectral universality. While this is true also for this model, it offers a peculiarity: strictly speaking time reversal invariance (TRI) is preserved, yet the spectrum does not follow GOE but instead GUE statistics occurring for systems with broken TRI. An explanation emerges in a semi-classical context, where the dynamical constraints of the system, *i.e.* unidirectionality, do not permit Sieber-Richter pairs. They are an essential ingredient to recover GOE universality (instead of GUE) from the sum over periodic orbits. Introducing a back-scattering element locally breaks unidirectionality and thus allows us to study the onset of an transition from GUE to GOE. In this case an adjusted RMT model was used to derive the level spacing distribution $p(s)$, which lies outside the three standard universality classes. A prerequisite to this calculation is the assumption of uniform localization of the eigenmodes on the edges of the graph. But, in cases where short loops were considered as positions for the back-scatterer we found strong deviations from the RMT predictions. From a semi-classical point of view they resulted from a scarring effect of the wave function. This example emphasizes the importance of a dynamical understanding of quantum chaos beyond RMT.

While the first part of the thesis revolves around long time scales of single particle quantum chaos, the second half treats a seemingly orthogonal case of spectral statistics in N-body systems at short time scales. To this end, we considered chain-like models with nearest neighbor interaction which can be thought of as a many-body extension of the kicked top. To overcome the exponential growth of the Hilbert space dimension with N, which plagues all of many-body quantum mechanics, we derived an exact duality between the traces of the unitary evolution operator $\hat{U}$ and a non-unitary dual counterpart $\tilde{W}$. The latter may be seen as an "evolution" along the particle direction for which the role of time and particle index is exchanged. From the point of complexity the operators dimension is given by $\dim \tilde{W} = (2j+1)^T \times (2j+1)^T$ instead of $\dim \hat{U} = (2j+1)^N \times (2j+1)^N$, where $2j+1$ is the dimension of the single particle subspace. Using the standard approach of quantum time evolution basically arbitrary times can be studied since T enters only as power to $\hat{U}$. On the other hand, one is restricted to few particle systems to keep the operators dimension small enough for numerical treatment. In a similar way $\tilde{W}$ provides information on the traces of $\hat{U}$ for an an arbitrary number of particles N, which enters through its power while the dimension of $\tilde{W}$ is controlled by T restricting us to short times. The independence of

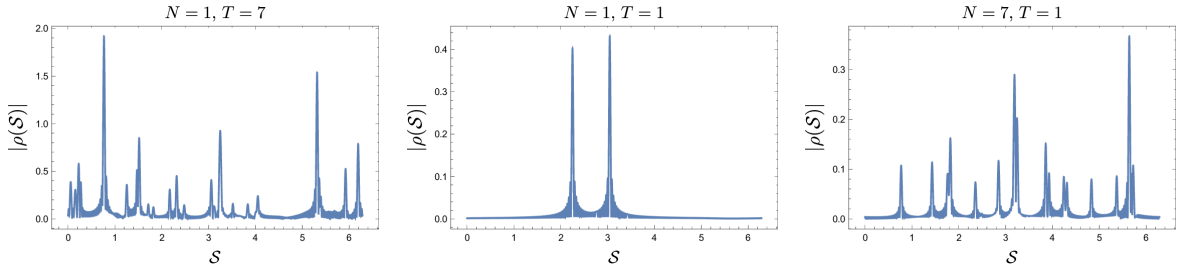

Fig. 8.1.: Action spectrum $|\varrho(\mathcal{S})|$ of the kicked spin chain for the chaotic parameters $J=0.5$, $b^x=1.1$ and $b^z=0.7$, the cut off is chosen as $j_{\text{cut}}=200$. The panels differ only in particle number and considered time: $N=1$, $T=7$; $N=1$, $T=1$; $N=7$, $T=1$ (from left to right).

$\tilde{W}$'s dimension from N indicates that for short times different parts of the system are not fully correlated as information can not propagate from one end of the chain to the other. In any case, it puts the two limits of either $N \sim 1$, $T \gg 1$ or $N \gg 1$, $T \sim 1$ on surprisingly similar grounds that can be explored in similar ways.

In the semi-classical limit ($j \gg 1$) system complexity may as well be judged by the number of involved periodic orbits. For the appearance of universality at long time scales of the order of the Heisenberg time exponentially many POs are involved and their contributions are accounted for in a statistical fashion, while for short, classical times their number is usually finite and the result highly system specific. But, in the many-body case the number of orbits also proliferates with N. For illustrational purposes figure 8.1 shows action spectra for a spin chain at increased times in comparison to an increased number of particles, which, except for different scaling, qualitatively resemble one another. Extending the notion of duality to the classical monodromy matrices we could show that the bifurcation mechanism that triggers the growth of orbits in time works very similar for an increase in particle numbers.

These two parallels to the long time regime of few-body quantum chaos might instigate the question of dual universality. If the parameters are chosen such that the system is self-dual we find $\tilde{W}$ to be unitary. In these cases conventional RMT applies and spectral measures, for instance the form-factor K_2, follow its predictions, but in N as parameter instead of T. However, generically the dual operator is non-unitary and this has a profound impact on the results. For most of our analysis it turned out to be sufficient to consider only the eigenvalues with the largest magnitude as they provide the dominant contributions to the traces for large powers N. The appearance of these largest eigenvalues differs between the cases considered in this thesis as the spectral structure of the dual operator reflects the dynamical state of the system. For the quantum Ising spin chain ($j=1/2$) the spectrum is, given a chaotic parameter regime and sufficient time, radially symmetric with a parameter specific inner and outer edge. For those edges, specifically the outer one containing the largest eigenvalues, a form of

universality might be recovered in terms of non-unitary random matrix ensembles. In the semi-classical regime the spectral structure is more involved. At first glance the $T=1$ case is of similar nature with an equally symmetric distribution and preliminary studies suggest that for $T=3$ the outcome will be comparable. But, for two time steps the appearance of the collective manifolds changes the picture. While the spectrum possesses a similar symmetry as long as they are absent, their presence corresponds to a pronounced cross like structure. In these cases the largest eigenvalues are given by the tips of the crosses, linking single eigenvalues to properties of the classical POs.

These collective PO manifolds are a good illustration for the rich dynamical structure present in many-body systems which stems from the interaction between the constituents, even if the underlying single particle system is something as well understood as a kicked top. Their importance for larger system sizes results from an increasing scaling of the stability prefactor $|A_\gamma| \sim j^{\alpha(N)}$ with $\alpha(N) \sim \alpha_0 N$. This linear growth can be studied from two complementary points of view. For integrable parameters, where one finds $\alpha_0 = 1/2$, such a scaling occurs naturally as the number of conserved quantities grows (linearly) with N. In these cases all directions of $\underline{M}_\gamma$ are exactly marginal. While the manifolds posses only four precisely marginal directions they contribute an ever growing number of quasi-marginal directions that causes the growth of $\alpha(N)$ with N. But, taking into account the contributions of all those directions in a quantitative manner seems to be a challenging problem at the least. Instead, $\tilde{W}$ offers a way to treat them in a systematic and quantitative fashion. Its largest eigenvalues, *i.e.* the crosses' tips, contain the scaling α_0 and cause the linear growth of $\alpha(N)$ when taken in the respective power. A qualitative understanding of α_0 is obtained when we apply semi-classical methods not to $\hat{U}$ but to the dual operator instead. This is a pathway more adapted for large N systems, compare figure 8.2. In this sense the particle-time duality is more than a handy tool, but offers a new perspective on chain-like models.

The example of the collective manifolds marks two important differences between few- and many-body quantum chaos. So far, we highlighted the similarities between the time and the particle direction. However, the dimension of the monodromy matrix depends only on N and, therefore, the number of marginal directions an orbit can acquire over time is bounded by $2N$. While repetitions of non-isolated orbits can also occur in time their scaling "$\alpha(T)$" can not systematically grow with T. From a dual perspective, where $\dim \underline{\tilde{M}}_\gamma = 2T \times 2T$ also does not grow with N, the increase of the marginal directions is reflected in the not entirely classical nature of the dual stabilities, which contain an additional "absorption" factor. This emphasizes that this collective phenomenon is a genuine many-particle one. The second, crucial, distinction has to be made with respect to the limiting process, the outcome depends on whether one considers either the pure semi-classical limit such that $j \to \infty$ with fixed N or a limit where N tends to infinity together with j. In the first case all quasi-marginal directions can be counted as isolated and the scaling would be given by only the precisely marginal directions of the PO manifold's stability matrices, *i.e.* $\alpha(N)=1$ would be N

independent. Only in the second type of limit the linear scaling is observed.

To conclude, for a well-founded understanding of quantum chaos, methods beyond RMT are imperative. In systems with single degrees of freedom semi-classics provides the sought for answers and the field already reached a point where missing links are a rare occurence. Given the tremendous insight obtained in this case an extension of the semi-classical method to many-body systems is highly desirable. Our study points out three central aspects that deserve special attention for this undertaking. At first, already short time dynamics are a worthy topic of research. Even for our simple model the system complexity is comparable to those of chaotic single particle systems at long times. Second, a strict semi-classical limit might not always be the most physical choice and theoretical considerations should take the interplay between both parameters, $\hbar_{\text{eff}}$ and N, into account. Third, mixed dynamics in many-body systems is much more prevalent as it is much harder to preserve full chaos, or full integrability. In a sense, the collective manifolds causing the large deviations in our model may be seen as residual integrable structures. Already in few-body systems the treatment of systems where regular and chaotic motion co-exists is one of those rare, less developed points.

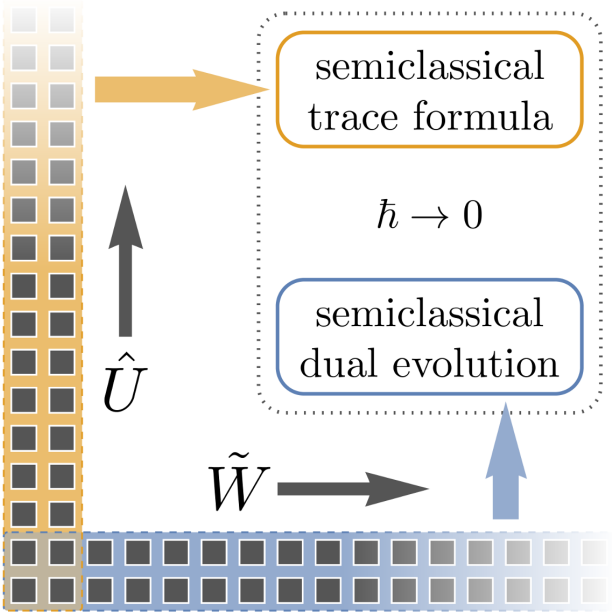

Fig. 8.2.: Visualization of the dual approach for kicked chain-like systems. Usual evolution in time by $\hat{U}$ enables one to calculate traces for arbitrary times but only few particles. In the same fashion $\tilde{W}$ empowers us to study arbitrary particle numbers, albeit only for short times. In the semi-classical limit $\hbar \to 0$ the former case is subjugated to the corresponding analysis based on periodic orbits. Similarly, the spectrum of $\tilde{W}$ is analyzable by semi-classical methods.

Part III.

Appendix

A. Single Particle Chaos

A.1. Calculation of F_{kl}

For the calculation of the double integrals in equation (3.26) it is convenient to expand the brackets and treat the four arising parts separately. Let us denote them by $F_{kl} = F_{kl}^{(0)} - F_{kl}^{(\epsilon)} - F_{kl}^{(\lambda)} + F_{kl}^{(\epsilon\lambda)}$, where *e.g.* $F_{kl}^{(\epsilon)}$ stands for the integral over the $\theta(\epsilon - \epsilon_{\min})\theta(\epsilon_{\max} - \epsilon)$ part only. Further on, to compactify the resulting expressions, we introduce $\tilde{k}{=}k-1-(N-1)/2$ and $\tilde{l}{=}l-1-(N-1)/2$. They are given by:

$$F_{kl}^{(0)} = \frac{2\mathrm{e}^{n_{\tilde{l}}\pi}}{n_{\tilde{k}}n_{\tilde{l}}}\sinh\left(n_{\tilde{k}}\pi\right) - \frac{2\pi}{n_{\tilde{l}}}\delta_{\tilde{k}+\tilde{l}}\,, \tag{A.1}$$

$$\begin{aligned} F_{kl}^{(\lambda)} =& \frac{2}{n_{\tilde{k}}}\frac{\sin\left((\tilde{k}+\tilde{l})\frac{\lambda_{\max}-\lambda_{\min}}{2}\right)}{\tilde{k}+\tilde{l}}\mathrm{e}^{\mathrm{i}(\tilde{k}+\tilde{l})(\lambda_{\max}+\lambda_{\min})/2} \\ &- \frac{2\mathrm{e}^{-n_{\tilde{k}}\pi}}{n_{\tilde{k}}n_{\tilde{l}}}\mathrm{e}^{n_{\tilde{l}}\frac{\lambda_{\max}+\lambda_{\min}}{2}}\sinh\left(\frac{n_{\tilde{l}}}{2}(\lambda_{\max}-\lambda_{\min})\right), \end{aligned} \tag{A.2}$$

$$\begin{aligned} F_{kl}^{(\epsilon)} =& \frac{2\mathrm{e}^{n_{\tilde{l}}\pi}}{n_{\tilde{k}}n_{\tilde{l}}}\mathrm{e}^{n_{\tilde{k}}(\epsilon_{\max}+\epsilon_{\min})/2}\sinh\left(\frac{n_{\tilde{k}}}{2}(\epsilon_{\max}-\epsilon_{\min})\right) \\ &- \frac{2}{n_{\tilde{l}}}\frac{\sin\left((\tilde{k}+\tilde{l})\frac{\epsilon_{\max}-\epsilon_{\min}}{2}\right)}{\tilde{k}+\tilde{l}}\mathrm{e}^{\mathrm{i}(\tilde{k}+\tilde{l})(\epsilon_{\max}+\epsilon_{\min})/2}\,, \end{aligned} \tag{A.3}$$

wherein $\delta_{\tilde{k}+\tilde{l}}$ stands for the Kronecker-Delta which is 1 if $\tilde{k}+\tilde{l}{=}0$ and zero otherwise while $n_{\tilde{l}}{=}\mathrm{i}\tilde{l}-N/(2\nu)$ and $n_{\tilde{k}}{=}\mathrm{i}\tilde{k}+N/(2\nu)$. In the case where all four θ-functions appear the general solution is slightly more complicated. Taking into account the position of the gap, see figure 3.5, it takes on the form:

$$\begin{aligned} F_{kl}^{(\epsilon\lambda)} =& \frac{2}{n_{\tilde{k}}n_{\tilde{l}}}\mathrm{e}^{n_{\tilde{l}}\lambda_{\max}}\sinh\left(n_{\tilde{k}}\frac{\pi}{N}s\right) - \frac{2}{n_{\tilde{l}}}\frac{\sin\left((\tilde{k}+\tilde{l})\frac{\pi}{N}s\right)}{\tilde{k}+\tilde{l}} \\ &+2\,\theta(\lambda_{\min}-\epsilon_{\min})\frac{\mathrm{e}^{n_{\tilde{l}}(\lambda_{\min}+\lambda_{\max})/2}}{n_{\tilde{k}}n_{\tilde{l}}}\left(\mathrm{e}^{n_{\tilde{k}}\lambda_{\min}}-\mathrm{e}^{n_{\tilde{k}}\epsilon_{\min}}\right)\sinh\left(n_{\tilde{l}}\frac{\lambda_{\max}-\lambda_{\min}}{2}\right), \end{aligned} \tag{A.4}$$

wherein the factor π/N stems from the scaling of the gap boundaries. The Heaviside θ-function distinguishes between the case of the internal splitting distribution, where

it is one, and the external splitting distribution, where it is zero. Please observe that equation (A.4) holds only for the numerator, compare equation (3.27). In the case of the denominator $F_{kl}^{(\epsilon\lambda)} = 0$. To obtain the expression for the numerator (in the case of internal splitting), see equation (3.27), we set $\epsilon_{\min} = -s\pi/N - \delta_\epsilon$, $\lambda_{\min} = -s\pi/N$, $\epsilon_{\max} = +s\pi/N$ and $\lambda_{\max} = +s\pi/N + \delta_\lambda$:[1]

$$\begin{aligned} F_{kl}^{(\mathrm{num})} \approx & \mathrm{e}^{\mathrm{i}(\tilde{k}+\tilde{l})\pi} - 2\pi \left(\mathrm{i}\tilde{k} + \frac{N}{2\nu}\right) \delta_{\tilde{k}+\tilde{l}} - 2 \left(\mathrm{i}\tilde{l} - \frac{N}{2\nu}\right) \frac{\sin\left((\tilde{k}+\tilde{l})\frac{\pi}{N}s\right)}{\tilde{k}+\tilde{l}} \\ & + 2\mathrm{e}^{(\mathrm{i}\tilde{l} - \frac{N}{2\nu})\pi/N\, s} \sinh\left(\left(\mathrm{i}\tilde{k} + \frac{N}{2\nu}\right)\frac{\pi}{N}\, s\right) + \mathrm{e}^{\mathrm{i}(\tilde{l}-\tilde{k})\pi/N\, s - 2\frac{\pi s}{N\nu}} \\ & \times \left(\left(\mathrm{i}\tilde{k} + \frac{N}{2\nu}\right)\delta_\epsilon - \left(\mathrm{i}\tilde{l} - \frac{N}{2\nu}\right)\delta_\lambda + \left(\mathrm{i}\tilde{l} - \frac{N}{2\nu}\right)\left(\mathrm{i}\tilde{k} + \frac{N}{2\nu}\right)\delta_\epsilon\delta_\lambda\right). \end{aligned} \tag{A.5}$$

Furthermore, we are only interested in the case where $N \gg 1$ which allows for some minor simplifications. After expansion of the equations (A.2-A.4) up to the order $\delta_\epsilon\delta_\lambda$ we obtain:

$$\begin{aligned} F_{kl}^{(\mathrm{num})} \approx & \mathrm{e}^{\mathrm{i}(\tilde{k}+\tilde{l})\pi} - 2\pi \left(\mathrm{i}\tilde{k} + \frac{N}{2\nu}\right) \delta_{\tilde{k}+\tilde{l}} - 2 \left(\mathrm{i}\tilde{l} - \frac{N}{2\nu}\right) \frac{\sin\left((\tilde{k}+\tilde{l})\frac{\pi}{N}s\right)}{\tilde{k}+\tilde{l}} \\ & + 2\mathrm{e}^{(\mathrm{i}\tilde{l} - \frac{N}{2\nu})\pi/N\, s} \sinh\left(\left(\mathrm{i}\tilde{k} + \frac{N}{2\nu}\right)\frac{\pi}{N}\, s\right) + \mathrm{e}^{\mathrm{i}(\tilde{l}-\tilde{k})\pi/N\, s - 2\frac{\pi s}{N\nu}} \\ & \times \left(\left(\mathrm{i}\tilde{k} + \frac{N}{2\nu}\right)\delta_\epsilon - \left(\mathrm{i}\tilde{l} - \frac{N}{2\nu}\right)\delta_\lambda + \left(\mathrm{i}\tilde{l} - \frac{N}{2\nu}\right)\left(\mathrm{i}\tilde{k} + \frac{N}{2\nu}\right)\delta_\epsilon\delta_\lambda\right). \end{aligned} \tag{A.6}$$

In the case of the denominator we choose $\epsilon_{\min} = -s\pi/N - \delta_\epsilon$, $\epsilon_{\max} = -s\pi/N$ and $\lambda_{\min} = \lambda_{\max} = 0$. Applying the same limit and expansions as for the numerator we arrive at:

$$F_{kl}^{(\mathrm{den})} \approx \mathrm{e}^{\mathrm{i}(\tilde{k}+\tilde{l})\pi} - 2\pi \left(\mathrm{i}\tilde{k} + \frac{N}{2\nu}\right) \delta_{\tilde{k}+\tilde{l}} + \mathrm{e}^{-\mathrm{i}(\tilde{k}+\tilde{l})\pi/N\, s} \left(\mathrm{i}\tilde{k} + \frac{N}{2\nu}\right) \delta_\epsilon\,. \tag{A.7}$$

Note that the alternating sign $\mathrm{e}^{\mathrm{i}(\tilde{k}+\tilde{l})\pi}$ appearing in both F_{kl} (A.6,A.7) does not affect the result of the determinant and can be neglected. With the notation introduced in section 3.3.2 we may cast both F_{kl} into the matrix forms given by equations (3.32) and (3.33).

[1] For the external splitting set: $\epsilon_{\min} = -s\pi/N$, $\lambda_{\min} = -s\pi/N - \delta_\lambda$, $\epsilon_{\max} = s\pi/N + \delta_\epsilon$ and $\lambda_{\max} = s\pi/N$

B. Many–Particle Chaos

B.1. Jordan Wigner Transform for the KIC

In the non-trivially integrable regime, $b^z = 0$ or equivalently $\varphi = \pi/2$, the spin-1/2 Hamiltonian of section 6 can be expressed after a Jordan Wigner transformation of the form

$$\hat{a}_n = \frac{1}{2}\left(\prod_{j=1}^{n-1}\hat{\sigma}_j^x\right)(\hat{\sigma}_n^z - i\hat{\sigma}_n^y)\ , \tag{B.1}$$

$$\hat{a}_n^\dagger = \frac{1}{2}\left(\prod_{j=1}^{n-1}\hat{\sigma}_j^x\right)(\hat{\sigma}_n^z + i\hat{\sigma}_n^y)\ , \tag{B.2}$$

$$\hat{\sigma}_n^x = 1 - 2\hat{a}_n^\dagger\hat{a}_n\,, \tag{B.3}$$

and the transformation to the Fourier domain

$$\hat{b}_k = \frac{1}{\sqrt{N}}\sum_{n=1}^{N}\mathrm{e}^{ikn}\hat{a}_n \tag{B.4}$$

as

$$H_I = 2J\sum_k\left[\cos k\left(\hat{b}_k^\dagger\hat{b}_k - 1/2\right) + \frac{i}{2}\left(\hat{b}_k^\dagger\hat{b}_{-k}^\dagger - \hat{b}_{-k}\hat{b}_k\right)\sin k\right] \tag{B.5}$$

and

$$H_K = -2b\sum_k\left(\hat{b}_k^\dagger\hat{b}_k - 1/2\right)\ , \tag{B.6}$$

where both $\hat{a}_n$ and $\hat{b}_k$ are fermionic operators satisfying the usual algebra relations

$$\{\hat{a}_n, \hat{a}_m^\dagger\} = \delta_{nm}\,, \qquad \{\hat{a}_n^\dagger, \hat{a}_m^\dagger\} = \{\hat{a}_n, \hat{a}_m\} = 0 \tag{B.7}$$

and identically for $\hat{b}_k$. This transformation can be performed in the same way as in [118]. Within this model the parity $\mathcal{P} = \prod_{i=1}^{N}\hat{\sigma}_n^x = (-1)^{\mathcal{N}}$ with the particle number $\mathcal{N} = \sum_{n=1}^{N}\hat{a}_n^\dagger\hat{a}_n = \sum_k\hat{b}_k^\dagger\hat{b}_k$ serves as a conserved quantity. In the original Hamiltonian the boundary conditions are periodic, *i.e.* $\sigma_{N+1}^z = \sigma_1^z$, but $\hat{a}_n$ break the translational invariance of the chain creating a parity dependent sign change at the boundary.

Therefore, the allowed k-values in the exponent on the r.h.s of (B.4) also depend on the parity and are given by

$$k_j = \frac{\pi}{N} \begin{cases} 2j & \mathcal{P}=-1 \\ 2j+1 & \mathcal{P}=+1 \end{cases}, \qquad j = 0,\, 1,\, \ldots,\, N-1\,. \tag{B.8}$$

Negative indices should thus be understood as $\hat{b}_{-k}=\hat{b}_{N-k}$. Using the transformation

$$\hat{\eta}_k = \cos\vartheta_k \hat{b}_k - i\sin\vartheta_k \hat{b}^\dagger_{-k}, \qquad\qquad \vartheta_k = k/2+\pi/2 \tag{B.9}$$

the Hamiltonian can be expressed as

$$\hat{H}_I = -2J\sum_k \left(\hat{\eta}^\dagger_k\hat{\eta}_k - 1/2\right) \tag{B.10}$$

and

$$\hat{H}_K = -2b\sum_k \left[\cos 2\vartheta_k \left(\hat{\eta}^\dagger_k\hat{\eta}_k - 1/2\right) + \frac{i}{2}\sin 2\vartheta_k \left(\hat{\eta}^\dagger_k\hat{\eta}^\dagger_{-k} - \hat{\eta}_{-k}\hat{\eta}_k\right)\right]. \tag{B.11}$$

Using that $\hat{b}_k$ and $\hat{\eta}_k$ are fermionic operators we obtain for the Ising and kick part of the Floquet operator

$$\begin{aligned} U_I &= \mathrm{e}^{2iJ\sum_k\left(\hat{\eta}^\dagger_k\hat{\eta}_k - 1/2\right)} = \mathrm{e}^{-iNJ}\prod_k \left[1+\left(\mathrm{e}^{2iJ}-1\right)\hat{\eta}^\dagger_k\hat{\eta}_k\right], \\ U_K &= \mathrm{e}^{2ib\sum_k\left(\hat{b}^\dagger_k\hat{b}_k - 1/2\right)} = \mathrm{e}^{-iNb}\prod_k \left[1+\left(\mathrm{e}^{2ib}-1\right)\hat{b}^\dagger_k\hat{b}_k\right] \\ &= \mathrm{e}^{-iNb}\prod_k \Big[1+\left(\mathrm{e}^{2ib}-1\right)\Big(\cos^2\vartheta_k\hat{\eta}^\dagger_k\hat{\eta}_k + \sin^2\vartheta_k\hat{\eta}_{-k}\hat{\eta}^\dagger_{-k} \\ &\quad + \frac{i}{2}\sin 2\vartheta_k\left(\hat{\eta}^\dagger_k\hat{\eta}^\dagger_{-k} - \hat{\eta}_{-k}\hat{\eta}_k\right)\Big)\Big]. \end{aligned} \tag{B.12}$$

In the latter expression k is only coupled to itself and to $-k$, the Floquet operator thus splits into 4×4 subblocks (k and $-k$ occupied, k and $-k$ unoccupied, only k occupied, only $-k$ occupied) that can be diagonalized analytically. The resulting eigenvalues are the entries of the sets

$$\Lambda(k) = \{\mu_-(k),\, 1,\, 1,\, \mu_+(k)\}\,, \tag{B.13}$$

where $\mu_\pm(k)=\alpha(k)\pm\sqrt{\beta(k)}$ with

$$\begin{aligned} \alpha(k) &= \frac{1}{4}\mathrm{e}^{2\mathrm{i}(J+b^x)}\left[\left(1+\cos 2\vartheta_k\right)\left(1+\mathrm{e}^{-4\mathrm{i}(J+b^x)}\right)+\left(1-\cos 2\vartheta_k\right)\left(\mathrm{e}^{-4\mathrm{i}J}+\mathrm{e}^{-4\mathrm{i}b^x}\right)\right] \\ \beta(k) &= \frac{\mathrm{e}^{4\mathrm{i}(J+b^x)}}{16}\left(\left(1+\mathrm{e}^{-4\mathrm{i}J}\right)\left(1+\mathrm{e}^{-4\mathrm{i}b^x}\right)+\left(1-\mathrm{e}^{-4\mathrm{i}J}\right)\left(1-\mathrm{e}^{-4\mathrm{i}b^x}\right)\cos 2\vartheta_k\right)^2 - 1\,. \end{aligned} \tag{B.14}$$

These quantities are symmetric under the exchange of J and b^x making it an almost exact symmetry of the non-trivially integrable system, a small deviation is discussed below. Furthermore, they fulfill the relation

$$\mu_+(k)\mu_-(k) = 1\,. \tag{B.15}$$

The corresponding occupation numbers to $\Lambda(k)$ in (B.13) are $\{0,1,1,2\}$.

Further on, we obtain two special sectors for $k=0\,,\pi$ which are not paired to any $-k$ sectors. The eigenvalues for those cases are

$$\begin{aligned} k=0: &\quad \Lambda(0) = \{\mathrm{e}^{\mathrm{i}(J-b^x)},\, \mathrm{e}^{\mathrm{i}(b^x-J)}\}\,, \\ k=\pi: &\quad \Lambda(\pi) = \{\mathrm{e}^{-\mathrm{i}(J+b^x)},\, \mathrm{e}^{+\mathrm{i}(J+b^x)}\} \end{aligned} \tag{B.16}$$

for an occupation value of 0 (left eigenvalue) and single fermion occupation (right), respectively. In the $\hat{\eta}$-basis the total occupation number $\sum_k \hat{\eta}_k^\dagger \hat{\eta}_k$ has to be even for both parities. Apart from this constraint the eigenvalues of $\hat{U}_N$ are combinatorial products,

$$\lambda = \prod_i \Lambda_{\sigma(i)}(k_i)\,, \tag{B.17}$$

whose components $\Lambda_{\sigma(i)}(k_i)$ are chosen from the sets (B.13) and (B.16).

To extend this result to the dual picture, *i.e.* the eigenvalues of $g^{-T}\tilde{U}_T$, it is necessary to replace J by K, b^x by $\tilde{b}$, as given by (6.16), and N by T in the definition of k_j in (B.8). This leads to purely real, but not necessarily positive, functions $\alpha(k)$ and $\beta(k)$. Due to (B.15), in the case where $\beta(k)$ is negative, $\mu_\pm(k)$ are complex conjugated numbers with absolute value 1 while in the case $\beta(k) > 0$ they are real and the absolute value of one of them is larger than unity. Throughout the remaining discussion $n \leq T/2$ denotes the number of negative radicands of $\sqrt{\beta(k)}$.

To simplify the discussion we restrict ourselves, at first, to the case of T even and $\mathcal{P}=+1$, where none of the special sectors enter (B.17). As pointed out before, we are interested in the largest eigenvalues. In these cases the combinatorial products must contain all $(T/2-n)$ of the $\mu_\pm(k)$ with $|\mu_\pm(k)| > 1$. All of those entries belong to an even occupation number and possess a $\beta(k) > 0$. The remaining n choices for the other factors $\Lambda_{\sigma(i)}(k_i)$ only have an influence on the phase, not on the absolute value. We therefore have freedom in combining them. In general, when all $\mu_\pm(k)$ are different, we can choose all 2^n possible combinations, each yielding a different phase and therefore eigenvalues of the same magnitude. Next, we are allowed to replace two (to keep an even occupation number) of the complex $\mu_\pm(k)$ by one of the two unit elements within the respective $\Lambda(k)$ set. This eigenvalue is therefore 2^2-fold degenerate and we find $2^{n-2}\binom{n}{2}$ different eigenvalues of this type. Replacing more $\mu_\pm(k)$ with absolute value one by unit elements, the degeneracies grow in multiples of 4 up to a maximum of 2^{2m} with $2m=n$ for even n ($2m=n-1$ if odd), which occurs if all "complex" contributions

to the eigenvalue are completely replaced by ones. Such an eigenvalue can only occur once $(2\binom{n}{2m} = 2n$ times for odd n, as one complex $\mu_\pm$ is left). This leads us to the degeneracies d_i and multiplicities m_i in (6.19).

In case of the other parity ($\mathcal{P}=-1$) the picture looks slightly more complicated, as now the special sectors in (B.16) have to be taken into account. The maximal absolute value resulting from these sets in the dual picture is $\mathrm{e}^{2|\operatorname{Im}\tilde{b}|}$ for an even and $\mathrm{e}^{2|\operatorname{Im}K|}$ for an odd occupation. Assuming the even contribution is the larger one we can select the remaining $\Lambda(k)$ as discussed before. However, in the odd case the larger of either $\mathrm{e}^{2|\operatorname{Im}\tilde{b}|}$ together with all $\mu_\pm(k)$ or $\mathrm{e}^{2|\operatorname{Im}K|}$ together with all but the smallest $\mu_\pm(k)$ (which has an absolute value larger 1 if $n=0$) has to be chosen. In the latter case the equations for d_i and m_i are slightly modified by replacing $2i \to 2i+1$ with $i=0, 1, \ldots, \lfloor (n-1)/2 \rfloor$ (in the special case of $n=0$ this implies only one doubly degenerate eigenvalue). This modification leaves the total number of eigenvalues (6.20) invariant, however the distinct eigenvalues (6.21) are then given by $(3^n-1)/2$.

B.2. Classical Action

The classical action, as used in (7.15), of the system contains two contributions, a part stemming from the interaction ($\mathcal{S}_I$) and one from the local kicking ($\mathcal{S}_K$). Along the orbit, or similarly on any other trajectory, it may be split according to

$$\mathcal{S}_\gamma = \sum_{t=0}^{T_\gamma - 1} \mathcal{S}_K\Big(\vec{q}(t), \vec{p}(t); \vec{q}(t+\epsilon), \vec{p}(t+\epsilon)\Big) + \mathcal{S}_I\Big(\vec{p}(t+\epsilon)\Big) \tag{B.18}$$

where the kick is restricted to times t to $t+\epsilon$ with $\epsilon \to 0$ and $\vec{q}, \vec{p}(t+\epsilon)$ are the positions of the spins directly after its application.

As long as the rotation of the spins is around the z-axis as in the interaction part, only the q component changes while p remains constant. This makes the evaluation of $\mathcal{S}_I$ straightforward and for the contribution to a single time step we find

$$\begin{aligned}
\mathcal{S}_I\Big(\vec{p}(t+\epsilon)\Big) &= \int_{\vec{q}(t+\epsilon)}^{\vec{q}(t+1)} \vec{p}\cdot \mathrm{d}\vec{q} - \int_{t+\epsilon}^{t+1} H(\vec{q},\vec{p})\,\mathrm{d}\tau \\
&= \sum_{n=1}^{N_\gamma} \Delta q_n(t+\epsilon) p_n(t+\epsilon) + \Delta t H_I(\vec{p}(t+\epsilon)) \qquad \text{(B.19)} \\
&= 4\sum_{n=1}^{N_\gamma} \left(J p_{n+1}(t+\epsilon) p_n(t+\epsilon) + V(p_n(t+\epsilon))^2\right) ,
\end{aligned}$$

wherein $\Delta t \to 1$ and $\Delta q_n(t+\epsilon) = q_n(t+1) - q_n(t+\epsilon) = 4J(p_{n-1}(t+\epsilon) + p_{n+1}(t+\epsilon)) + 8V p_n(t+\epsilon)$ is the angle of rotation. Throughout one type of dynamics "energy" is

conserved and thus H_I is constant along the trajectory segment. From a conceptual point of view $\mathrm{d}p_i\mathrm{d}q_i$ are the area elements on the Bloch sphere and the integrals thus measure the area swept by the spin vectors $\vec{n}_i$.

The kicking part is given by the Larmor rotation of all spins about $\vec{b}$ around the same angle. Is is local for every spin and its action is thus a sum of single spin actions. But, besides the integrable case ($b^x=0$) both p and q change. However, we may change our coordinate system $(q,p)\to(Q,P)$ into a basis where the rotation is around the Z-axis instead of $\vec{b}$. The transformations are given by

$$q(Q,P) = \arctan\frac{\sqrt{1-P^2}\sin Q}{\sqrt{1-P^2}\cos\varphi\cos Q - P\sin\varphi}\,, \tag{B.20}$$

$$p(Q,P) = P\cos\varphi + \sqrt{1-P^2}\sin\varphi\cos Q \tag{B.21}$$

with respect to the angle φ between the magnetic field and the z-direction. The inverse transformation is obtained by $\varphi\to-\varphi$. Neglecting particle indices we may cast the integral part of $\mathcal{S}_K$ into

$$\begin{aligned}
\int_{q(t)}^{q(t+\epsilon)} p\,\mathrm{d}q &= \int_{t}^{t+\epsilon} p(\tau)\dot{q}(\tau)\,\mathrm{d}\tau \\
&= \int_{t}^{t+\epsilon} p(Q(\tau),P)\left(\partial_\tau q(Q(\tau),P)\right)\,\mathrm{d}\tau \\
&= \int_{Q(t)}^{Q(t+\epsilon)} p(Q,P)\left(\partial_Q q(Q,P)\right)\,\mathrm{d}Q \\
&= \Phi(Q(t+\epsilon),P) - \Phi(Q(t),P)
\end{aligned} \tag{B.22}$$

for which we use that P is constant under rotation. The change in angle, $Q(t+\epsilon) = Q(t)+\Delta Q$, is given by the rotation matrix $\underline{R}_{\vec{b}}$ as $\Delta Q = 2b$ and is independent of ϵ. After some calculation the antiderivative Φ may be found as

$$\begin{aligned}
\Phi(Q,P) \quad &= QP + \arctan w_-(Q,P) - \arctan w_+(Q,P) \\
&\text{with} \quad w_\pm = \frac{P\cos\varphi + \sqrt{1-P^2}\sin\varphi \pm 1}{P\pm\cos\varphi}\tan\frac{Q}{2}\,.
\end{aligned} \tag{B.23}$$

While using this equation one has to keep track of increased winding numbers when Q passes from $+\pi$ to $-\pi$. The remaining part of $\mathcal{S}_K$ is the (time) integral over H_K. Again, along the segment H_K is constant and may be evaluated at an arbitrary point. This part will compensate the $P\,\Delta Q$ contribution from the previous integral. Although the time interval of the kick tends to zero the delta distribution is adjusted such that the integral remains of unit measure. As a side remark, for $\varphi=0$ we find $\mathcal{S}_K=0$.

B.3. Kick Action for two Time Steps

For periodic orbits with $T_\gamma^{(P)}=2$ the kick action $\mathcal{S}_K^{(n,1)}$ for the n-th spin at the first time step is identical to $\pm\mathcal{S}_K^{(n,2)}$ at the other time step. It can therefore either add up to double its value or cancel all together. In the case of the 4D manifolds this cancellation, occurring for all of the spins, leads to their simple action formula (7.22). To understand this property we have to look at trajectories (not necessarily parts of periodic orbits) connecting two different values of p, $p^i \to p^f$, under the action of $\underline{R}_{\vec{b}}$. For simplicity, we restrict our argument to a single spin. Generically, there are either none or two, and only two, trajectories $z_{1,2}$,

$$(q^i_{1,2}, p^i) \to (q^f_{1,2}, p^f)\,, \tag{B.24}$$

connecting the initial and final momenta (compare with the spin rotation about the y-axis relevant for the evaluation of the Wigner d-function in [138]). As we show subsequently the action along the two trajectories fulfills

$$\mathcal{S}_K(z_1) = -\mathcal{S}_K(z_2)\,. \tag{B.25}$$

This is important as for any $T_\gamma^{(P)}=2$ periodic orbit the spin, in the second time step has to return via $p^f \to p^i$ along any one of the two possible trajectories $z'_{1,2}$:

$$(-q^f_{1,2}, p^f) \to (-q^i_{1,2}, p^i) \tag{B.26}$$

which are time reversed reflections of $z_{1,2}$ flipped perpendicular to the xz-plane. Due to symmetry we find the associated actions $\mathcal{S}_K(z_{1,2})=\mathcal{S}_K(z'_{1,2})$, compare equations (B.20) and (B.23). A periodic orbit with the first kick segment given by, for example, z_1 may close either via z'_1 or z'_2 as its second segment. In the first case the actions of the kicks will add up, it is further easy to show that the orbit will then be highly symmetric with all its four points in the same plane orthogonal to the field. On the contrary, if the orbit is composed of z_1 and z'_2 the overall kick action is zero.

To prove (B.25) we point out that the action is path independent and we may safely use the Euler decomposition, see (7.7), of the rotation into z, x and z-rotations. The z contributions lead to vanishing actions and only the x part has to be dealt with. Denoting the corresponding segments of the two trajectories by either $(q^i_{1x}, p^i) \to (q^f_{1x}, p^f)$ or $(q^i_{2x}, p^i) \to (q^f_{2x}, p^f)$ one may from purely geometrical reasons conclude that $q^i_{2x}=\pi - q^i_{1x}$. In other words, the second possible trajectory segment connecting two different p values under $\underline{R}_x$ is obtained by reflection at the yz-plane. Using the rotated coordinate system Q, P aligned to the field, see B.2, we find that $Q^i_{1x}=Q^i_{2x}$, $P^i_{2x}=-P^i_{1x}$ corresponds to this reflection. Looking at (B.23) for $\varphi=\pi/2$ it is straightforward to see that $P \to -P$ leads to a sign change in Φ, which concludes the proof of (B.25).

A generic PO with $T_\gamma^{(P)}=2$ consists of both types of spins, those for which the (local) kick action cancels as well as those where it adds up leading still to a non-trivial

result for the overall $\mathcal{S}_K$. What remains to be argued is that for the manifolds' orbits only the cancelling type occurs. To make this plausible, let us again look at a single spin $\vec{n}_1$ of the manifold. It is mapped under time evolution onto

$$\vec{n}_2 = \underline{R}_I \underline{R}_{\vec{b}} \vec{n}_1 \,, \tag{B.27}$$

where by construction of the manifold we may assume $\underline{R}_I$ to be a fixed, given matrix independent of our concrete choice of $\vec{n}_1$. Proving our statement by contradiction, let us assume that the new vector belongs to those mirror reflected trajectories that have identical action. In this case it may also be obtained as

$$\vec{n}_2 = \underline{P}_y \underline{R}_{\vec{b}} \vec{n}_1 \,, \tag{B.28}$$

where $\underline{P}_y$ denotes the reflection along the xz-plane. While these two equations can be satisfied for single vectors $\vec{n}_1$ for the manifold it would have to be satisfied for the set of linear independent vectors residing on it. Thus, we would require that a rotation equates a reflection, $\underline{R}_I = \underline{P}_y$, which can not be satisfied. Therefore, orbits on $T_\gamma^{(P)} = 2$ manifolds have to feature vanishing $\mathcal{S}_K$ contributions wherever the dimension of the manifold (locally) does not collapse. As a remark, while the construction of the point $\vec{n}_2$ belonging to the cancelling trajectory is slightly more involved it necessarily involves a further reflection $\underline{P}_x$ and two reflections can be expressed by a rotation.

In conclusion the action to the PO manifolds is only given by $\mathcal{S}_I$ as the kick parts fully cancel. Looking at B.2 we thus find equation (7.22)

$$\mathcal{S} = \mathcal{S}_I(\vec{p}^{(1)}) + \mathcal{S}_I(\vec{p}^{(2)}) = 4J \sum_{t=1}^{2} \sum_{n=1}^{N} p_{n+1}^{(t)} p_n^{(t)} \tag{B.29}$$

with the momenta $\vec{p}^{(t)}$ for the first and second time steps, respectively. Importantly, the action (B.29) can be expressed entirely in terms of $\chi_i^{(t)} = p_{i+1}^{(t)} + p_{i-1}^{(t)}$ variables. In particular, for $N_\gamma^{(P)} = 4$ this results in the simple equation (7.23). As the $\chi_i^{(t)}$ are the same for a given PO manifold the action is independent of the specific choice of the orbit.

B.4. 2D Manifolds

In the body of the text we considered the cases where (7.18) holds for all spins, giving rise to 4D manifolds. However, for the existence of manifolds it is sufficient to demand (7.18) for only half of the spins, *e.g.* the odd indexed ones. In this case the manifold will be only two dimensional as we are sparing out half of the chain. For the even indexed spins this implies that they still fulfill (7.20). While this ensures that the trajectories of the odd spins are closed regardless of their initial conditions, we need

further restrictions to ensure that also the trajectories of the even ones are periodic. A way to realize this, already possible for 4 spins, is by aligning the even spins along the rotational axis, *i.e.* $\underline{R}_z\big(4J\chi_{2i}^{(t)}\big)\underline{R}_{\vec{b}}(2b)\vec{n}_{2i}=\vec{n}_{2i}$, $t=1,2$, such that $\vec{n}_{2i}$ is constant over time. From this equation we derive several constraints for the spins initial conditions. The first one on the coordinates of each of the two even spins,

$$\sin\left(q_{2i}+\gamma\right)=\frac{p_{2i}\tan\beta/2}{\sqrt{1-p_{2i}^2}}\,, \tag{B.30}$$

which is independent of the Ising interaction. Therein β,γ are the Euler angles of the kick rotation as defined in (7.8). Another pair of equation constrains the sum $\chi_{2i}^{(t)}$ of the odd spin momenta,

$$\begin{aligned} p_{2i-1}+p_{2i+1} &= \frac{q_{2i}}{2J} \qquad \mathrm{mod}\ \ \pi/(2J)\,, && \text{(B.31)}\\ (p_{2i-1}+p_{2i+1})\tan\beta/2 &= \sqrt{1-p_{2i-1}^2}\sin\left(q_{2i-1}+\gamma\right) && \text{(B.32)}\\ &+ \sqrt{1-p_{2i+1}^2}\sin\left(q_{2i+1}+\gamma\right) \qquad \mathrm{mod}\ \ \pi/(2J\sin\beta)\,. \end{aligned}$$

Up to the differing value of $\chi_{2i}^{(t)}$, these equations are similar in nature to the ones used in (7.20) and (7.21). To this we still need to add $\underline{R}_z\big(4J\chi_{2i+1}^{(t)}\big)\underline{R}_{\vec{b}}(2b)\big)^2=\mathbb{1}$ which poses another restriction on

$$p_{2i}=\frac{\chi_{2i+1}}{2}\,, \tag{B.33}$$

where χ_{2i+1} is fixed by (7.19). (B.30) and (B.33) define the initial position of the even spins. The remaining two equations, (B.31) and (B.32), leave two degrees of freedom undetermined, resulting in two dimensional manifolds of possible initial conditions.

B.5. Dual Matrix Spectrum

In this appendix we provide an approximation for the spectrum of the dual evolution $\tilde{W}$. Rather than considering the dual operator itself it is instructive to analyze the spectrum of its square $\tilde{W}^2=\tilde{W}_I\tilde{W}_0$, with $\tilde{W}_0=\tilde{W}_K\tilde{W}_I\tilde{W}_K$. The idea is that the operator $\tilde{W}_0$ can be thought of as an approximate permutation. To see this we notice that its matrix elements can be written down as

$$\begin{aligned} \langle\sigma_1\sigma_2|\tilde{W}_0|\sigma_1'\sigma_2'\rangle &= \sum_{s_1=-j}^{j}\sum_{s_2=-j}^{j}\exp\left[\frac{-\mathrm{i}4J(s_1\sigma_1+s_2\sigma_2)}{j+1/2}\right]\langle s_1|\mathrm{e}^{-2\mathrm{i}\,\vec{b}\cdot\hat{\vec{S}}}\,|s_2\rangle\cdot\\ &\quad\cdot\exp\left[\frac{-\mathrm{i}4J(s_1\sigma_1'+s_2\sigma_2')}{j+1/2}\right]\langle s_2|\mathrm{e}^{-2\mathrm{i}\,\vec{b}\cdot\hat{\vec{S}}}\,|s_1\rangle\,. \end{aligned} \tag{B.34}$$

Using $\hat{S}^z$ operators it can be rewritten as

$$\begin{aligned}\langle\sigma_1\sigma_2|\tilde{W}_0|\sigma_1'\sigma_2'\rangle &= \sum_{s_1=-j}^{j}\sum_{s_2=-j}^{j}\langle s_1|\mathrm{e}^{-\mathrm{i}\kappa_1\hat{S}^z}|s_1\rangle\langle s_1|\mathrm{e}^{-2\mathrm{i}\,\vec{b}\cdot\hat{\vec{S}}}|s_2\rangle\cdot\\ &\quad\cdot\langle s_2|\mathrm{e}^{-\mathrm{i}\kappa_2\hat{S}^z}|s_2\rangle\langle s_2|\mathrm{e}^{-2\mathrm{i}\,\vec{b}\cdot\hat{\vec{S}}}|s_1\rangle\\ &= \mathrm{Tr}\left(\mathrm{e}^{-\mathrm{i}\Phi\,(\vec{n}\cdot\hat{\vec{S}})}\right),\end{aligned}$$

where

$$\kappa_1=\frac{2\pi a(\sigma_1+\sigma_1')}{2j+1},\quad \kappa_2=\frac{2\pi a(\sigma_2+\sigma_2')}{2j+1},\qquad a=4J/\pi,$$

and the operator

$$\mathrm{e}^{-\mathrm{i}\Phi\,(\vec{n}\cdot\hat{\vec{S}})}=\mathrm{e}^{-\mathrm{i}\kappa_1\hat{S}^z}\mathrm{e}^{-2\mathrm{i}\,\vec{b}\cdot\hat{\vec{S}}}\mathrm{e}^{-\mathrm{i}\kappa_2\hat{S}^z}\mathrm{e}^{-2\mathrm{i}\,\vec{b}\cdot\hat{\vec{S}}},$$

describes the rotation around some axis $\vec{n}$ by an angle Φ. From the last representation follows

$$\langle\sigma_1\sigma_2|\tilde{W}_0|\sigma_1'\sigma_2'\rangle=\sum_{s=-j}^{j}\mathrm{e}^{-\mathrm{i}s\Phi}=\frac{\sin(j+1/2)\Phi}{\sin\Phi/2}. \tag{B.35}$$

The matrix elements are of order $2j+1$ if $\Phi\approx 0$ and of order 1, otherwise. The rotation angle $\Phi=\Phi(\kappa_1,\kappa_2)$ can be determined straightforwardly through the relation

$$\mathrm{Tr}\left(\underline{R}_z(\kappa_1)\underline{R}_{\vec{b}}(2\vec{b})\underline{R}_z(\kappa_2)\underline{R}_{\vec{b}}(2\vec{b})\right)=1+2\cos\Phi\,,$$

where $\underline{R}_z(\kappa_1)$, $\underline{R}_{\vec{b}}(2\vec{b})$ are rotations along the z and $\vec{b}$ directions, respectively. At this point it is convenient to use the Euler decomposition $\underline{R}_{\vec{b}}(2\vec{b})=\underline{R}_z(\alpha)\underline{R}_x(\beta)\underline{R}_z(\alpha)$, see also (7.8), leading to

$$\mathrm{Tr}\,(\underline{R}_z(\kappa_1+\theta)\underline{R}_x(\beta)\underline{R}_z(\kappa_2+\theta)\underline{R}_x(\beta))=1+2\cos\Phi(\kappa_1+\theta,\kappa_2+\theta) \tag{B.36}$$

with $2\alpha=\theta$. This allows the explicit evaluation of the function $\Phi(x,y)$:

$$\begin{aligned}2\cos\Phi(x,y) &= \cos x\cos y(1+\cos^2\beta)\\ &- 2\sin x\sin y\cos\beta-(\cos x+\cos y+1)\sin^2\beta.\end{aligned}$$

The solutions of the equations $\Phi(\kappa_1+\theta,\kappa_2+\theta)=0$ are provided by all κ_1,κ_2 such that

$$\underline{R}_z(\kappa_1+\theta)\underline{R}_x(\beta)=(\underline{R}_z(\kappa_2+\theta)\underline{R}_x(\beta))^{-1}. \tag{B.37}$$

After writing down the left and the right hand side of this equation in the matrix form and comparing them element-wise (see e.g., [139]) we conclude that both rotations about the z-direction must be by π modulo 2π:

$$\kappa_1+\theta=\pi+2\pi m_1,\qquad \kappa_2+\theta=\pi+2\pi m_2, \tag{B.38}$$

with $m_1, m_2 \in \mathbb{Z}$, or equivalently:

$$\frac{\sigma_1 + \sigma_1'}{2j+1} = \frac{1 + 2m_1 - \theta/\pi}{2a}, \qquad \frac{\sigma_2 + \sigma_2'}{2j+1} = \frac{1 + 2m_2 - \theta/\pi}{2a}. \tag{B.39}$$

Since $-j \leq \sigma_i, \sigma_i' \leq j$ holds, the above solutions exist only if the interval $[-2a + \frac{\theta}{\pi}, 2a + \frac{\theta}{\pi}]$ contains a point from $\{1 + 2m | m \in \mathbb{Z}\}$. This is, in fact, the necessary condition for the existence of 4-dimensional manifolds. In particular, for the case $b^z = 0$ it reduces to $|a| > 1/2$.

Single PO Manifold — In what follows we will consider parameters a, θ such that (B.39) admits at most one solution $\sigma_1, \sigma_2 \in [-j, j]$, $m_1 = m_2 = m$ for each pair σ_1', σ_2'. In that case we can write $\tilde{W}_0 = (2j+1)\tilde{P}\tilde{G}$, where

$$\langle \sigma_1 \sigma_2 | \tilde{P} | \sigma_1' \sigma_2' \rangle = \delta_{\sigma_1 + \sigma_1', g}\, \delta_{\sigma_2 + \sigma_2', g}, \tag{B.40}$$

$$-j \leq g = \left\lfloor \frac{(2j+1)(1 + 2m - \theta/\pi)}{2a} \right\rfloor \leq j \tag{B.41}$$

is a truncated permutation while $\tilde{G}$ has a band like structure. The last matrix has approximate unit elements on the diagonal, $\langle \sigma_1 \sigma_2 | \tilde{G} | \sigma_2 \sigma_1 \rangle \approx 1$, while its off-diagonal elements are highly fluctuating with absolute values decaying as the distance to the diagonal grows:

$$|\langle \sigma_1 \sigma_2 | \tilde{G} | \sigma_1' \sigma_2' \rangle| \sim \left((\sigma_1' - \sigma_1)^2 + (\sigma_2 - \sigma_2')^2 \right)^{-1/2}.$$

To facilitate the study of the $\tilde{W}$ spectrum we make a crude approximation $\tilde{G} \approx \mathbb{1}$ (resp. $\tilde{W}_0 \approx (2j+1)\tilde{P}$). It amounts to picking up the largest element from each row of the matrix $\tilde{W}_0$. Since $\tilde{W}_I$ is a diagonal matrix and $\tilde{P}$ is a permutation, the eigenvectors of $(2j+1)\tilde{W}_I \tilde{P}$ take a simple form:

$$\psi_{(\sigma_1, \sigma_2)} = C_1 |\sigma_1 \sigma_2\rangle \pm C_2 |g - \sigma_1\, g - \sigma_2\rangle, \tag{B.42}$$

with

$$(C_1/C_2)^2 = \langle \sigma_1 \sigma_2 | \tilde{W}_I | \sigma_1 \sigma_2 \rangle / \langle g - \sigma_1\, g - \sigma_2 | \tilde{W}_I | g - \sigma_1\, g - \sigma_2 \rangle\,, \tag{B.43}$$

The corresponding eigenvalues $\Omega_{(\sigma_1, \sigma_2)}$ are given by

$$\Omega^2_{(\sigma_1, \sigma_2)} = (2j+1)^2 \langle \sigma_1 \sigma_2 | \tilde{W}_I | \sigma_2 \sigma_1 \rangle \langle g - \sigma_1\, g - \sigma_2 | \tilde{W}_I | g - \sigma_1\, g - \sigma_2 \rangle\,.$$

This in turn can be written down in terms of the Wigner d-functions as

$$\Omega_{(\sigma_1, \sigma_2)} = (2j+1)\, \mathrm{e}^{-\mathrm{i}(\theta - \pi)g} d^j_{\sigma_2, \sigma_1}(\beta)\, d^j_{g - \sigma_2, g - \sigma_1}(\beta). \tag{B.44}$$

Multiple PO Manifolds — In this case equation (B.39) admits multiple solutions corresponding to several different combinations of (m_1, m_2). Each pair (m_1, m_2) determines uniquely the pair of constants

$$g_1 = \left\lfloor \frac{(2j+1)(1+2m_1-\theta/\pi)}{2a} \right\rfloor, \qquad g_2 = \left\lfloor \frac{(2j+1)(1+2m_2-\theta/\pi)}{2a} \right\rfloor$$

such that $\tilde{W}_0$ can be thought of as an approximate sum of permutations (if only the largest elements in each row are left), *i.e.* $\tilde{W}_0 \approx \tilde{P}$, where

$$\tilde{P} = (2j+1) \sum_{(m_1,m_2)} \tilde{P}_{(m_1,m_2)}, \tag{B.45}$$
$$\langle \sigma_1\, \sigma_2 | \tilde{P}_{(m_1,m_2)} | \sigma_1'\, \sigma_2' \rangle = \delta_{\sigma_1+\sigma_1', g_1}\, \delta_{\sigma_2+\sigma_2', g_2}.$$

As opposed to the single manifold case, even employing the above approximation it seems to be impossible to provide an explicit formula for the spectrum of $\tilde{W}_I \tilde{P}$ for generic system parameters. However, after the crossover from the regime of a single PO manifold to one containing multiple PO manifolds there exists a certain range of parameters where the permutations $\tilde{P}_{(m_1,m_2)}$ are mutually orthogonal:

$$\tilde{P}_{(m_1',m_2')} \tilde{P}_{(m_1,m_2)} = 0, \qquad \text{for} \quad (m_1', m_2') \neq (m_1, m_2).$$

In this case the total spectrum of $\tilde{W}_I \tilde{P}$ is composed of subspectra of the operators of $\tilde{W}_I \tilde{P}_{(m_1,m_2)}$ and can be easily evaluated. As in the single manifold case, the eigenvectors take a simple form

$$\psi_{(\sigma_1,\sigma_2)} = C_1 |\sigma_1\, \sigma_2\rangle \pm C_2 |g_1 - \sigma_1\, g_2 - \sigma_2\rangle, \tag{B.46}$$

with the corresponding eigenvalues given by:

$$\Omega_{(\sigma_1,\sigma_2)} = (2j+1)\, \mathrm{e}^{-\mathrm{i}(\theta-\pi)(g_1+g_2)/2} d^j_{\sigma_2,\sigma_1}(\beta)\, d^j_{g_2-\sigma_2,g_1-\sigma_1}(\beta). \tag{B.47}$$

The eigenstates with the largest eigenvalues must still be localized at the boundary of the ellipse (7.56). The localization points (σ_1, σ_2) are, therefore, determined by the demand that both points $(g_1 - \sigma_1, g_2 - \sigma_2)$ and (σ_1, σ_2) belong to the ellipse boundary. To see that these are also eigenstates of $\tilde{W}_I \tilde{P}$ it is sufficient to notice that the action of other permutations $\tilde{P}_{(m_1',m_2')} \neq \tilde{P}_{(m_1,m_2)}$ on the states (B.46) brings them to zero.

The numerical computation of the actual spectrum of the operator $\tilde{W}_I \tilde{W}_0$ shows that the localization points of its eigenvectors associated with the highest eigenvalues indeed have the same localization points as the states (B.46), see figure 7.12. Furthermore, as can be seen on the same figure, the bulk of the spectrum is composed of a number of cross-like structures. Each such cross is associated with one of the pairs (m_1, m_2) in the sum (B.46).

B.6. Symplecticity of the Dual Monodromy

To show that $\underline{\tilde{M}}_\gamma$ is symplectic, we first recall that symplectic matrices form a group and thus it suffices to show that $\underline{\tilde{M}}_n$ is symplectic for any $n \in \{1, 2, \dots N\}$. Therefore, if

$$\underline{\tilde{M}}_n^T \, \underline{W} \, \underline{\tilde{M}}_n = \underline{W} \tag{B.48}$$

is fulfilled for a given skew-symmetric $\underline{W}$ $\underline{\tilde{M}}_\gamma$ is symplectic. Choosing the $2N \times 2N$ block diagonal matrix $\underline{W}$ as

$$\underline{W} = \mathrm{diag}(\underline{\Omega}, \dots, \underline{\Omega}) \quad \text{with} \quad \underline{\Omega} = \begin{pmatrix} 0 & 1 \\ -1 & 0 \end{pmatrix} \tag{B.49}$$

reduces the left hand side of (B.48) to calculations of the same type with respect to the possible combinations of $\underline{A}_{n,t}$ and $\underline{B}^{\pm}_{n,t}$ for which we find

$$\underline{B}^{\pm}_{i,t} \, \underline{\Omega} \, \underline{B}^{\pm}_{j,t} = 0 \,, \tag{B.50}$$

$$\underline{A}^T_{n,t} \, \underline{\Omega} \, \underline{B}^{\pm}_{j,t} = \underline{B}^{\pm}_{j,t} \,, \tag{B.51}$$

$$\underline{B}^{\pm}_{i,t} \, \underline{\Omega} \, \underline{A}_{n,t} = -\underline{B}^{\pm}_{i,t} \,. \tag{B.52}$$

For the first line we employed $(\underline{B}^{\pm}_{n,t})^T = \underline{B}^{\pm}_{n,t}$ while the remaining line conveniently cancel each other inside of (B.48). The final condition along the diagonal is

$$\underline{A}^T_{n,t} \underline{\Omega} \underline{A}_{n,t} = \begin{pmatrix} 0 & \frac{\beta^-_{n,t}}{\beta^+_{nt}} \\ -\frac{\beta^-_{n,t}}{\beta^+_{nt}} & 0 \end{pmatrix} \,, \tag{B.53}$$

which is apparently identical to $\underline{\Omega}$ if $\beta^+_{n,t} = \beta^-_{n,t}$. For the Kicked Spin Chain presented here this condition is trivially fulfilled. However, while it is a sufficient condition it is not a necessary one due to the dependence on the concrete basis. Repeating the same calculation for $\underline{M}_\gamma$ instead of $\underline{\tilde{M}}_\gamma$ leads to $\alpha^+_{n,t} = \alpha^-_{n,t}$ which is violated although $\underline{M}_\gamma$ is necessarily symplectic. This might indicate that also for $\underline{\tilde{M}}_\gamma$ a more general proof exists.

B.7. Single Kick Monodromy Matrix

The monodromy of a single kick,

$$S = \begin{pmatrix} a & b \\ c & d \end{pmatrix} \,, \tag{B.54}$$

is only determined by the non-trivial rotational part around the x-axis by angle β, see (7.7) for the Euler decomposition. It is therefore convenient to describe the deviations $(\delta q, \delta p)$ in terms of the unit vectors $\vec{n}$, namely

$$\delta\vec{n} = \begin{pmatrix} -\frac{p}{\sqrt{1-p^2}}\cos q\,\delta p - \sqrt{1-p^2}\sin q\,\delta q \\ -\frac{p}{\sqrt{1-p^2}}\sin q\,\delta p + \sqrt{1-p^2}\cos q\,\delta q \\ \delta p \end{pmatrix} . \tag{B.55}$$

In this case the new deviation is merely given by $\delta\vec{n}' = \underline{R}_x(\beta)\delta\vec{n}$ and the change in δp is readily obtained from the $\delta n_z'$ component. Therefore we find

$$c = \sqrt{1-p^2}\cos(q+\alpha)\sin\beta\,, \tag{B.56}$$

$$d = \cos\beta - \frac{p}{\sqrt{1-p^2}}\sin(q+\alpha)\sin\beta\,, \tag{B.57}$$

where the additional angle α is due to the trivial rotation around z previous to the x rotation. The other two entries follow along the same line using one of the remaining equations. They are

$$n_y' a = \sqrt{1-p^2}\sin(q+\alpha) - \theta'(1-p^2)\cos(q+\alpha)\sin\beta\,, \tag{B.58}$$

$$n_y' b = \sqrt{1-p^2}\cos(q+\alpha)\left(\theta - \theta'(\cos\beta - \theta\sin\beta\sqrt{1-p^2}\sin(q+\alpha))\right) , \tag{B.59}$$

where we introduced the further "short-hand" notations

$$\theta = \frac{p}{1-p^2}\,, \qquad \theta' = \frac{p'}{1-p'^2}\,, \tag{B.60}$$

as well as

$$n_y' = \sqrt{1-p^2}\sin(q+\alpha)\cos\beta - p\sin\beta\,, \tag{B.61}$$

$$p' = \sqrt{1-p^2}\cos(q+\alpha)\sin\beta + p\cos\beta\,. \tag{B.62}$$

List of Figures

Bibliography

[1] M. Akila and B. Gutkin, "Spectral statistics of nearly unidirectional quantum graphs," *Journal of Physics A: Mathematical and Theoretical*, vol. 48, no. 34, p. 345101, 2015.

[2] M. Akila, D. Waltner, B. Gutkin, and T. Guhr, "Particle-time duality in the kicked Ising spin chain," *Journal of Physics A: Mathematical and Theoretical*, vol. 49, no. 37, p. 375101, 2016.

[3] M. Akila, D. Waltner, B. Gutkin, P. Braun, and T. Guhr, "Semiclassical Identification of Periodic Orbits in a Quantum Many-Body System," *Phys. Rev. Lett.*, vol. 118, p. 164101, Apr 2017.

[4] M. Akila, B. Gutkin, P. Braun, D. Waltner, and T. Guhr, "Semiclassical prediction of large spectral fluctuations in interacting kicked spin chains," *Annals of Physics*, vol. 389, pp. 250–282, 2018.

[5] M. Akila, D. Waltner, B. Gutkin, P. Braun, and T. Guhr, "Collectivity and Periodic Orbits in a Chain of Interacting, Kicked Spins," *Acta Physica Polonica A*, vol. 132, pp. 1661–1665, Dec 2017.

[6] D. Waltner, P. Braun, M. Akila, and T. Guhr, "Trace formula for interacting spins," *Journal of Physics A: Mathematical and Theoretical*, vol. 50, no. 8, p. 085304, 2017.

[7] N. B. D. phil., "I. On the constitution of atoms and molecules," *Philosophical Magazine*, vol. 26, no. 151, pp. 1–25, 1913.

[8] P. Ehrenfest, "Adiabatische Invarianten und Quantentheorie," *Annalen der Physik*, vol. 356, no. 19, pp. 327–352, 1916.

[9] W. W. Ph.D., "LXXXIII. The quantum-theory of radiation and line spectra," *Philosophical Magazine*, vol. 29, no. 174, pp. 795–802, 1915.

[10] A. Sommerfeld, "Zur Quantentheorie der Spektrallinien," *Annalen der Physik*, vol. 356, no. 17, pp. 1–94, 1916.

[11] J. H. Van Vleck, "The correspondence principle in the statistical interpretation of quantum mechanics," *Proceedings of the National Academy of Sciences*, vol. 14, no. 2, pp. 178–188, 1928.

[12] R. G. Littlejohn, "The Van Vleck formula, Maslov theory, and phase space geometry," *Journal of Statistical Physics*, vol. 68, pp. 7–50, Jul 1992.

[13] M. C. Gutzwiller, "Periodic Orbits and Classical Quantization Conditions," *Journal of Mathematical Physics*, vol. 12, no. 3, pp. 343–358, 1971.

[14] D. Wintgen, K. Richter, and G. Tanner, "The semiclassical helium atom," *Chaos: An Interdisciplinary Journal of Nonlinear Science*, vol. 2, no. 1, pp. 19–33, 1992.

[15] D. Wintgen and H. Friedrich, "Regularity and Irregularity in Spectra of the Magnetized Hydrogen Atom," *Phys. Rev. Lett.*, vol. 57, pp. 571–574, Aug 1986.

[16] D. Wintgen, "Connection between long-range correlations in quantum spectra and classical periodic orbits," *Phys. Rev. Lett.*, vol. 58, pp. 1589–1592, Apr 1987.

[17] K. Nakamura and T. Harayama, *Quantum Chaos and Quantum Dots*. Mesoscopic physics and nanotechnology, Oxford University Press, 2004.

[18] F. Haake, *Quantum Signatures of Chaos*. Springer Series in Synergetics, Springer, 3 ed., 2010.

[19] F. Haake and D. L. Shepelyansky, "The Kicked Rotator as a Limit of the Kicked Top," *EPL (Europhysics Letters)*, vol. 5, no. 8, p. 671, 1988.

[20] F. Haake, M. Kuś, and R. Scharf, "Classical and quantum chaos for a kicked top," *Zeitschrift für Physik B Condensed Matter*, vol. 65, pp. 381–395, Sep 1987.

[21] S. Chaudhury, A. Smith, B. E. Anderson, S. Ghose, and P. S. Jessen, "Quantum signatures of chaos in a kicked top," *Nature*, vol. 461, pp. 768–771, Oct 2009.

[22] G. Berkolaiko and P. Kuchment, *Introduction to Quantum Graphs*, vol. 186 of *Mathematical Surveys and Monographs*. AMS, 2013.

[23] S. Gnutzmann and U. Smilansky, "Quantum graphs: Applications to quantum chaos and universal spectral statistics," *Advances in Physics*, vol. 55, no. 5-6, pp. 527–625, 2006.

[24] T. Kottos and U. Smilansky, "Quantum Chaos on Graphs," *Phys. Rev. Lett.*, vol. 79, pp. 4794–4797, Dec 1997.

[25] S. Gnutzmann, H. Schanz, and U. Smilansky, "Topological Resonances in Scattering on Networks (Graphs)," *Phys. Rev. Lett.*, vol. 110, p. 094101, Feb 2013.

[26] S. Müller, S. Heusler, P. Braun, and F. Haake, "Semiclassical approach to chaotic quantum transport," *New Journal of Physics*, vol. 9, no. 1, p. 12, 2007.

[27] K. Richter, *Semiclassical Theory of Mesoscopic Quantum Systems*, vol. 161 of *Springer tracts in modern physics*. Berlin: Springer, 2000. war: Habilitationsschrift 1997.

[28] T. Guhr, A. Müller-Groeling, and H. A. Weidenmüller, "Random-matrix theories in quantum physics: common concepts," *Physics Reports*, vol. 299, no. 4–6, pp. 189–425, 1998.

[29] M. Mehta, *Random Matrices*. No. Bd. 142 in Pure and applied mathematics, Elsevier/Academic Press, 2004.

[30] E. P. Wigner, "Characteristic Vectors of Bordered Matrices With Infinite Dimensions," *Annals of Mathematics*, vol. 62, no. 3, pp. 548–564, 1955.

[31] E. P. Wigner, "On the Distribution of the Roots of Certain Symmetric Matrices," *Annals of Mathematics*, vol. 67, no. 2, pp. 325–327, 1958.

[32] O. Bohigas, R. U. Haq, and A. Pandey, "Fluctuation Properties of Nuclear Energy Levels and Widths : Comparison of Theory with Experiment," in *Nuclear Data for Science and Technology: Proceedings of the International Conference Antwerp 6–10 September 1982* (K. H. Böckhoff, ed.), (Dordrecht), pp. 809–813, Springer Netherlands, 1983.

[33] F. J. Dyson, "Statistical Theory of the Energy Levels of Complex Systems. I," *Journal of Mathematical Physics*, vol. 3, no. 1, pp. 140–156, 1962.

[34] G. Casati, F. Valz-Gris, and I. Guarnieri, "On the connection between quantization of nonintegrable systems and statistical theory of spectra," *Lettere al Nuovo Cimento (1971-1985)*, vol. 28, no. 8, pp. 279–282, 1980.

[35] O. Bohigas, M. J. Giannoni, and C. Schmit, "Characterization of Chaotic Quantum Spectra and Universality of Level Fluctuation Laws," *Phys. Rev. Lett.*, vol. 52, pp. 1–4, Jan 1984.

[36] M. V. Berry, "Semiclassical Theory of Spectral Rigidity," *Proceedings of the Royal Society of London A: Mathematical, Physical and Engineering Sciences*, vol. 400, no. 1819, pp. 229–251, 1985.

[37] M. Sieber and K. Richter, "Correlations between periodic orbits and their rôle in spectral statistics," *Physica Scripta*, vol. 2001, no. T90, p. 128, 2001.

[38] S. Müller, S. Heusler, P. Braun, F. Haake, and A. Altland, "Semiclassical Foundation of Universality in Quantum Chaos," *Phys. Rev. Lett.*, vol. 93, p. 014103, Jul 2004.

[39] M. Robnik and M. V. Berry, "False time-reversal violation and energy level statistics: the role of anti-unitary symmetry," *Journal of Physics A: Mathematical and General*, vol. 19, no. 5, p. 669, 1986.

[40] I. Bloch, J. Dalibard, and W. Zwerger, "Many-body physics with ultracold gases," *Rev. Mod. Phys.*, vol. 80, pp. 885–964, Jul 2008.

[41] N. Goldman, J. C. Budich, and P. Zoller, "Topological quantum matter with ultracold gases in optical lattices," *Nat Phys*, vol. 12, pp. 639–645, Jul 2016. Progress Article.

[42] M. Greiner, O. Mandel, T. Esslinger, T. W. Hansch, and I. Bloch, "Quantum phase transition from a superfluid to a Mott insulator in a gas of ultracold atoms," *Nature*, vol. 415, pp. 39–44, Jan 2002.

[43] S. Baier, M. J. Mark, D. Petter, K. Aikawa, L. Chomaz, Z. Cai, M. Baranov, P. Zoller, and F. Ferlaino, "Extended Bose-Hubbard models with ultracold magnetic atoms," *Science*, vol. 352, no. 6282, pp. 201–205, 2016.

[44] D. Basko, I. Aleiner, and B. Altshuler, "Metal–insulator transition in a weakly interacting many-electron system with localized single-particle states," *Annals of Physics*, vol. 321, no. 5, pp. 1126–1205, 2006.

[45] S. Murmann, F. Deuretzbacher, G. Zürn, J. Bjerlin, S. M. Reimann, L. Santos, T. Lompe, and S. Jochim, "Antiferromagnetic Heisenberg Spin Chain of a Few Cold Atoms in a One-Dimensional Trap," *Phys. Rev. Lett.*, vol. 115, p. 215301, Nov 2015.

[46] C. Senko, P. Richerme, J. Smith, A. Lee, I. Cohen, A. Retzker, and C. Monroe, "Realization of a Quantum Integer-Spin Chain with Controllable Interactions," *Phys. Rev. X*, vol. 5, p. 021026, Jun 2015.

[47] B. Yan, S. A. Moses, B. Gadway, J. P. Covey, K. R. A. Hazzard, A. M. Rey, D. S. Jin, and J. Ye, "Observation of dipolar spin-exchange interactions with lattice-confined polar molecules," *Nature*, vol. 501, pp. 521–525, Sep 2013. Letter.

[48] M. Žnidarič, T. Prosen, and P. Prelovšek, "Many-body localization in the Heisenberg XXZ magnet in a random field," *Phys. Rev. B*, vol. 77, p. 064426, Feb 2008.

[49] T. Langen, R. Geiger, and J. Schmiedmayer, "Ultracold Atoms Out of Equilibrium," *Annual Review of Condensed Matter Physics*, vol. 6, no. 1, pp. 201–217, 2015.

[50] A. Eckardt, "Colloquium," *Rev. Mod. Phys.*, vol. 89, p. 011004, Mar 2017.

[51] S. Diehl, A. Micheli, A. Kantian, B. Kraus, H. P. Buchler, and P. Zoller, "Quantum states and phases in driven open quantum systems with cold atoms," *Nat Phys*, vol. 4, pp. 878–883, Nov 2008.

[52] F. Renzoni, "Chapter 1 Driven Ratchets for Cold Atoms," *Advances In Atomic, Molecular, and Optical Physics*, vol. 57, pp. 1–32, 2009. Advances in Atomic Molecular and Optical Physics.

[53] T. Engl, J. Dujardin, A. Argüelles, P. Schlagheck, K. Richter, and J. D. Urbina, "Coherent Backscattering in Fock Space: A Signature of Quantum Many-Body Interference in Interacting Bosonic Systems," *Phys. Rev. Lett.*, vol. 112, p. 140403, Apr 2014.

[54] T. Engl, J. D. Urbina, and K. Richter, "Periodic mean-field solutions and the spectra of discrete bosonic fields: Trace formula for Bose-Hubbard models," *Phys. Rev. E*, vol. 92, p. 062907, Dec 2015.

[55] T. Engl, P. Plößl, J. D. Urbina, and K. Richter, "The semiclassical propagator in fermionic Fock space," *Theoretical Chemistry Accounts*, vol. 133, p. 1563, Sep 2014.

[56] R. Dubertrand and S. Müller, "Spectral statistics of chaotic many-body systems," *New Journal of Physics*, vol. 18, no. 3, p. 033009, 2016.

[57] J. Hämmerling, B. Gutkin, and T. Guhr, "Collective vs. single-particle motion in quantum many-body systems: Spreading and its semiclassical interpretation in the perturbative regime," *EPL (Europhysics Letters)*, vol. 96, no. 2, p. 20007, 2011.

[58] J. Hämmerling, B. Gutkin, and T. Guhr, "Collective versus single-particle motion in quantum many-body systems from the perspective of an integrable model," *Journal of Physics A: Mathematical and Theoretical*, vol. 43, no. 26, p. 265101, 2010.

[59] V. Molinari, D. Mostacci, and B. D. Ganapol, "Wave Propagation in an Ideal Gas: First and Second Sound," *Journal of Computational and Theoretical Transport*, vol. 45, no. 4, pp. 268–274, 2016.

[60] T. Simula, "Collective dynamics of vortices in trapped Bose-Einstein condensates," *Phys. Rev. A*, vol. 87, p. 023630, Feb 2013.

[61] D. A. Butts and D. S. Rokhsar, "Predicted signatures of rotating Bose-Einstein condensates," *Nature*, pp. 327–329, 1999.

[62] M. Knobel, W. C. Nunes, L. M. Socolovsky, E. De Biasi, J. M. Vargas, and J. C. Denardin, "Superparamagnetism and Other Magnetic Features in Granular Materials: A Review on Ideal and Real Systems," *Journal of Nanoscience and Nanotechnology*, vol. 8, no. 6, pp. 2836–2857, 2008.

[63] W. Nazarewicz, "The nuclear collective motion," in *An Advanced Course in Modern Nuclear Physics* (J. Arias and M. Lozano, eds.), vol. 581 of *Lecture Notes in Physics*, pp. 102–140, Springer Berlin Heidelberg, 2001.

[64] A. V. D. Woude, "Giant resonances," *Progress in Particle and Nuclear Physics*, vol. 18, no. 0, pp. 217–293, 1987.

[65] K. A. Snover, "Giant Resonances in Excited Nuclei," *Annual Review of Nuclear and Particle Science*, vol. 36, no. 1, pp. 545–603, 1986.

[66] F. E. Bertrand, "Giant multipole resonances — perspectives after ten years," *Nuclear Physics A*, vol. 354, no. 1–2, pp. 129–156, 1981.

[67] B. Gutkin and V. Osipov, "Classical foundations of many-particle quantum chaos," *Nonlinearity*, vol. 29, no. 2, p. 325, 2016.

[68] H.-J. Stöckmann, *Quantum Chaos – an introduction*. Cambridge University Press, 2006.

[69] F. Calogero, V. Zakharov, N. Ercolani, H. Flaschka, V. Marchenko, A. Mikhailov, A. Newell, E. Schulman, A. Shabat, E. Siggia, *et al.*, *What Is Integrability?* Springer Series in Nonlinear Dynamics, Springer Berlin Heidelberg, 2012.

[70] B. Chirikov and D. Shepelyansky, "Chirikov standard map," *Scholarpedia*, vol. 3, no. 3, p. 3550, 2008. revision #183857.

[71] M. Richter, S. Lange, A. Bäcker, and R. Ketzmerick, "Visualization and comparison of classical structures and quantum states of four-dimensional maps," *Phys. Rev. E*, vol. 89, p. 022902, Feb 2014.

[72] F. Onken, S. Lange, R. Ketzmerick, and A. Bäcker, "Bifurcations of families of 1D-tori in 4D symplectic maps," *Chaos: An Interdisciplinary Journal of Nonlinear Science*, vol. 26, no. 6, p. 063124, 2016.

[73] F. Leyvraz, C. Schmit, and T. H. Seligman, "Anomalous spectral statistics in a symmetrical billiard," *Journal of Physics A: Mathematical and General*, vol. 29, no. 22, p. L575, 1996.

[74] C. H. Joyner, S. Müller, and M. Sieber, "Semiclassical approach to discrete symmetries in quantum chaos," *Journal of Physics A: Mathematical and Theoretical*, vol. 45, no. 20, p. 205102, 2012.

[75] F. J. Dyson, "The Threefold Way. Algebraic Structure of Symmetry Groups and Ensembles in Quantum Mechanics," *Journal of Mathematical Physics*, vol. 3, no. 6, pp. 1199–1215, 1962.

[76] T. Prosen and M. Žnidarič, "Is the efficiency of classical simulations of quantum dynamics related to integrability?," *Phys. Rev. E*, vol. 75, p. 015202, Jan 2007.

[77] A. M. O. de Almeida and J. H. Hannay, "Resonant periodic orbits and the semiclassical energy spectrum," *Journal of Physics A: Mathematical and General*, vol. 20, no. 17, p. 5873, 1987.

[78] M. de Aguiar, C. Malta, M. Baranger, and K. Davies, "Bifurcations of periodic trajectories in non-integrable Hamiltonian systems with two degrees of freedom: Numerical and analytical results," *Annals of Physics*, vol. 180, no. 2, pp. 167–205, 1987.

[79] H. Schomerus and M. Sieber, "Bifurcations of periodic orbits and uniform approximations," *Journal of Physics A: Mathematical and General*, vol. 30, no. 13, p. 4537, 1997.

[80] C. Manderfeld and H. Schomerus, "Semiclassical singularities from bifurcating orbits," *Phys. Rev. E*, vol. 63, p. 066208, May 2001.

[81] M. V. Berry, J. P. Keating, and H. Schomerus, "Universal twinkling exponents for spectral fluctuations associated with mixed chaology," *Proceedings of the Royal Society of London A: Mathematical, Physical and Engineering Sciences*, vol. 456, no. 1999, pp. 1659–1668, 2000.

[82] S. Heusler, S. Müller, A. Altland, P. Braun, and F. Haake, "Periodic-Orbit Theory of Level Correlations," *Phys. Rev. Lett.*, vol. 98, p. 044103, Jan 2007.

[83] B. Gutkin, "Dynamical 'breaking' of time reversal symmetry," *Journal of Physics A: Mathematical and Theoretical*, vol. 40, no. 31, p. F761, 2007.

[84] B. Gutkin, "Note on converse quantum ergodicity," *Proc. Amer. Math. Soc.*, vol. 137, no. 8, pp. 2795–2800, 2009.

[85] G. Veble, T. Prosen, and M. Robnik, "Expanded boundary integral method and chaotic time-reversal doublets in quantum billiards," *New Journal of Physics*, vol. 9, no. 1, p. 15, 2007.

[86] B. Dietz, T. Guhr, B. Gutkin, M. Miski-Oglu, and A. Richter, "Spectral properties and dynamical tunneling in constant-width billiards," *Phys. Rev. E*, vol. 90, p. 022903, Aug 2014.

[87] M. Sieber, "Spectral statistics in chaotic systems with a point interaction," *Journal of Physics A: Mathematical and General*, vol. 33, no. 36, p. 6263, 2000.

[88] E. Bogomolny, P. Leboeuf, and C. Schmit, "Spectral Statistics of Chaotic Systems with a Pointlike Scatterer," *Phys. Rev. Lett.*, vol. 85, pp. 2486–2489, Sep 2000.

[89] I. L. Aleiner and K. A. Matveev, "Shifts of Random Energy Levels by a Local Perturbation," *Phys. Rev. Lett.*, vol. 80, pp. 814–816, Jan 1998.

[90] C. E. Porter and R. G. Thomas, "Fluctuations of Nuclear Reaction Widths," *Phys. Rev.*, vol. 104, pp. 483–491, Oct 1956.

[91] F. M. Marchetti, I. E. Smolyarenko, and B. D. Simons, "Universality of parametric spectral correlations: Local versus extended perturbing potentials," *Phys. Rev. E*, vol. 68, p. 036217, Sep 2003.

[92] M. Hentschel, D. Ullmo, and H. U. Baranger, "Fermi edge singularities in the mesoscopic regime: Anderson orthogonality catastrophe," *Phys. Rev. B*, vol. 72, p. 035310, Jul 2005.

[93] A. Bäcker, "Numerical Aspects of Eigenvalue and Eigenfunction Computations for Chaotic Quantum Systems," in *The Mathematical Aspects of Quantum Maps* (M. D. Esposti and S. Graffi, eds.), vol. 618 of *Lecture Notes in Physics, Berlin Springer Verlag*, pp. 91–144, 2003.

[94] G. Berkolaiko and B. Winn, "Relationship between scattering matrix and spectrum of quantum graphs," *Trans. Amer. Math. Soc.*, vol. 362, no. 12, pp. 6261–6277, 2010.

[95] B. Gutkin and V. A. Osipov, "Clustering of periodic orbits in chaotic systems," *Nonlinearity*, vol. 26, no. 1, p. 177, 2013.

[96] H. Schanz and T. Kottos, "Scars on Quantum Networks Ignore the Lyapunov Exponent," *Phys. Rev. Lett.*, vol. 90, p. 234101, Jun 2003.

[97] W. B. Hayes, "Is the outer Solar System chaotic?," *Nat Phys*, vol. 3, pp. 689–691, Oct 2007.

[98] K. Mon and J. French, "Statistical properties of many-particle spectra," *Annals of Physics*, vol. 95, no. 1, pp. 90–111, 1975.

[99] R. A. Small and S. Müller, "Particle diagrams and statistics of many-body random potentials," *Annals of Physics*, vol. 356, no. Supplement C, pp. 269–298, 2015.

[100] L. Benet and H. A. Weidenmüller, "Review of the k -body embedded ensembles of Gaussian random matrices," *Journal of Physics A: Mathematical and General*, vol. 36, no. 12, p. 3569, 2003.

[101] H. Primack and U. Smilansky, "On the accuracy of the semiclassical trace formula," *Journal of Physics A: Mathematical and General*, vol. 31, no. 29, p. 6253, 1998.

[102] H. Primack and U. Smilansky, "The quantum three-dimensional Sinai billiard – a semiclassical analysis," *Physics Reports*, vol. 327, no. 1, pp. 1–107, 2000.

[103] M. Gessner, V. M. Bastidas, T. Brandes, and A. Buchleitner, "Semiclassical excited-state signatures of quantum phase transitions in spin chains with variable-range interactions," *Phys. Rev. B*, vol. 93, p. 155153, Apr 2016.

[104] M. Žnidarič, "Exact Large-Deviation Statistics for a Nonequilibrium Quantum Spin Chain," *Phys. Rev. Lett.*, vol. 112, p. 040602, Jan 2014.

[105] B. Buča and T. Prosen, "Exactly Solvable Counting Statistics in Open Weakly Coupled Interacting Spin Systems," *Phys. Rev. Lett.*, vol. 112, p. 067201, Feb 2014.

[106] J. Simon, W. S. Bakr, R. Ma, M. E. Tai, P. M. Preiss, and M. Greiner, "Quantum simulation of antiferromagnetic spin chains in an optical lattice," *Nature*, vol. 472, pp. 307–312, apr 2011.

[107] K. Kim *et al.*, "Quantum simulation of frustrated Ising spins with trapped ions," *Nature*, vol. 465, pp. 590–593, June 2010.

[108] J. Smith *et al.*, "Many-body localization in a quantum simulator with programmable random disorder," *Nat Phys*, vol. 12, pp. 907–911, 10 2016.

[109] F. Verstraete, V. Murg, and J. Cirac, "Matrix product states, projected entangled pair states, and variational renormalization group methods for quantum spin systems," *Advances in Physics*, vol. 57, no. 2, pp. 143–224, 2008.

[110] D. Perez-Garcia, F. Verstraete, M. M. Wolf, and J. I. Cirac, "Matrix Product State Representations," *Quantum Info. Comput.*, vol. 7, pp. 401–430, July 2007.

[111] M. C. Bañuls, M. B. Hastings, F. Verstraete, and J. I. Cirac, "Matrix Product States for Dynamical Simulation of Infinite Chains," *Phys. Rev. Lett.*, vol. 102, p. 240603, Jun 2009.

[112] M. B. Hastings and R. Mahajan, "Connecting entanglement in time and space: Improving the folding algorithm," *Phys. Rev. A*, vol. 91, p. 032306, Mar 2015.

[113] A. Georges, G. Kotliar, W. Krauth, and M. J. Rozenberg, "Dynamical mean-field theory of strongly correlated fermion systems and the limit of infinite dimensions," *Rev. Mod. Phys.*, vol. 68, pp. 13–125, Jan 1996.

[114] T. Prosen, "Exact Time-Correlation Functions of Quantum Ising Chain in a Kicking Transversal Magnetic Field: Spectral Analysis of the Adjoint Propagator in Heisenberg Picture," *Progress of Theoretical Physics Supplement*, vol. 139, p. 191, 2000.

[115] T. Prosen, "General relation between quantum ergodicity and fidelity of quantum dynamics," *Phys. Rev. E*, vol. 65, p. 036208, Feb 2002.

[116] C. Pineda and T. Prosen, "Universal and nonuniversal level statistics in a chaotic quantum spin chain," *Phys. Rev. E*, vol. 76, p. 061127, Dec 2007.

[117] T. Prosen, "Chaos and complexity of quantum motion," *Journal of Physics A: Mathematical and Theoretical*, vol. 40, no. 28, p. 7881, 2007.

[118] E. Lieb, T. Schultz, and D. Mattis, "Two soluble models of an antiferromagnetic chain," *Annals of Physics*, vol. 16, no. 3, pp. 407–466, 1961.

[119] H. A. Kramers and G. H. Wannier, "Statistics of the Two-Dimensional Ferromagnet. Part I," *Phys. Rev.*, vol. 60, pp. 252–262, Aug 1941.

[120] H. A. Kramers and G. H. Wannier, "Statistics of the Two-Dimensional Ferromagnet. Part II," *Phys. Rev.*, vol. 60, pp. 263–276, Aug 1941.

[121] C. Pineda, T. Prosen, and E. Villaseñor, "Two dimensional kicked quantum Ising model: dynamical phase transitions," *New Journal of Physics*, vol. 16, no. 12, p. 123044, 2014.

[122] Y. Y. Atas and E. Bogomolny, "Spectral density of a one-dimensional quantum Ising model: Gaussian and multi-Gaussian approximations," *Journal of Physics A: Mathematical and Theoretical*, vol. 47, no. 33, p. 335201, 2014.

[123] J. Keating, N. Linden, and H. Wells, "Random matrices and quantum spin chains," *Markov Processes and Related Fields*, vol. 21, no. 3, pp. 537–555, 2015. cited By 2.

[124] J. P. Keating, N. Linden, and H. J. Wells, "Spectra and Eigenstates of Spin Chain Hamiltonians," *Communications in Mathematical Physics*, vol. 338, no. 1, pp. 81–102, 2015.

[125] M. Kardar, *Statistical Physics of Fields:*. Cambridge University Press, 2007.

[126] D. Waltner, *Semiclassical Approach to Mesoscopic Systems*. Springer Tracts in Modern Physics, Springer Berlin Heidelberg, 2012.

[127] D. Waltner and J. Kuipers, "Ehrenfest-time dependence of quantum transport corrections and spectral statistics," *Phys. Rev. E*, vol. 82, p. 066205, Dec 2010.

[128] P. W. Brouwer, S. Rahav, and C. Tian, "Spectral form factor near the Ehrenfest time," *Phys. Rev. E*, vol. 74, p. 066208, Dec 2006.

[129] P. A. Braun, P. Gerwinski, F. Haake, and H. Schomerus, "Semiclassics of rotation and torsion," *Zeitschrift für Physik B Condensed Matter*, vol. 100, no. 1, pp. 115–127, 1996.

[130] C. Neill *et al.*, "Ergodic dynamics and thermalization in an isolated quantum system," *Nat Phys*, vol. 12, pp. 1037–1041, 11 2016.

[131] S. Keppeler, *Spinning particles: Semiclassical quantisation and spectral statistics*. PhD thesis, Universität Ulm, 2002.

[132] D. Wintgen, "Connection between long-range correlations in quantum spectra and classical periodic orbits," *Phys. Rev. Lett.*, vol. 58, pp. 1589–1592, Apr 1987.

[133] H.-J. Stöckmann and J. Stein, ""Quantum" chaos in billiards studied by microwave absorption," *Phys. Rev. Lett.*, vol. 64, pp. 2215–2218, May 1990.

[134] A. Holle, J. Main, G. Wiebusch, H. Rottke, and K. H. Welge, "Quasi-Landau Spectrum of the Chaotic Diamagnetic Hydrogen Atom," *Phys. Rev. Lett.*, vol. 61, pp. 161–164, Jul 1988.

[135] M. Kuś, F. Haake, and D. Delande, "Prebifurcation periodic ghost orbits in semiclassical quantization," *Phys. Rev. Lett.*, vol. 71, pp. 2167–2171, Oct 1993.

[136] V. Namias, "The Fractional Order Fourier Transform and its Application to Quantum Mechanics," *IMA Journal of Applied Mathematics*, vol. 25, no. 3, pp. 241–265, 1980.

[137] C. Candan, M. A. Kutay, and H. M. Ozaktas, "The discrete fractional Fourier transform," *IEEE Transactions on Signal Processing*, vol. 48, pp. 1329–1337, May 2000.

[138] C. Braun, F. Li, A. Garg, and M. Stone, "The semiclassical coherent state propagator in the Weyl representation," *Journal of Mathematical Physics*, vol. 56, no. 12, p. 122106, 2015.

[139] D. Varshalovich, A. Moskalev, and V. Khersonskii, *Quantum Theory Of Angular Momentum*. World Scientific, 1988.